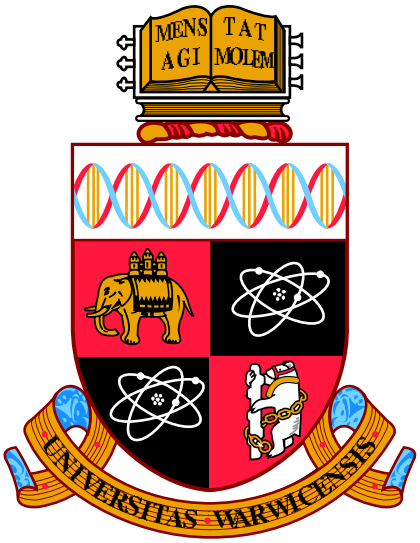

Development and Application of High-Resolution Solid-State NMR Methods for Probing Polymorphism of Active Pharmaceutical Ingredients

by

Jonathan Paul Bradley

Thesis

Submitted to the University of Warwick

for the degree of

Doctor of Philosophy

Department of Physics

April 2011

THE UNIVERSITY OF
WARWICK

CONTENTS

LIST OF TABLES

LIST OF FIGURES

ACKNOWLEDGEMENTS

I would like to thank my supervisor, Prof. Steven Brown, for giving me the opportunity to undertake an interesting and exciting research project and for the help and guidance he has provided throughout my PhD studies. I am also very grateful to the rest of the solid-state NMR group, especially those who have (very patiently) taught me how to use the spectrometers and resolved many technical problems for me.

I would also like to acknowledge the contributions of several people to the projects presented in this thesis, notably Les Hughes and Dave Martin, for their involvement in the sibenadet HCl project, and for allowing me to make use of the solid-state NMR facilities at AstraZeneca; Carmen Tripon and Claudiu Filip for their advice and assistance in the DQ simulations work and Oleg Antzutkin, for his involvement in the indomethacin project. Funding from AstraZeneca is gratefully acknowledged.

Many thanks to all of my friends, but in particular Ruth, who has been so kind and supportive, and has always cheered me up on days when the thesis writing was not going well. Finally I wish to thank my parents, my sister, Louise and the rest of my family, for their support and encouragement, not just during my PhD, but for all of the last twenty-six years.

DECLARATION

The work presented in this thesis is my own, except where stated otherwise in the text. The research was conducted under the supervision of Prof. Steven P. Brown at the University of Warwick between July 2007 and April 2011.

This thesis has not been submitted for a degree at another university.

Some of the results presented in this work, specifically those presented in chapter 4, have been published:

J. P. Bradley, C. Tripon, C. Filip and S. P. Brown. Determining relative proton-proton proximities from the build-up of two-dimensional correlation peaks in ^{1}H double-quantum MAS NMR: insight from multi-spin density matrix simulations. *Phys. Chem. Chem. Phys.*, 11(32):6941–6952, 2009. [1]

ABSTRACT

The objective of the work presented in this thesis is to apply advanced high-resolution solid-state NMR methods for the structural characterisation of organic crystalline systems, specifically active pharmaceutical ingredients (APIs). The determination of the crystal packing is an important stage in the development of new APIs, and solid-state magic angle spinning (MAS) NMR is well suited to complement existing techniques. Improvements in spectral resolution in recent years have led to the development of homonuclear correlation experiments capable of identifying intermolecular proximities between ^{1}H nuclei. These experiments provide a powerful probe of the local environment of each ^{1}H nucleus in the three-dimensional structure, and the majority of the research presented in this thesis is focussed on the development of detailed analysis methods that may be used to extract more detailed structural information from 2D solid-state NMR correlation spectra.

Throughout this thesis, experimental solid-state NMR results are analysed alongside computational data, including density matrix simulations of experiments and first-principles calculations of shielding tensors. The results of simulations of a ^{1}H DQ (double-quantum) correlation experiment are compared to experiment, in order to investigate the dependence of the DQ build-up (change in peak intensity as a function of the recoupling pulse duration) on the precise nature of the dipolar coupled proton network. It is found (for a simple dipeptide) that quantitative information on the relative H–H distance may be obtained by comparison of the maximum intensity reached in the corresponding ^{1}H DQ build-up curves. This method is then applied to pharmaceutically relevant systems. It is shown that differences between two polymorphs of an API may be identified in the ^{1}H DQ build-up of particular peaks, and, following the analysis for the dipeptide, this difference may be ascribed to differences in specific intermolecular distances. In the study of a second API, γ-indomethacin, it is shown that the standard ^{1}H DQ experiment provides insufficient resolution to identify specific DQ peaks. A recently developed ^{1}H(DQ)–^{13}C correlation experiment is used to exploit the higher resolution in the ^{13}C dimension, hence allowing the extraction of DQ build-up curves which may be used, in conjunction with simulations, to obtain structural data.

Finally, a recently discovered polymorph of the API ibuprofen is studied using ^{13}C CPMAS (cross polarisation) solid-state NMR. Through the use of first-principles calculations, the ^{13}C spectra of both the well known and new polymorphs are assigned, and the conversion of an amorphous solid to the new polymorph is monitored through the use of temperature-controlled solid-state NMR experiments.

ABBREVIATIONS

ABMS	Anisotropic Bulk Magnetic Susceptibility
API	Active Pharmaceutical Ingredient
BABA	BAck-to-BAck
CP	Cross Polarisation
CRAMPS	Combined Rotation And Multiple Pulse Spectroscopy
CSA	Chemical Shift Anisotropy
DFT	Density Functional Theory
DQ	Double Quantum
DUMBO	Decoupling Using Mind Boggling Optimisation
FID	Free Induction Decay
FSLG	Frequency-Switched Lee-Goldburg
FT	Fourier Transform
FWHMH	Full Width at Half Maximum Height
GIPAW	Gauge-Including Projector Augmented Waves
INEPT	Insensitive Nuclei Enhanced by Polarisation Transfer
MAS	Magic Angle Spinning
NMR	Nuclear Magnetic Resonance
PAS	Principal Axis System
PMLG	Phase-Modulated Lee Goldburg
ppm	Parts Per Million
POSTC7	Permutationally Offset Stabilised C7
REDOR	Rotational-Echo DOuble Resonance
rf	Radio Frequency
S/N	Signal-to-Noise

SPINAL	Small Phase INcremental ALternation
SQ	Single Quantum
TPPI	Time Proportional Phase Increment
TPPM	Two Pulse Phase Modulated

CHAPTER

ONE

INTRODUCTION

1.1 Solid-State NMR Background

The field of nuclear magnetic resonance (NMR) has experienced an extraordinary pace of development since the first observations of NMR signals from bulk materials, in experiments performed independently by Purcell [2] and Bloch [3] and co-workers in 1946. It is notable that although some of the initial experiments by both Purcell and Bloch were performed on solid samples, the majority of the development in NMR for many years was focussed on liquids. A simple NMR experiment performed on a static solid sample will usually result in a broad featureless peak, due to the many anisotropic interactions present in a solid sample. Solution-state NMR is unencumbered of such considerations due to the rapid and essentially random molecular motion inherent to liquids, which results in an averaging of anisotropic interactions over an extremely short time-scale. Consequently, high resolution NMR spectra are readily obtainable from solutions and so the technique has become a routine analytical tool in many branches of chemistry.

Despite the inherent difficulty of performing NMR experiments on solid-state samples, a wealth of information unobtainable by other spectroscopic techniques is potentially available if these problems can be overcome. For many practical applications, it is useful to study the solid, rather than a solution. For example, the work presented in later chapters of this thesis is principally concerned with the use of NMR to investigate the way in which organic molecules pack together in the solid state. In order

to obtain useful information from an NMR spectrum of a solid sample, the resolution of the spectrum must be improved. The most widely applied method to reduce the width of spectral lines in solid-state NMR is magic-angle spinning (MAS). This technique involves rapid rotation of the sample about an axis inclined at an angle of $\arctan\sqrt{2} \approx 54.7^\circ$ relative to the externally applied magnetic field, which results in a partial averaging of the anisotropic interactions.

The use of MAS to improve the resolution of a solid-state NMR spectrum was first reported independently by Andrew *et. al.* [4, 5] and Lowe [6] in the late 1950s. The advancement in MAS technology has resulted in ever increasing spinning frequencies being achieved, with a corresponding decrease in the diameter of the rotor used to hold the sample [7]. While MAS at relatively low frequencies (of the order of several kilohertz) is sufficient to produce high resolution spectra for nuclei such as ^{13}C or ^{15}N, it is not effective in the removal of the very strong ^{1}H–^{1}H or ^{19}F–^{19}F homonuclear dipolar coupling interactions. Consequently homonuclear decoupling techniques, which involve the application of high powered *rf* pulses to the sample, have been developed to provide an alternative method of line narrowing in solid-state NMR experiments on ^{1}H or ^{19}F nuclei [8, 9].

Early examples of homonuclear decoupling techniques were designed to be applied to static samples. In the mid-1960s Lee and Goldburg demonstrated the use of radio-frequency (*rf*) irradiation to narrow the ^{19}F lines in a sample of calcium fluoride. Their method involved the application of continuous, off-resonance *rf* to create an effective field aligned at the magic angle to the external field [10]. The precession of the nuclear magnetisation about this effective field resulted in an averaging of the first order dipolar Hamiltonian, and a corresponding decrease in the line width. An alternative approach was proposed three years later by Waugh and co-workers [11, 12]. Their method, again applied in the static case, involved the use of a series of on-resonance *rf* pulses of varying phase. The use of this sequence, designated WaHuHa or WHH, resulted in an averaging of the first and second order dipolar Hamiltonian terms. The introduction of WHH also marked the first use of windowed decoupling sequences. Since the sequence consisted of a series of *rf* pulses and delays rather than continuous irradiation, the NMR signal could be acquired during the delays.

While homonuclear decoupling on static samples results in a narrowing of the

spectral lines as the homonuclear dipolar coupling is reduced, broadening due to the chemical shift anisotropy (CSA) remains. The emergence of combined rotation and multiple pulse spectroscopy (CRAMPS) [13–15], in which multiple pulse homonuclear decoupling schemes combined with physical rotation of the sample by MAS has therefore led to further improvements in spectral resolution for ^{1}H solid-state NMR. Examples of commonly used CRAMPS sequences include frequency-switched [16] and phase-modulated [17] Lee-Goldberg sequences (FSLG and PMLG respectively) and the DUMBO (decoupling using mind boggling optimisation) [18] sequence. The DUMBO sequence and in particular the eDUMBO [19] variant, which is directly optimised through experiment, are used extensively in experiments presented in later chapters of this thesis, in both windowed and windowless forms.

While the discussion so far has focussed on the efforts to improve the spectral resolution by removing the anisotropic interactions that cause line broadening in a solid-state NMR experiment, a total removal of these interactions at all times during the course of an experiment is not always desirable. Indeed, rather than representing a lack of information, the broad featureless peak seen in a static experiment without decoupling on a solid sample can be thought of as far too much information being presented in the spectrum. The anisotropic chemical shift and dipolar coupling interactions that cause the broadening are dependent on the precise arrangement of nuclei in the solid-state. If this information can be selectively re-introduced into a high-resolution spectrum, it provides a powerful probe of the local chemical environment of each nuclear site in the sample.

One application of the dipolar coupling is the cross polarisation (CP) technique in which magnetisation is transferred from one nuclear species to another, via the heteronuclear dipolar interaction [20]. CP allows the study of less sensitive nuclei [21, 22], such as ^{13}C and ^{15}N, usually with magnetisation transferred from ^{1}H nuclei. With the addition of magic-angle spinning and ^{1}H decoupling during acquisition, the CPMAS experiment [23] has become a standard technique in the study of less sensitive nuclei and allows the acquisition of spectra in a short time-scale at natural abundance.

In addition to the use of the dipolar interaction to overcome the low sensitivity of certain nuclei, experiments have been developed to exploit the dependence of the interaction on the relative positions of nuclei within a solid structure. Specifically the

magnitude of the dipolar coupling interaction depends on the internuclear distance to the inverse third power. It therefore provides an extremely sensitive measurement of the separation between the two nuclei. Experiments to measure the dipolar coupling between a pair of spins use rotor synchronised pulse sequences to recouple the interaction, re-introducing the dipolar coupling removed by magic angle spinning. In the case of heteronuclear couplings, pulse sequences such as REDOR (Rotational-echo double resonance) [24] may be used.

Much of the work presented in this thesis involves the use of the homonuclear dipolar interaction between coupled ^{1}H nuclei to obtain structural information. A homonuclear approach to the measurement of the dipolar coupling is therefore required. This relies on the use of double-quantum (DQ) filtered experiments, which excite the DQ coherence between dipolar coupled nuclei [25]. Following the initial development of rotor synchronised sequences for the recoupling of the dipolar interaction [26, 27], a wide variety of different recoupling sequences have been introduced [28–31]. A two-dimensional experiment is required, since the DQ coherence is not directly observable. It must be allowed to evolve during an indirectly observed time dimension, before conversion to a single-quantum coherence which results in an observable NMR signal. DQ filtered experiments have been successfully used to measure the dipolar coupling, and hence distance, between pairs of ^{13}C nuclei in selectively labelled compounds [32]. A simple two-dimensional DQ experiment will result in a spectrum showing correlation peaks for dipolar coupled nuclei at the isotropic chemical shift in one dimension, and at sums of chemical shifts in the other. Such a spectrum acts rather like a map of the nuclei within the sample, identifying which nuclei are in close spatial proximity.

The use of these experiments for ^{1}H nuclei was first reported in the mid-1980s [33], in studies of spin-clusters in deuterated materials. The increase in the available MAS rate led to the use of ^{1}H DQ experiments combined with fast MAS to achieve spectra of natural abundance organic compounds, with sufficient resolution to identify DQ peaks due to specific dipolar-coupling interactions [34–36]. The addition of CRAMPS decoupling schemes during both t_1 and t_2 gave further increases in the resolution of ^{1}H DQ spectra [37–39]. A striking example of the superior resolution provided by CRAMPS compared to fast MAS alone is shown in reference [38], in which ^{1}H line widths as narrow as 0.3 ppm are shown in the direct dimension of a DQ CRAMPS

(12.5 kHz MAS) spectrum of the dipeptide β-AspAla, in contrast to widths of 1.5 ppm in a spectrum recorded at 30 kHz. Although recent advances in MAS technology have resulted in modern commercially available equipment capable of spinning frequencies in excess of 60 kHz, the resolution in ^{1}H DQ spectra of organic solids achieved through the use of such fast MAS still does not in general reach that for spectra acquired at lower spinning frequencies with the addition of homonuclear decoupling.

Recent years have seen an increasing use of computational techniques in conjunction with solid-state NMR experiments. Simulations are now regarded as an essential counterpart to experiment in the field of developing new solid-state NMR techniques [40]. Several numerical simulation software packages capable of accurately reproducing experimental results are now freely available [41–43] and these have been used to study a wide variety of areas, including double-quantum build-up [1], spin-echo dephasing [44] and homonuclear [45] and heteronuclear [46, 47] decoupling techniques.

First principles calculations based on density functional theory (DFT) also play an important role in the investigation of crystal structures by solid-state NMR. The CASTEP [48] program uses plane-wave pseudopotentials [49] to describe the electron density throughout a material. The dependence of this method on periodic structure makes it ideally suited to the study of crystalline systems. CASTEP may be used to calculate a variety of properties of a crystalline system, including the optimum atomic positions and, through the use of the GIPAW (gauge including projector augmented waves) method [50, 51], the shielding effect due to electrons at each nuclear position, and hence the chemical shift. The GIPAW approach has been successfully implemented in the investigation of a wide range of systems in conjunction with solid-state NMR experiments [52–61]. Both density matrix simulations and DFT calculations have been used extensively in the work presented in this thesis to aid in the interpretation of solid-state NMR spectra.

1.2 Polymorphism and Pharmaceuticals

In the context of crystallography, the term polymorphism describes the existence of multiple forms of a crystalline solid, characterised by a different arrangement of the constituent molecules [62]. These differences in intermolecular interactions can result

in profound variations in the physical properties of the bulk material. For example, it is easy to picture a situation whereby differences in the strength of intermolecular bonds between two polymorphs could result in significant differences in the melting point or solubility of the solid. The existence of multiple polymorphs of an organic molecular crystal, under normal pressure conditions is extremely common, with research suggesting that over one third of organic solids exhibit polymorphic behaviour [63].

The identification of polymorphs is possible by a variety of means including microscopy, thermal analysis, density measurements and diffraction experiments. Single crystal x-ray diffraction in particular is an ideal technique to identify the differences in crystal structure which are, by definition, present between different polymorphs of the same molecule [62]. In contrast to diffraction techniques, solid-state NMR allows the study of the local environment of each nucleus, rather than long range order. Consequently, solid-state NMR has the potential to provide complementary information to other structural determination techniques. Solid-state NMR remains useful in situations where a single crystal cannot be obtained, indeed a powdered sample is almost always preferable and the technique even remains applicable to amorphous solids [64]. There are numerous examples of studies of amorphous organic samples [65–67], although the spectra of such samples are likely to exhibit broader lines.

Solid-state NMR studies can reveal a wide variety of information useful in understanding the crystallographic structure of an organic material. For example, the shielding interaction is sensitive to differences in intermolecular arrangements, hence differences between polymorphs can be identified based on changes in isotropic chemical shifts [68]. Different polymorphs of the same substance would not necessarily be expected to have the same number of distinct molecules in the asymmetric unit cell. This information is readily available in a relatively high resolution solid-state NMR spectrum, such as ^{13}C CPMAS, of an organic solid. Peaks in such a spectrum will be split according to the number of distinct molecules, due to the slight differences in the local electronic environment. Solid-state NMR also offers the possibility of directly investigating intermolecular interactions, such as hydrogen bonding, which would typically be expected to differ between polymorphs [62].

Since the first reported use of solid-state NMR (^{13}C CPMAS) to investigate polymorphism in 1980 [69], the majority of studies of polymorphism in organic solids by

solid-state NMR have involved the use of the CPMAS experiment, usually applied to ^{13}C, although ^{15}N studies are also reasonably commonplace [70,71]. The reason for the predominant focus on these nuclei is the ease with which high resolution spectra can be obtained. Using only moderately fast MAS and heteronuclear decoupling, spectra of resolution approaching that obtained from solution-state experiments can be acquired; in many cases, the resolution is sufficient to clearly separate all peaks due to different nuclear sites. Due to the greater difficulty in obtaining spectra of sufficient resolution, there has been considerably less use of ^{1}H solid-state NMR in the investigation of polymorphism. However as a result of recent improvements in resolution due to fast MAS and homonuclear decoupling, ^{1}H solid-state NMR experiments have been used to differentiate between different solid forms of pharmaceutical products [72].

There are clear benefits to using ^{1}H solid-state NMR in structural investigations of organic solids. Due to the high natural abundance, double-quantum correlation experiments can be performed in a relatively short time without the need for isotopic enrichment. These experiments have been used extensively to investigate intermolecular interactions in a variety of different systems [25, 35, 73–76]. It is therefore clear that the ^{1}H DQ solid-state NMR experiment has the potential to provide new insight into the investigation of polymorphic systems.

In the context of the pharmaceutical industry, where a large number of drugs are prepared in the form of solid tablets, polymorphism is a central concern at all stages in the design and manufacture of a drug product. Different polymorphs of an active pharmaceutical ingredient (API) may exhibit considerable differences in a wide variety of physical and chemical properties, many of which have the potential to significantly influence the performance of the drug product. There are numerous examples in the literature of cases where the bioavailability of an API, predominantly determined by the solubility and dissolution properties [62], differs between solid forms [77–80].

Polymorphism is also a concern for the pharmaceutical industry in regard to intellectual property rights. Although variations exist between the legal systems of different countries, in principle a patent applies only to the particular polymorphic form that results from the process described in the patent. There are numerous examples of court cases resulting from disputes regarding the identity and uniqueness of polymorphs and other crystal modifications (hydrates, solvates, etc.) [62]. One particularly interesting

case is that of the API ranitidine hydrochloride. A dispute arose between the original manufacturer, Glaxo Group (now Glaxo SmithKline), and a manufacturer of generic drugs over the question of which of two known polymorphs were produced by the process described in the original patent [81]. The case was settled in Glaxo's favour only after analysis of the product produced by the process indicated that only the correct polymorph could be produced, in the absence of seed crystals of the other polymorph.

For reasons such as those outlined above, the identification and characterisation of polymorphs, and the control of the polymorph produced during drug manufacture, is of critical importance to the pharmaceutical industry. A number of analytical techniques can be used for this purpose, and it is clear that solid state NMR has the potential to play a key role. Although there is already reasonably widespread use of relatively simple experiments such as ^{13}C CPMAS, the combination of these with more advanced homo- and hetero-nuclear correlation experiments, and first principles calculations, will lead to a greater understanding of the structure and properties of a wider variety of polymorphic systems. The purpose of this thesis is to present such novel solid-state NMR techniques for the investigation of the structural properties of organic solids, with particular emphasis on the identification and characterisation of polymorphic forms, and to demonstrate their application to real pharmaceutical systems.

1.3 Thesis Overview

The purpose of this thesis is to present the results of investigations into the use of solid-state NMR techniques in the study of pharmaceutical systems, with particular emphasis on the identification and characterisation of polymorphic forms. Chapter two provides an overview of the relevant underlying theory in terms of nuclear magnetic moments, and the various interactions with internal and external magnetic fields. Chapter three discusses the more practical aspects of performing one and two-dimensional NMR experiments, including the origin of the observed line shapes and the process of phase cycling. Particular considerations relevant to solid-state NMR are then discussed. These generally involve manipulation of the anisotropic interactions which are present in a solid system. The techniques used to increase the spectral resolution, including magic-angle spinning and decoupling sequences are introduced as well as recoupling

techniques used to probe these interactions and hence extract useful information. Several pulse sequences using these techniques are then presented. Finally there is a short discussion of computational methods used in the analysis and interpretation of the experimental results.

Chapter four presents the results of density matrix simulations of a ^{1}H DQ experiment, applied to small clusters of nuclei, with positions extracted from the crystal structure of the dipeptide β-AspAla. The dependence of the DQ peak intensity on the duration of the recoupling sequence was investigated, and the corresponding DQ build-up curves compared to those obtained from DQ CRAMPS experiments. It was found that the DQ build-up behaviour for a particular interaction is strongly influenced by the associated internuclear distance, even within a dense network of strongly coupled spins. Chapter five shows the application of the DQ build-up experiments investigated in the previous chapter to the study of two polymorphs of an active pharmaceutical ingredient. Density functional theory (DFT) calculations are used to optimise a crystal structure and calculate chemical shift values, which are used in assigning the high ppm ^{1}H peaks due to hydrogen-bonded protons. The similarity in the ^{1}H DQ CRAMPS spectra of two polymorphs indicates the same intermolecular hydrogen bonding arrangement, however subtle differences in the ^{1}H DQ build-up behaviour of peaks corresponding to intermolecular interactions indicate small differences in the intermolecular packing.

Chapter six presents an NMR crystallography study of the gamma polymorph of the API indomethacin. DFT calculations are performed, both to aid in the assignment of the ^{1}H and ^{13}C solid-state NMR spectra, and to investigate the effects of intermolecular interactions on the ^{1}H chemical shifts by performing calculations for an isolated molecule. The ^{1}H DQ CRAMPS spectrum is shown to be of limited value in terms of ^{1}H DQ build-up analysis, due to the inability to resolve peaks due to individual H–H interactions, except those involving the single hydrogen bonded proton. Consequently a ^{1}H(DQ)–^{13}C(SQ) refocussed INEPT correlation spectrum is used to transfer magnetisation from protons involved in homonuclear DQ coherences to directly bonded ^{13}C nuclei. The resulting spectrum enables individual peaks in the aromatic region to be resolved, and consequently ^{1}H DQ build-up curves for individual ^{1}H nuclei may be extracted.

The final experimental chapter presents the results of ^{13}C CPMAS experiments and

DFT calculations on two polymorphs of ibuprofen. Using calculated chemical shift values for geometry optimised structures of both the well-known, pharmaceutically used form, and a recently discovered polymorph formed by annealing amorphous ibuprofen, ^{13}C solid-state NMR spectra of both polymorphs are fully assigned. Variable temperature solid-state NMR experiments are used to monitor the emergence of the new polymorph from the amorphous solid, and the reconversion to the original polymorph upon heating of the sample. Further DFT calculations are used to investigate a potential modification to the published crystal structure of the new polymorph.

CHAPTER

TWO

SOLID-STATE NMR THEORY

A solid-state NMR experiment is able to provide detailed atomic-level structural information on a sample by probing the interactions experienced by a system of nuclear spins. In order to understand and properly interpret the results of such experiments, it is necessary to introduce the underlying quantum mechanics describing the behaviour of systems of nuclear spins. This chapter discusses the theory of nuclear magnetism in relation to NMR, and applies this to describing the internal interactions, such as the chemical shift and dipolar coupling, which are probed during an NMR experiment, and the external interactions which allow this information to be obtained. The material presented in this chapter follows the theory and derivations presented in references [82–84].

2.1 Nuclear Magnetism

Nuclear magnetic resonance spectroscopy is concerned with the measurement of the precession frequencies of nuclear spins in a magnetic field. Through the use of complex sequences of radio-frequency (rf) pulses to manipulate interacting nuclear spins, detailed localised information can be obtained. Although simple NMR experiments on systems consisting of a number of non-interacting spin-$\frac{1}{2}$ nuclei can be visualised using an intuitive model of rotations of the bulk nuclear magnetism within a sample, this approach is not sufficient to understand complex experiments involving many coupled nuclei. An approach based on a quantum mechanical model of nuclear magnetism is therefore required.

2.1.1 Spin Angular Momentum

Spin angular momentum is an intrinsic property of each nuclear isotope, and takes on discrete values of integer, or half-integer multiples of $\hbar$. The magnetic moment of the nucleus is directly proportional to the nuclear spin. Considering a single, isolated atomic nucleus, with non-zero spin, in an externally applied, static magnetic field, the energy of the spin is described by the Zeeman Hamiltonian, $\hat{H}$ which is given by

$$\hat{H} = -\hat{\boldsymbol{\mu}} \cdot \boldsymbol{B_0} \tag{2.1}$$

where $\boldsymbol{B_0}$ is the applied magnetic field and $\hat{\boldsymbol{\mu}}$ is the nuclear magnetic moment operator, which can be defined in terms of the spin angular momentum operator, $\hat{\boldsymbol{I}}$

$$\hat{\boldsymbol{\mu}} = \gamma \hat{\boldsymbol{I}} \tag{2.2}$$

where γ is the gyromagnetic ratio, a constant for each nuclear isotope. By convention, the direction of the external field is aligned along the z direction. Due to this convention, z is commonly referred to as the longitudinal direction, with x and y referred to as transverse. Applying this convention, equation 2.1 therefore becomes

$$\begin{aligned} \hat{H} &= -\gamma \hat{I}_z B_0 \\ &= \omega_0 \hat{I}_z \end{aligned} \tag{2.3}$$

where $\hat{I}_z$ is the z- component of $\hat{\boldsymbol{I}}$ and the angular frequency, ω_0, is the Larmor frequency, which is related to the strength of the applied magnetic field by the gyromagnetic ratio.

$$\omega_0 = -\gamma B_0 \tag{2.4}$$

It is possible to construct a wavefunction, $|\psi\rangle$, which completely describes all properties of an atomic nucleus. For an NMR experiment, the property of interest is the nuclear spin. To determine the spin properties of a nucleus, the wavefunction is acted upon by the spin angular momentum operator, $\hat{\boldsymbol{I}}$. For a single nuclear spin, the operator, $\hat{I}^2$, which describes the magnitude of the nuclear spin angular momentum, and $\hat{I}_x$, $\hat{I}_y$, $\hat{I}_z$, which describe the Cartesian components of the spin angular momentum, are

related by the equation

$$\hat{I}^2 = \hat{I}_x^2 + \hat{I}_y^2 + \hat{I}_z^2 \tag{2.5}$$

The $\hat{I}^2$ operator commutes with the operator for only one component of the spin angular momentum, by convention, the $\hat{I}_z$ operator. More specifically, the following commutation relations apply:

$$[\hat{I}^2, \hat{I}_z] = 0 \tag{2.6}$$

$$[\hat{I}_x, \hat{I}_y] = i\hbar\hat{I}_z \tag{2.7}$$

where $\hbar$ is the reduced Planck constant ($h/2\pi$). The commutation relations for other combinations of the Cartesian spin angular momentum operators are provided by subsequent cyclical permutations. These single spin angular momentum operators may also be expressed as 2×2 matrices:

$$\hat{I}_x = \begin{pmatrix} 0 & \frac{1}{2} \\ \frac{1}{2} & 0 \end{pmatrix}, \qquad \hat{I}_y = i\begin{pmatrix} 0 & -\frac{1}{2} \\ \frac{1}{2} & 0 \end{pmatrix}, \qquad \hat{I}_z = \begin{pmatrix} \frac{1}{2} & 0 \\ 0 & -\frac{1}{2} \end{pmatrix} \tag{2.8}$$

The $\hat{I}^2$ and $\hat{I}_z$ operators have eigenvalues, I and m, respectively:

$$\hat{I}^2 \left|\psi\right\rangle = \hbar I(I+1) \left|\psi\right\rangle \tag{2.9}$$

$$\hat{I}_z \left|\psi\right\rangle = \hbar m \left|\psi\right\rangle \tag{2.10}$$

The value $I(I+1)$ is the square of the magnitude of the nuclear spin angular momentum, and m is its z component. The factor of $\hbar$ is commonly omitted such that angular momenta are expressed in units of $\hbar$; this convention will be followed from here on.

I may take any integer or half integer value, with m then taking any value in the range $-I$, $-I+1$, to $+I$. All nuclei studied in this thesis have spin $I = 1/2$, referred to as *spin-$\frac{1}{2}$* nuclei. Such nuclei include isotopes of many elements commonly found in organic molecules, such as ^{1}H and ^{13}C. For a spin-$\frac{1}{2}$ nucleus, m can have values of $+1/2$ or $-1/2$. The Zeeman eigenstates of a spin-$\frac{1}{2}$ nucleus are commonly referred to

as "spin up" for $m = +1/2$, denoted $|\alpha\rangle$, and "spin down" for $m = -1/2$, denoted $|\beta\rangle$.

$$\hat{I}_z |\alpha\rangle = +\frac{1}{2} |\alpha\rangle \tag{2.11}$$

$$\hat{I}_z |\beta\rangle = -\frac{1}{2} |\beta\rangle \tag{2.12}$$

By combining the above expressions with equation 2.3, the energies of spins in each of the Zeeman eigenstates can be found to be

$$\hat{H} |\alpha\rangle = +\frac{1}{2}\omega_0 |\alpha\rangle \tag{2.13}$$

$$\hat{H} |\beta\rangle = -\frac{1}{2}\omega_0 |\beta\rangle \tag{2.14}$$

showing that the separation in energy between the $|\alpha\rangle$ and $|\beta\rangle$ eigenstates is equal to the Larmor frequency, ω_0.

An isolated spin-$\frac{1}{2}$ nucleus need not necessarily exist purely in either eigenstate. In order to fully describe the spin state of the nucleus, a superposition of the Zeeman eigenstates must be used. The contributions of each of the basis states to the wavefunction is governed by the complex coefficients c_α and c_β.

$$|\psi\rangle = c_\alpha |\alpha\rangle + c_\beta |\beta\rangle \tag{2.15}$$

where the normalisation condition $|c_\alpha|^2 + |c_\beta|^2 = 1$ applies.

A generalised operator, $\hat{A}$, can be represented as a matrix, where $\langle r | \hat{A} | s \rangle$ forms the element A_{rs}:

$$\boldsymbol{A} = \begin{pmatrix} A_{\phi_1\phi_1} & A_{\phi_1\phi_2} \\ A_{\phi_2\phi_1} & A_{\phi_2\phi_2} \end{pmatrix} = \begin{pmatrix} \langle\phi_1|\hat{A}|\phi_1\rangle & \langle\phi_1|\hat{A}|\phi_2\rangle \\ \langle\phi_2|\hat{A}|\phi_1\rangle & \langle\phi_2|\hat{A}|\phi_2\rangle \end{pmatrix} \tag{2.16}$$

For the case of an operator, $\hat{A}$ acting on a spin-$\frac{1}{2}$ nucleus, the expectation value of $\hat{A}$ may therefore be expressed as a matrix multiplication

$$\begin{aligned} \langle\hat{A}\rangle &= \begin{pmatrix} c_\alpha^* & c_\beta^* \end{pmatrix} \begin{pmatrix} A_{\alpha\alpha} & A_{\alpha\beta} \\ A_{\beta\alpha} & A_{\beta\beta} \end{pmatrix} \begin{pmatrix} c_\alpha \\ c_\beta \end{pmatrix} \\ &= c_\alpha^* c_\alpha A_{\alpha\alpha} + c_\alpha^* c_\beta A_{\alpha\beta} + c_\beta^* c_\alpha A_{\beta\alpha} + c_\beta^* c_\beta A_{\beta\beta} \end{aligned} \tag{2.17}$$

where the wavefunctions $|\psi\rangle$ and $\langle\psi|$ have been expressed as column and row vectors respectively, the elements of which are the coefficients of the wavefunction's eigenstates. The expectation value of the operator $\hat{I}_z$ operating on $|\psi\rangle$ may therefore be expressed as

$$\begin{aligned}\langle\hat{I}_z\rangle &= \langle\psi|\,\hat{I}_z\,|\psi\rangle \\ &= \frac{1}{2}(c_\alpha c_\alpha^* - c_\beta c_\beta^*) \\ &= \frac{1}{2}|c_\alpha|^2 - \frac{1}{2}|c_\beta|^2 \end{aligned} \tag{2.18}$$

The values of $|c_\alpha|^2$ and $|c_\beta|^2$ therefore correspond to the probability of a measurement of the nuclear spin in the z-direction returning a value of $+1/2$ or $-1/2$ respectively.

As implied by the commutation relations expressed in equations 2.6 and 2.7, the operators $\hat{I}_x$ and $\hat{I}_y$ do not share the $|\,\alpha\rangle$ and $|\,\beta\rangle$ eigenstates. The effect of these operators is to convert between $|\,\alpha\rangle$ and $|\,\beta\rangle$

$$\hat{I}_x\,|\,\alpha\rangle = \frac{1}{2}\,|\,\beta\rangle \tag{2.19}$$

$$\hat{I}_x\,|\,\beta\rangle = \frac{1}{2}\,|\,\alpha\rangle \tag{2.20}$$

$$\hat{I}_y\,|\,\alpha\rangle = \frac{1}{2}i\,|\,\beta\rangle \tag{2.21}$$

$$\hat{I}_y\,|\,\beta\rangle = -\frac{1}{2}i\,|\,\alpha\rangle \tag{2.22}$$

The expectation values of the transverse spin angular momentum operators are also expressed in terms of the coefficients c_α and c_β.

$$\langle\hat{I}_x\rangle = \frac{1}{2}(c_\alpha c_\beta^* + c_\beta c_\alpha^*) \tag{2.23}$$

$$\langle\hat{I}_y\rangle = \frac{1}{2}i(c_\alpha c_\beta^* - c_\beta c_\alpha^*) \tag{2.24}$$

2.1.2 Density Operator Theory

The expression for the expectation value in equation 2.17 shows that the expectation values of $\hat{A}$ are comprised of the products of the coefficients c_α and c_β. This can also be seen in the more specific case of the expectation values of the spin angular momentum operators in equations 2.18, 2.23 and 2.24. It is therefore useful to define the density

matrix, $\boldsymbol{\rho}$ as

$$\boldsymbol{\rho} = \begin{pmatrix} c_\alpha \\ c_\beta \end{pmatrix} \begin{pmatrix} c_\alpha^* & c_\beta^* \end{pmatrix} = \begin{pmatrix} c_\alpha c_\alpha^* & c_\alpha c_\beta^* \\ c_\beta c_\alpha^* & c_\beta c_\beta^* \end{pmatrix} \tag{2.25}$$

Taking the product of the density matrix and $\boldsymbol{A}$ produces a matrix with terms of the form $c_\alpha c_\alpha^* A_{\alpha\alpha}$ such as those that appear in the expectation value of $\hat{A}$

$$\begin{aligned} \boldsymbol{\rho A} &= \begin{pmatrix} c_\alpha c_\alpha^* & c_\alpha c_\beta^* \\ c_\beta c_\alpha^* & c_\beta c_\beta^* \end{pmatrix} \begin{pmatrix} A_{\alpha\alpha} & A_{\alpha\beta} \\ A_{\beta\alpha} & A_{\beta\beta} \end{pmatrix} \\ &= \begin{pmatrix} c_\alpha c_\alpha^* A_{\alpha\alpha} + c_\alpha c_\beta^* A_{\beta\alpha} & c_\alpha c_\alpha^* A_{\alpha\beta} + c_\alpha c_\beta^* A_{\beta\beta} \\ c_\beta c_\alpha^* A_{\alpha\alpha} + c_\beta c_\beta^* A_{\beta\alpha} & c_\beta c_\alpha^* A_{\alpha\beta} + c_\beta c_\beta^* A_{\beta\beta} \end{pmatrix} \end{aligned} \tag{2.26}$$

Inspection of the above matrix reveals that the terms in the expectation value of $\hat{A}$ lie on the principal diagonal. The expectation value may therefore be found by taking the trace of the matrix

$$\langle \hat{A} \rangle = \mathrm{Tr}(\boldsymbol{\rho A}) \tag{2.27}$$

The above description of the density matrix is limited to the case of a single spin-$\frac{1}{2}$ nucleus, however the power of the density matrix formalism lies in the ability to describe large systems comprised of many nuclear spins. In a more general case, the density operator, $\hat{\rho}$, may be defined as

$$\hat{\rho} = \overline{|\,\psi\rangle\langle\psi\,|} \tag{2.28}$$

where the overbar signifies an ensemble average over the entire system under consideration. The corresponding density matrix consists of elements ρ_{rs} defined in terms of the density operator, as in equation 2.16:

$$\rho_{rs} = \langle r\,|\,\hat{\rho}\,|\,s\rangle \tag{2.29}$$

For the case of an ensemble of non-interacting systems of isolated spin-$\frac{1}{2}$ nuclei, each nucleus may be described by a superposition of the states $|\,\alpha\rangle$ and $|\,\beta\rangle$, as previously

described in equation 2.15. The coefficients c_α and c_β may be expanded in terms of an amplitude, a and a phase, ϕ:

$$|\psi\rangle = a_\alpha e^{i\phi_\alpha} |\alpha\rangle + a_\beta e^{i\phi_\beta} |\beta\rangle \tag{2.30}$$

The density matrix describing the system is therefore

$$\boldsymbol{\rho} = \begin{pmatrix} \overline{a_\alpha a_\alpha^*} & \overline{a_\alpha a_\beta^* e^{i(\phi_\alpha - \phi_\beta)}} \\ \overline{a_\beta a_\alpha^* e^{i(\phi_\beta - \phi_\alpha)}} & \overline{a_\beta a_\beta^*} \end{pmatrix} \tag{2.31}$$

For simplicity of notation, the overbars will be omitted in subsequent expressions, where the density operator and its matrix representation, the density matrix, will always be used to describe ensemble averages. Examining the density matrix in the above expression, and comparing to the expectation values of $\hat{I}_z$, $\hat{I}_x$ and $\hat{I}_y$ in equations 2.18, 2.23 and 2.24 it is clear that the elements on the principal diagonal of the density matrix correspond to the expectation values of the $\hat{I}_z$ operator. These are known as the *populations* of the $|\alpha\rangle$ and $|\beta\rangle$ states. Similarly, the off-diagonal elements are related to the expectation values of the $\hat{I}_x$ and $\hat{I}_y$ operators. The phase dependence of these terms is such that if the phases of the individual spin systems comprising the ensemble are the same, then $e^{i\phi_\alpha - \phi_\beta}$ will in general have some non-zero value, and a coherence will exist between the systems. Conversely, if the values of the phases are random, over the ensemble average the value of $e^{i\phi_\alpha - \phi_\beta}$ will be zero and therefore no coherence will exist. These off diagonal elements are therefore referred to as *coherences*.

The density matrix representation of a spin system is easily expanded to accommodate systems comprised of coupled spins. A dipolar coupled spin pair may be described by a wavefuntion with eigenstates such as $|\beta\beta\rangle$ (both spin-down) analogous to the eigenstates of an isolated spin-$\frac{1}{2}$ nucleus in equations 2.11 and 2.12. The wavefunction may be expressed in terms of the corresponding eigenvalues $c_{\alpha\alpha}$, $c_{\alpha\beta}$, $c_{\beta\alpha}$ and $c_{\beta\beta}$:

$$|\psi\rangle = \begin{pmatrix} c_{\alpha\alpha} \\ c_{\alpha\beta} \\ c_{\beta\alpha} \\ c_{\beta\beta} \end{pmatrix} \tag{2.32}$$

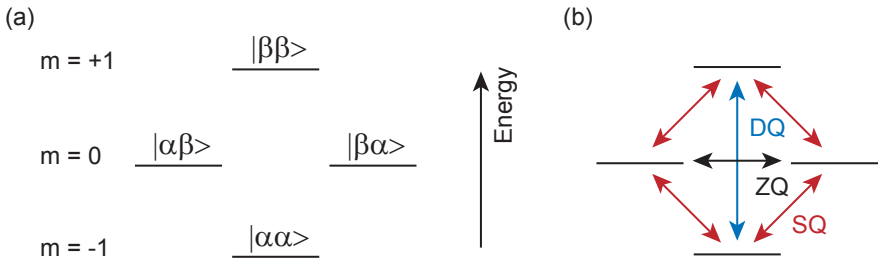

Figure 2.1: (a) energy level diagram for a system comprised of two coupled spin-$\frac{1}{2}$ nuclei. (b) graphical representation of zero-quantum (black), single-quantum (red) and double-quantum (blue) coherences in a coupled spin-$\frac{1}{2}$ pair.

These states may be represented as an energy level diagram, with the $\alpha\beta$ and $\beta\alpha$ states degenerate, as shown in figure 2.1(a).

The density matrix describing an ensemble of coupled spin-$\frac{1}{2}$ pairs is therefore

$$\begin{aligned}\rho =& |\psi\rangle\langle\psi| \\ =& \begin{pmatrix} c_{\alpha\alpha}c^*_{\alpha\alpha} & c_{\alpha\alpha}c^*_{\alpha\beta} & c_{\alpha\alpha}c^*_{\beta\alpha} & c_{\alpha\alpha}c^*_{\beta\beta} \\ c_{\alpha\beta}c^*_{\alpha\alpha} & c_{\alpha\beta}c^*_{\alpha\beta} & c_{\alpha\beta}c^*_{\beta\alpha} & c_{\alpha\beta}c^*_{\beta\beta} \\ c_{\beta\alpha}c^*_{\alpha\alpha} & c_{\beta\alpha}c^*_{\alpha\beta} & c_{\beta\alpha}c^*_{\beta\alpha} & c_{\beta\alpha}c^*_{\beta\beta} \\ c_{\beta\beta}c^*_{\alpha\alpha} & c_{\beta\beta}c^*_{\alpha\beta} & c_{\beta\beta}c^*_{\beta\alpha} & c_{\beta\beta}c^*_{\beta\beta} \end{pmatrix}\end{aligned} \tag{2.33}$$

The principal diagonal terms ($c_{\alpha\alpha}c^*_{\alpha\alpha}$, $c_{\alpha\beta}c^*_{\alpha\beta}$ etc.) again correspond to the populations of the individual eigenstates of the coupled system. The remaining terms are coherences linking these states. The coherences are classified according to the difference in the quantum number, m, of the states they link. Consequently $c_{\alpha\beta}c^*_{\beta\alpha}$ and its complex conjugate $c_{\beta\alpha}c^*_{\alpha\beta}$ are described as zero-quantum coherences, $c_{\alpha\alpha}c^*_{\beta\beta}$ and $c_{\beta\beta}c^*_{\beta\beta}$ as double-quantum coherences and the remaining terms as single-quantum coherences. A graphical representation of these terms on an energy level diagram for a two-spin system is shown in figure 2.1(b). In comparison with the density matrix for an ensemble of isolated spin-$\frac{1}{2}$ nuclei in equation 2.31, it is notable that a system of two (or more) coupled spin-$\frac{1}{2}$ nuclei is required for a double-quantum coherence to exist. The double-quantum coherence may therefore be probed to investigate the spin–spin interactions in a system.

In the context of a practical NMR experiment, only in-phase single-quantum coherences are detectable. Thus for other coherences to be probed they must first be converted to a single-quantum coherence.

2.1.3 Evolution of the Density Operator

Since the density matrix represents a complete description of the nuclear spin system, it provides a convenient way of following the evolution of such a system under a Hamiltonian. This permits the calculation of the state of a nuclear spin system at any stage of an NMR experiment, providing Hamiltonians for all relevant interactions are known.

Differentiating the density operator with respect to time gives

$$\begin{aligned}\frac{\mathrm{d}\hat{\rho}(t)}{\mathrm{d}t} &= \frac{\mathrm{d}}{\mathrm{d}t}(|\,\psi\rangle\langle\psi\,|) \\ &= \left(\frac{\mathrm{d}}{\mathrm{d}t}\,|\,\psi\rangle\right)\langle\psi\,| + |\,\psi\rangle\left(\frac{\mathrm{d}}{\mathrm{d}t}\langle\psi\,|\right)\end{aligned} \tag{2.34}$$

The time dependent Schrödinger equations for $|\,\psi\rangle$ and $\langle\psi\,|$ are

$$\frac{\mathrm{d}}{\mathrm{d}t}\,|\,\psi\rangle = -i\hat{H}\,|\,\psi\rangle \tag{2.35}$$

$$\frac{\mathrm{d}}{\mathrm{d}t}\langle\psi\,| = i\langle\psi\,|\,\hat{H} \tag{2.36}$$

Substitution of these expressions into equation 2.34 gives:

$$\begin{aligned}\frac{\mathrm{d}\hat{\rho}(t)}{\mathrm{d}t} &= -i\hat{H}\,|\,\psi\rangle\langle\psi\,| + i\,|\,\psi\rangle\langle\psi\,|\,\hat{H} \\ &= -i\left[\hat{H}, \hat{\rho}(t)\right]\end{aligned} \tag{2.37}$$

This is known as the *Liouville-von Neumann equation* and may be solved subject to the approximation that the Hamiltonian is constant with respect to time. In practice, this is a valid assumption provided that the Hamiltonian is considered over a small time interval, dt. Under conditions of a time-constant Hamiltonian, the solution to the Liouville-von Neumann equation is:

$$\begin{aligned}\hat{\rho}(t) &= e^{-i\hat{H}t}\hat{\rho}(0)e^{i\hat{H}t} \\ &= \hat{U}(t)\,\hat{\rho}(0)\,\hat{U}(t)^{-1}\end{aligned} \tag{2.38}$$

The term $\hat{U}(t)$ is known as a propagator. Propagators may be formulated to describe different interactions experienced by a system of nuclear spins, for example, chemical shielding or dipolar coupling. In the case of time-dependent Hamiltonians, the solution

in the above expression becomes

$$\hat{\rho}(t) = \hat{T}\, e^{-i\int_0^t \hat{H}t'\mathrm{d}t'}\, \hat{\rho}(0)\, e^{i\int_0^t \hat{H}t'\mathrm{d}t'} \tag{2.39}$$

where the Dyson time ordering operator, $\hat{T}$, is required in situations where $\hat{H}$ does not commute with itself at different times.

2.1.4 Product Operators

Product operators provide an alternative method of describing NMR experiments [85]. While the use of product operators is limited to situations of weak coupling, this remains useful for describing experiments which exploit the J-coupling interaction.

In the case of a single spin system, the operators $\hat{I}_x$, $\hat{I}_y$ and $\hat{I}_z$, corresponding to the x, y, and z magnetisation of a single spin respectively (expressed in matrix form in equation 2.8), suffice to describe the experiment in a manner equivalent to a simple vector model. In a system of two coupled spins, I and S (which may describe either like or unlike nuclei), the matrix representations of the $\hat{I}_x$, $\hat{I}_y$ and $\hat{I}_z$ operators are found by taking the direct product of the matrices for a single-spin system (equation 2.8) and the identity matrix. For $\hat{I}_x$:

$$\hat{I}_x = \begin{pmatrix} 0 & \frac{1}{2} \\ \frac{1}{2} & 0 \end{pmatrix} \otimes \begin{pmatrix} 1 & 0 \\ 0 & 1 \end{pmatrix} = \begin{pmatrix} 0 & 0 & \frac{1}{2} & 0 \\ 0 & 0 & 0 & \frac{1}{2} \\ \frac{1}{2} & 0 & 0 & 0 \\ 0 & \frac{1}{2} & 0 & 0 \end{pmatrix} \tag{2.40}$$

Similarly for $\hat{I}_y$ and $\hat{I}_z$:

$$\hat{I}_y = \begin{pmatrix} 0 & 0 & -\frac{1}{2}i & 0 \\ 0 & 0 & 0 & -\frac{1}{2}i \\ \frac{1}{2}i & 0 & 0 & 0 \\ 0 & \frac{1}{2}i & 0 & 0 \end{pmatrix}, \qquad \hat{I}_z = \begin{pmatrix} \frac{1}{2} & 0 & 0 & 0 \\ 0 & \frac{1}{2} & 0 & 0 \\ 0 & 0 & -\frac{1}{2} & 0 \\ 0 & 0 & 0 & -\frac{1}{2} \end{pmatrix} \tag{2.41}$$

The corresponding S spin operators may be similarly found by reversing the order of the direct product. It is notable that the $\hat{I}_z$ operator contains elements only on the principal diagonal, corresponding to populations of eigenstates, whereas the $\hat{I}_x$ and $\hat{I}_y$

operators contain only off-diagonal elements, corresponding to the coherences linking those states.

The power of the product operator approach lies in the creation of two-spin operators describing coupled systems. These operators are formed from the products of the single-spin operators. Under the influence of a J coupling between two spin-$\frac{1}{2}$ nuclei (J_{IS}), the $\hat{I}_x$ operator evolves with time as:

$$\hat{I}_x \rightarrow \hat{I}_x \cos(\pi J_{IS} t) + 2\hat{I}_y \hat{S}_z \sin(\pi J_{IS} t) \tag{2.42}$$

i.e., evolution under the J-coupling interaction results in magnetisation being created on the S spin, from an initial state in which magnetisation exists only on the I spin. This transfer of magnetisation is exploited in experiments such as INEPT, which will be discussed in chapter 3.

2.2 Solid-State NMR Interactions

In a solid-state NMR experiment, it is necessary to consider interactions both between the nuclear spin system and the external environment, and between multiple nuclear spins. The external interactions due to the applied magnetic fields are the methods used to probe or manipulate the internal interactions, which provide useful information on the sample.

2.2.1 Interaction Hamiltonians

The total nuclear spin Hamiltonian, $\hat{H}_{\text{total}}$ is comprised of components due to the interactions with external fields, and internal spin–spin interactions. These components can then be broken down further into contributions from the specific interactions

$$\begin{aligned} \hat{H}_{\text{total}} &= \hat{H}_{\text{ext.}} + \hat{H}_{\text{int.}} \\ &= \hat{H}_{\text{Z}} + \hat{H}_{rf} + \hat{H}_{\sigma} + \hat{H}_{\text{D}} + \hat{H}_{\text{J}} + \hat{H}_{\text{Q}} \end{aligned} \tag{2.43}$$

where $\hat{H}_{\text{Z}}$ and $\hat{H}_{rf}$ are the external interactions (Zeeman and rf pulses, respectively) and the $\hat{H}_{\sigma}$, $\hat{H}_{\text{D}}$, $\hat{H}_{\text{J}}$ and $\hat{H}_{\text{Q}}$ terms represent the internal interactions (respectively: chemical shielding, dipolar coupling, J coupling and quadrupolar interaction).

It is clear from the above that if appropriate Hamiltonians can be formulated for all interactions present in the system, the evolution of the density operator can be followed using the method presented in the previous section.

The general form for the Hamiltonian of a particular interaction, $\tilde{A}$, is

$$\begin{aligned}\hat{H}_A &= \hat{I}\tilde{A}\hat{S} \\ &= \begin{pmatrix}\hat{I}_x & \hat{I}_y & \hat{I}_z\end{pmatrix}\begin{pmatrix}A_{xx} & A_{xy} & A_{xz} \\ A_{yx} & A_{yy} & A_{yz} \\ A_{zx} & A_{zy} & A_{zz}\end{pmatrix}\begin{pmatrix}\hat{S}_x \\ \hat{S}_y \\ \hat{S}_z\end{pmatrix}\end{aligned} \tag{2.44}$$

where $\tilde{A}$ is a second rank tensor describing the interaction, $\hat{I}$ is a spin operator and $\hat{S}$ may be either a second spin operator, or an operator representing an external field.

For each interaction, a principal axis system (PAS) can be defined, such that the interaction tensor is diagonal. Hence the interaction Hamiltonian in the PAS, $\hat{H}_A^P$, is

$$\begin{aligned}\hat{H}_A^P &= \hat{I}\tilde{A}^P\hat{S} \\ &= \begin{pmatrix}\hat{I}_x & \hat{I}_y & \hat{I}_z\end{pmatrix}\begin{pmatrix}A_{xx} & 0 & 0 \\ 0 & A_{yy} & 0 \\ 0 & 0 & A_{zz}\end{pmatrix}\begin{pmatrix}\hat{S}_x \\ \hat{S}_y \\ \hat{S}_z\end{pmatrix}\end{aligned} \tag{2.45}$$

This principal axis system is useful when describing individual interactions; however, tensors of different interactions do not, in general, share the same PAS. For example, in the case of the dipolar coupling the PAS is defined by the internuclear vector, whereas the PAS of the shielding tensor depends on the electronic environment.

In NMR experiments, it is often necessary to consider multiple frames of reference, and to be able to transform between these frames, for example, transforming from the PAS of a dipolar coupling interaction to the lab frame.

2.2.2 Rotations: Euler Angles and Spherical Tensors

Transformations between different reference frames are expressed in terms of *Euler angles*. These are a set of three angles, denoted α, β and γ, which fully describe the transformation of one set of three orthogonal axes to another by successively performing

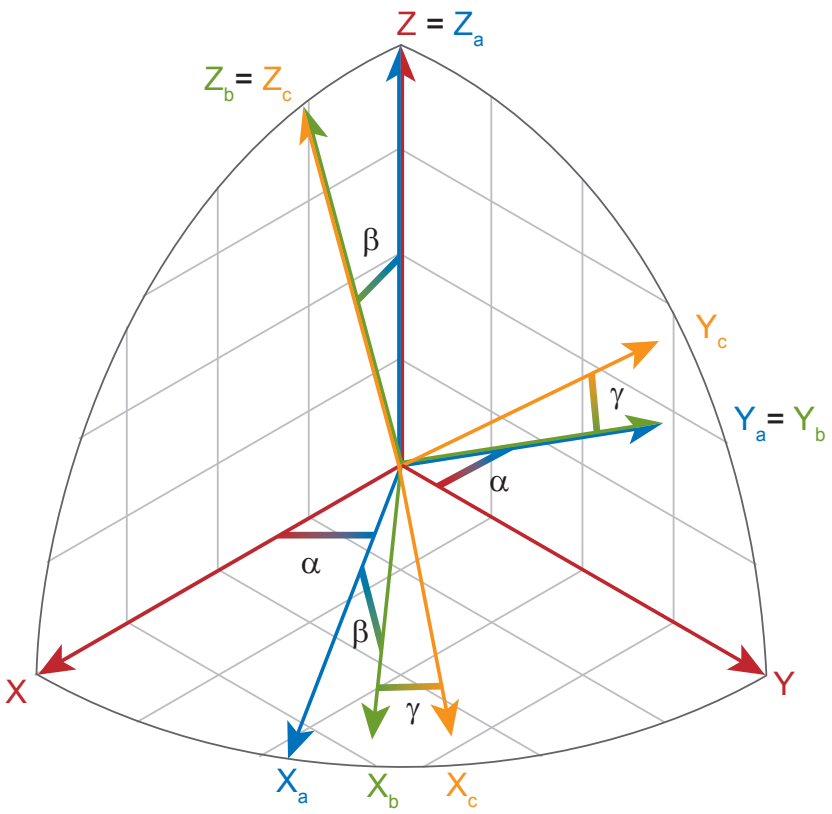

Figure 2.2: Rotation of a set of orthogonal axes (X,Y,Z) through Euler angles α, β and γ. The figure shows each stage of the rotation (colour coded). Initial axes are shown in red followed by blue (one rotation), green (two rotations) and yellow (three rotations - final axes). Grey grid lines are aligned to the initial axes.

rotations about different axes. The rotation, R is expressed as

$$R(\alpha, \beta, \gamma) = R_z(\alpha)\, R_y(\beta)\, R_z(\gamma) \tag{2.46}$$

This expression describes the three rotations necessary to move between any two frames. Considering an "intial" set of three axes X, Y, and Z, the first rotation is about the Z axis by an angle α. This creates a new set of axes, X_a, Y_a and Z_a. A rotation about the Y_a axis by an angle of β is then performed, resulting in axes X_b, Y_b and Z_b. The final rotation is by an angle of γ about the Z_b axis, giving the final X_c, Y_c and Z_c axes. A graphical representation of the rotation of a set of axes through a set of Euler angles is shown in figure 2.2.

Transformations between reference frames are more easily achieved by expressing

interaction Hamiltonians in terms of spherical tensors.

$$\hat{H} = \sum_{j=0}^{2} \sum_{m=-j}^{+j} (-1)^m A_{jm} \hat{T}_{j-m} \tag{2.47}$$

where the tensors A_{jm} and $\hat{T}_{j-m}$ are the spatial and spin components of the Hamiltonian, respectively. Changes to the reference frame due to rotations affect only the spatial components. The subscripts j and m refer to the rank of the tensor and the order of the tensor component, respectively. From the limits imposed on the values of j and m, it is clear that there are nine possible spatial spherical tensors. These tensors can be expressed in terms of the components of the Cartesian tensors, and will be defined as such when necessary.

It is, however, notable that the spherical tensors A_{00}, A_{20} and $A_{2\pm2}$ are the only spatial spherical tensors to have a dependence on the diagonal elements of A, therefore only these four components can appear in the equation for the Hamiltonian in the PAS:

$$\hat{H}_A^{PAS} = A_{00}^{PAS}\,\hat{T}_{00} + A_{20}^{PAS}\,\hat{T}_{20} + A_{22}^{PAS}\,\hat{T}_{2-2} + A_{2-2}^{PAS}\,\hat{T}_{22} \tag{2.48}$$

The primary advantage of working with spherical tensors comes when moving between reference frames using a rotational transformation. The rank of a spherical tensor is invariant under rotation - this feature greatly reduces the complexity of performing such an operation. In general, a tensor A_{jm} is converted into a sum of tensors of the same rank, but of different orders

$$R(A_{jm}) = \sum_{m'=-j}^{+j} D^j_{m'm}(\alpha, \beta, \gamma) A_{jm'} \tag{2.49}$$

where the terms $D^j_{m'm}(\alpha, \beta, \gamma)$ are the Wigner rotation matrices. This shows that a rotation operation may be simplified to a matrix multiplication involving only the spatial spherical tensors. The $D^j_{kl}(\alpha, \beta, \gamma)$ terms may be defined in terms of the reduced Wigner rotation matrix elements, $d^j_{kl}(\beta)$, which are trigonometric functions:

$$D^j_{kl}(\alpha, \beta, \gamma) = \exp(-ik\alpha)\; d^j_{kl}(\beta)\; \exp(-il\gamma) \tag{2.50}$$

The interaction tensor in the lab frame can therefore be found by rotation by the set

of Euler angles linking the PAS to the lab frame:

$$\hat{A}^{\mathrm{LAB}}_{jm'} = \sum_{m=-j}^{+j} D^{j}_{mm'}(\alpha_{PL}, \beta_{PL}, \gamma_{PL}) A^{\mathrm{PAS}}_{jm} \tag{2.51}$$

2.2.3 High Field Approximation

The expression for an interaction Hamiltonian in terms of spherical tensors in equation 2.47 may also be simplified by applying the high field, or secular, approximation. This approximation relies on the large magnitude of the externally applied magnetic field, resulting in the Zeeman Hamiltonian being the dominant term in equation 2.43. First order perturbation theory may then be applied:

$$\hat{H}_{\mathrm{Total}} = \hat{H}_0 + \hat{H}_1 \tag{2.52}$$

where

$$\begin{aligned} \hat{H}_0 &= \hat{H}_{\mathrm{Z}} \\ \hat{H}_1 &= \hat{H}_{rf} + \hat{H}_{\sigma} + \hat{H}_{\mathrm{D}} + \hat{H}_{\mathrm{J}} + \hat{H}_{\mathrm{Q}} \end{aligned} \tag{2.53}$$

i.e., the non-Zeeman interactions are treated as perturbations to the Zeeman Hamiltonian. From this approximation, it follows that the eigenfunctions of the perturbation must be eigenfunctions of the Zeeman Hamiltonian. This allows the simplification of the Hamiltonian, as the only terms that will contribute to the spin energy levels are those that commute with the Zeeman Hamiltonian. More specifically, the following commutation relation applies:

$$\left[\hat{I}_z, \hat{T}_{jm}\right] = m\hat{T}_{jm} \tag{2.54}$$

This relation shows that only when $m = 0$ will the commutator equal zero.

2.3 Interactions With External Fields

External interactions can be broken down into interactions between the nuclear spin system and the static, $\boldsymbol{B_0}$ field, and interactions with the magnetic field due to the

application of *rf* pulses. Considering first the interaction with the $\boldsymbol{B_0}$ field, the initial state of the system, before the application of any *rf* pulses, can be described by finding the density operator at thermal equilibrium.

2.3.1 Zeeman Interaction

The Zeeman interaction is the interaction between a nuclear spin and the external static magnetic field. When expressed in the manner presented in equation 2.44, the Zeeman interaction Hamiltonian (for a magnetic field aligned along the z-axis) is:

$$\begin{aligned}\hat{H}_Z &= \hat{I}\tilde{Z}\hat{B} \\ &= -\begin{pmatrix}\hat{I}_x & \hat{I}_y & \hat{I}_z\end{pmatrix}\gamma\begin{pmatrix}1 & 0 & 0\\ 0 & 1 & 0\\ 0 & 0 & 1\end{pmatrix}\begin{pmatrix}0\\ 0\\ B_0\end{pmatrix} \\ &= \omega_0\hat{I}_z \end{aligned} \tag{2.55}$$

This gives the same result previously stated in equation 2.3 (except the now omitted factor of $\hbar$). From this equation it follows that the equilibrium density operator is:

$$\rho_{eq} = \frac{e^{-\beta\omega_0\hat{I}_z}}{\mathrm{Tr}\left(e^{-\beta\omega_0\hat{I}_z}\right)} \tag{2.56}$$

where k_B, the Boltzmann constant and T, the temperature, are contained in the term $\beta = 1/k_BT$. In the case of high temperatures (in this case "high temperature" means any value of T above a very small fraction of a Kelvin, thus this is in practice always the case for NMR experiments), the approximations $\beta \ll 1$, and $e^n \approx 1 + n$ may be applied. The above expression is now simplified to:

$$\rho_{eq} = \frac{1}{\mathrm{Tr}(1-\beta\omega_0\hat{I}_z)} - \frac{\beta\omega_0}{\mathrm{Tr}(1-\beta\omega_0\hat{I}_z)}\hat{I}_z \tag{2.57}$$

$$= \frac{1}{\mathrm{Tr}(1)} - \frac{\beta\omega_0}{\mathrm{Tr}(1)}\hat{I}_z \tag{2.58}$$

which, given that $\mathrm{Tr}(1) = 2^N$ for a system of N spins, and assuming N is very large, gives the density operator at thermal equilibrium as

$$\rho_{eq} \propto \hat{I}_z \tag{2.59}$$

Hence the density matrix only contains terms on the principal diagonal, i.e. only terms corresponding to the populations of the Zeeman eigenstates. This is an important result as this state of thermal equilibrium is assumed at the start of an experiment. This is a valid assumption provided sufficient time is allowed between successive experiments to allow the system to relax back to this state.

2.3.2 Radio-Frequency Pulses

In order to create coherences, a pulse (or series of pulses) of current oscillating at a frequency close to ω_0, referred to as an *rf* pulse, is passed through a coil wrapped around the sample. This generates a magnetic field in the transverse plane, $\boldsymbol{B_1}(t)$. Although this field is typically much weaker than the B_0 field, it can still have a strong effect on the nuclear magnetisation if it is a resonant pulse, i.e., ω_{rf} is close to ω_0.

The form of the $\boldsymbol{B_1}(t)$ magnetic field during the duration of the pulse is (assuming a pulse oscillating along the x-direction):

$$\boldsymbol{B_1}(t) = \mathbf{i}\, 2B_1 \cos(\omega_{rf}\, t + \phi) \tag{2.60}$$

where $\mathbf{i}$ is the unit vector aligned along the x-axis. This oscillation may be broken down into two components, at frequencies $\pm\omega_{rf}$

$$\boldsymbol{B_1}(t) = \mathbf{i}\, B_1 \left(e^{i(\omega_{rf}\, t+\phi)} + e^{-i(\omega_{rf}\, t+\phi)} \right) \tag{2.61}$$

Only one of these components (by convention $+\omega_{rf}$) is considered, as the $-\omega_{rf}$ term will be so far off resonance as to have no significant effect on the nuclear spin.

NMR experiments are considered in the rotating frame, in which the x and y axes precess about the z axis at a frequency equal to ω_{rf}. In practice, this corresponds to the experimental process of "downmixing" in which the observed signal is mixed with the *rf* frequency. The magnitude of the resonance offset is typically very much less

than ω_{rf} (kHz rather than hundreds of MHz). This process therefore has a practical purpose, as these lower frequencies are easier for the spectrometer hardware to digitise.

Considering a pulse inducing a magnetic field along the x-axis (a pulse of phase x) the Hamiltonian, in the rotating frame, $\hat{H}_{rf}$ for this pulse is

$$\hat{H}_{rf} = \omega_1 \hat{I}_x \tag{2.62}$$

where ω_1 is the nutation frequency, $\omega_1 = -\gamma B_1$, i.e. the frequency at which the pulse rotates the magnetisation about the x-axis (in this case). The evolution of the density operator under the effect of this pulse may be followed using the Liouville von-Neumann equation. The propagators formed from the above Hamiltonian may be expressed as matrices using the relation

$$e^{\pm i\omega_1 t\hat{I}_x} = \begin{pmatrix} \cos\left(\frac{1}{2}\omega_1 t\right) & \pm i\sin\left(\frac{1}{2}\omega_1 t\right) \\ \pm i\sin\left(\frac{1}{2}\omega_1 t\right) & \cos\left(\frac{1}{2}\omega_1 t\right) \end{pmatrix} \tag{2.63}$$

Assuming the system starts at thermal equilibrium, $\hat{\rho} = \hat{I}_z$, and evolves only under the influence of the *rf* pulse, the density matrix has the following form:

$$\begin{aligned} \hat{\rho}(t) &= e^{-i\hat{H}t}\hat{\rho}(0)e^{i\hat{H}t} \\ &= \begin{pmatrix} \cos\left(\frac{1}{2}\omega_1 t\right) & -i\sin\left(\frac{1}{2}\omega_1 t\right) \\ -i\sin\left(\frac{1}{2}\omega_1 t\right) & \cos\left(\frac{1}{2}\omega_1 t\right) \end{pmatrix} \begin{pmatrix} \frac{1}{2} & 0 \\ 0 & \frac{1}{2} \end{pmatrix} \begin{pmatrix} \cos\left(\frac{1}{2}\omega_1 t\right) & i\sin\left(\frac{1}{2}\omega_1 t\right) \\ i\sin\left(\frac{1}{2}\omega_1 t\right) & \cos\left(\frac{1}{2}\omega_1 t\right) \end{pmatrix} \\ &= \frac{1}{2}\begin{pmatrix} \cos\left(\omega_1 t\right) & i\sin\left(\omega_1 t\right) \\ -i\sin\left(\omega_1 t\right) & -\cos\left(\omega_1 t\right) \end{pmatrix} \end{aligned} \tag{2.64}$$

Inspection of the above expression shows that in the specific case where $\omega_1 t = \pi/2$ (a "90°" pulse), the population terms go to zero, while the coherence terms become non-zero. Similarly for a 180° pulse ($\omega_1 t = \pi$), the populations are inverted.

2.3.3 Resonance Offset and Detection

Finally, it is necessary to discuss the evolution of the density operator under the influence of a resonance offset, $\Omega = \omega_0 - \omega_{rf}$.

The system will be considered to initially be in a state of pure transverse magneti-

sation, immediately following a 90° pulse, i.e. $\hat{\rho} = \hat{I}_x$. The Hamiltonian describing the evolution is

$$\hat{H}_\Omega = \Omega \hat{I}_z \tag{2.65}$$

In a similar manner to that previously used to calculate $\hat{\rho}(t)$ for evolution under an *rf* pulse, the solution to the Liouville von-Neumann equation can be found:

$$\hat{\rho}(t) = \frac{1}{2} \begin{pmatrix} 0 & e^{-i\Omega t} \\ e^{i\Omega t} & 0 \end{pmatrix} \tag{2.66}$$

This result shows that under a resonance offset, the coherence terms of the density matrix oscillate at a frequency Ω.

In an NMR experiment, the technique of quadrature detection is employed, in which signals are acquired in two orthogonal directions (x and y) within the transverse plane. This method of detection is equivalent to acting on the density matrix with the raising operator, defined as:

$$\begin{aligned} \hat{I}_+ &= \hat{I}_x + i\hat{I}_y \\ &= \begin{pmatrix} 0 & 1 \\ 0 & 0 \end{pmatrix} \end{aligned} \tag{2.67}$$

Using equation 2.27, the expression for the expectation value of an operator, the form of the NMR signal, $s(t)$ can be found by evaluating the trace of the product of the raising operator and the density operator for the system as it evolves under an offset:

$$\begin{aligned} s(t) &= \mathrm{Tr}(\hat{I}_+ \hat{\rho}) \\ &= \mathrm{Tr}\left(\begin{pmatrix} 0 & 1 \\ 0 & 0 \end{pmatrix} \begin{pmatrix} 0 & e^{-i\Omega t} \\ e^{i\Omega t} & 0 \end{pmatrix} \right) \\ &= \frac{1}{2} \left(\cos(\Omega t) + i \sin(\Omega t) \right) \end{aligned} \tag{2.68}$$

Hence a cosine modulated signal is acquired in the real part, and a sine modulated signal in the imaginary part. For the case of magnetisation precessing within the transverse

plane it is clear that these signals correspond to the signals in orthogonal directions. This expression for the NMR signal neglects the loss of transverse magnetisation due to relaxation mechanisms.

2.4 Internal Interactions

In addition to the interactions described in the previous section between the nuclear spin system and externally applied magnetic fields, there are also interactions with magnetic fields inside the sample, either between nuclei and electrons, or between multiple nuclei. Without the presence of these interactions, an NMR spectrum would simply comprise a single peak at the Larmor frequency of the nuclear species being studied, however, by exploiting these interactions, it is possible to gain access to a large amount of chemical and structural information. The interactions relevant to experiments described in later chapters are the chemical shielding, the dipolar coupling and the J coupling. These interactions will be described in individual sub-sections below. The quadrupolar coupling is also relevant in many NMR experiments, although not so in the context of the work presented in this thesis, as all experiments were performed on spin-$\frac{1}{2}$ nuclei, which do not have an electric quadrupole moment and hence do not couple to the electric field gradient. Therefore there will be no further discussion of the quadrupolar interaction.

2.4.1 Chemical Shift

The shielding interaction describes the effect of the local electronic environment on the magnetic field experienced by individual nuclear spins. The presence of the strong $\boldsymbol{B_0}$ field causes the electrons to orbit about the field, hence inducing a secondary magnetic field, opposing the external field. This secondary field has the effect of shielding the atomic nuclei from the external field. The magnitude of this shielding effect, and hence the local magnetic field strength, will vary between different nuclear sites due to differences in the distribution of electrons across a molecule. Consequently nuclei experiencing different shieldings will precess at different frequencies, producing an NMR signal with components corresponding to a range of resonance offsets and hence leading to an NMR spectrum comprised of peaks at a range of frequencies.

In practice, the frequency at which a peak appears in an NMR spectrum is expressed as a chemical shift which is defined relative to a reference frequency. The isotropic chemical shift, δ_{iso}, is defined in terms of the measured frequency, ω, and the reference frequency, ω_{ref}, as:

$$\delta_{\text{iso}} = \frac{\omega - \omega_{\text{ref}}}{\omega_{\text{ref}}} \times 10^6 \tag{2.69}$$

The factor of 10^6 is required to express the chemical shift in term of parts per million (ppm) of ω_{ref}. Expressing the frequency in this way removes the dependence on the strength of the B_0 field, allowing results obtained from experiments using different magnet field strengths to be compared.

The shielding interaction is described by the shielding tensor, $\tilde{\sigma}$, a second rank, Cartesian tensor. The Hamiltonian describing the shielding interaction is:

$$\hat{H}_\sigma = \gamma \hat{I} \cdot \tilde{\sigma} \cdot \hat{B}_0 \tag{2.70}$$

Expressed in terms of spherical tensors, the shielding interaction Hamiltonian becomes:

$$\hat{H}_\sigma^{PAS} = A_{00}^{PAS}\,\hat{T}_{00} + A_{20}^{PAS}\,\hat{T}_{20} + A_{22}^{PAS}\,\hat{T}_{2-2} + A_{2-2}^{PAS}\,\hat{T}_{22} \tag{2.71}$$

where the spatial terms are expressed in terms of components of the Cartesian shielding tensor as:

$$A_{00}^{PAS} = -\gamma\sqrt{\frac{1}{3}}\left(\sigma_{xx}^{PAS} + \sigma_{yy}^{PAS} + \sigma_{zz}^{PAS}\right) \tag{2.72}$$

$$A_{20}^{PAS} = \gamma\sqrt{\frac{1}{6}}\left(2\sigma_{zz}^{PAS} - \sigma_{xx}^{PAS} - \sigma_{yy}^{PAS}\right) \tag{2.73}$$

$$A_{2\pm2}^{PAS} = \gamma\frac{1}{2}\left(\sigma_{xx}^{PAS} - \sigma_{yy}^{PAS}\right) \tag{2.74}$$

The A_{00} spherical tensor is unaffected by the rotation and corresponds to the isotropic component of the shielding interaction. The A_{20}^{PAS} tensor may be rotated

from the PAS frame to the LAB frame using equations 2.51 and 2.50:

$$\begin{aligned} A_{20}^{LAB} &= \sum_{m=-2}^{2} A_{2m}^{PAS}\, d_{m0}^{2}(\beta_{PL}) \exp(-im\alpha_{PL}) \\ &= A_{20}^{PAS}\, d_{00}^{2}(\beta_{PL}) + A_{22}^{PAS}\, d_{20}^{2}(\beta_{PL}) \exp(-2i\alpha_{PL}) + A_{2-2}^{PAS}\, d_{-20}^{2}(\beta_{PL}) \exp(2i\alpha_{PL}) \\ &= A_{20}^{PAS}\, \frac{1}{2}(3\cos^2\theta - 1) + A_{2\pm2}^{PAS} \sqrt{\frac{3}{8}} \sin^2\beta_{PL} \left(\exp(-2i\alpha_{PL}) + \exp(2i\alpha_{PL})\right) \end{aligned} \tag{2.75}$$

In the NMR spectrum of a powder, consisting of many crystallites with random orientations, the angular dependence in the shielding causes an anisotropic broadening of the spectral lines.

In practice it is the chemical shift, rather than the shielding, which is directly measured in an NMR experiment. A corresponding chemical shift tensor, $\tilde{\delta}$ may therefore be defined such that the the components of $\tilde{\delta}$ are related to the the shielding tensor components as:

$$\delta_{\alpha\beta} = \frac{\sigma_{\alpha\beta}(\mathrm{ref}) - \sigma_{\alpha\beta}}{1 - \sigma_{\alpha\beta}(\mathrm{ref})} \tag{2.76}$$

The isotropic chemical shift, δ_{iso}, chemical shift anisotropy, δ_{aniso} (CSA) and asymmetry η are defined in terms of the elements of this Cartesian chemical shift tensor:

$$\delta_{\mathrm{iso}} = \frac{1}{3}\left(\delta_{xx}^{\mathrm{PAS}} + \delta_{yy}^{\mathrm{PAS}} + \delta_{zz}^{\mathrm{PAS}}\right) \tag{2.77}$$

$$\delta_{\mathrm{aniso}} = \delta_{zz}^{\mathrm{PAS}} - \delta_{\mathrm{iso}} \tag{2.78}$$

$$\eta = \frac{\delta_{xx}^{\mathrm{PAS}} - \delta_{yy}^{\mathrm{PAS}}}{\delta_{\mathrm{aniso}}} \tag{2.79}$$

These three parameters contain information on all of the principal components of the chemical shift tensor, and may be used to completely describe the form of the shape of the CSA pattern that appears in a static solid-state NMR experiment. By convention [86], the components of the chemical shift tensor are ordered such that

$$|\delta_{zz}^{\mathrm{PAS}} - \delta_{\mathrm{iso}}| \geq |\delta_{xx}^{\mathrm{PAS}} - \delta_{\mathrm{iso}}| \geq |\delta_{yy}^{\mathrm{PAS}} - \delta_{\mathrm{iso}}| \tag{2.80}$$

The concept of the chemical shift anisotropy may be understood by considering an

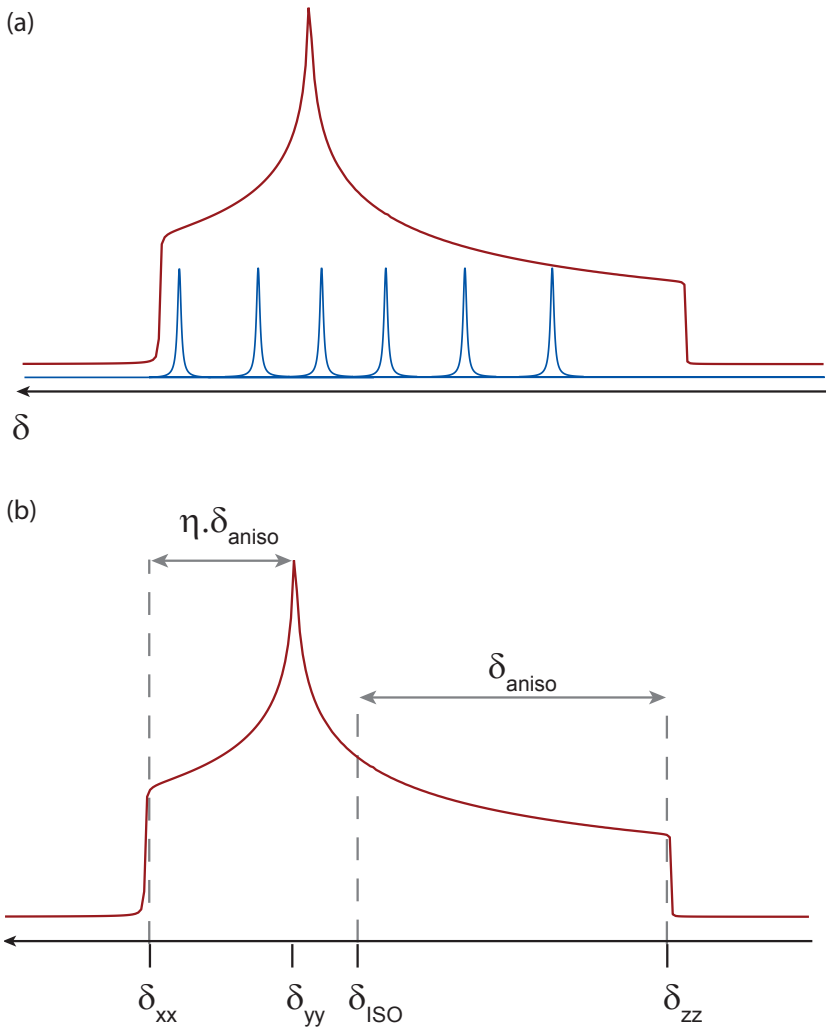

Figure 2.3: (a) overlapping peaks due to different orientations of crystallites (blue) contributing to an anisotropic chemical shift powder pattern. (b) schematic spectrum showing positions of the principal components of the chemical shift tensor, the location of the isotropic chemical shift, and the measurement corresponding to the chemical shift anisotropy (for $\eta = 0.5$).

NMR experiment performed on a single crystal. In this case, all chemically identical nuclei within the sample will be aligned with the same orientation with respect to the magnetic field. The local electronic distribution at each of these sites will therefore be the same, and hence a single peak at a specific chemical shift will appear in the NMR spectrum. Considering the case for a powder comprising many crystallites at random orientations with respect to the field, a large number of peaks at a range of different chemical shifts will now be present in the spectrum, due to the differences in the total magnetic field strength at each nuclear site. The result is a broad line formed from these many overlapping peaks, as shown in figure 2.3a.

Different conventions exist for the reporting of the line shape due to the anisotropic

chemical shift. Figure 2.3b shows the conventions used when discussing CSA in later chapters. The isotropic chemical shift is located at the average of the three principal component values. The chemical shift anisotropy is used to define the maximum separation of the principal tensor components from the isotropic value. The asymmetry, η is related to the measurement $\eta \cdot \delta_{\text{aniso}}$ in the figure. In the case of an axially symmetric tensor, ($\delta_{xx} = \delta_{yy}$) the asymmetry has a value of zero.

2.4.2 Dipolar Coupling

The dipolar coupling arises due to the through-space interaction between nuclear spins. As a through-space interaction, each nuclear spin interacts with every other spin via this mechanism, however a strong dependence on the spin-spin separation (proportional to $1/r^3$) limits the practical effect of this interaction in NMR experiments to relatively short distances, on the order of several angstrom.

A system comprised of a pair of spin-$\frac{1}{2}$ nuclei may be represented by products of the Zeeman eigenstates, $|\,\alpha\rangle$ and $|\,\beta\rangle$. An energy level diagram for such a system was previously shown in figure 2.1(a). The $|\,\alpha\beta\rangle$ and $|\,\beta\alpha\rangle$ states are degenerate.

Following the generalised expression in equation 2.44 for the Hamiltonian due to an interaction, the dipolar Hamiltonian is given by:

$$\hat{H}_D = \hat{I}\tilde{D}\hat{S} \tag{2.81}$$

where $\tilde{D}$ is the second-rank Cartesian dipolar coupling tensor describing the interaction between spins I and S. The discussion of the dipolar coupling in this section will focus mainly on the homonuclear dipolar coupling case, in which the spins I and S are of the same nuclear species. In the principal axis system of the dipolar interaction, the tensor component D_{zz}^{PAS} is equal to the dipolar coupling constant, b_{IS}, which describes the magnitude of the dipolar interaction between spins I and S, and is in units of rad s^{-1}.

$$b_{IS} = -\frac{\hbar\mu_0}{4\pi}\frac{\gamma_I\gamma_S}{r^3} \tag{2.82}$$

where μ_0 is the permeability of free space, r is the internuclear separation, and the γ terms are the gyromagnetic ratios of the two nuclear species involved in the interaction. Of particular importance is the $1/r^3$ dependence, as this term indicates the

strong sensitivity of the dipolar interaction to the internuclear separation. This dependence is exploited in experiments and simulations presented in later chapters to investigate molecular arrangements in crystalline solids. Note that in later chapters, dipolar couplings are expressed as:

$$d_{IS} = b_{IS}/2\pi \tag{2.83}$$

The $\tilde{D}$ tensor is traceless and axially symmetric, consequently, when expressed in terms of spherical tensors, the dipolar Hamiltonian in the PAS is greatly simplified:

$$\hat{H}_D^{PAS} = A_{20}^{PAS}\,\hat{T}_{20} \tag{2.84}$$

where

$$A_{20}^{PAS} = \sqrt{6}\,b_{IS} \tag{2.85}$$

When rotated to the laboratory frame, using equations 2.51 and 2.50, the spatial component of the dipolar Hamiltonian is expressed in terms of a single reduced Wigner rotation matrix. Due to the high field approximation, presented in section 2.2.3, only the A_{20}^{LAB} term remains:

$$\begin{aligned} A_{20}^{LAB} &= A_{20}^{PAS} D_{00}^{2} \\ &= \sqrt{6}\,b_{IS}\,d_{00}^{2} \\ &= \sqrt{6}\,b_{IS}\,\frac{1}{2}(3\cos^2\theta - 1) \end{aligned} \tag{2.86}$$

where, in the case of a powdered sample, the angle θ for a particular crystallite lies in the range 0 to π, with a $\sin\theta$ weighting. The $\hat{T}_{20}$ term is given by:

$$\hat{T}_{20} = \frac{1}{\sqrt{6}}\left(\hat{I}_z\,\hat{S}_z - \frac{1}{2}\left(\hat{I}_x\hat{S}_x + \hat{I}_y\hat{S}_y\right)\right) \tag{2.87}$$

Combining this spin term with the spatial term, the full expression for the dipolar

Hamiltonian can be found:

$$\hat{H}_D = -b_{IS}\left(3\cos^2\theta - 1\right)\left(2\hat{I}_z\hat{S}_z - \left(\hat{I}_x\hat{S}_x + \hat{I}_y\hat{S}_y\right)\right) \tag{2.88}$$

The broadening effects of the dipolar coupling on the solid-state NMR spectrum may be understood by examining the spin angular momentum terms in equation 2.88. These terms may be represented as the following matrices:

$$2\hat{I}_z\hat{S}_z = \begin{pmatrix} \frac{1}{2} & 0 & 0 & 0 \\ 0 & -\frac{1}{2} & 0 & 0 \\ 0 & 0 & -\frac{1}{2} & 0 \\ 0 & 0 & 0 & \frac{1}{2} \end{pmatrix}, \qquad \hat{I}_x\hat{S}_x + \hat{I}_y\hat{S}_y = \begin{pmatrix} 0 & 0 & 0 & 0 \\ 0 & 0 & \frac{1}{2} & 0 \\ 0 & \frac{1}{2} & 0 & 0 \\ 0 & 0 & 0 & 0 \end{pmatrix} \tag{2.89}$$

From inspection of the above matrices it can be seen that the eigenfunctions of the $\hat{I}_z\hat{S}_z$ operator are the product Zeeman states $|\,\alpha\alpha\rangle$, $|\,\alpha\beta\rangle$, $|\,\beta\alpha\rangle$ and $|\,\beta\beta\rangle$. This term therefore corresponds to a energy shift to each of the coupled states. The effect of the $\hat{I}_x\hat{S}_x + \hat{I}_y\hat{S}_y$ is to introduce a mixing of the of the degenerate $|\,\alpha\beta\rangle$ and $|\,\beta\alpha\rangle$ states. In the more general case of many coupled spin-$\frac{1}{2}$ nuclei, these terms appear in the dipolar coupling Hamiltonian for each coupled spin pair and result in a splitting of the previously degenerate energy levels. It is this splitting that results in a wide range of transition frequencies between the energy levels, causing the strong line broadening effects seen in spectra of a dense dipolar coupled network of nuclear spins.

In addition to this line broadening effect, further line broadening is caused by the orientation dependence of the $\left(3\cos^2\theta - 1\right)$ term, in a similar way to the chemical shift anisotropy. The heteronuclear dipolar coupling Hamiltonian has a similar form, although the $\hat{I}_x\hat{S}_x + \hat{I}_y\hat{S}_y$ term does not appear, resulting in broadening only due to the orientation dependence.

In practical terms, the line broadening due to the dipolar coupling, and the chemical shift anisotropy described in the previous section, severely limit the achievable resolution in a solid state NMR experiment. Due to the anisotropic nature of these interactions, they are effectively removed in solution-state experiments by the rapid molecular tumbling motion experienced by the molecules. This motion cancels out the dipolar coupling, and the anisotropic component of the chemical shift, leaving only

isotropic interactions (the isotropic chemical shift and the J coupling). In solid-state NMR experiments these interactions are partially removed by magic angle spinning (MAS). The effect of this process on the anisotropic interactions will be discussed in the next chapter.

2.4.3 *J* Coupling

In addition to the through-space dipolar interaction, nuclear spins may also couple in a through-bond interaction, denoted the "J coupling". This interaction is mediated via the shared pair of electrons that comprise a covalent bond. As a result of the Pauli exclusion principle, the electrons must have opposite spins eigenstates, i.e., a spin-up electron paired with a spin-down electron. When these spins are coupled to the nuclear spins, there exists a difference in energy levels between systems in which the nuclear spins are aligned parallel (higher energy) and anti-parallel (lower energy). This difference is manifested as a splitting in the spectral peaks.

Like the chemical shift, the J coupling comprises both isotropic and anisotropic components, however the anisotropic J coupling is sufficiently small to be ignored, particularly when compared to the magnitude of the dipolar coupling. The strength of the isotropic J coupling is relatively small (of the order of 10-100 Hz), consequently the splitting of peaks that may be observed in solution-state NMR experiments, is usually lost due to the broadness of the peaks that appear in solid-state NMR spectra. Nevertheless the J coupling remains a powerful tool in the study of solids by NMR, as several experiments exist that exploit this interaction to transfer magnetisation across covalent bonds, allowing the identification of directly bonded pairs of nuclei. Such techniques are employed in experiments presented in later chapters.

CHAPTER

THREE

EXPERIMENTAL PRINCIPLES

3.1 Pulsed Fourier Transform NMR

3.1.1 One-Dimensional NMR

The simplest NMR experiment consists of applying an *rf* pulse to flip the bulk magnetisation from the longitudinal direction to the transverse plane, then observing the precession of the magnetisation about the longitudinal direction as a free induction decay (FID). Pulses are applied by passing a current, oscillating at a frequency of ω_{rf} through a coil arranged around the sample. As discussed in the previous chapter, ω_{rf} is close to the precession frequency of the nuclear species being studied, i.e. a resonant pulse. The coil is then used to detect the precession of the bulk magnetisation in the transverse plane. In order to digitise the signal, the observed signal is mixed with the spectrometer reference frequency, ω_{rf} (approximately ω_0) such that only the resonance offset remains, as discussed in chapter 2. It is to be noted that this is equivalent to observing the nuclei in a frame of reference rotating at the frequency ω_{rf}.

The mixing down of the signal is performed in such a way that it is equivalent to detection of the signal in two orthogonal directions (x and y), a technique known as quadrature detection. Due to the $\pi/2$ phase difference between the signals that will be observed in orthogonal directions, these signals, are cosine and sine functions of the effective precession frequency, Ω. These signals may be regarded as the real and

imaginary components of the NMR signal, $s(t)$.

$$\begin{aligned} s(t) &= (\cos p\Omega t - i \sin p\Omega t) \exp(-t/T_2) \\ &= \exp(-ip\Omega t) \exp(-t/T_2) \qquad t \geq 0 \\ s(t) &= 0 \qquad t \leq 0 \end{aligned} \tag{3.1}$$

where p is the coherence order. This expression for the NMR signal was (with the exception of the relaxation term) derived in chapter 2 (equation 2.68). Only single-spin single quantum coherences ($p = \pm 1$) are directly detectable in an NMR experiment, i.e. other coherences may exist, but do not induce a current in the coil. This can be seen by calculating the product of the raising operator (for a two spin system) with the density matrix for a system of coupled spin-$\frac{1}{2}$ pairs (equation 2.33). The trace of the resulting matrix (calculating the NMR signal as in equation 2.68) then contains only single-quantum coherence terms. Throughout this discussion, signals will be observed with $p = -1$.

In general NMR terminology, the $\exp(-t/T_2)$ term in equation 3.1 describes the loss of signal characterised by the time T_2: after T_2, the intensity of the FID will have reduced to $1 - \mathrm{e}^{-1} \approx 63\%$ of the original intensity [87]. In solids, this loss of transverse magnetisation is better described as a dephasing of the initial coherence, and is typically of the order of milliseconds for the crystalline organic solids studied in later chapters of this thesis. This is very much less than the time taken for the the system to return to an equilibrium state ($\rho_{eq} \propto \hat{I}_z$, as stated in equation 2.59), which is similarly characterised by the time T_1.

A more informative representation of the data is obtained by Fourier transformation of the time domain signal into the frequency domain. The spectrum, $S(\omega)$ resulting from a Fourier transform of the signal expressed in equation 3.1 is

$$S(\omega) = A(\omega) - iD(\omega) \tag{3.2}$$

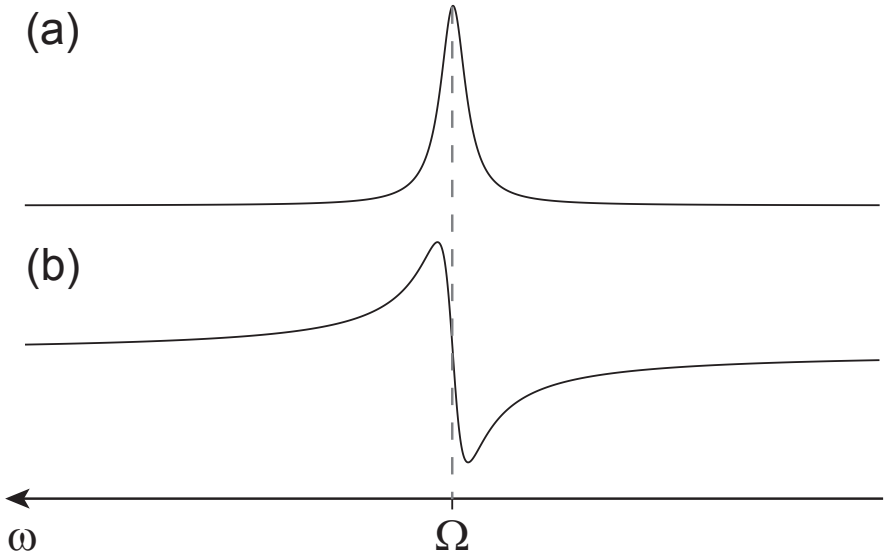

Figure 3.1: Absorptive (a) and dispersive (b) Lorentzian one-dimensional lineshapes, illustrating the difference in the width of the shapes.

where the functions $A(\omega)$ and $D(\omega)$ are expressed as

$$A(\omega) = \frac{1/T_2}{(1/T_2)^2 + (\omega - \Omega)^2} \tag{3.3}$$

$$D(\omega) = \frac{\omega - \Omega}{(1/T_2)^2 + (\omega - \Omega)^2} \tag{3.4}$$

These expressions for A and D correspond to *absorptive* and *dispersive* Lorentzian line shapes, respectively. Each shape is centred on the resonance offset frequency, Ω. Only the absorptive line shape is desired as it has a narrower width than the dispersive shape (full width at half maximum height of $1/\pi T_2$ in Hz). Examples of absorptive and dispersive line shapes are shown in figure 3.1. Furthermore, at the frequency of the resonant offset the absorptive line shape is at its maximum value, whereas the value of the dispersive line shape is zero, making it easier to identify the central frequency of the shape. As such, in this idealised situation, the imaginary component of the spectrum would simply be discarded. However, the above analysis relies on the alignment of the magnetisation in the transverse plane lying in the x-direction, such that the real component of the signal is a cosine function, and the imaginary component a sine function. In practice the real and imaginary components of the spectrum both contain some absorptive and dispersive components, and in order to achieve a pure absorptive line shape in the final spectrum, it is necessary to take linear combinations of the real and imaginary components. This process is described as "phasing" the spectrum.

The importance of using quadrature detection can be seen by considering the case in which the transverse magnetisation is measured in only one direction, in this case the x-direction. The observed signal is now simply the cosine modulated component.

$$\begin{aligned} s(t) &= \cos \Omega t \exp(-t/T_2) \\ &= \frac{\exp(-i\Omega t) + \exp(i\Omega t)}{2} \exp(-t/T_2) \end{aligned} \tag{3.5}$$

When Fourier transformed, the form of the resulting spectrum will be the same as in equation 3.2, however, the functions $A(\omega)$ and $D(\omega)$ become

$$A(\omega) = \frac{1}{2}\left(\frac{1/T_2}{(1/T_2)^2 + (\omega - \Omega)^2} + \frac{1/T_2}{(1/T_2)^2 + (\omega + \Omega)^2}\right) \tag{3.6}$$

$$D(\omega) = \frac{1}{2}\left(\frac{\omega - \Omega}{(1/T_2)^2 + (\omega - \Omega)^2} + \frac{\omega + \Omega}{(1/T_2)^2 + (\omega + \Omega)^2}\right) \tag{3.7}$$

The above expressions describe a pair of peaks mirrored at $\pm\Omega$. This shows that only observing transverse magnetisation in one direction has resulted in an inability to determine the sign of the offset, i.e. there is no sign discrimination.

Finally, it is to be noted that when processing the data from a real NMR experiment, the spectrometer uses a discrete Fourier transform algorithm, in contrast to the analytical Fourier transform described above. This method results in a spectral width, SW, equal to the inverse of the dwell time (time between acquisition of data points). The central point of the spectrum is set at $\Omega = 0$.

3.1.2 Two-Dimensional NMR

In order to perform more sophisticated NMR experiments, for example to identify correlations between nuclei or probe coherences that may not be directly observed, it is possible to use experiments with more than one time dimension [88]. While the experiments performed in this work used no more than two dimensions, it is in principle possible to extend this approach further to higher numbers of dimensions [89, 90]. Fourier transformation of a 2D time-domain data set results in a spectrum with peaks in two frequency dimensions. 2D experiments are a commonly used technique to probe specific interactions within a sample. For example, a heteronuclear correlation experiment will excite one nuclear species, allow that coherence to evolve during the first

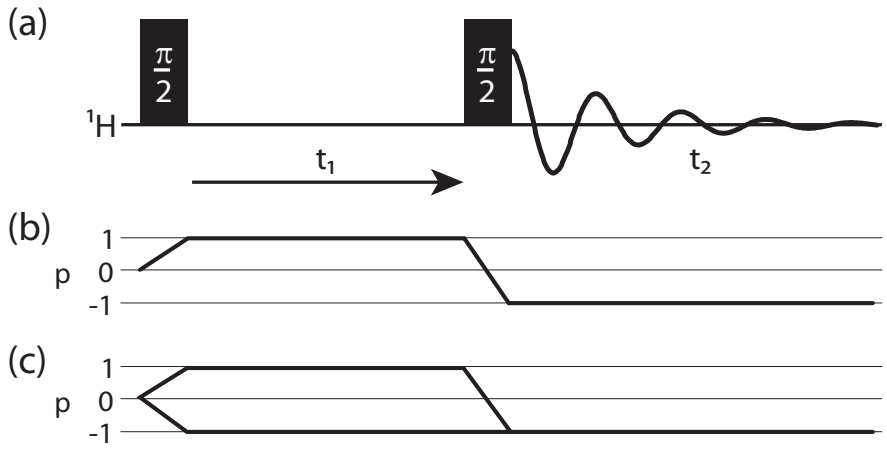

Figure 3.2: (a) Pulse sequence diagram for a simple two dimensional NMR experiment. Coherence transfer pathway diagrams for (b) a phase modulated experiment and (c) an amplitude modulated experiment.

time delay, then transfer the magnetisation to a second nuclear species before acquiring a FID. The resulting 2D spectrum will consist of peaks at the resonances of the pairs of nuclei linked by the interaction used to transfer the magnetisation.

A pulse sequence for a simple generalised 2D experiment is shown in figure 3.2. The first pulse (or sequence of pulses) creates transverse magnetisation, which is allowed to evolve during t_1. This time period is incremented in successive experiments, for example it may have a duration of 0 μs during the first experiment, 10 μs during the second experiment, etc. The second pulse (or sequence) converts the magnetisation to an observable coherence, which is then acquired (using quadrature detection as in the 1D case) in t_2. In this discussion, it will be assumed that during $t_1$and t_2, the system evolves only under the resonance offset Ω. Whereas in the one dimensional case, a pure absorptive line shape is simply achieved by combining real and imaginary components of the FID, in the two dimensional case, achieving absorptive line shapes in both dimensions, with sign discrimination, is more challenging and requires more complex methods.

Experiments may be designed using either a phase modulated or amplitude modulated scheme. This depends upon the coherence transfer pathway, which is manipulated by phase cycling as will be described in section 3.1.3. In the case of the phase modulated scheme, the form of the two dimensional signal as a function of t_1 and t_2 will

be

$$s(t_1, t_2) = \exp(-i\Omega t_1) \exp(-t_1/T_2^{(1)}) \exp(i\Omega t_2) \exp(-t_2/T_2^{(2)}) \tag{3.8}$$

which is simply analogous to the one dimensional NMR signal described in equation 3.1. This expression for the signal may be Fourier transformed in both dimensions

$$s(t_1, \omega_2) = \exp(-i\Omega t_1) \exp(-t_1/T_2^{(1)})(A_2^+ - iD_2^+) \tag{3.9}$$

$$\begin{aligned} s(\omega_1, \omega_2) &= (A_1^- - iD_1^-)(A_2^+ - iD_2^+) \\ &= (A_1^- A_2^+ - D_1^- D_2^+) - i(A_1^- D_2^+ + D_1^- A_2^+) \end{aligned} \tag{3.10}$$

In the above expression, the plus and minus superscripts refer to the sign of the offset frequency. It is clear that the phase modulated sequence has achieved sign discrimination as all terms in the ω_1 dimension are negative, and all terms in the ω_2 dimension are positive. However the spectrum contains a mixture of absorptive and dispersive components. This results in peaks taking on a *phase twist* line shape. The contribution of dispersive elements in these shapes leads to similar problems to the purely dispersive one dimensional line shape, notably the large width of the lines. An example of the real and imaginary components of a phase twist line shape are shown in figure 3.3(a) and (b).

It is possible to achieve pure absorptive two dimensional peaks using an amplitude modulated scheme. The evolution under both $p = 1$ and $p = -1$ coherences during t_1 results in a signal of the form

$$\begin{aligned} s(t_1, t_2) &= (\exp(-i\Omega t_1) + \exp(i\Omega t_1)) \exp(-t_1/T_2^{(1)}) \exp(i\Omega t_2) \exp(-t_2/T_2^{(2)}) \\ &= 2\cos(\Omega t_1) \exp(-t_1/T_2^{(1)}) \exp(i\Omega t_2) \exp(-t_2/T_2^{(2)}) \end{aligned} \tag{3.11}$$

Performing sequential Fourier transforms on the signal will not achieve the desired absorptive spectrum. Instead, a hypercomplex Fourier transform is required in which the real and imaginary components are separated before performing the Fourier transform

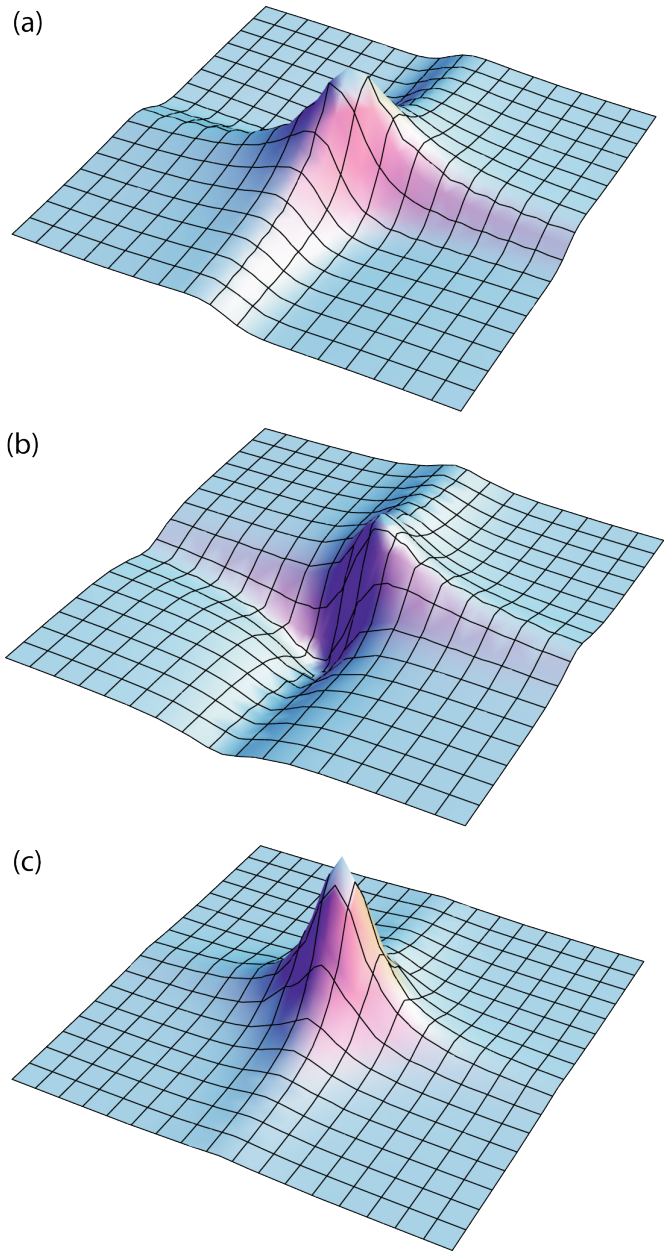

Figure 3.3: Two-dimensional NMR line shapes. (a) real and (b) imaginary components of a phase twist line shape, containing both absorptive and dispersive contributions (plotted using the real and imaginary components of equation 3.10, respectively). (c) pure absorptive line shape, as would result from the States procedure (plotted using the real component of the expression in equation 3.19).

in t_1.

$$\begin{aligned} s(t_1,\omega_2) &= 2\cos(\Omega t_1)\exp(-t_1/T_2^{(1)})(A_2^+ - iD_2^+) \\ &= (\exp(-i\Omega t_1) + \exp(i\Omega t_1))\exp(-t_1/T_2^{(1)})(A_2^+ - iD_2^+) \end{aligned} \tag{3.12}$$

The Fourier transforms in t_1 of the real and imaginary components of equation 3.12 are then performed separately

$$\begin{aligned} s(t_1,\omega_2)^{\mathrm{Re}} &= (\exp(-i\Omega t_1) + \exp(i\Omega t_1))\exp(-t_1/T_2^{(1)})A_2^+ \\ s(\omega_1,\omega_2)^{\mathrm{Re}} &= (A_1^- + A_1^+)A_2^+ - i(D_1^- + D_1^+)A_2^+ \end{aligned} \tag{3.13}$$

$$\begin{aligned} s(t_1,\omega_2)^{\mathrm{Im}} &= (\exp(-i\Omega t_1) + \exp(i\Omega t_1))\exp(-t_1/T_2^{(1)})D_2^+ \\ s(\omega_1,\omega_2)^{\mathrm{Im}} &= (A_1^+ + A_1^-)D_2^+ - i(D_1^+ + D_1^-)D_2^+ \end{aligned} \tag{3.14}$$

The real component of the Fourier transform of the real component is now purely absorptive. However, sign discrimination has been lost in the ω_1 dimension. Sign discrimination may be restored by the use of the States method [91]. In addition to recording the amplitude modulated experiment, which results in a signal of a cosine form in t_1, a second experiment is performed with the phase of the first pulse shifted by $\pi/2|p|$ where p is the order of the coherence that evolves during t_1. In the case of the simple 2D experiment under consideration, $|p| = 1$, and this second signal is therefore shifted in phase by $\pi/2$ so as to give sine modulation in t_1.

$$\begin{aligned} s_{\sin}(t_1,t_2) &= \left[\exp\left(-i\left(\Omega t_1 + \frac{\pi}{2}\right)\right) - \exp\left(i\left(\Omega t_1 + \frac{\pi}{2}\right)\right)\right]\exp(-t_1/T_2^{(1)}) \\ &\quad \times \exp(-i\Omega t_2)\exp(-t_2/T_2^{(2)}) \\ &= 2\cos\left(\Omega t_1 + \frac{\pi}{2}\right)\exp(-t_1/T_2^{(1)})\exp(i\Omega t_2)\exp(-t_2/T_2^{(2)}) \\ &= 2\sin(\Omega t_1)\exp(-t_1/T_2^{(1)})\exp(i\Omega t_2)\exp(-t_2/T_2^{(2)}) \end{aligned} \tag{3.15}$$

Note that this sine modulated signal is denoted $s_{\sin}$. The cosine modulated signal in equation 3.11 will henceforth be referred to as $s_{\cos}$. Both $s_{\cos}$ and $s_{\sin}$ are then Fourier

transformed in t_2.

$$s_{\cos}(t_1, \omega_2) = 2\cos(\Omega t_1)\exp(-t_1/T_2^{(1)})(A_2^+ - iD_2^+) \tag{3.16}$$

$$s_{\sin}(t_1, \omega_2) = 2\sin(\Omega t_1)\exp(-t_1/T_2^{(1)})(A_2^+ - iD_2^+) \tag{3.17}$$

The real components of both $s_{\cos}$ and $s_{\sin}$ are then combined (the dispersive imaginary components are discarded) to form the real and imaginary components respectively, of a new "States signal", s_{States}:

$$\begin{aligned} s_{\text{States}}(t_1, \omega_2) &= \text{Re}(s_{\cos}(t_1, \omega_2)) + i\text{Re}(s_{\sin}(t_1, \omega_2)) \\ &= 2\exp(\Omega t_1)\exp(t_1/T_2^{(1)})A_2^+ \end{aligned} \tag{3.18}$$

A final Fourier transform in t_1 is then applied:

$$\begin{aligned} s_{\text{States}}(\omega_1, \omega_2) &= 2(A_1^+ - iD_1^+)A_2^+ \\ &= 2A_1^+A_2^+ - 2iA_2^+D_1^+ \end{aligned} \tag{3.19}$$

The real component of the above expression represents a spectrum with purely absorptive line shapes and sign discrimination in both ω_1 and ω_2 dimensions. An example of a purely absorptive 2D line shape is shown in figure 3.3(c).

3.1.3 Phase Cycling

The importance of allowing particular coherences to exist at certain times within an NMR experiment was shown in the previous section, where the existence of both $p = \pm 1$ coherences during t_1 was necessary to achieve absorptive line shapes in the 2D spectrum. In more complex experiments, coherences are often selected to allow the system to evolve under certain interactions, which provide useful information. For example, the ^{1}H double-quantum experiment, which will be described in section 3.3.2, uses a series of pulses to excite double-quantum coherence between dipolar coupled nuclei. The coherence transfer pathway is chosen such that only $p = \pm 2$ coherences exist during t_1 and that this double-quantum coherence is reconverted to a state of $p = 0$ after t_1. This experiment will be used as an example in this section, as it is extensively used throughout the experimental work presented in later chapters and involves a number of

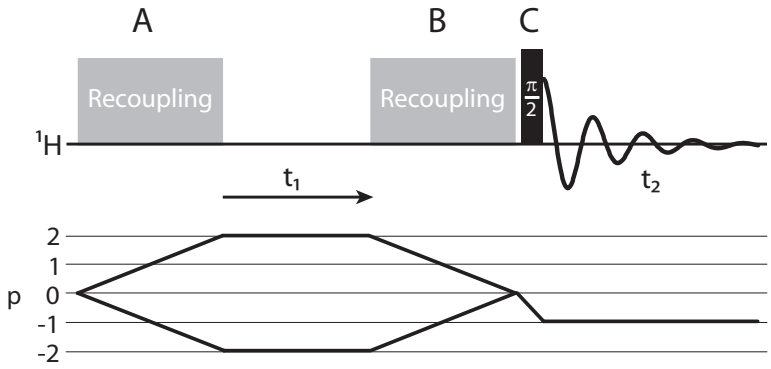

Figure 3.4: Pulse sequence and coherence transfer pathway diagram for the ^{1}H DQ correlation experiment. Further experimental details, including the construction of the recoupling pulses will be discussed in later sections.

coherence order transitions. The pulse sequence for a generic version of this experiment is shown in figure 3.4.

Application of *rf* pulses to a system of coupled spins can result in the creation of a variety of coherence orders. The pulse, or series of pulses, may be designed to excite particular changes in coherence with higher efficiencies than others, however allowing only these desired coherences to evolve while removing the undesired coherences requires the use of phase cycling.

This technique involves performing several experiments, incrementing the phases of several of the pulses through 2π radians over the duration of the phase cycle. For example, a pulse undergoing a four step phase cycle will have phases in successive experiments incremented by $2\pi/4 = \pi/2$ radians, such that the pulse phase in the fifth experiment has returned to the same value as in the first experiment. The phases of the pulses are chosen such that when the transients recorded over the phase cycle are summed, the signals due to any undesired coherence pathways interfere destructively and cancel out, while the signal due to the desired coherence pathway remains.

The phase cycle necessary to follow a given coherence transfer pathway may be found by the application of the following two rules:

- If the phase of a pulse, or of a group of pulses, is shifted by $\Delta\phi$, then a coherence undergoing an change in coherence order of Δp will experience a phase shift of $-\Delta\phi \cdot \Delta p$, as detected by the receiver.

- If a phase cycle uses steps of $360°/N$ then, along with the desired coherence order change of Δp, pathways corresponding to a change of $\Delta p \pm nN$ where $n = 1, 2, 3 \ldots$

Table 3.1: Selection of double-quantum coherence by phase cycling.

			$\Delta p = +2$		$\Delta p = -1$	
Step	ϕ_A	ϕ_R	$-\Delta\phi_A\Delta p = -2\phi_A$	Difference	$-\Delta\phi_A\Delta p = \phi_A$	Difference
1	0	0	0	0	0	0
2	90	180	180	0	90	90
3	180	0	0	0	180	-180
4	270	180	180	0	270	-90

will also be selected. All other pathways are suppressed.

The first rule makes reference to the phase of the receiver. While phases of pulses produced by the spectrometer can take any value, the receiver phase is often limited to multiples, of $\pi/2$. A particular pathway can be selected by making the receiver phase, ϕ_R, synchronise with the phase of the desired coherence, $\phi_R = -\phi\Delta p$. In practice, this is achieved by multiplying the signal by $-i$ for $\phi_R = \pi/2$ (i.e. switching the real and imaginary components) and by -1 for $\phi_R = \pi$ (i.e. inverting the FID).

It is clear from the second of the above rules that is is never possible to completely eliminate all pathways except the desired one, however it is important to consider which coherences can be created for a given nuclear spin system. When considering systems of dipolar coupled nuclei, as is relevant for the ^{1}H DQ correlation experiment, double-quantum coherences of order $|p| = 2$ are created between pairs of coupled nuclei, however significantly higher order coherences may safely be ignored.

One other relevant consideration is the predetermined states at the beginning and end of the experiment. The density matrix at thermal equilibrium, as derived in chapter 2, has no terms corresponding to a coherence, hence $p = 0$. Similarly, at the end of the experiment, the coherence $p = -1$ does not need to be selected as this is the only observable coherence, therefore there is no value in cancelling out other coherences. The result of these limitations is that the phase(s) of one pulse (or set of pulses) in the sequence need not be cycled. In the example of the ^{1}H DQ experiment, the first pulse will be phase cycled to select double-quantum coherence, and the third pulse will be phase cycled to create a coherence of $p = -1$ only from $p = 0$.

The ^{1}H DQ sequence is a simplified version of that used to record data presented later in the thesis. Notably, homonuclear decoupling sequences have been omitted and the details of the recoupling sequences used are not important for understanding of the

Table 3.2: Full phase cycle for the DQ experiment shown in figure 3.4. Pulses A and C are each cycled through four steps to produce the desired coherences.

Step	ϕ_A	$-\Delta\phi_A\Delta p = -2\phi_A$	ϕ_C	$-\Delta\phi_C\Delta p = \phi_C$	$\phi_R = -2\phi_A + \phi_C$
1	0	0	0	0	0
2	90	180	0	0	180
3	180	0	0	0	0
4	270	180	0	0	180
5	0	0	90	90	90
6	90	180	90	90	270
7	180	0	90	90	90
8	270	180	90	90	270
9	0	0	180	180	180
10	90	180	180	180	0
11	180	0	180	180	180
12	270	180	180	180	0
13	0	0	270	270	270
14	90	180	270	270	90
15	180	0	270	270	270
16	270	180	270	270	90

phase cycle. In practice, these blocks are formed of a combination of pulses and delays, which have been replaced in this example by a single block. Where phase shifts between successive experiments are derived in this example, the phases of all components of the blocks would be incremented in a real experiment.

Considering firstly the pulse sequence element used to excite double-quantum coherence (labelled "A" in figure 3.4), a change in coherence order of $\Delta p = \pm 2$ is required. Using a four step phase cycle to select $p = +2$ (from $p = 0$) will also result in coherences $\Delta p = -2, 6, -6 \ldots$ being selected. This successfully selects the two desired coherences, as well as other coherences of sufficiently high orders that they may be safely neglected.

Table 3.1 shows the effect of a four step phase cycle on the first pulse, for a desired coherence ($\Delta p = +2$) and an undesired coherence ($\Delta p = -1$). The data presented in the table shows that the required $\Delta p = 2$ coherence is selected as the receiver phase follows the phase of the coherence throughout the pulse sequence. Conversely the $\Delta p = -1$ coherence is out of phase with the receiver and hence will be cancelled out when all four transients recorded over the phase cycle are added.

It is similarly possible to design a phase cycle for the final pulse, such that a coherence change of $\Delta p = -1$ is selected. Since only $p = -1$ coherence is observable, only signal from the desired coherence pathway will then be detected. This is again achieved

with a four step phase cycle, selecting coherences $\Delta p = -1, 3, -5, 7$ etc. In practice, these two phase cycles for the first and third pulses are performed in a nested fashion, i.e., for each pulse phase value in the cycle for pulse C, the entire cycle for pulse A is performed. The pulse phases used in the experiment are shown in table 3.2.

3.2 Solid-State NMR Techniques

Performing an NMR experiment on a solid sample requires additional considerations as compared to a solution-state experiment. The primary difference lies in the presence of anisotropic interactions, such as the dipolar coupling or chemical shift anisotropy, which are rapidly averaged by the fast molecular tumbling inherent to a liquid sample. The presence of these interactions causes broadening of the spectral lines, often sufficient to completely obscure the locations of peaks. It is therefore necessary to remove, or limit the effect of these interactions, either by introducing physical motion, or by the application of specifically designed *rf* pulse sequences.

The presence of these interactions is also one of the primary strengths of solid-state NMR. For example, the strong dependence of the dipolar coupling on the internuclear separation provides a powerful method to identify internuclear proximities. The required manipulation of the spin system to access this information requires further *rf* pulse schemes to re-introduce various interactions.

3.2.1 Magic Angle Spinning

Recalling the discussion of the chemical shift and dipolar coupling in the previous chapter, both of these interactions contain anisotropic terms with an angular dependence of the form $\left(3\cos^2\theta - 1\right)$. In solid-state NMR, spectral resolution may be improved by removing or limiting these interactions, primarily using the technique of magic angle spinning (MAS). MAS experiments involve placing the sample into a rotor, which is aligned along an axis at the magic angle ($= 54.7°$) relative to the B_0 field, and rotated rapidly about that axis.

To follow the effect of MAS on the interactions, it is necessary to introduce the rotor frame as a new frame of reference. Moving from the interaction PAS to the laboratory frame now requires two transformations, going via the rotor frame. These rotations are

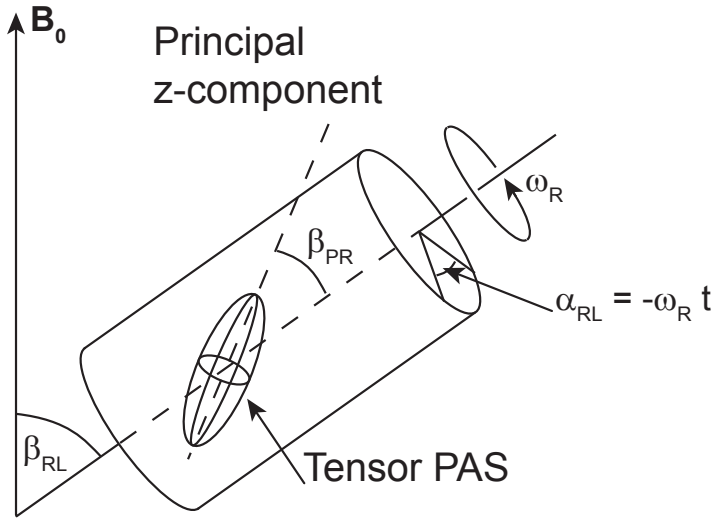

Figure 3.5: Rotation of a sample relative to the B_0 field in a magic angle spinning experiment. The angle β_{PR} relates the principal z-axis of an interaction to the axis of rotation, which is aligned at an angle β_{RL} to the B_0 field. The time dependent angle α_{RL} describes the physical rotation of the sample.

each described in terms of sets of Euler angles, $R_{PR}(\alpha_{PR}, \beta_{PR}, \gamma_{PR})$ to move from the PAS to the rotor frame, and $R_{RL}(\alpha_{RL}, \beta_{RL}, \gamma_{RL})$ to move from the rotor frame to the laboratory frame.

These transformations, applied to the second rank spatial spherical tensor, A_{20}^{PAS}, which appears in the expressions for the dipolar coupling and chemical shift, may be expressed in terms of Wigner rotation matrices as:

$$A_{20}^{\mathrm{LAB}} = A_{20}^{\mathrm{PAS}} \sum_{m'=-2}^{2} D_{0m'}^{2}(\alpha_{PR}, \beta_{PR}, \gamma_{PR}) D_{m'0}^{2}(\alpha_{RL}, \beta_{RL}, \gamma_{RL}) \tag{3.20}$$

In terms of the physical set-up of the NMR experiment, the angle β_{RL} is the angle between the axis of the rotor and the B_0 field. The angle α_{RL} is time dependent due to the rotation of the sample, and is given by:

$$\alpha_{RL} = -\omega_R t \tag{3.21}$$

where ω_R is the angular frequency of the rotation. Figure 3.5 shows the relative alignment of the interaction PAS, the rotor and the B_0 field, including the β angles linking these frames and the α_{RL} angle describing the rotation. The angle γ_{PR} defines the relative phase of the rotor.

Equation 3.20 may therefore be re-written with the rotor to laboratory transforma-

tion expressed in terms of reduced Wigner rotation matrix elements, as was shown in equation 2.50:

$$A_{20}^{\mathrm{LAB}} = A_{20}^{\mathrm{PAS}} \sum_{m'=-2}^{2} D_{0m'}^{2}(\alpha_{PR}, \beta_{PR}, \gamma_{PR})\, d_{m'0}^{2}(\beta_{RL}) e^{im'\omega_R t} \tag{3.22}$$

The effect of the rotation of the sample may be followed by considering the effect of an integral over the course of a rotor period, τ_R, on the time dependent exponential term in the above expression.

$$\int_0^{\tau_R} e^{im'\omega_R t} \mathrm{d}t = 0 \qquad \text{if} \qquad m' \neq 0 \tag{3.23}$$

This condition therefore leaves only the one $m' = 0$ term from equation 3.22.

$$\begin{aligned} \langle \hat{A_{20}^{\mathrm{LAB}}} \rangle_{\tau_R} &= A_{20}^{\mathrm{PAS}} d_{00}^{2}(\beta_{PR})\, d_{m'0}^{2}(\beta_{RL}) \\ &= A_{20}^{\mathrm{PAS}} \left(3\cos^2\beta_{PR} - 1\right)\left(3\cos^2\beta_{RL} - 1\right) \end{aligned} \tag{3.24}$$

Setting the angle $\beta_{RL} = \arctan\sqrt{2} \approx 54.7^\circ$ results in this term going to zero, in which case the interaction is completely removed, when averaged over one rotor period.

Considering the integral over one rotor period is equivalent to acquiring the NMR signal under conditions of rotor synchronisation, that is detecting the magnetisation at intervals of τ_R. To consider the more general case of detection with an arbitrary time interval, it is necessary to go back to equation 3.20, and fully expanding the expression in terms of reduced Wigner rotation matrix elements:

$$A_{20}^{\mathrm{LAB}} = A_{20}^{\mathrm{PAS}} \left[\begin{array}{l} d_{00}^{2}(\beta_{PR}) d_{00}^{2}(\beta_{RL}) \\ + d_{01}^{2}(\beta_{PR}) d_{10}^{2}(\beta_{RL}) \exp(-i\gamma_{PR}) \exp(-i\alpha_{RL}) \\ + d_{0-1}^{2}(\beta_{PR}) d_{-10}^{2}(\beta_{RL}) \exp(i\gamma_{PR}) \exp(i\alpha_{RL}) \\ + d_{02}^{2}(\beta_{PR}) d_{20}^{2}(\beta_{RL}) \exp(-2i\gamma_{PR}) \exp(-2i\alpha_{RL}) \\ + d_{0-2}^{2}(\beta_{PR}) d_{-20}^{2}(\beta_{RL}) \exp(2i\gamma_{PR}) \exp(2i\alpha_{RL}) \end{array} \right] \tag{3.25}$$

Substituting in the reduced Wigner rotation matrix components and combining the terms in the angles α_{RL} $(= \omega_r t)$ and γ_{PR}, the expression for the spatial component in

the laboratory frame is simplified to:

$$A_{20}^{\mathrm{LAB}} = A_{20}^{\mathrm{PAS}} \begin{bmatrix} \frac{1}{4}\left(3\cos^2\beta_{PR}-1\right)\left(3\cos^2\beta_{RL}-1\right) \\ -\frac{3}{4}\sin 2\beta_{PR}\sin 2\beta_{RL}\cos(-\omega_r t+\gamma_{PR}) \\ +\frac{3}{4}\sin^2\beta_{PR}\sin^2\beta_{RL}\cos(-2\omega_r t+2\gamma_{PR}) \end{bmatrix} \tag{3.26}$$

Setting the angle $\beta_{RL} = \arctan\sqrt{2}$ further simplifies the expression, leaving the following rotation-frequency dependent terms:

$$A_{20}^{\mathrm{LAB}} = A_{20}^{\mathrm{PAS}}\left[-\frac{1}{2}\sin^2\beta_{PR}\cos(2\gamma_{PR}-2\omega_r t)-\frac{1}{\sqrt{2}}\sin 2\beta_{PR}\cos(\gamma_{PR}-\omega_r t)\right] \tag{3.27}$$

These terms are manifested in the solid-state NMR spectrum as spinning sidebands, small peaks separated from the larger peak at the isotropic chemical shift by the spinning frequency, $\nu_R = \omega_R/2\pi$ (converted to units of Hertz).

3.2.2 Heteronuclear Decoupling Techniques

In addition to the use of the magic angle spinning technique described in the previous section, it is possible to assist in the removal of the heteronuclear dipolar coupling interaction through the use of decoupling sequences [92]. Such sequences are typically applied to the ^{1}H channel while a signal is acquired on a channel tuned to the Larmor frequency of, for example, ^{13}C or ^{15}N. Experiments performed in this work use decoupling schemes based on continuous, high power *rf* irradiation, such as TPPM [93] (two pulse phase modulation) or SPINAL-64 [94] (small phase incremental alternation with 64 steps).

The application of high power decoupling sequences influences the heteronuclear dipolar Hamiltonian. Recalling the form of this Hamiltonian from section 2.4.2, the decoupling has the effect of causing transition of the I nuclear spins (^{1}H) between the $|\,\alpha\rangle$ and $|\,\beta\rangle$ states at the frequency, ω_1 of the decoupling pulses. This causes an averaging of the heteronuclear dipolar coupling through the $\hat{I}_z\hat{S}_z$ term. If the ω_1 frequency, and hence the transition frequency is significantly higher than the magnitude of the heteronuclear dipolar coupling, the interaction will be effectively removed.

The use of high power decoupling requires careful calibration of the experimental set-up. The power of the applied *rf* is typically set to give a ^{1}H nutation frequency

of 100 kHz. For many probes, this is close to the maximum power that may safely be applied. Additionally the duration for which the decoupling is applied, effectively the acquisition time, is limited, again based on the limits for safe operation of the probe. A typical limit of 40 ms is sufficient to record the signal in many experiments. However it is important to also consider the full time during the pulse sequence in which high powered decoupling is applied, which in many experiments includes homonuclear decoupling used during periods of free evolution. This will reduce the duration of the acquisition period that may be used.

3.2.3 Homonuclear Decoupling Techniques

The discussion in section 3.2.1 of the effect of magic angle spinning is valid for the chemical shift anisotropy and heteronuclear dipolar coupling interactions. In the case of a system in which the homonuclear dipolar coupling between several nuclear spins has a significant effect, such as the dense networks of ^{1}H nuclei studied in later chapters, magic angle spinning serves only to reduce the dipolar coupling, and hence reduce the line width. The spinning frequency required to achieve this effect is very high, requiring the use of very small rotors capable of achieving such high MAS frequencies. An alternative is to combine MAS with homonuclear decoupling sequences, which reduce the dipolar interaction by rotation of the nuclear spins.

This technique is known as CRAMPS (combined rotation and multiple pulse spectroscopy). For the crystalline organic solids studied in later chapters, the use of CRAMPS techniques typically provides ^{1}H line widths comparable to, or better than, those obtained at high MAS frequencies. Homonuclear dipolar decoupling can be achieved using a wide variety of sequences. Several such schemes are based on the Lee-Goldburg condition [10], in which the effective field experienced by the nuclear spins is aligned at the magic angle with respect to the B_0 field. In the case of the frequency switched Lee-Goldburg (FSLG) sequence [16], this is achieved by applying a train of *rf* pulses of flip angle 2π. The pulses are applied off-resonance, with the offset alternating by $\pm\Delta\omega$. If the relationship between $\Delta\omega$ and the nutation frequency ω_1 is chosen such that $\Delta\omega = \omega_1/\sqrt{2}$, then it can be shown that the Lee-Goldburg condition is met.

Experiments in this work used homonuclear decoupling sequences based on the

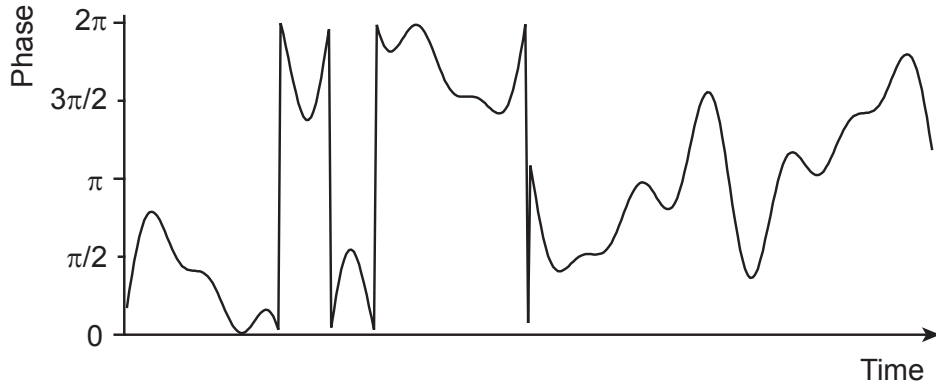

Figure 3.6: Continuous phase profile of a DUMBO pulse. The *rf* amplitude remains constant while the phase is varied.

DUMBO [18, 95] (decoupling using mind boggling optimisation) scheme. In contrast to Lee-Goldburg based sequences, DUMBO uses on-resonance *rf* pulses to achieve homonuclear decoupling. The sequence is applied as a series of discrete pulses of constant ω_1, but with varying phase, following the shape of a continuously varying phase pattern. The sequence was derived from the BLEW-12 scheme [96], which consists of twelve 90° pulses, with phase shifts of 90° between each pulse. This sequence was expressed as a Fourier series, the coefficients for which were computationally optimised to produce the DUMBO sequence. Further optimisation, performed experimentally, led to the development of the eDUMBO-1_{22} [19] sequence, which is optimised for moderately fast MAS conditions (specifically 22 kHz - although a lower spinning frequency of 12.5 kHz is generally used in experiments presented in later chapters, for reasons which will be discussed in detail in the next section). The continuous phase shape of a DUMBO sequence is shown in figure 3.6.

Homonuclear decoupling sequences may be used in either a windowed or windowless fashion. Windowless sequences are applied continuously, and are therefore useful during delays in a pulse sequence, in which magnetisation is allowed to freely evolve, for example during t_1 in a two dimensional experiment. Windowed decoupling is used during the acquisition period. Since the same coil is used to apply *rf* pulses and measure the magnetisation of the sample, it is necessary to alternate between periods of decoupling and data acquisition. A schematic pulse sequence for a simple one-pulse experiment with windowed DUMBO decoupling during acquisition is shown in figure 3.7. Also shown in this figure are the pre-pulses of flip angles θ and $-\theta$. These pulses are necessary to rotate the magnetisation into a tilted transverse plane while the decoupling

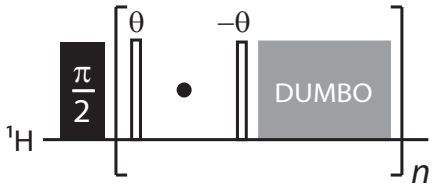

Figure 3.7: Pulse sequence diagram illustrating windowed decoupling. Acquisition is represented by the single dot in t_2. The bracketed section is repeated n times until the required number of data points has been acquired.

sequence is applied, then back into the transverse plane.

The use of windowed decoupling sequences often results in the presence of an artefact in the NMR spectrum at the frequency of the *rf* pulses. As a result, it is necessary to choose a frequency slightly off resonance, such that the artefact does not interfere with spectral peaks. Typically offsets are chosen such that there is a small separation between the artefact and lowest frequency peak of the order of between one and two ppm. The magnitude of the artefact peak can be minimised by optimising the duration and phase of the pre-pulses.

An additional complication when performing experiments that use homonuclear decoupling is the scaling effect on the spectrum. This is caused by the evolution of the magnetisation outside of the usual transverse plane (about a tilted axis relative to the B_0 magnetic field). The result is a spectrum in which the chemical shift axes are compressed by a factor related to the effective field experienced by the nuclear spins during decoupling. If the decoupling sequence has been applied under ideal conditions, such that the effective field is aligned at the magic angle to the B_0 field, this scaling factor will be equal to $1/\sqrt{3} \approx 0.58$. In practice, this factor will vary slightly between experiments and as such it is necessary to record a spectrum without decoupling in order to ensure that the scaling factor used is correct and the spectrum is properly calibrated. This is typically done at a high MAS frequency, and while the resulting spectrum usually has inferior resolution to the CRAMPS spectrum, it is normally sufficient to obtain an accurate scaling factor, provided that at least two known resonances are resolved.

3.2.4 Recoupling Sequences

Despite the use of magic angle spinning and *rf* decoupling to reduce the influence of the homonuclear dipolar coupling on the solid-state NMR spectrum, the $1/r^3$ dependence

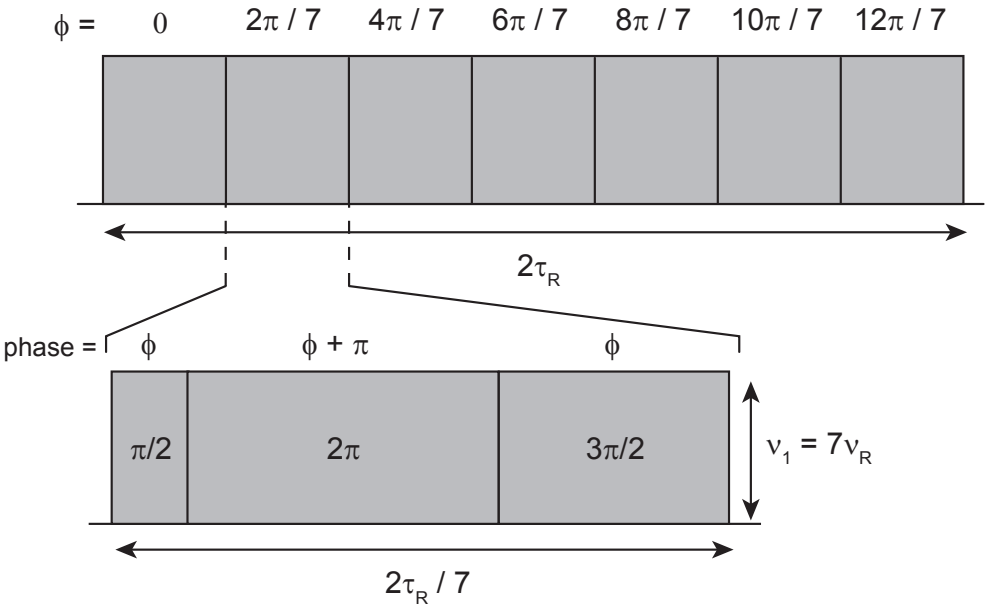

Figure 3.8: Full POST-C7 cycle consisting of seven elements with incremental changes in phase, over a period of $2\tau_R$. The composition of a single element is also shown.

provides a powerful way to measure inter-nuclear distances. Consequently experimental pulse sequences are often designed, as will be discussed in section 3.3.2, to re-introduce the dipolar coupling at particular times. This allows the nuclear spin system to evolve under the influence of the dipolar coupling in a controlled fashion and hence provide a way in which internuclear distances can be experimentally measured.

A number of different recoupling schemes may be used, however, the POST-C7 [31] (permutationally offset stabilised C7) sequence is used extensively in experiments presented in later chapters to achieve this dipolar recoupling. This is a rotor synchronised pulse sequence which excites the double-quantum (DQ) coherence between pairs of dipolar coupled spins. Note that this coherence must still be selected by the use of an appropriate phase cycle for the block of pulses.

The sequence is comprised of a cycle through seven elements, each consisting of a series of *rf* pulses of different phases, as shown in figure 3.8. The phase pattern within each element remains constant, while the base phase for the elements are incremented over the cycle.

The POST-C7 sequence is a modified version of the C7 sequence [30], which is itself a member of a more general family of symmetry based recoupling sequences [97], with designations of the form CN_n^ν, where the sequence is divided into N elements over the time taken for n physical rotations of the sample. During each element, *rf* pulses are

applied which form a complete cycle, i.e., a rotation of the nuclear spins through an angle of an integer multiple of 2π. Successive elements have a phase incremented by $2\pi\nu/N$. The difference between a "standard" C7 sequence, and the POST-C7 sequence is in the construction of the elements, with each POST-C7 element consisting of a series of pulses with flip angles of $\pi/2 - 2\pi - 3\pi/2$, in place of the 4π element used in the C7 sequence. The effect of this difference is to compensate for *rf* field inhomogeneity and resonance offsets, which results in a more broadband excitation of double-quantum coherence. The discussion of the symmetry selection rules below does not depend on the internal construction of the elements, and is therefore equally valid for a C7 or POST-C7 sequence.

The symmetry patterns of the CN_n^ν family of sequences provide selection rules which block specific interaction Hamiltonians depending on combinations of the rank and component of the relevant spatial and spin tensors. Spatial tensors have rank j and component m, with $-j \leq m \leq j$. Spin tensors are analogously indexed by rank λ and component μ.

The effect of the recoupling sequence will be considered for the cases of the chemical shift interaction (separated into isotropic and anisotropic components) and the dipolar coupling. The selection rule for a CN_n^ν sequence is [97]:

$$\bar{H}^{(1)} = 0 \qquad \text{if} \qquad nm - \nu\mu \neq NZ \tag{3.28}$$

where Z is any integer, including zero. Specifically, for the $C7_2^1$ (and hence POST-C7) sequence:

$$\bar{H}^{(1)} = 0 \qquad \text{if} \qquad 2m - \mu \neq 0, \pm 7, \pm 14 \ldots \tag{3.29}$$

Considering first the simplest case of the isotropic chemical shift, for which $m = 0$, $\mu = -1, 0, 1$. Hence $2m - \mu = 0$ for $\mu = 0$ and so $\bar{H}^{(1)} \neq 0$, so the interaction is not blocked by the sequence. For the anisotropic chemical shift, $m = -2, -1, 1, 2$ and $\mu = -1, 0, 1$. Here the absence of an $m = 0$ spatial component is due to rotational averaging, and prevents the satisfaction of the selection rule using the same values as in the isotropic case. No combination of m and μ exist such that the selection criterion is met, and consequently the anisotropic chemical shift is blocked. Finally considering

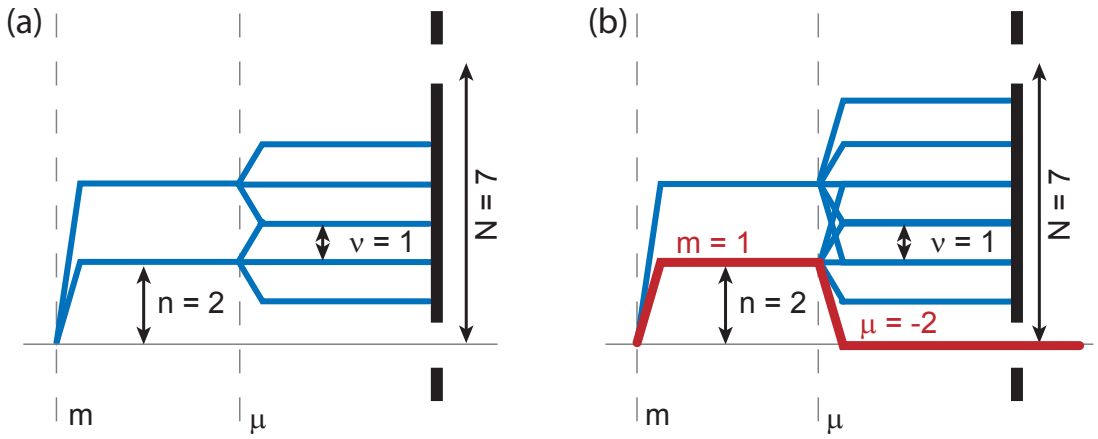

Figure 3.9: Selection rules for a $C7_2^1$ based recoupling sequence. (a) The chemical shift anisotropy is blocked by the sequence. (b) The dipolar interaction is allowed by the sequence, following the path highlighted in red. This figure is adapted from reference [97].

the dipolar interaction, for which $m = -2, -1, 1, 2$ and $\mu = -2, -1, 0, 1, 2$, the specific values of $m = 1$ and $\mu = -2$ allow through the dipolar interaction. A graphical representation of the selection rules applied to the CSA and dipolar coupling is shown in figure 3.9

Due to the requirement of the POST-C7 sequence to have a series of pulses of specific flip angles filling a time interval specified as a fraction of the rotor period, the nutation frequency of the applied *rf* pulses is dependent on the MAS frequency. Specifically, $\nu_1 = 7\nu_R$. The limitations of the NMR probes used in this work are such that the maximum *rf* nutation frequency that may be applied without risking damage to the equipment is typically $\nu_1 \approx 100$ kHz. Consequently, the MAS frequency is limited to approximately 14 kHz. In practice, experiments were generally performed with an MAS frequency of 12.5 kHz, which requires an *rf* frequency of 87.5 kHz.

3.3 Solid-State NMR Pulse Sequences

Beyond the simple one pulse experiment, several more advanced pulse sequences have been used throughout the work presented in this thesis. These experiments typically involve the exploitation of nuclear interactions to enhance signal strength from insensitive nuclei, or to provide correlation data, for example, identifying nuclear proximities or bonding arrangements. Several such experiments are introduced in this section in general terms. Specific details of the experimental parameters (frequencies, pulse du-

rations etc.) are stated in the relevant experimental chapters.

3.3.1 Cross Polarisation

Differences in the properties of nuclear isotopes result in different challenges in solid state NMR. Since organic molecules are predominantly composed of carbon and hydrogen atoms, NMR spectra of these nuclei often contain a large quantity of useful information. The ^{1}H isotope of hydrogen is approximately 99.99% naturally abundant, which, combined with its high gyromagnetic ratio, results in a strong NMR signal. However, these two factors also contribute to a strong dipolar coupling (proportional to γ^2/r^3), which must be reduced using magic angle spinning and possibly homonuclear decoupling in order to produce useful spectra. The case for lower-γ, less naturally abundant nuclei such as ^{13}C or ^{15}N, is very different. With a lower gyromagnetic ratio (approximately one quarter that of ^{1}H) ^{13}C NMR is an inherently less sensitive technique. The signal to noise ratio in an NMR experiment is proportional to the cube of the gyromagnetic ratio, due to the fact that the nuclear magnetic moment, the Boltzmann distribution at thermal equilibrium and the induced current in the coil are all proportional to the gyromagnetic ratio. The signal obtained from a ^{13}C experiment is also reduced by the low natural abundance of ^{13}C. The spin-0 ^{12}C isotope is over 98.9% naturally abundant, leaving only 1.1% of the NMR active, spin-$\frac{1}{2}$ ^{13}C isotope. The lower gyromagnetic ratio and natural abundance result in spectra of considerably higher resolution than for ^{1}H, due to the reduction in the homonuclear dipolar couplings, however this is at the cost of a greatly reduced signal to noise ratio.

The cross polarisation (CP) technique provides a method of improving the signal to noise ratio in solid-state NMR experiments on nuclei such as ^{13}C. CP transfers magnetisation from a high-γ nucleus, I (typically ^{1}H) to a nucleus with a lower gyromagnetic ratio, S (such as ^{13}C or ^{15}N), resulting in an enhancement of up to a factor of the ratio of the gyromagnetic ratio (γ_I/γ_S), corresponding to enhancement factors of up to approximately 4 for ^{13}C and 10 for ^{15}N. A pulse sequence and coherence transfer pathway diagram for this sequence is shown in figure 3.10.

The use of CP experiments is beneficial in the study of nuclei such as ^{13}C for two reasons. The γ_I/γ_S increase in the signal is typically complemented by a decrease in the effective T_1 relaxation time. In simple terms, relaxation arises due to motion of all

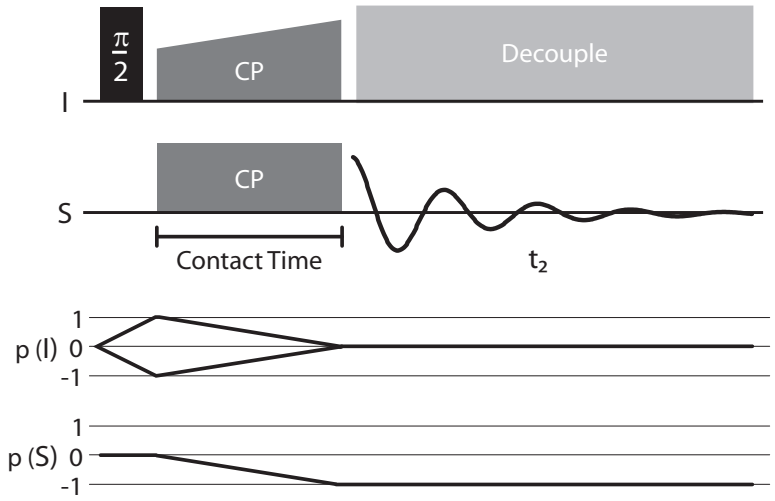

Figure 3.10: Pulse sequence and coherence transfer pathway diagram for the cross polarisation (CP) experiment, in which magnetisation is transferred from the I nuclei, to a lower γ nuclear species, S

or part of a molecule changing an anisotropic interaction, such as the dipolar coupling or CSA. ^{1}H T_1 relaxation times are usually shorter than ^{13}C T_1 relaxation times due to the extensive dipolar coupled network of ^{1}H nuclei within an organic solid. Since the magnetisation on the ^{13}C nuclei is transferred from the faster relaxing ^{1}H it is not necessary to wait for the ^{13}C magnetisation to relax between experiments. This allows the use of a shorter interval between individual experiments, reducing the time needed to record a spectrum.

Magnetisation transfer occurs during the pulses labelled "CP" in figure 3.10. In order to achieve transfer of magnetisation, the amplitude of the pulses must be set such that the B_1 fields for the two nuclear species satisfy the Hartmann-Hahn condition [20], which in the case of a magic angle spinning experiment is modified to include the spinning frequency, ν_R:

$$\gamma_I B_1(I) = \gamma_S B_1(S) \pm n\nu_R \tag{3.30}$$

In practice, efficient CP transfer is achieved through the use of a ramped pulse on the ^{1}H channel, i.e., the *rf* nutation frequency gradually increases over the duration of the pulse [98]. The transfer is achieved through the dipolar coupling, and hence relies on relatively close proximity between the I and S nuclei. In an organic solid, this is rarely a problem for transfer from ^{1}H to ^{13}C, however the degree and rate of

magnetisation transfer will vary depending on the strength of the dipolar interaction. For example, the carbon nucleus in a CH or CH_2 group would typically experience a strong heteronuclear dipolar coupling, due to the relatively high local density of ^{1}H nuclei. Conversely a quarternary carbon, which is not directly bonded to any hydrogen atoms will experience a much weaker dipolar coupling. A higher heteronuclear dipolar coupling will lead to a faster build-up and decay of the peak intensity as the contact time is increased. Consequently there is a loss of quantitative information in the CP NMR spectrum, since the integrated intensity of a peak cannot be regarded purely as a measurement of the number of nuclei at that chemical shift, and will also include a contribution due to the heteronuclear dipolar coupling, with this contribution varying according to the duration of the contact pulses.

3.3.2 ^{1}H Double-Quantum Correlation

^{1}H double-quantum correlation experiments [25] are used extensively in later chapters to identify internuclear proximities and obtain quantitative data on internuclear distances. Due to the large proportion of ^{1}H nuclei in a typical organic solid, a large number of intra- and inter-molecular ^{1}H-^{1}H proximities are present. Probing these inter-molecular proximities is of particular interest, as they often reflect differences in the molecular packing arrangement between different polymorphs.

The pulse sequence for these experiments consists of a period of POST-C7 dipolar recoupling, so as to excite the double-quantum coherence ($p = \pm 2$) between a dipolar coupled pair, followed by t_1 in which the system is able to evolve under the influence of the DQ coherence. A further period of POST-C7, of equal duration to the first reconverts the $p = \pm 2$ coherence to $p = 0$. A 90° pulse is then used to create an observable signal ($p = -1$). ^{1}H homonuclear decoupling is employed during both t_1 and t_2 (windowed) to obtain a high resolution spectrum. A pulse sequence and coherence transfer pathway diagram for this sequence is shown in figure 3.11.

The result of a ^{1}H DQ experiment is a two dimensional spectrum, in which peaks only appear for pairs of ^{1}H in close proximity to one another. In practice, peaks are typically present for internuclear distances ≤ 3.5Å [25]. The appearance of the double-quantum spectrum may be understood by considering a model system comprised of a pair of dipolar coupled nuclei, with chemical shifts δ_A and δ_B. This arrangement will

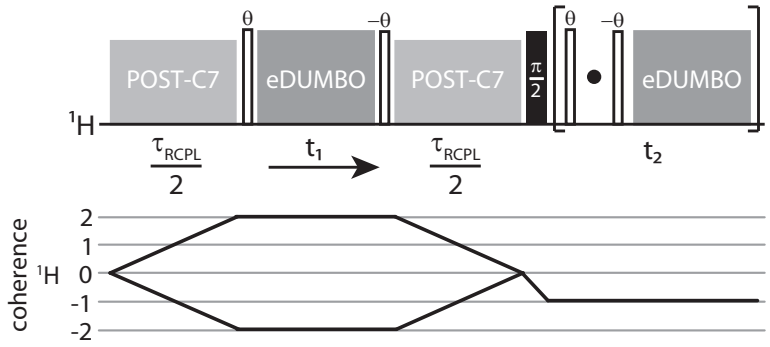

Figure 3.11: Pulse sequence and coherence transfer pathway diagrams for a ^{1}H double-quantum correlation experiment [38]. The POST-C7 sequence is used to achieve dipolar recoupling, and eDUMBO-1_{22} homonuclear decoupling is applied in t_1 (windowless) and t_2 (windowed).

result in a pair of peaks at $\delta_{SQ} = \delta_A$ and $\delta_{SQ} = \delta_B$ in the single-quantum dimension (F_2) and at $\delta_{DQ} = \delta_A + \delta_B$ in the double-quantum dimension (F_1). If a third nucleus is introduced into the system, with a chemical shift of δ_B, an additional peak will appear at $\delta_{SQ} = \delta_B$ in F_2 and $\delta_{DQ} = \delta_B + \delta_B$ in F_1. A schematic diagram of this spectrum is shown in figure 3.12. It is notable that in contrast to other methods used to identify internuclear proximity, such as two-dimensional ^{1}H spin-diffusion experiments [99], information is available on pairs of nuclei with the same chemical shift, since the experiment does not lead to peaks at $(\delta_{SQ}, \delta_{DQ}) = (\delta_A, \delta_A + \delta_A)$ unless there are two or more nuclei at $\delta_{SQ} = \delta_A$ in close proximity.

An additional consideration in the interpretation of these ^{1}H DQ CRAMPS spectra (and indeed all other spectra recorded using homonuclear decoupling) is the scaling effect on the chemical shift axis caused by the decoupling. In the absence of homonuclear decoupling, magnetisation will precess in the transverse plane during acquisition. Homonuclear decoupling creates an effective field aligned at an angle to the B_0 field, about which the magnetisation precesses, resulting a scaling factor of approximately $1/\sqrt{3}$ in any frequency dimension corresponding to an acquisition period in which homonuclear decoupling is applied.

In order to properly calibrate both axes of the spectrum, it is therefore necessary to acquire an additional spectrum, without the use of homonuclear decoupling. These experiments are typically performed at high MAS rates (30 kHz is typical), which provides sufficient narrowing of the spectral lines to allow unambiguous identification of some distinct peaks. Since POST-C7 at this frequency would require an excessively

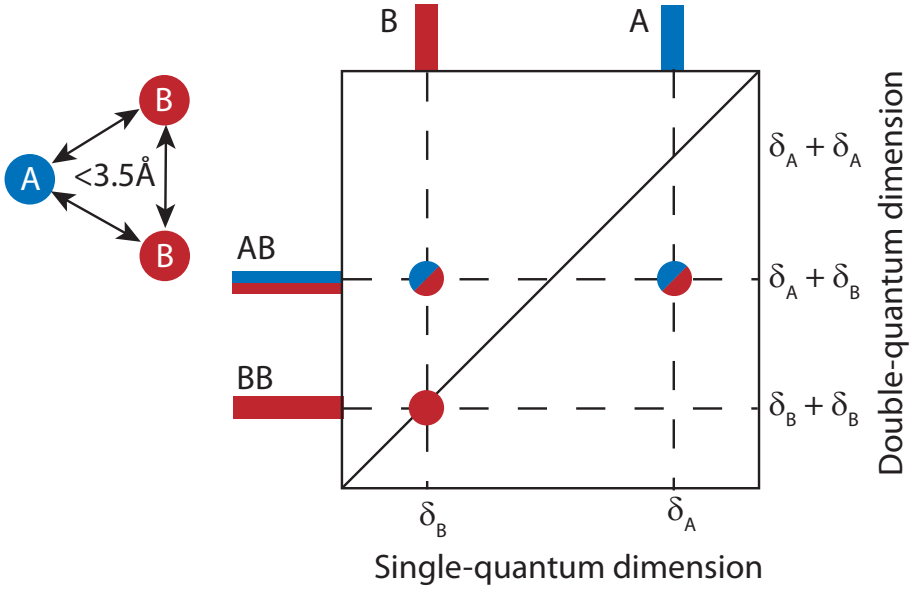

Figure 3.12: Schematic DQ correlation spectrum for a system of three dipolar coupled nuclei separated by < 3.5 Å. Peaks appear at the isotropic chemical shift in the single-quantum dimension, and at the sum of the chemical shifts in the double-quantum dimension.

high *rf* power ($\nu_1 = 210$ kHz for 30 kHz MAS), other recoupling sequences such as BABA (back-to-back) [29], in which the *rf* nutation frequency is independent of the MAS frequency, may be used.

3.3.3 C–H Correlation

The INEPT (insensitive nuclei enhanced by polarisation transfer) experiment [100,101], is used to transfer magnetisation between directly bonded nuclei. This is a widely used technique in solution-state NMR spectroscopy, exploiting the difference in the gyromagnetic ratios to enhance the signal obtained from nuclei such as ^{13}C or ^{15}N, using the ^{1}H magnetisation. This is conceptually similar to the cross polarisation technique often used in solid-state NMR, except using the J coupling, rather than the dipolar interaction.

The applicability of the INEPT sequence to ^{1}H–^{13}C solid-state NMR has been limited by the rapid dephasing of the ^{1}H signal, due to the strong heteronuclear decoupling. The 2D refocussed INEPT experiment has been adapted for application to solid-state NMR by the addition of efficient homonuclear decoupling schemes, which reduce the dipolar interaction and hence increase the ^{1}H transverse dephasing time [19]. Consequently the efficiency of the INEPT transfer is increased [102]. This experiment is used

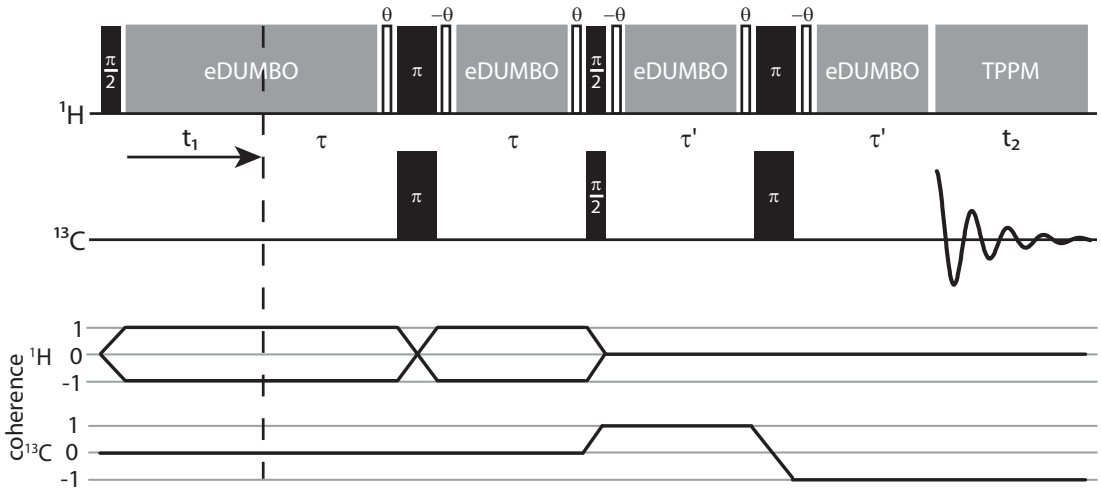

Figure 3.13: Pulse sequence and coherence transfer pathway diagrams for a two dimensional ^{1}H–^{13}C refocussed INEPT experiment. Windowless eDUMBO-1_{22} homonuclear decoupling is applied in t_1. Heteronuclear decoupling is applied to the ^{1}H channel during t_2.

to identify directly bonded ^{1}H–^{13}C pairs. Transverse magnetisation is created on the ^{1}H nuclei, and is allowed to evolve during t_1. Under the influence of the J coupling, the magnetisation is transferred to the ^{13}C nuclei. This experiment results in a two dimensional spectrum, correlating ^{1}H and ^{13}C isotropic chemical shifts. The INEPT sequence is highly selective: when used with short τ periods it identifies nuclei linked by a single bond. This selectivity makes the experiment useful in the assignment of both ^{1}H and ^{13}C chemical shifts. In comparison to a CP experiment, which will result in a spectrum containing peaks from all carbon nuclei present in a system (unless a very short contact time (typically < 100 μs) is used, which also results in a greatly reduced intensity), the INEPT spectrum will only contain signals from those directly bonded to hydrogen atoms. A pulse sequence and coherence transfer pathway diagram for this sequence is shown in figure 3.13.

It can be seen from the coherence transfer pathway diagram that magnetisation transfer occurs by means of the second $\pi/2$ pulse on the ^{1}H channel that is applied simultaneously with a $\pi/2$ pulse on ^{13}C after which a single quantum coherence exists on the ^{13}C channel. The spectrum that would result from acquiring data at this point would consist of a pair of peaks, separated in frequency by the J coupling, and out-of phase with each other (i.e., a positive absorptive peak and a negative absorptive peak). The separation between these peaks would generally not be resolvable in a solid-state NMR experiment, hence they would overlap and cancel each other out. The second

heteronuclear spin echo block ($\tau' - \pi - \tau'$) that follows has the effect of refocussing the signal. The splitting due to the J coupling now results in an in-phase pair of peaks. An analysis of the INEPT experiment in terms of product operators may be found in ref. [84]. This analysis may easily be continued to describe the refocussed INEPT sequence.

In a solution-state experiment, the duration of the τ and τ' delays would be set to $\frac{1}{4J}$ where J is the J coupling (in units of Hz) between the ^{1}H and ^{13}C nuclei. In solid-state NMR the use of such long delays usually results in a loss of the signal due to the dephasing of the transverse ^{1}H and ^{13}C magnetisation, consequently these parameters are optimised experimentally for each sample.

3.4 Computational Methods

In addition to the experimental techniques described in the previous section, valuable insight may also be gained by using computational methods. Numerical simulations can be used to investigate the effect of a pulse sequence on a limited, controllable system, which can assist in the interpretation of experimental results for more complex samples. First principles calculations can also be used to determine NMR parameters for three dimensional crystal structures.

3.4.1 Density Matrix Simulations

In chapter 2, it was shown that a system of coupled nuclear spins may be described using a density matrix. Furthermore, the evolution of the density matrix in an NMR experiment can be followed by solving the Liouville-von Neumann equation, using propagators formed from Hamiltonians of the relevant interactions. Consequently, by performing a series of matrix multiplications, it is possible to simulate an NMR experiment on a limited system of coupled nuclear spins.

The computational time required to perform density matrix simulations rises exponentially with the size of the simulated nuclear spin system. The use of efficient computational techniques which exploit the sparsity of the Hamiltonian allow the simulation of systems containing a relatively large number of spins [40]. Despite the use of such optimisation techniques, the size of system that can be simulated remains rela-

tively limited: density matrix simulations have been performed on systems as large as eleven nuclei [103]. Larger spin systems may be simulated through the use of approximations limiting the number of coherences that are included in the simulation [104], although the use of this method has been limited to the simulation of spin diffusion, involving the transfer of z magnetisation. In this work, simulations of up to eight spin systems have been performed, using the SPINEVOLUTION [42] software package. As will be shown in chapter 4, this is sufficient to obtain data which provides a close, though not perfect, agreement with experimental data, for the ^{1}H double-quantum correlation experiment.

The efficiency of the simulation calculations may be further improved by making changes in the implementation of the pulse sequence, exploiting the greater flexibility of a simulation compared to an experiment. For example, explicit simulation of decoupling sequences, which would be simulated as a series of short pulses of different phases, would significantly increase the required computation time. While this is necessary when examining the performance of a particular decoupling sequence, in most cases it is possible to simply switch off the relevant dipolar couplings during periods of the simulation when decoupling would be applied experimentally, i.e., corresponding to perfect decoupling. Similarly, the selection of particular coherences through phase cycling requires repetition of the pulse sequence, hence increasing the simulation time linearly with the length of the phase cycle. Recalling the density matrix for a system of coupled spin-$\frac{1}{2}$ pairs in equation 2.33, coherences of a particular order correspond to certain elements of the density matrix. It is therefore possible to achieve an equivalent result to phase cycling in a single simulation by applying filters which set to zero the density matrix elements corresponding to coherences which would have been removed by phase cycling, at the relevant points in the pulse sequence [40].

The simulation of two-dimensional experiments may also be achieved more efficiently than in experiments. The necessity to record a large number of signals, at different t_1 intervals, would make the simulation of complex pulse sequences on large nuclear spin systems prohibitively time consuming. In simulations it is possible to specify a particular detection operator, such that the magnetisation of an individual spin may be observed. Hence if a single data point is acquired in t_2 for a range of t_1 values, the Fourier transform of the resulting time-domain data provides a slice through the

2D spectrum. This corresponds to the spectrum in F_1 at the isotropic chemical shift of the observed nucleus in F_2, as the first point in a time domain signal is equal to the integrated signal in the frequency domain.

3.4.2 Density Functional Theory Calculations

Density functional theory (DFT) calculations, performed using the CASTEP [48, 105] software, are used to obtain the shielding tensor for each nuclear site in a crystalline unit cell. DFT calculations use plane-wave pseudo-potentials to describe the electronic wavefunction [106]. This approach relies on a periodic system, which makes it highly applicable to the organic crystalline systems studied in this work.

In practice, to obtain NMR shielding data, calculations are performed in two distinct stages [107]. Starting from a crystal structure which has been obtained from diffraction data, a geometry optimisation calculation is performed to find the minimum energy position of each atom in the system. This is particularly necessary to find the location of hydrogen atoms in a crystal structure obtained by x-ray diffraction. Since x-rays interact with the electrons in a sample, the locations of hydrogen atoms, where there is a low electronic density, are frequently inaccurate. The result of a geometry optimisation calculation is a revised crystal structure with refined atomic positions. This is required for the second stage of the calculation in which NMR parameters are calculated. However it is also useful as an input to the density matrix simulations described in the previous section, in which the dipolar coupling constants are calculated from a list of atomic positions.

NMR calculations are performed using the GIPAW (gauge including projector augmented waves) approach [50, 51]. This overcomes the approximations inherent to the use of pseudo-potentials, which in order to reduce the complexity of the calculation and hence the resources required, deliberately neglect the electronic wavefunction near to the atomic nucleus, on the grounds that the core electrons have a negligible effect on the physical and chemical properties of a material compared to the valence electrons. However, accurate calculation of the shielding tensor requires the use of an all-electron approach, i.e. including the core electrons. The GIPAW method reconstructs an accurate representation of the electronic wavefuntion in the core region. The result of the NMR calculation is the shielding tensor for each nuclear site. From this the full

isotropic and anisotropic chemical shift data for each nucleus can be obtained.

The result of a GIPAW calculation is a shielding tensor for each atom within the unit cell. From this tensor, the isotropic chemical shift can be found, although this requires shifting relative to a reference value to achieve agreement with experimental chemical shifts [107]. The calculated isotropic shielding (in ppm), σ_{calc} is related to the experimental isotropic chemical shift, δ_{iso}, by the reference σ_{ref} (in ppm):

$$\delta_{iso} = \sigma_{ref} - \sigma_{calc} \tag{3.31}$$

This expression is equivalent to equation 2.76, however the denominator term in 2.76 has been neglected as $\sigma_{ref} \ll 1$. The value of σ_{ref} used was, unless otherwise stated, the sum of the mean value of σ_{calc} and the mean value of the experimentally determined chemical shifts. Consequently, the averages (over the full spectrum) of the referenced calculated values (δ_{iso} in equation 3.31) and experimental values of the isotropic chemical shifts coincided, consistent with the approach used in references [107, 108]. For the calculation results presented in this thesis, the values of σ_{ref} used were consistent with those used in the published literature [56, 108–111].

All calculations used in the work presented in this thesis were performed using the academic release version 4.3 of CASTEP, and used the PBE exchange-correlation functional [112] and "ultrasoft" pseudopotentials [49]. The majority of calculations (specifically those used in the work presented in chapters 4, 6 and 7) were performed on an IBM high performance computing system, operated by the Centre for Scientific Computing at the University of Warwick. The cluster is comprised of 240 2-way dual-core 3 GHz Intel Xeon 5160 processors (960 cores total). The calculations used in chapter 5 were performed by Prof. Chris Pickard, University College London. Specific computational details (cut-off energy, sampling density of the Monkhorst-Pack grid [113], etc.) are stated in the relevant experimental results chapters.

CHAPTER

FOUR

DETERMINING RELATIVE PROTON-PROTON PROXIMITIES THROUGH THE BUILD-UP OF ^{1}H DOUBLE-QUANTUM CORRELATION PEAKS

4.1 Introduction

This chapter, based on recently published results [1], investigates the use of ^{1}H double-quantum correlation experiments in the determination of internuclear distances. The dipolar coupling between a pair of nuclei is dependent on the internuclear distance to the inverse cubed power and hence provides an extremely sensitive way to measure short range distances - on the order of a few angstroms - within a solid structure. The ^{1}H double-quantum correlation experiment, described in chapter 3 can be used to identify nuclear proximities through the dipolar coupling. Varying the duration of the recoupling pulses, used in this experiment during the excitation and reconversion periods before and after t_1, causes the intensity of the ^{1}H DQ correlation peaks to change. It is this change in the peak intensity, plotted against the recoupling time as double-quantum build-up curves that is investigated in this chapter.

In addition to studying experimental results, the experiment was simulated on small clusters of ^{1}H nuclei, using density matrix based software. These simulations provide additional insight into the factors affecting the double-quantum build-up, and allow manipulation of both the experimental parameters and the nuclear spin system in ways that would not be possible using a purely experimental approach.

The dipeptide β-AspAla has been chosen as a suitable model compound for this

work. As a crystalline solid comprised of small organic molecules, it is a similar system to many pharmaceutical compounds, and hence provides a good test of the wider applicability of this technique. Many organic crystalline systems contain a large number of hydrogen atoms, which are often involved in inter-molecular interactions, for example hydrogen bonding, and as such the NMR of ^{1}H nuclei may be used probe these regions of the molecule. β-AspAla contains eight different ^{1}H environments, each of which may be readily resolved in a two dimensional DQ CRAMPS spectrum. In this way it is an ideal model to use in this work, as the build-up behaviour of each individual peak can be monitored in isolation.

4.2 Computational Details

First-principles calculations were performed using the academic release version 4.3 of the CASTEP [48] software package, which implements density-functional theory using a planewave basis set. An initial geometry optimisation, starting with the X-ray single-crystal structure [114] of the dipeptide β-AspAla (Cambridge Crystal Database reference FUMTEM), and only allowing the hydrogen atoms to move, employed a cut-off energy of 1.2 keV, and was performed using a Monkhurst-Pack grid with a k-point spacing (upper bound) of 0.1 Å^{-1}. The calculations of the shielding tensors utilised the gauge-including projector augmented-wave (GIPAW) [50, 51] method, with a cut-off energy of 1.1 keV, and was performed using a Monkhurst-Pack grid with a k-point spacing (upper bound) of 0.3 Å^{-1}. The reference shielding was obtained as described in chapter 3.

^{1}H DQ build-up curves were simulated using SPINEVOLUTION [42] Simulations of the DQ (t_1) evolution (sandwiched between POST-C7 [31] recoupling periods for the excitation and reconversion of DQ coherence) were performed in a one-dimensional fashion by incrementing t_1 and determining (at $t_2 = 0$) the transverse magnetisation for a single detect spin. During t_1, perfect homonuclear decoupling was achieved by switching off all dipolar interactions. Powder averaging was performed, using 16 gamma angles, and a set of 34 alpha and beta angles, provided by SPINEVOLUTION. It was verified that increasing the number of powder averaging angles did not change the shape of the simulated ^{1}H DQ build-up curves. The default SPINEVOLUTION time

step of 2 μs was used - it was verified that decreasing this did not change the shape of the simulated ^{1}H DQ build-up curves. 1024 complex time points were simulated for a rotor-synchronised dwell time of 80 μs, resulting in a total t_1 (DQ) acquisition time of 82 ms. 10 Hz line broadening was applied. Representative SPINEVOLUTION input files are provided in appendix A. The simulations were performed on a desktop computer, running in parallel on four CPU cores, and taking approximately 70 minutes to perform the seven simulations required for a single build-up curve.

The simulation process was repeated six times, using a different ^{1}H in the β-AspAla molecule as the detect nucleus. In this way, a series of one dimensional spectra were acquired, each corresponding to a slice through the two dimensional spectrum at a particular F_1 value. For each different detect nucleus, the eight nuclei included in the simulation comprised it, and the seven ^{1}H nuclei closest to it in the crystal structure. A full list of the eight spin systems used for each set of simulations is listed in table 4.1. Chemical shift anisotropy data, obtained from the density functional theory calculations and listed in table 4.2 was included in the simulations. Using the output of the DFT calculations, Euler angles were calculated to find the transformation required to move between the PAS of the CSA, and the Cartesian axes in which the nuclear positions are expressed.

It is to be noted that no simulations were performed with observation on either the CH_3 or NH_3 protons, to avoid complications in the analysis due to the rotation of these groups about the C—C or N—C bond that occurs at room temperature [115, 116]. In cases where a simulation set included a full CH_3 or NH_3 group, the rotation of the group was included in the simulation, by specifying a fast cyclic exchange between the three nuclei. This rotation causes a scaling of the H–H dipolar coupling by a factor of $|(1/2)(3\cos^2\beta - 1)|$, where β is the angle between the internuclear vector and the axis of rotation, i.e. in this case 90°. Consequently the H–H couplings within the CH_3 and NH_3 groups are scaled by a factor of 1/2. In cases where CH_3 or NH_3 groups were only partially included in the simulated spin system, no rotation was specified.

The SPINEVOLUTION time-domain output files were processed using GSim, [117] applying an additional 10 Hz line broadening and zero filling to 16384 complex points before Fourier transformation. Build-up curves were produced by phasing each spectrum so as to achieve an in-phase absorptive line shape for each resonance (correspond-

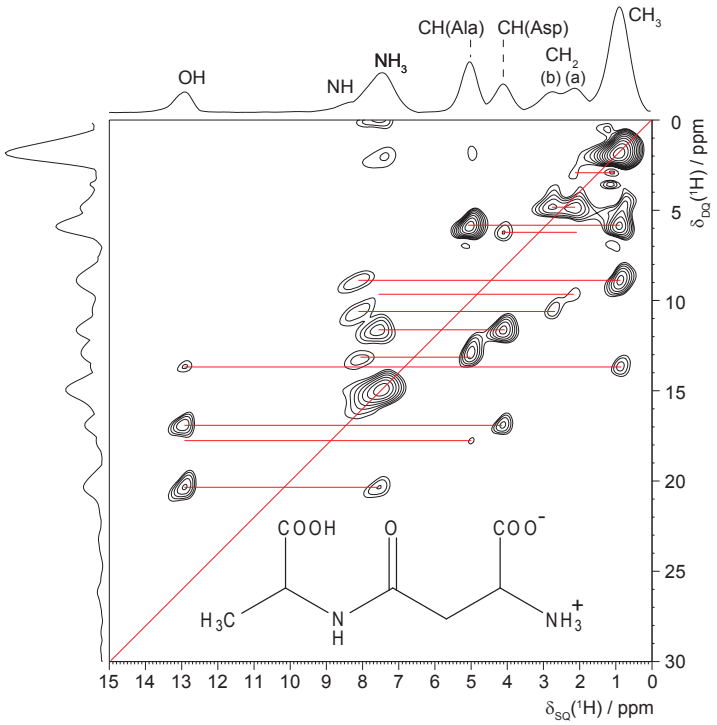

Figure 4.1: A Two-dimensional ^{1}H (500 MHz) DQ CRAMPS spectrum of β-AspAla, recorded using the DQ CRAMPS pulse sequence described in chapter 3, at 12.5 kHz MAS. Three elements of the POST-C7 recoupling sequence were used in both the excitation and reconversion periods (corresponding to a total recoupling time of 138 μs). The *rf* nutation frequency was set to $\nu_1 = 87.5$ kHz during the recoupling periods, and to $\nu_1 = 100$ kHz for decoupling during the t_1 and t_2 periods. A structural diagram of the β-AspAla molecule is inset.

ing to a distinct DQ coherence), and then determining the peak intensity.

4.3 Results and Discussion

4.3.1 Comparison of Simulated and Experimental Double-Quantum Build-up

The ^{1}H DQ CRAMPS spectrum shown in figure 4.1 features peaks in the single-quantum (F_2) dimension corresponding to each of the eight ^{1}H sites in the β-AspAla molecule. The high resolution, achieved through the use of homonuclear decoupling, allows each peak to be clearly individually resolved, with the exception (in the F_2 dimension) of the NH_3 and NH resonances at 7.5 and 8.0 ppm respectively. However double-quantum peaks corresponding to interactions involving one or other of these sites may be clearly distinguished in the full two dimensional spectrum.

Table 4.3 lists the fifteen double-quantum peaks visible in the F_1 projection of

Table 4.1: Nuclear spin systems used in the SPINEVOLUTION simulations.

^{1}H Number[a]	δ_{SQ}/ppm	DQ pair	δ_{DQ}/ppm	Distance(s)/Å
(a) CH_2(a) simulation				
2	2.7	CH_2(a)–CH_2(b)	4.9	1.55
3	4.1	CH_2(a)–CH(Asp)	6.3	2.39
4, 5	7.5	CH_2(a)–NH_3	9.7	2.41, 2.67
6[b], 7[b], 8[b]	0.9	CH_2(a)–CH_3	3.1	2.69, 2.76, 3.03
(b) CH_2(b) simulation				
2	2.2	CH_2(b)–CH_2(a)	4.9	1.55
3	8.0	CH_2(b)–NH	10.7	2.15
4, 7	7.5	CH_2(b)–NH_3	10.2	2.48, 3.03
5, 8	4.1	CH_2(b)–CH(Asp)	6.8	2.82, 3.92
6	0.9	CH_2(b)–CH_3	3.6	2.88
(c) CH(Asp) simulation				
2[b], 3[b], 6[b], 7	7.5	CH(Asp)–NH_3	11.6	2.27, 2.31, 2.76, 2.77
4	2.2	CH(Asp)–CH_2(a)	6.8	2.39
5	12.9	CH(Asp)–OH	17.0	2.45
8	2.7	CH(Asp)–CH_2(b)	6.3	2.82
(d) CH(Ala) simulation				
2[b], 3, 5[b], 6[b]	0.9	CH(Ala)–CH_3	5.9	2.40, 2.40, 2.81, 2.87
4	8.0	CH(Ala)–NH	13.0	2.78
7	7.5	CH(Ala)–NH_3	12.5	3.06
8	12.9	CH(Ala)–OH	17.9	3.25
(e) NH simulation				
2	2.7	NH–CH_2(b)	10.7	2.15
3, 5, 6	0.9	NH–CH_3	8.9	2.57, 3.00, 3.00
4, 8	5.0	NH–CH(Ala)	13.0	2.78, 3.26
7	2.2	NH–CH_2(a)	10.2	3.13
(f) OH simulation				
2	4.1	OH–CH(Asp)	17.0	2.49
3, 4, 5, 6	7.5	OH–NH_3	20.4	2.56, 2.66, 2.74, 3.08
7, 8	0.9	OH–CH_3	13.8	3.13, 3.17

[a] The eight ^{1}H nuclei included in the simulations are numbered in order of increasing distance from the central proton. Intermolecular proximities are in italics.
[b] Rotation of the CH_3 or NH_3 group is considered in the SPINEVOLUTION simulations (by calculating the average dipolar coupling Hamiltonians obtained by exchanging the CH_3 or NH_3 protons).

Table 4.2: CASTEP (GIPAW) calculation of ^{1}H chemical shifts.

	δ_{iso}/ppm		Shielding Tensor					
^{1}H	Exp.	Calc.[a]	σ_{xx}	σ_{yy}	σ_{zz}	σ_{iso}/ppm	δ_{aniso}/ppm[b]	η[c]
CH_3(a)	0.9	1.3	24.6	26.9	36.0	29.2	6.9	0.33
CH_3(b)	0.9	0.5	26.9	29.7	33.4	30.0	3.4	0.83
CH_3(c)	0.9	0.2	26.4	27.6	36.9	30.3	6.6	0.18
CH_2(a)	2.2	2.1	25.0	28.1	32.1	28.4	3.7	0.82
CH_2(b)	2.7	2.7	31.2	28.3	23.8	27.8	-3.9	0.71
CH(Asp)	4.1	4.1	31.4	26.8	21.0	26.4	-5.4	0.84
CH(Ala)	5.0	5.0	22.2	24.5	29.7	25.5	4.2	0.53
NH_3(a)	7.5	6.2	18.0	20.3	34.7	24.3	10.4	0.22
NH_3(b)	7.5	8.1	13.6	17.4	36.1	22.4	13.8	0.28
NH_3(c)	7.5	9.6	11.8	13.4	37.6	20.9	16.7	0.09
NH	8.0	8.4	14.8	21.2	30.3	22.1	8.2	0.78
OH	12.9	14.0	7.0	9.7	32.7	16.5	16.3	0.16

[a] $\delta_{iso} = \sigma_{ref} - \sigma_{iso}$ where $\sigma_{ref} = 30.5$ ppm.
[b] $\delta_{aniso} = \sigma_{zz} - \sigma_{iso}$
[c] $\eta = (\sigma_{yy} - \sigma_{xx})/(\sigma_{zz} - \sigma_{iso})$

the DQ CRAMPS spectrum (the two on-diagonal peaks for the CH_3–CH_3 and NH_3–NH_3 interactions, and the thirteen off-diagonal pairs of peaks marked in red in figure 4.1), and assigns each peak to a particular dipolar-coupled pair of nuclei. Figure 4.2 shows rows extracted from β-AspAla DQ CRAMPS spectra at the frequency (in F_2) of each of the fifteen double-quantum peaks. The spectra were recorded with a range of recoupling times, varied by changing the number of POST-C7 elements used during the excitation and reconversion periods. Note that because of strong dipolar couplings between ^{1}H nuclei in close proximity, due to the dependence of the coupling on the square of the gyromagnetic ratio, the maximum peak intensity is achieved at relatively short total recoupling times (typically in the range 100 - 250 μs). Consequently it is the number of basic POST-C7 elements (duration $2\tau_R/7$) rather than full POST-C7 cycles (duration $2\tau_R$) that is incremented.

The data in figure 4.2 (reproduced from reference [25]) shows that as the recoupling time varies, the intensity of the double-quantum peaks builds up to a maximum point before decreasing. The value of the maximum, and the time taken to reach it varies significantly for different internuclear interactions. In order to gain a greater understanding of this double-quantum build-up behaviour, this experimental data, published in reference [25], was analysed alongside the results of simulations of the DQ correlation experiment on clusters of ^{1}H nuclei taken from the crystal structure of β-AspAla.

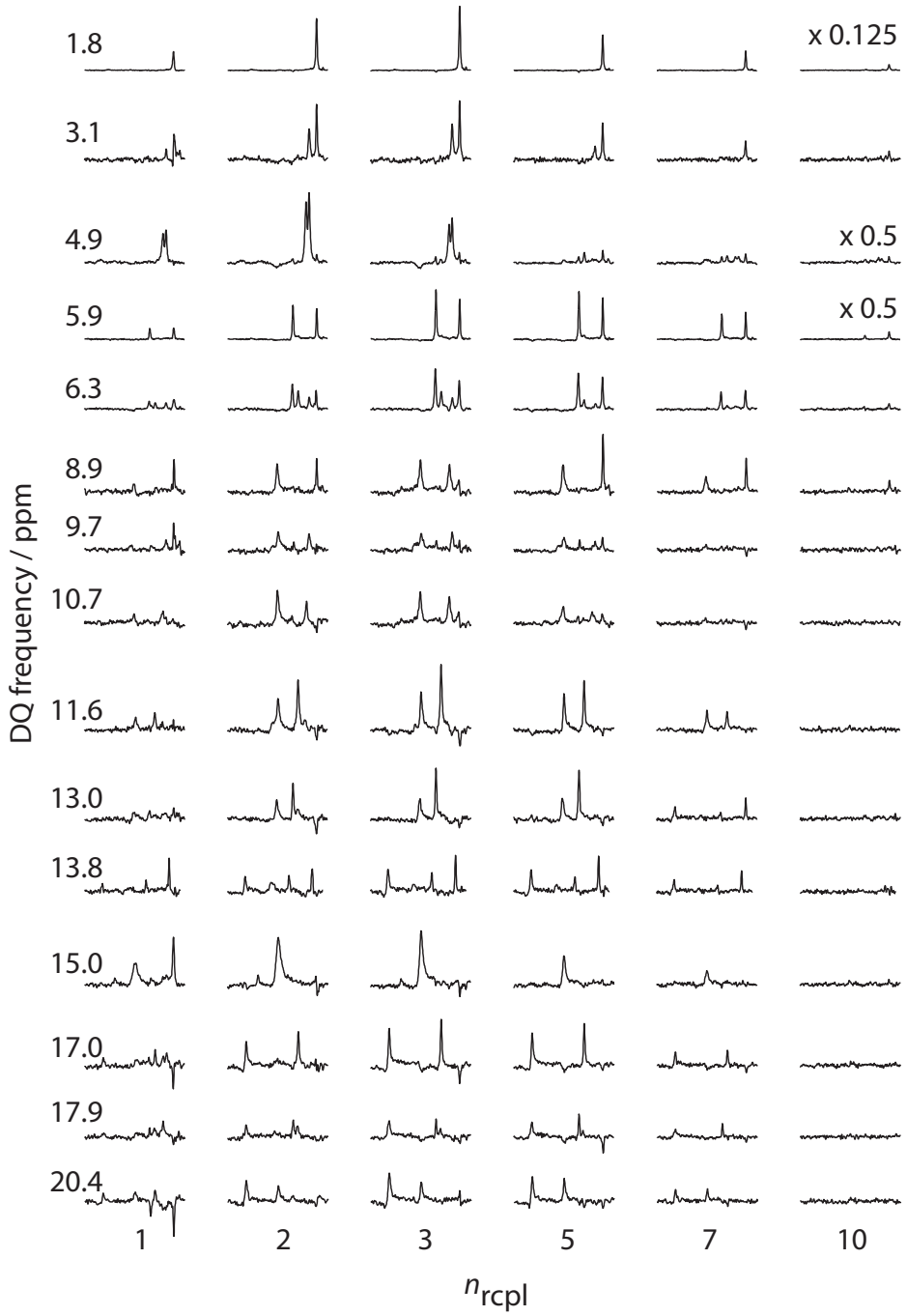

Figure 4.2: Rows extracted from two-dimensional ^{1}H DQ CRAMPS spectra of β-AspAla. The value n_{RCPL} corresponds to the number of POST-C7 recoupling elements used for excitation and reconversion of the DQ coherence. A single element is of duration 22.8 μs. The DQ frequencies of the rows correspond to the interaction listed in table 4.3. Figure reproduced from reference [25].

Table 4.3: Observed DQ peaks[a] in the ^{1}H DQ CRAMPS spectrum of β-AspAla.

	DQ Pair	$\delta_{SQ1} + \delta_{SQ2}$/ ppm	δ_{DQ}/ppm
1	CH_3–CH_3	0.9+0.9	1.8
2	*CH_3–CH_2(a)*	*0.9+2.2*	*3.1*
3	$CH2_2$(a)–CH_2(b)	2.2+2.7	4.9
4	CH_3–CH(Ala)	0.9+5.0	5.9
5	CH2(a)–CH(Asp)	2.2+4.1	6.3
6	CH_3–NH	0.9+8.0	8.9
7	CH_2(a)–NH_3	2.2+7.5	9.7
8	CH_2(b)–NH	2.7+8.0	10.7
9	CH(Asp)–NH_3	4.1+7.5	11.6
10	CH(Ala)–NH	5.0+8.0	13.0
11	*CH_3–OH*	*0.9+12.9*	*13.8*
12	NH_3–NH_3	7.5+7.5	15.0
13	*CH(Asp)–OH*	*4.1+12.9*	*17*
14	CH(Ala)–OH	5.0+12.9	17.9
15	*NH_3–OH*	*7.5+12.9*	*20.4*

[a] Intermolecular proximities are in italics.

Figure 4.3 shows the experimental and simulated DQ build-up curves for each of the ^{1}H nuclei in the β-AspAla molecule (with the exception of the CH_3 and NH_3 protons). Each of the curves (both simulated and experimental) are normalised to the intensity of the CH(Ala)–CH_3 curve at $n_{RCPL} = 5$, which is the maximum intensity simulated point. Inspection of the build-up curves in figure 4.3 in conjuntion with the data in table 4.1 reveals that the maximum DQ peak intensity for a given single-quantum frequency corresponds to the shortest H–H distance (with the exception of the simulation data for the NH proton). This result is unsurprising given the dependence of the dipolar coupling on the internuclear distance. The following analysis considers the extent to which quantitative information on internuclear distances may be obtained from examining the lower intensity DQ build-up curves.

Figure 4.4 shows simulated and experimental double-quantum build-up curves for several of the internuclear interactions. Specifically the CH(Asp)–OH ($\delta_{DQ} = 4.1 + 12.9 = 17.0$ ppm), CH(Ala)–NH ($\delta_{DQ} = 5.0 + 8.0 = 13.0$ ppm) and CH(Ala)–OH ($\delta_{DQ} = 5.0 + 12.9 = 17.9$ ppm) curves. The closest H–H distances are 2.49 Å ($|d_{jk}| =$ 7.8 kHz), 2.78 Å ($|d_{jk}| = 5.6$ kHz) and 3.30 Å ($|d_{jk}| = 3.5$ kHz) respectively. Note that there is no simulated data for the CH(Ala)–OH interaction observed on the OH, as the CH(Ala) is not within the seven closest protons. These build-up curves provide a good

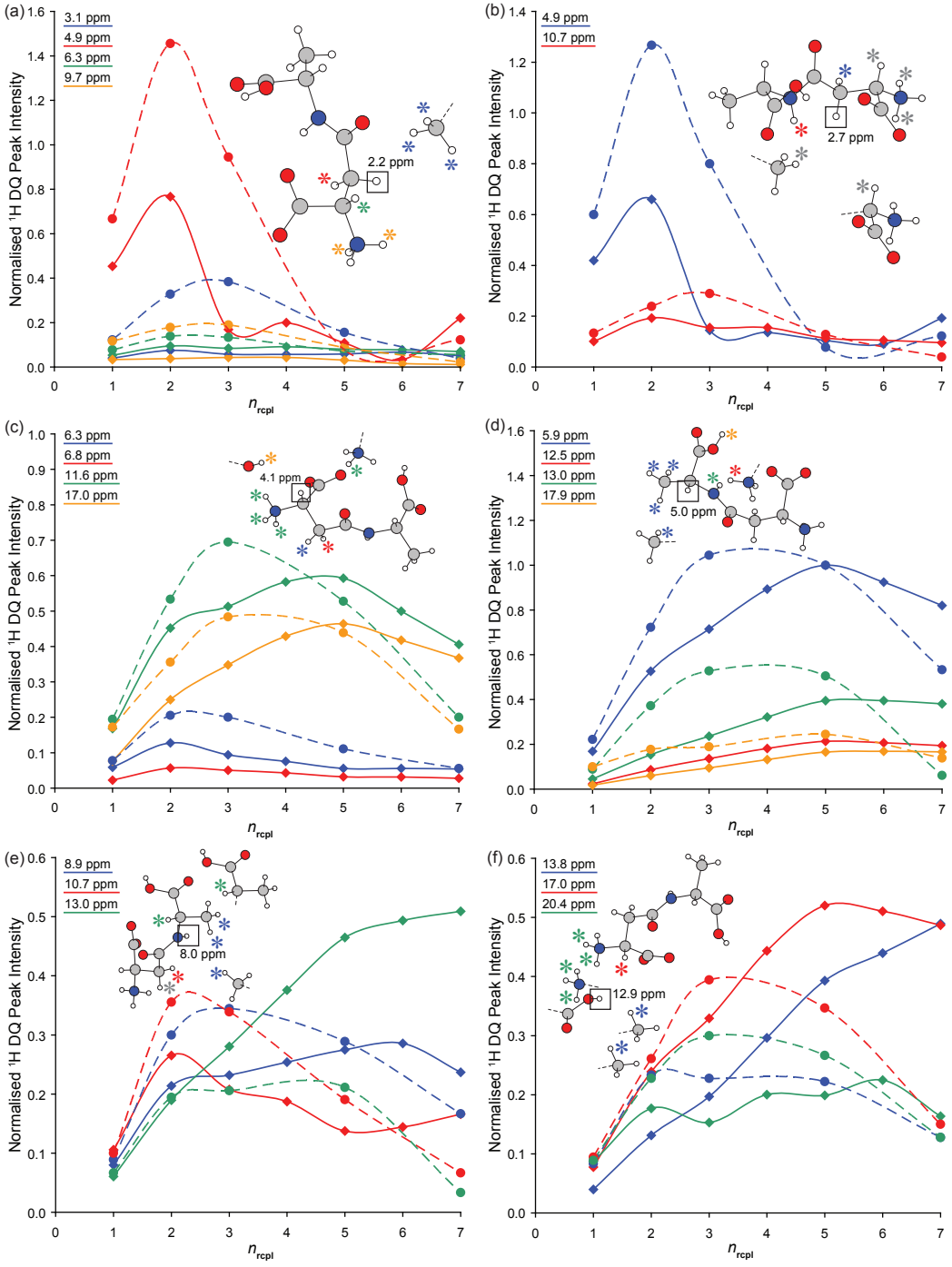

Figure 4.3: Simulated (diamonds, solid lines) and experimental (circles, dashed lines) β-AspAla ^{1}H DQ build-up curves for (a) CH_2(a), (b) CH_2(b), (c) CH(Asp), (d) CH(Ala), (e) NH and (f) OH protons. In each case the simulations (SPINEVOLUTION, 500 MHz, 12.5 kHz) were performed on the eight spin cluster shown in the inset structural diagrams. The observed proton is marked with a box and the seven other included protons are highlighted with asterisks (colour coded to the build-up curve for the interaction between that proton and the observe proton). DQ peak intensities are normalised to the corresponding DQ peak intensity for the CH(Ala)–CH_3 interaction at $n_{RCPL} = 5$. Lines linking the peak intensities are included as guides for the eye.

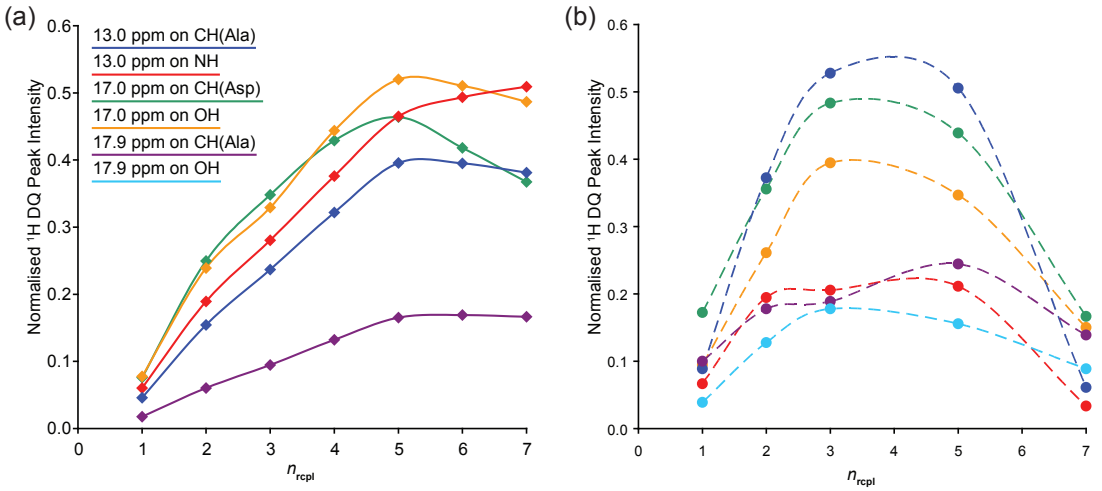

Figure 4.4: Comparison of (a) simulated and (b) experimental (500 MHz, 12.5 kHz) ^{1}H DQ build-up curves for the CH(Asp)–OH ($\delta_{DQ} = 4.1 + 12.9 = 17.0$ ppm), CH(Ala)–NH ($\delta_{DQ} = 5.0 + 8.0 = 13.0$ ppm) and CH(Ala)–OH ($\delta_{DQ} = 5.0 + 12.9 = 17.9$ ppm) dipolar-coupled proton pairs in β-AspAla. The closest H–H distances are 2.49 Å ($|d_{jk}| =$ 7.8 kHz), 2.78 Å ($|d_{jk}| = 5.6$ kHz) and 3.30 Å ($|d_{jk}| = 3.5$ kHz) respectively. DQ peak intensities are normalised to the corresponding DQ peak intensity for the CH(Ala)–CH_3 interaction at $n_{RCPL} = 5$. Lines linking the peak intensities are included as guides for the eye.

basis for the discussion of the recoupling time corresponding to the maximum peak intensity, and the relative maximum intensity reached, in terms of the H–H distance.

Of particular interest are the two sets of peaks in this set at the CH(Ala) and OH single-quantum frequencies. Considering first the simulated CH(Ala) peaks, the highest intensity is reached for the CH(Ala)–NH peak (dark blue build-up curves in figure 4.4), at five recoupling elements. The CH(Ala)–OH peak (purple) reaches a considerably lower maximum intensity, again at five recoupling elements. The experimental peaks observed on the OH SQ frequency exhibit a similar pattern. The higher intensity OH–CH(Asp) peak (orange) reaches its maximum value at three recoupling elements, as does the lower intensity OH–CH(Ala) peak (pale blue). In both cases, and in both experiment and simulation, it is the shorter range distance that leads to the highest maximum intensity double-quantum build up. The ratio of the heights reached by the curves observed at a particular SQ frequency is found to correspond approximately to the ratio of the squares of the dipolar couplings. For example the ratio of the dipolar couplings of the CH(Ala)–NH and CH(Ala)–OH interactions is $d_1^2/d_2^2 = 5.6^2/3.5^2 = 2.56$. This value is close to the ratios of the maxima in the experimental and simulated build-up curves, which are 2.20 and 2.35 respectively. This behaviour is in agreement

with the analysis for isolated spin pairs in references [118] and [119].

The data acquired for peaks corresponding to interactions including the CH_2 protons, in figure 4.3(a) and (b) also reveals interesting double-quantum build-up behaviour. As expected from the above analysis, the peaks due to the very short range CH_2(a)–CH_2(b) interaction ($\delta_{DQ} = 2.2 + 4.7 = 4.9$ ppm), with an internuclear distance of 1.55 Å($|d_{jk}| = 32.2$ kHz), reach the highest maximum intensity at their respective single-quantum frequencies, and do so in an extremely short recoupling time (at $n_{RCPL} = 2$). The build-up curve for the CH_2(b)–NH peak ($\delta_{DQ} = 2.7 + 8.0 = 10.7$ ppm), with an internuclear distance of 2.15 Å($|d_{jk}| = 12.1$ kHz), shown in figure 4.3(b) is of a much lower intensity, and also reaches maximum intensity in a short recoupling time ($n_{RCPL} = 2$ for simulation, 3 for experiment).

In order to investigate the effect the shorter range interaction has on the build-up of other DQ peaks at the same SQ frequency, the eight spin simulations centred on the CH_2(b) and NH protons were repeated with the CH_2(a) proton removed from the simulation set, leaving a total of seven spins. The results of these simulations are presented in figure 4.5, where they are compared to the full eight spin simulation, and to the experimental data.

The results show that in the absence of the CH_2(a) proton, the maximum in the simulated double-quantum build-up curve shifts from $n_{RCPL} = 2$ to $n_{RCPL} = 4$ in both cases. Additionally the intensity of the CH_2(b)–NH peak is greatly increased. These results indicate that the presence of the strong CH_2(a)–CH_2(b) interaction reduces the reliability of proton - proton distance measurements made via the double-quantum build-up, as a consequence of the phenomenon of dipolar truncation in homonuclear solid-state NMR experiments, as described in reference [120]. Note that a similar truncation effect will exist for CH_3 and NH_3 groups, though reduced by the scaling factor of 1/2 as described in section 4.2.

4.3.2 Differences Between Simulated and Experimental Data

It is clear from the results presented in the previous section that the eight spin density matrix simulations accurately reproduce many of the features seen in the experimental DQ build-up curves, including the approximate ratio of the build-up curve intensities, which may be used to gain information on the relative H–H proximities. However

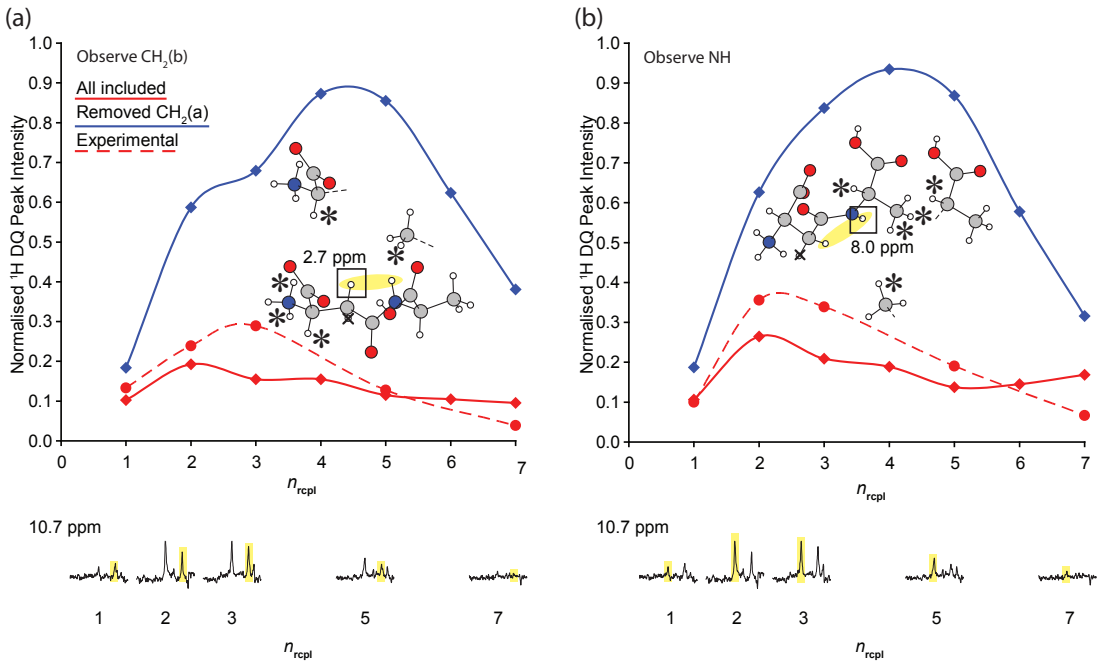

Figure 4.5: A comparison of simulated (diamonds, solid lines) and experimental (circles, dashed lines) β-AspAla ^{1}H double-quantum build-up curves for the CH_2(b)–NH peak ($\delta_{DQ} = 2.7{+}8.0 = 10.7$ ppm), with an internuclear distance of 2.15 Å($|d_{jk}| = 12.1$ kHz). Observation is performed on the (a) CH_2(b) and (b) NH protons. Simulations are performed on eight or seven spin clusters, either including (red) or not including (blue) the CH_2(a) proton. DQ peak intensities are normalised to the corresponding DQ peak intensity for the CH(Ala)–CH_3 interaction at $n_{RCPL} = 5$. Lines linking the peak intensities are included as guides for the eye. Experimental spectra highlight the relevant peak and are rows extracted from the DQ CRAMPS spectra.

inspection of figure 4.3 shows that the simulated build-up curves often reach their maximum value at a longer recoupling time than the experimental curves. For example in the build-up curves observed at the OH single-quantum frequency shown in figure 4.3(f) this behaviour is apparent in all three sets of curves.

These differences between simulation and experiment may be attributed to the limited size of the set of nuclei used in the simulations. In practice this is limited by the availability of computational resources, specifically the time taken to perform simulations increases exponentially with the number of simulated spins [42].

In order to investigate the effect that the simulation size has on the resultant DQ build-up curve, a set of experiments were performed using the CH(Ala) and CH(Asp) centred simulation sets. Specifically the build-up of the CH(Ala)–NH and CH(Asp)–OH peaks was considered. In both cases the maximum DQ peak intensity is observed at $n_{RCPL} = 5$ in simulation and $n_{RCPL} = 3$ in experiment. For each observe nucleus, a series of simulations were performed, starting with a two spin system comprised of the

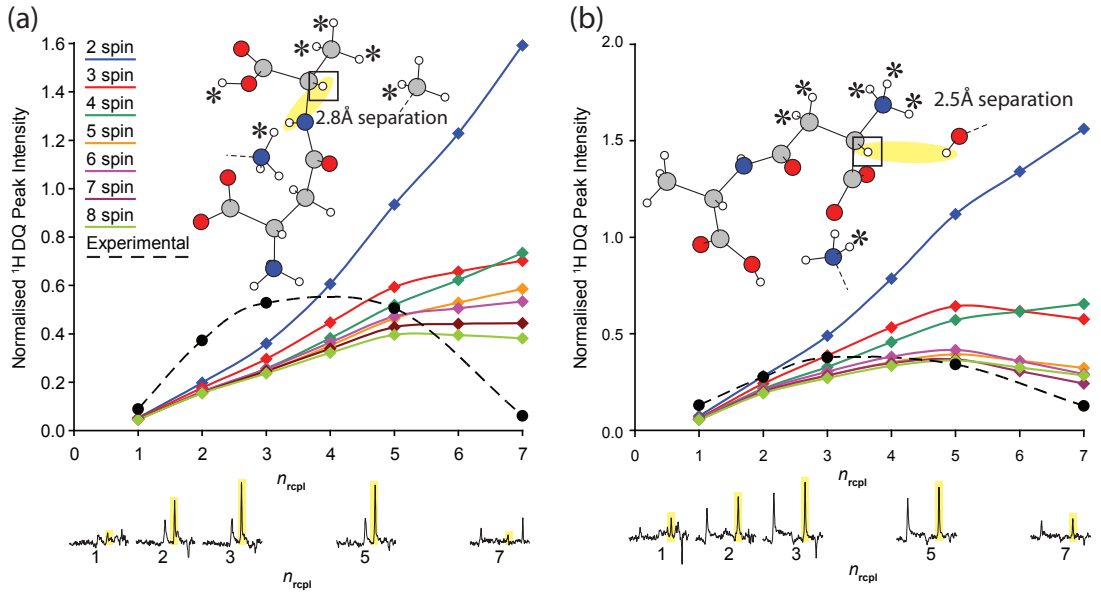

Figure 4.6: A comparison of simulated (diamonds, solid lines) and experimental (circles, dashed lines) β-AspAla ^{1}H double-quantum build-up curves for the (a) CH(Ala)–NH ($\delta_{DQ} = 5.0 + 8.0 = 13.0$ ppm; internuclear distance of 2.78 Å($|d_{jk}| = 5.6$ kHz)) and (b) CH(Asp)–OH ($\delta_{DQ} = 4.1 + 12.9 = 17.0$ ppm; internuclear distance of 2.49 Å($|d_{jk}| = 7.8$ kHz)) interactions. Simulations are performed on sets of between two and eight nuclei, starting with the observed nucleus and the relevant coupled nucleus (e.g. CH(Ala) and NH) and adding more nuclei with increasing distance from the observe nucleus. DQ peak intensities are normalised to the corresponding DQ peak intensity for the CH(Ala)–CH_3 interaction at $n_{RCPL} = 5$. Lines linking the peak intensities are included as guides for the eye. Experimental spectra highlight the relevant peak and are rows extracted from the DQ CRAMPS spectra.

observed nucleus and the other nucleus involved in the interaction of interest (either NH or OH). In each successive set of simulations, the next closest nucleus to the observe nucleus was added to the system, until the full eight spin system was used. The results of these simulations, and the relevant experimental DQ build-up curves, are shown in figure 4.6

The results of these simulations show that in both cases, the build-up curves for the two-spin system does not reach a maximum in at least the first six recoupling elements. In the larger spin systems, a peak in the build-up curve appears at $n_{RCPL} = 5$, and the maximum intensity of the curve decreases as more spins are included in the simulations. This result supports the suggestion that limiting the size of the simulated cluster causes a deviation from the experimental result, and indicates that the simulation of faster DQ build-up seen in experiment could be reproduced in simulations of larger spin systems. It is however notable that each successive spin added to the simulation would in general be expected to have a lesser effect on the simulated build-up curve, due to the larger

distance to the observe nucleus, and would significantly increase the computation time. The eight spin simulations used in this work are approaching the largest density matrix simulation spin system currently reported in published literature, of eleven spins [103].

4.3.3 Investigation into the Effect of Magnetic Field Strength and MAS Frequency on ^{1}H DQ Build-up Behaviour

The use of density matrix simulations in this work allows the investigation of the effects of changing a variety of experimental parameters on the double-quantum build-up curves. The advantage of investigating these effects through simulation is that the parameters can be varied over a wider range than would be possible experimentally, while ensuring consistency in all other factors. In all of the simulations presented to this point, parameters of a ^{1}H Larmor frequency of 500 MHz and MAS frequency of 12.5 kHz have been used, matching the parameters for the DQ CRAMPS experimental data. In order to investigate these effects, the eight spin system centred on the CH(Asp) proton will be used (as listed in table 4.1(c)). Specifically, the CH(Asp)–CH_2(a) (δ_{DQ} = 4.1 + 2.2 = 6.3 ppm) and CH(Asp)–OH (δ_{DQ} = 4.1 + 12.9 = 17.0 ppm) interactions present interesting cases to study. In the 500 MHz, 12.5 kHz MAS simulations, the CH(Asp)–OH build-up curve reaches maximum intensity at $n_{RCPL} = 5$, whereas the maximum point in the CH(Asp)–CH_2(a) build-up curve is shifted to $n_{RCPL} = 2$, and reaches a significantly reduced intensity due to the perturbing effect of the strong dipolar coupling within the CH_2 group, as described in section 4.3.1.

The experimental DQ build-up curves for these interactions exhibit consistent behaviour with the simulated data. The CH(Asp)–$CH_2(a)$ curve reaches its maximum intensity at $n_{RCPL} = 2$, and at a significantly lower intensity than the CH(Asp)–OH curve, for which the maximum value is reached at $n_{RCPL} = 3$, consistent with the faster build-up usually seen in the experimental data as described in the previous section.

Figure 4.7 compares the simulated double-quantum build-up curves for the two interactions at ^{1}H Larmor frequencies of 500 MHz and 1 GHz. These results show that there is no significant effect on the build-up behaviour as a result of changing the magnetic field strength. Specifically, there is no change in either the maximum build-up curve intensity, or the recoupling time at which it is reached for either interaction, the only visible difference being a small alteration in the shape of the build-up curves.

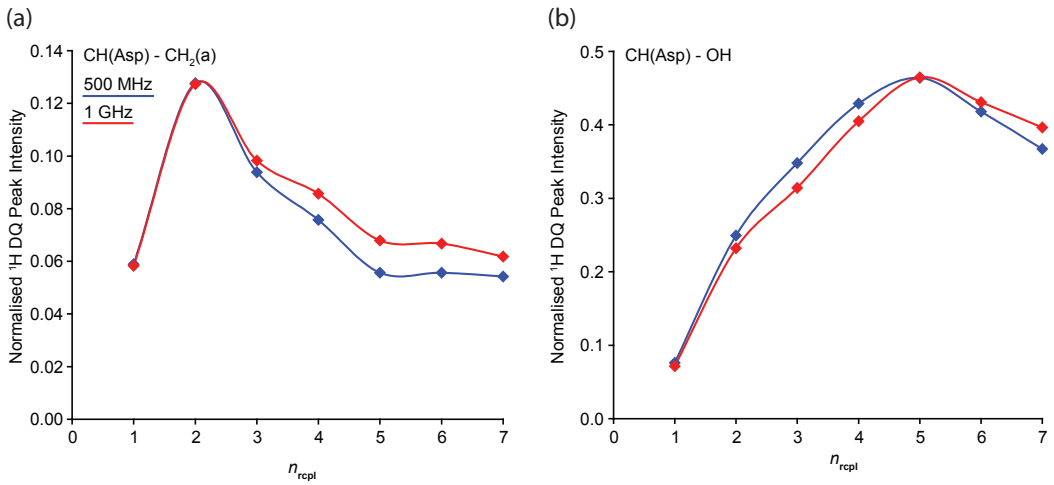

Figure 4.7: A comparison of simulated (eight spin, SPINEVOLUTION) ^{1}H DQ build-up curves for the (a) CH(Asp)–$CH_2(a)$ ($\delta_{DQ} = 4.1 + 2.2 = 6.3$ ppm; internuclear distance of 2.39 Å($|d_{jk}| = 8.8$ kHz)) and (b) CH(Asp)–OH ($\delta_{DQ} = 4.1 + 12.9 = 17.0$ ppm; internuclear distance of 2.49 Å($|d_{jk}| = 7.8$ kHz)) interactions in β-AspAla, as the ^{1}H Larmor frequency is changed between values of 500 MHz (blue) and 1 GHz (red), observing the transverse magnetisation on the CH(Asp) proton. DQ peak intensities are normalised to the corresponding DQ peak intensity for the CH(Ala)–CH_3 interaction at $n_{RCPL} = 5$. Lines linking the peak intensities are included as guides for the eye.

Considering the same pair of interactions, figure 4.8 shows the effect of changing the MAS frequency on the double-quantum build-up behaviour. In contrast to the other figures presented in this chapter, here DQ peak intensity is shown as a function of the total recoupling time, rather than the number of recoupling elements (i.e., the combined time of the recoupling periods before and after t_1). This accounts for the rotor synchronisation requirements of the POST-C7 pulse sequence, as described in chapter 3. As the MAS frequency is increased, the required *rf* nutation frequency increases, and hence the pulse duration for a given flip-angle decreases. For example, the data point in figure 4.8 at approximately 92 μs used two POST-C7 elements for both excitation and reconversion at 12.5 kHz MAS, and twenty elements for both at 125 kHz MAS.

In this case it is clear that changing the MAS frequency, and concomitantly the *rf* nutation frequency, has a noticable effect on the double-quantum build-up curves. For both the CH(Asp)–CH_2(a) and CH(Asp)–OH interactions, the maximum double-quantum peak intensity increases at higher MAS frequencies. Additionally changes are apparent in the shape of the build-up curves, most notably the maximum point in the CH(Asp)–OH build-up curve shifts from 230 to 184 μs at 25 kHz and higher MAS

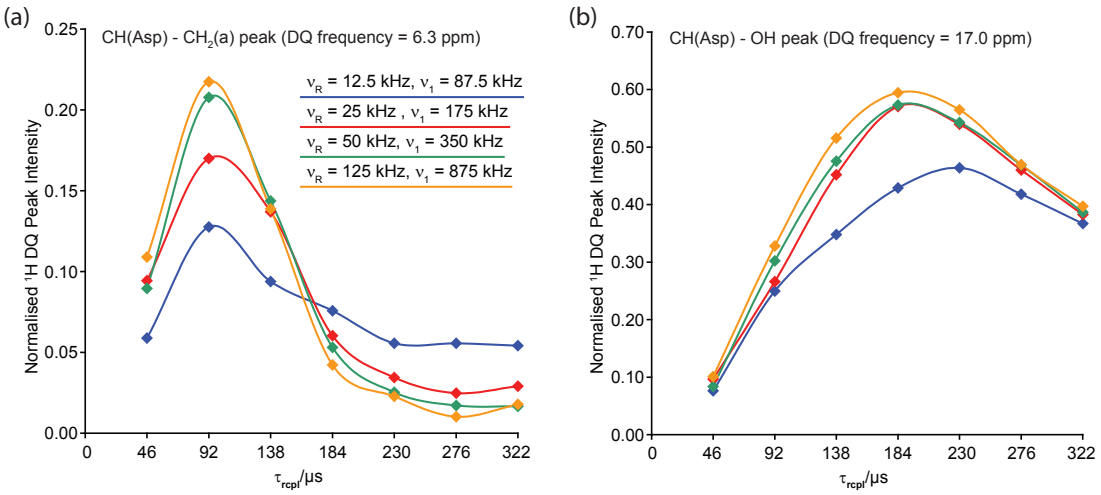

Figure 4.8: A comparison of simulated (eight spin, SPINEVOLUTION) ^{1}H DQ build-up curves for the (a) CH(Asp)–CH_2(a) ($\delta_{DQ} = 4.1 + 2.2 = 6.3$ ppm; internuclear distance of 2.39 Å($|d_{jk}| = 8.8$ kHz)) and (b) CH(Asp)–OH ($\delta_{DQ} = 4.1 + 12.9 = 17.0$ ppm; internuclear distance of 2.49 Å($|d_{jk}| = 7.8$ kHz)) interactions in β-AspAla, observing the transverse magnetisation on the CH(Asp) proton. The DQ build-up curves show the effect of changing the MAS frequency (and consequently the *rf* nutation frequency used for the recoupling pulses). DQ peak intensities are normalised to the corresponding DQ peak intensity for the CH(Ala)–CH_3 interaction at $n_{RCPL} = 5$. Lines linking the peak intensities are included as guides for the eye.

frequencies. However, for the purpose of comparing DQ build-up curves recorded at the same SQ frequency, the basic features of the curves generally remain unaltered by the change in the MAS frequency. Notably the CH(Asp)–$CH_2(a)$ curve still reaches its maximum value at a significantly shorter recoupling time than the CH(Asp)–OH curve. Furthermore the peak intensity in the CH(Asp)–CH_2(a) curve remains at approximately one third of the CH(Asp)–OH curve. This result indicates that the perturbing effect of the CH_2–CH_2 interaction is unaffected by the increase in MAS frequency. This is unsurprising as while the higher MAS would be expected to significantly reduce the CH_2–CH_2 dipolar interaction, the POST-C7 scheme used to achieve recoupling is specifically designed to counteract the effects of MAS, hence the dipolar truncation effect remains.

4.4 Summary and Conclusions

The work presented in this chapter has shown that eight spin density matrix simulations performed using SPINEVOLUTION [42] are able to reproduce most of the features of the build-up behaviour of ^{1}H double-quantum correlation peaks in the DQ CRAMPS

spectrum of the dipeptide β-AspAla. The comparison of experimental and simulated data has enabled relationships between the form of the DQ build-up curves and the internuclear distance to be determined. Specifically, the following guidelines may be established to aid in the analysis of build-up data from two-dimensional DQ CRAMPS spectra :

- At a given single-quantum frequency, the build-up curve that reaches the maximum intensity will usually correspond to the shortest range H–H interaction involving the proton at that single-quantum frequency.

- The highest intensity DQ build-up curves at a range of different single-quantum frequencies may be compared in terms of the recoupling time at which they reach their maximum intensity. A shorter recoupling time corresponds to a shorter range H–H interaction. For example, the experimental CH_2(a)–CH_2(b) curve (H–H distance of 1.55 Å) reaches its maximum value at $n_{RCPL} = 2$, whereas the CH(Asp)–OH curve (H–H distance of 2.49 Å) reaches its maximum value at $n_{RCPL} = 3$.

- Within a set of build-up curves for DQ peaks at the same single-quantum frequency, the recoupling time at which the maximum peak intensity is reached is often the same as for the highest intensity curve. However, the maximum intensity reached by each curve is indicative of the relative H–H interaction distance. Specifically the ratio of the maximum values of the DQ build-up curves is found to scale approximately with the ratio of the squares of the dipolar couplings. This behaviour shows that the analysis for isolated two spin systems remains approximately valid in the more complex case of a large network of dipolar coupled spin-$\frac{1}{2}$ nuclei.

- The perturbing effect of a strong dipolar coupling (for example the interaction between the two protons in a CH_2 group) reduces the reliability of relative H–H distance measurements made through the DQ build-up. Specifically for DQ peaks corresponding to interactions including a CH_2 proton, observed at a non-CH_2 single-quantum frequency, the intensity of the DQ peak is greatly reduced at all recoupling times, and the maximum point in the build-up curves is shifted to a shorter recoupling time.

Increasing either the ^{1}H Larmor frequency (effectively the B_0 magnetic field) or the MAS frequency was found to have no significant effect on the DQ build-up behaviour, in terms of the applicability of the guidelines listed above. It has also been shown that while the eight-spin simulations are able to produce many of the features that are observed experimentally, differences often occur in the recoupling times taken to reach the maximum peak intensity. This feature was attributed to the limited number of atoms that can be included in the simulations.

In conclusion, this work shows that even within a dense network of dipolar coupled nuclei, quantitative information on relative internuclear distances can be obtained from measuring the build-up of the double-quantum correlation peaks in a set of two-dimensional DQ CRAMPS spectra. This method is likely to be of use in the study of a wide variety of different systems. In later chapters of this thesis, DQ build-up analysis will be applied to several pharmaceutically relevant molecules, including those for which single-crystal x-ray data is unavailable. Given the dependence of solid-state NMR on local structure rather than long range order, it is in such systems that techniques such as that presented in this chapter have the potential to provide structural data unobtainable by other methods.

CHAPTER

FIVE

HYDROGEN BONDING IN POLYMORPHS OF THE API SIBENADET HYDROCHLORIDE

5.1 Introduction

The identification and characterisation of polymorphs of an active pharmaceutical ingredient (API) is an important stage in the development of new drugs. Between 80 and 90% of commercially marketed drugs are solids [121] and there is a clear need to understand the properties of all possible polymorphs, as well as the stability of the pharmaceutically relevant forms. The identity of the API polymorph used in the final drug product may significantly influence the efficacy of the drug. For example, in the case of the antibiotic chloramphenicol, the bioavailability varies between two polymorphs to such a large degree that the concentration of the API in the blood differs by an order of magnitude depending on which polymorph is used in the formulation [77]. Due to such considerations, a thorough investigation of all new pharmaceutical products is required to identify all polymorphs (in addition to solvates and any amorphous forms) [122].

An example of an API exhibiting polymorphism is Sibenadet Hydrochloride [123, 124], which is also known by the trade name Viozan. This is an API designed to treat chronic obstructive pulmonary disease (COPD), a disease of the small airways, closely associated with smoking, which causes symptoms including a chronic cough and difficulty in breathing. The sibenadet HCl API was developed by the pharmaceutical company AstraZeneca to be delivered via inhalation to act in the lung and relieve breathlessness [125]. Development of sibenadet HCl was halted by AstraZeneca in

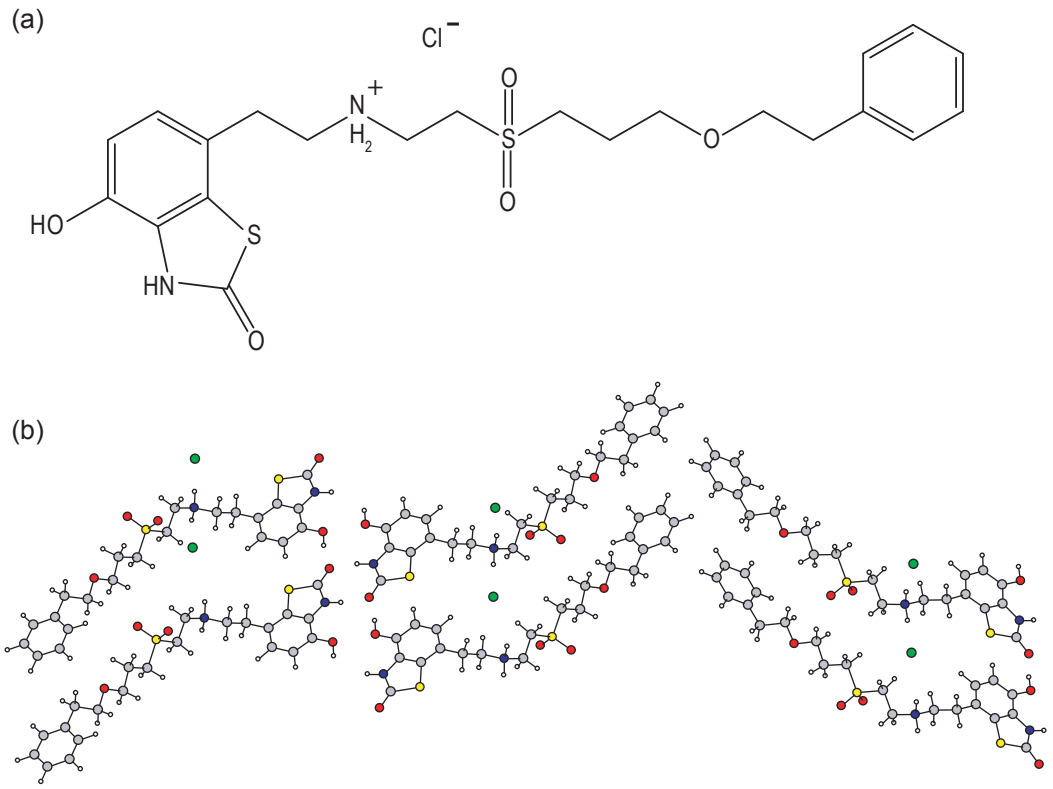

Figure 5.1: (a) Molecular structure of sibenadet HCl. (b) Crystal structural diagram showing the arrangement of sibenadet HCl molecules in form I. This diagram shows the CASTEP geometry optimised crystal structure.

2001, at the phase III stage [126].

A diagram of a sibenadet HCl molecule is shown in figure 5.1(a). The molecule consists of a long alkyl-based backbone, linking phenyl and benzothiazole groups. The combination of the flexibility of the alkyl chain, and the presence of numerous hydrogen bonding opportunities increases the possibility of sibenadet HCl to exhibit polymorphism. Three polymorphs are known, two of which, designated form I (the form developed for pharmaceutical use) and form II, are studied in this work.

Both form I and form II have previously been studied using a wide variety of characterisation techniques [125]. Differences between the polymorphs are evident in powder x-ray diffraction, vibrational spectroscopy, thermal analysis and ^{13}C CPMAS solid-state NMR. Powder x-ray diffraction also indicated that both polymorphic forms are crystalline, with a unit cell significantly longer in one direction than the other two. A single crystal x-ray diffraction experiment was also performed for form I, which resulted in the crystal structure being obtained. However a sufficiently large single crystal of form II could not be grown, and as such no crystal structure could be obtained.

^{1}H solid-state NMR provides an alternative approach for the investigation of the solid-state packing. As a technique dependent on short-range interactions rather than long range order, the inability to obtain a single crystal does not prevent a solid-state NMR experiment being performed. The molecular packing in form I is strongly influenced by hydrogen bonding interactions. Consequently the ^{1}H DQ experiment provides a method to investigate intermolecular distances in both polymorphic forms. ^{1}H NMR has been shown to be a powerful technique in the investigation of hydrogen bonded systems [34, 118, 127]. This chapter presents the results of ^{1}H DQ experiments used to identify and quantify H–H proximities, together with DFT and density matrix simulations, and shows that by comparing the results obtained from the two polymorphs, information on the packing arrangement in the unknown structure of form II can be obtained.

5.2 Experimental Details

5.2.1 Solid-State NMR Experiments

Samples of sibenadet HCl form I and form II were obtained from AstraZeneca PAR&D, Charnwood, UK, and used without further processing. All ^{1}H experiments were performed using a Bruker Avance III 500 spectrometer, operating at a ^{1}H Larmor frequency of 500.1 MHz. A Bruker 4 mm triple channel probe was used (operating in double resonance mode) at an MAS frequency of 12.5 kHz.

A one dimensional ^{1}H experiment was performed with eDUMBO-1_{22} [19] decoupling applied at a ^{1}H nutation frequency of 100 kHz in a windowed manner during acquisition. Each 24 μs eDUMBO-1_{22} cycle was divided into 320 steps of 75 ns. 800 data points were acquired in 12.1 ms, giving an effective dwell time of 15 μs. The duration of the eDUMBO-1_{22} pre-pulses was optimised to 0.8 μs. The phase of these pulses was also optimised, in order to minimise the intensity of artefacts.

For the two-dimensional ^{1}H DQ correlation experiment, eDUMBO-1_{22} decoupling was employed in t_1 and t_2 at a ^{1}H nutation frequency of 100 kHz (using windowless and windowed schemes respectively). Each 24 μs eDUMBO-1_{22} cycle was divided into 320 steps of 75 ns. The duration of the eDUMBO-1_{22} pre-pulses were optimised to 0.85 μs for both t_1 and t_2. Recoupling of the dipolar interaction was achieved using

POST-C7 [31] elements to excite and re-convert double-quantum coherence before and after t_1. POST-C7 pulses were applied at a ^{1}H *rf* frequency of 87.5 kHz. A single POST-C7 element ($\pi/2_\phi - 2\pi_{(\phi+180)} - 3\pi/2_\phi$) had a duration of 22.9 μs. The number of elements used in each recoupling period was incremented from one to eight in successive experiments, in order to observe the build-up of double-quantum peaks. A 16 step phase cycle [38] was used to select the desired coherence transfer pathway. For each of the 160 t_1 FIDs, 16 transients were co-added, with a recycle delay of three seconds. The total duration of a single experiment was 2.1 hours.

The ^{1}H CRAMPS spectra were scaled to obtain correct chemical shift values, referenced to experiments performed on the same sample at 30 kHz MAS without the use of homonuclear decoupling (figure 5.4). The scaling factors used for the Form I spectra were 1.50 for ^{1}H 1D CRAMPS, and 1.46(F_2) and 1.56 (F_1) for ^{1}H DQ CRAMPS. For form II, the scaling factors were 1.60 for ^{1}H 1D CRAMPS, and 1.63(F_2) and 1.66 (F_1) for ^{1}H DQ CRAMPS.

^{13}C CPMAS spectra were recorded using a Bruker Avance III 500 spectrometer at AstraZeneca, operating at Larmor frequencies of 499.7 MHz for ^{1}H and 125.6 MHz for ^{13}C. Transverse magnetisation was transferred from ^{1}H to ^{13}C using a 2 ms contact pulse, ramped from 50% to 100% power on the ^{1}H channel. During the 27 ms acquisition period, TPPM decoupling, with a pulse duration of 4.3 μs and a phase shift of 15°, was applied to the ^{1}H channel at a nutation frequency of 100 kHz. 1024 transients were co-added, with a recycle delay of 10 s, resulting in a total acquisition time of 2.8 hours per spectrum.

5.2.2 Computational Details

Density functional theory calculations for sibenadet HCl form I were performed by Prof. Chris Pickard at University College London, using the CASTEP Academic Release, version 4.3 [48]. An initial geometry optimisation calculation was performed to relax the positions of all (252) atoms within the crystal structure. The maximum forces acting upon the atoms within the optimised structure, in units of eV/Å, were 0.010(H), 0.011(C), 0.006(N), 0.013(O), 0.008(S) and 0.009(Cl). Calculations using the GIPAW method [50, 51] were performed to find the shielding tensor for each atomic nucleus in the crystal structure.

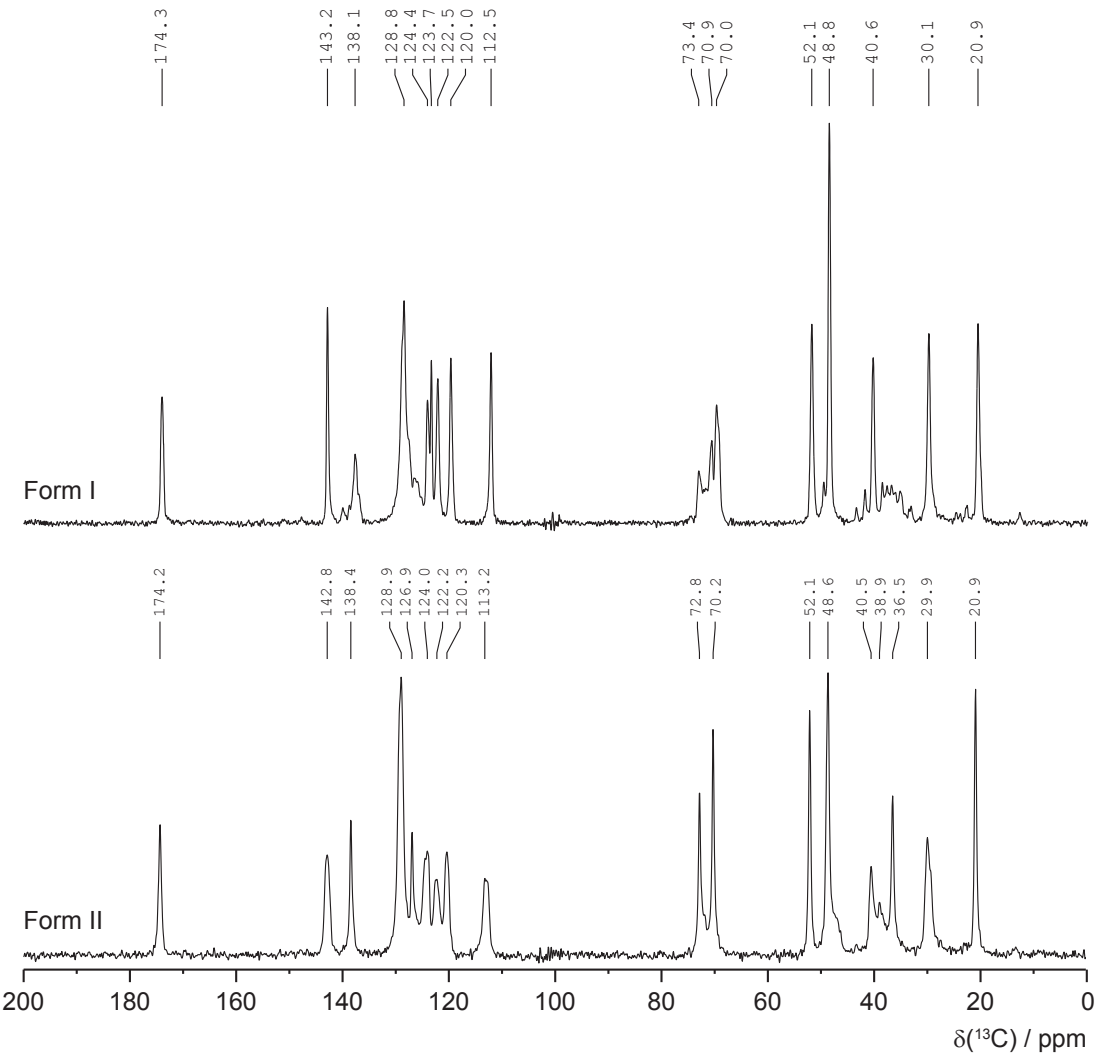

Figure 5.2: ^{13}C (125 MHz) CP MAS (12.5 kHz) spectra of sibenadet HCl forms I (upper spectrum) and II (lower spectrum). Both spectra were recorded with a 2 ms contact time and decoupling at a ^{1}H nutation frequency of 100 kHz during acquisition.

Density matrix simulations were performed using SPINEVOLUTION [42], version 3.4.2. Atomic positions from the geometry optimised crystal structure were used in the input file from which the dipolar couplings are calculated. The simulation method was identical to that described in chapter 4, for the simulation of the double-quantum build up behaviour of the dipeptide βAsp-Ala. Simulations were performed on an eight spin system comprised of the observed NH proton, and the seven closest ^{1}H nuclei.

5.3 Results and Discussion

The previous investigation into the polymorphs of sibenadet HCl by Cosgrove *et. al.* [125], showed that differences between forms I and II were evident from a number of

different experimental techniques, including ^{13}C solid-state NMR. The samples used in this work had been stored for a number of years since this original investigation and consequently the results of new ^{13}C CP MAS experiments were compared to the previously published data, in order to confirm that the samples had not degraded in the intervening time.

^{13}C CPMAS spectra of sibenadet HCl forms I and II are shown in figure 5.2. Neither spectrum shows evidence of the peaks splitting into multiplets, thus indicating the presence of one distinct molecule in the asymmetric unit cell of each polymorph. Although the spectra show similar ^{13}C chemical shift values, there are significant differences in certain regions, particularly in the relative peak intensities between the two forms. This data is consistent with the previously published ^{13}C solid-state NMR spectra for sibenadet HCl forms I and II, indicating that the samples used in this work are the same as those previously studied, showing no evidence of any chemical or structural changes.

5.3.1 Density Functional Theory Calculation Results

Due to the availability of a structure obtained by x-ray single crystal diffraction [125], it was possible to perform geometry optimisation and NMR shielding calculations for sibenadet HCl form I. The CASTEP geometry optimised structure, obtained by relaxing the positions of all atoms within the unit cell, indicates that the molecules form a hydrogen bonded network, with the benzothiazolone groups aligning in a planar arrangement, as shown in figure 5.1(b). Figure 5.3(a) shows the hydrogen bonding arrangement within the planar benzothiazolone groups in more detail. There are a number of intermolecular interactions present in this planar region, with the optimised crystal structure suggesting that each molecule interacts via hydrogen bonds to two others, via an O–H$\cdots$N interaction (O–N distance of 2.86 Å, O–H–N angle of 171°) in one direction, and via an O–H$\cdots$O interaction (2.75 Å, 172°) and a possible weaker C–H$\cdots$S interaction (3.40 Å, 178°) in the approximately orthogonal direction within the plane. In the O–H$\cdots$N and O–H$\cdots$O interactions, the same C=O acceptor in one molecule is bonded to NH and OH donors in two different molecules. While these interactions are suggestive of a relatively rigid intermolecular structure within this plane, there is no evidence of any hydrogen bonding interactions outside of the plane. Fur-

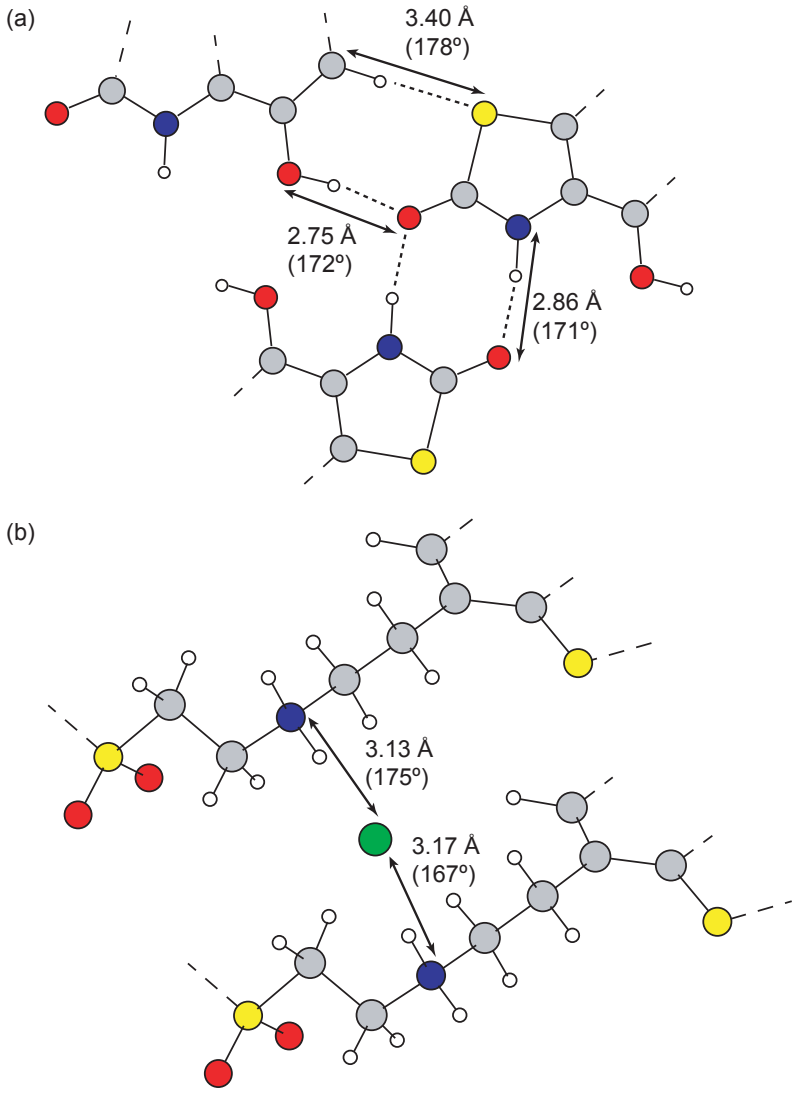

Figure 5.3: Structural diagram illustrating the intermolecular interactions in the sibenadet HCl form I structure. The diagram shows the CASTEP optimised structure. (a) Hydrogen bonding interactions in the planar benzothiazolone region of the molecule, with the XHY bond angle and XY distance labelled. (b) The structure in the region of the NH_2 group, with the N–Cl distances stated.

Table 5.1: GIPAW calculated (form I) and experimental (forms I and II) chemical shift values.

	δ_{iso} / ppm		
^{1}H	GIPAW (Form I)[a]	Experiment (Form I)	Experiment (Form II)
CH_2	-0.9 to 3.7	2.1 to 3.5	1.1 to 2.9
CH	4.6 to 5.0	6.6	6.4
OH	7.0	7.6	7.3
NH_2	7.8	8.7	8.0
NH_2	8.8	9.7	8.8
NH	10.9	10.9	10.9

[a] $\delta_{iso} = \sigma_{ref} - \sigma_{iso}$ where $\sigma_{ref} = 28.5$ ppm.

ther investigation of the intermolecular interactions would be possible by calculating the NMR shielding parameters for a molecule extracted from the crystal structure and effectively isolated through the use of a very large unit cell. This approach has been successfully used in investigations into several organic crystalline systems [56, 108, 111] and will be demonstrated in chapter 6 for the pharmaceutical molecule indomethacin.

The optimised structure also indicates that the Cl^- ion interacts with the NH_2^+ group located within the aliphatic chain. N–Cl distances of 3.13 and 3.17 Å, and N–H–Cl angles of 175° and 167°, are indicative of an electrostatic interaction between the NH_2^+ group and the Cl^- ion. These interactions take place in a different plane to the hydrogen bonding interactions in the benzothiazolone region. This region of the crystal structure is shown in figure 5.3(b).

The GIPAW calculated ^{1}H chemical shift values were calibrated relative to a one-dimensional ^{1}H CRAMPS spectrum of sibenadet HCl form I, which is shown in figure 5.4(a). The large number of overlapping peaks in the range 2.1 ppm to 6.6 ppm makes the identification of individual resonances impossible. However since this investigation is primarily focussed on the hydrogen bonded region of the molecule, it is the peaks at higher chemical shifts (7.6 and 10.9 ppm), which are of more interest. The calculation results indicate that the NH proton has the highest chemical shift value. This may therefore be assigned to the 10.9 ppm peak. The calculated chemical shift difference to the OH peak is 4.0 ppm, which approximately corresponds to the peak at 7.6 ppm.

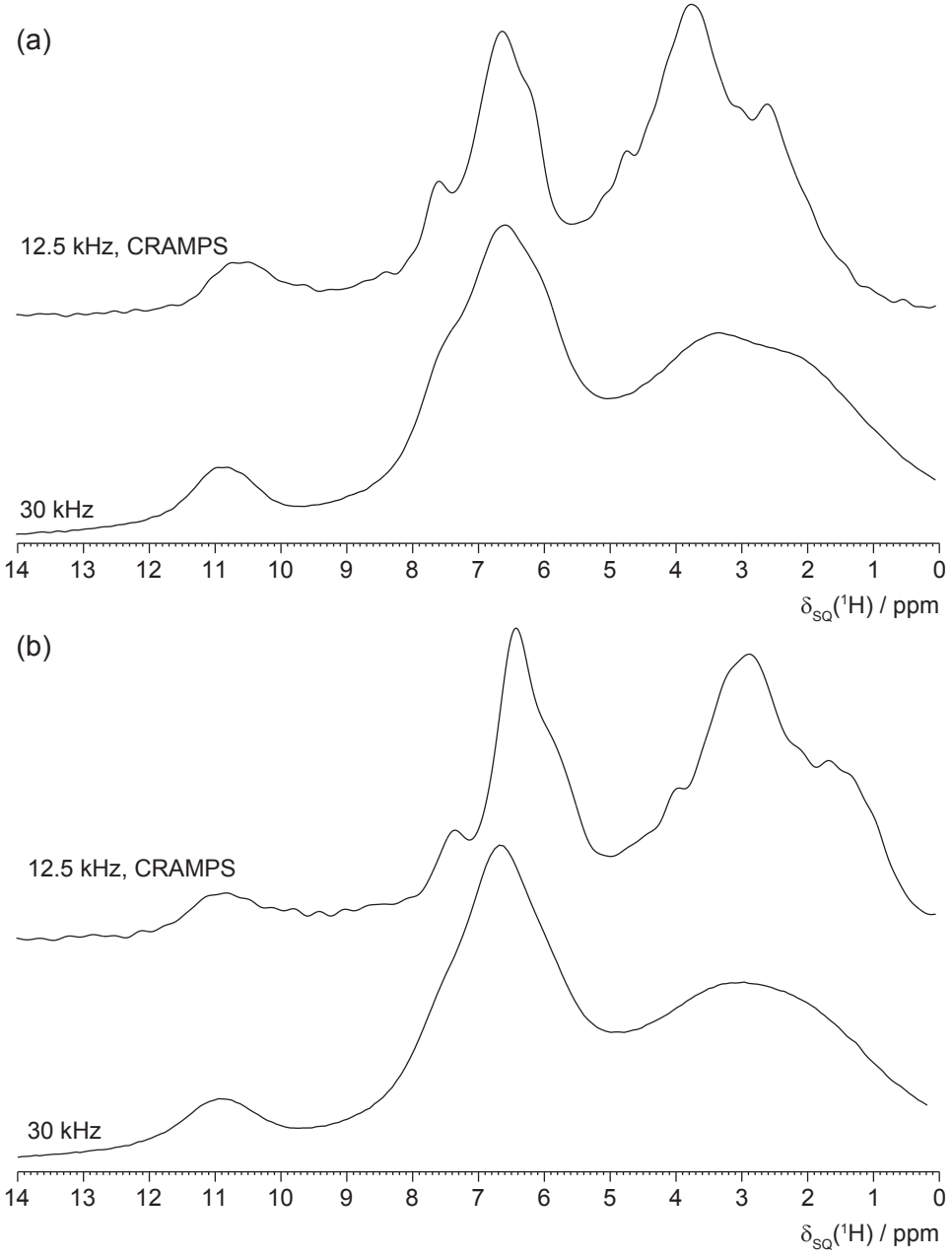

Figure 5.4: One dimensional ^{1}H spectra of sibenadet HCl form I (a) and form II (b). For each polymorph, upper spectrum: recorded at an MAS frequency of 12.5 kHz, windowed eDUMBO-1_{22} decoupling at a ^{1}H nutation frequency of 100 MHz was applied during acquisition. Lower spectrum: recorded at an MAS frequency of 30 kHz (no homonuclear decoupling).

Table 5.2: List of ^{1}H atoms within 3.5 Å of the NH and OH protons in the optimised crystal structure of sibenadet HCl form I. Table entries corresponding to inter-planar distances are italicised. Asterisks indicate inter-molecular distances.

^{1}H	δ_{SQ}/ppm	δ_{DQ}/ppm	Distance Å
Distances from NH (10.9 ppm)			
NH	10.9	21.8	2.62*
OH	7.6	18.5	2.87*
OH	*7.6*	*18.5*	*3.40**
NH	*10.9*	*21.8*	*3.53**
Distances from OH (7.6 ppm)			
CH	6.6	14.0	2.38
NH	10.9	18.5	2.87*
OH	7.6	15.2	3.18*
NH	*10.9*	*18.5*	*3.40**

5.3.2 ^{1}H DQ CRAMPS Results: Form I

A ^{1}H DQ CRAMPS spectrum of sibenadet HCl form I is shown in figure 5.5(a). The peaks between approximately $\delta_{DQ} = 5$ ppm and $\delta_{DQ} = 13$ ppm are due to predominantly intra-molecular interactions between aliphatic and aromatic protons. This is consistent with the data obtained from the geometry optimised crystal structure, which indicates many such interactions within 3.5 Å.

Table 5.2 lists the hydrogen atoms within 3.5 Å of the NH and OH protons, which would be expected to contribute to the peaks in the DQ spectrum. The pair of peaks at $\delta_{DQ} = 7.6 + 10.9 = 18.5$ ppm and the on diagonal peak at $\delta_{DQ} = 10.9 + 10.9 = 21.8$ ppm are clearly resolved and may be readily assigned from the calculation data. The $\delta_{DQ} = 18.5$ ppm peaks are due to the proximity of the NH and OH protons in a pair of sibenadet HCl molecules positioned adjacently in the crystal structure. An OH–NH distance of 2.87 Å between in-plane molecules, as shown in figure 5.6(a), is consistent with the presence of this peak. The NH proton is also separated by distances of 3.40 Å and 3.53 Å from OH protons in molecules outside of the plane, as shown in figure 5.6(b). Although within the 3.5 Å usually considered as a practical maximum for the presence of a DQ correlation peak, the NH–OH correlation peak will be dominated by the stronger dipolar coupling due to the shorter, in-plane distance. The on-diagonal peak at $\delta_{DQ} = 10.9 + 10.9 = 21.8$ ppm is due to the inter-molecular NH–NH dipolar coupling, with an inter-nuclear distance of 2.62 Å obtained from the optimised crystal structure again consistent with the presence of this peak. The intermolecular OH–OH

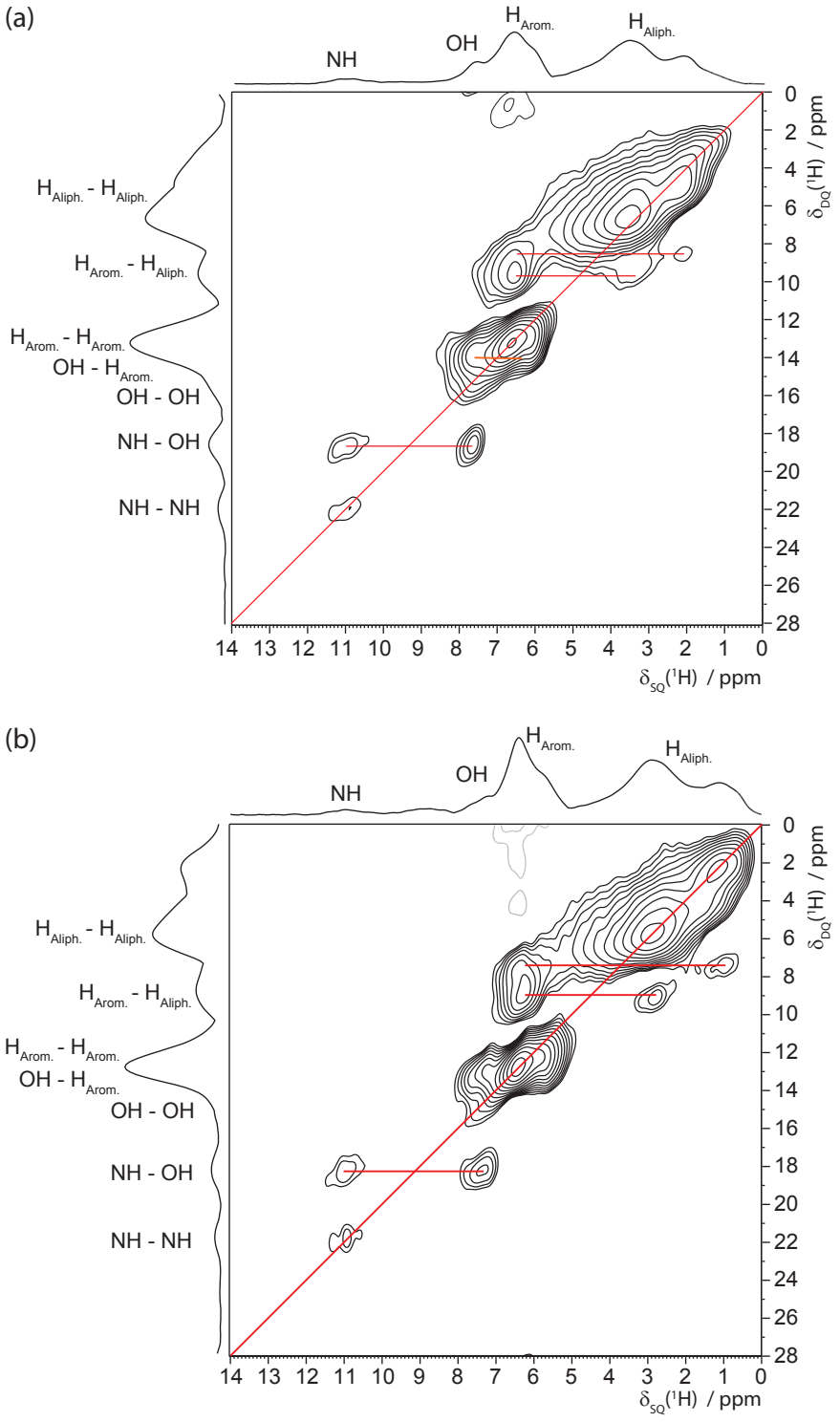

Figure 5.5: ^{1}H (500 MHz) DQ CRAMPS spectra of (a) sibenadet HCl form I and (b) form II, recorded at an MAS frequency of 12.5 kHz. eDUMBO-1$_{22}$ decoupling at a ^{1}H nutation frequency of 100 MHz was applied during t_1 and t_2. Three elements of POST-C7 recoupling were used for the excitation and reconversion of DQ coherence, corresponding to a total recoupling time of 138 μs. The base contour level is at (a) 6% and (b) 5% of the maximum peak intensity.

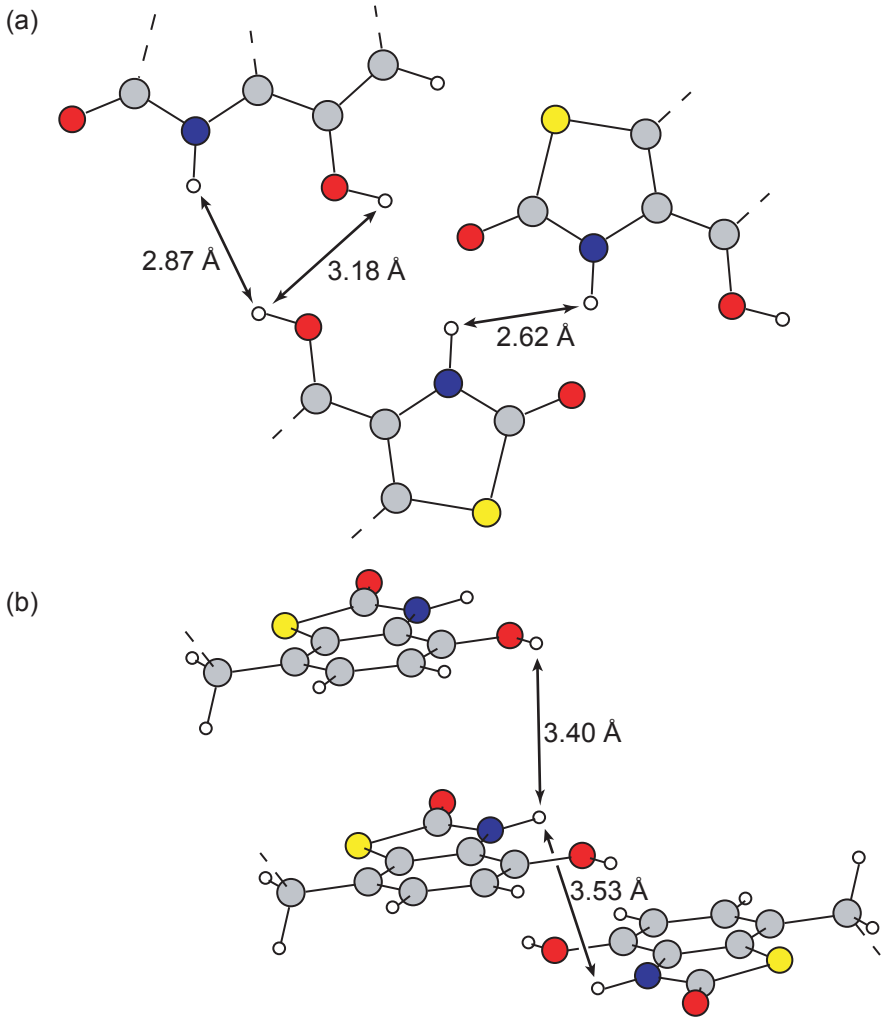

Figure 5.6: (a) Intermolecular H–H proximities involving hydrogen-bonded protons. All atoms shown in this projection lie approximately on the same plane. (b) Out-of-plane 3.40 Å and 3.53 Å NH–OH proximities. Both diagrams show the CASTEP optimised structure.

distance of 3.18 Å, while longer than the NH–NH and NH–OH distances, would still be expected to result in a DQ peak at $\delta_{DQ} = 7.6 + 7.6 = 15.2$ ppm. However this is within the range covered by the large aromatic - aromatic peak. Consequently, while this peak is clearly present, it is not possible to isolate it and observe the double-quantum build up without the influence of the aromatic - aromatic peak.

The calculated chemical shift data indicate that the NH_2 protons should appear in the spectrum between the NH and OH peaks, at chemical shifts of 7.8 ppm and 8.8 ppm. These peaks are not apparent in either the one dimensional, or DQ CRAMPS (figure 5.5(a)) spectra. Due to the small separation of the NH_2 protons (1.71 Å in the optimised crystal structure), the ^{1}H DQ build-up behaviour of the NH_2 peaks would be expected to be similar to that of the CH_2 protons in β-AspAla, as presented in

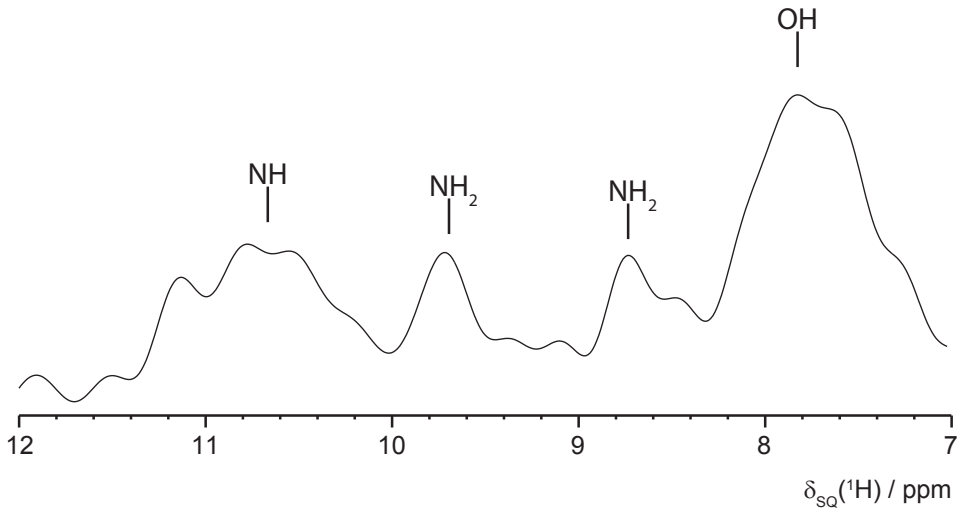

Figure 5.7: A row extracted from a ^{1}H DQ CRAMPS spectrum of sibenadet HCl form I, showing NH_2–NH_2 peaks at 8.7 and 9.7 ppm. The spectrum was recorded using two elements of POST-C7 recoupling in the excitation and reconversion periods (corresponding to a total recoupling time of 92 μs). The extracted row is at $\delta_{DQ} = 8.7 + 9.7 = 18.4$ ppm and is parallel to the single-quantum axis.

chapter 4. Consequently the maximum DQ peak intensity would be expected in the spectrum recorded using two elements of POST-C7 recoupling in the excitation and reconversion periods (total recoupling time of 92 μs). A slice from this spectrum (form I) at $\delta_{DQ} = 18.4$ ppm is shown in figure 5.7, indicating what appear to be the NH_2 resonances at 8.7 and 9.7 ppm. A list of the calculated and experimental ^{1}H chemical shifts value is presented in table 5.1.

In order to perform a more quantitative investigation of the intermolecular distances within the hydrogen bonded region of the molecule, it is possible to analyse the build-up behaviour of the NH–NH and NH–OH double-quantum correlation peaks, as the recoupling time is changed. In chapter 4 and reference [1] it was shown that even within a dense network of dipolar coupled nuclear spins, the maximum peak intensity is indicative of the proton - proton separation.

A comparison of simulated and experimental ^{1}H double-quantum build-up curves for the NH proton in form I are shown in figure 5.8. Considering first the experimental results, the build-up data show that the curve for the NH–NH peak reaches a greater maximum intensity than the NH–OH curve. While this is consistent with the shorter NH–NH distance (2.62 Å compared to 2.87 Å) in the optimised structure, the peak intensity of the NH–OH curve is higher than would be expected if only these shortest range NH–NH and NH–OH interactions are considered. The ratio of the NH–OH to

NH–NH build-up curve maximum intensities is 0.85 ± 0.06, compared to a ratio in the squares of the dipolar couplings (equal to the ratio of the distances to the inverse sixth power) of

$$\frac{d^2_{NH-OH}}{d^2_{NH-NH}} = \frac{r^6_{NH-NH}}{r^6_{NH-OH}} = \frac{2.62^6}{2.87^6} = 0.58$$

In order to reach a closer agreement with the experimentally observed value, it is necessary to consider the contributions to the double-quantum build-up peaks from longer range interactions. The commonly used convention in the interpretation of ^{1}H DQ CRAMPS experiments, that peaks are visible for interactions of up to 3.5 Å suggests that this may be an appropriate limit. However, examination of the geometry optimised crystal structure shows that there are two NH–OH interactions at slightly greater separations of 3.62 Å and 3.68 Å, then there are no further NH–NH or NH–OH interactions until 4.13 Å. When all NH–NH and NH–OH interactions $\leq$ 3.68 Å are considered, combined as the root-sum-square of the individual H–H dipolar coupling interactions [128], the ratio of the dipolar couplings is

$$\frac{r^6_{NH-NH(rss)}}{r^6_{NH-OH(rss)}} = \frac{\sqrt{2.62^2 + 3.53^2}^6}{\sqrt{2.87^2 + 3.40^2 + 3.62^2 + 3.68^2}^6} = 0.91$$

which agrees, within error, with the experimentally observed value.

The simulated build-up curves both reach maximum intensity at a total recoupling time of 320 μs, later than the experimentally observed maximum at 230 μs. As discussed in chapter 4, this shift in the maximum is expected due to the limited size of the simulated set of nuclei. As in the experimental data, the NH–NH curve reaches a higher maximum intensity than the NH–OH curve, with a ratio in the maximum peak intensities of 0.84 , which agrees within error with the experimentally observed value. These simulations were performed on a cluster of nuclei comprised of the observed NH and the seven closest nuclei, listed in table 5.3.

5.3.3 ^{1}H DQ CRAMPS Results: Form II

A ^{1}H DQ CRAMPS spectrum of sibenadet HCl form II is presented in figure 5.5(b). This spectrum shows the same DQ peaks as that for form I. For the DQ peaks corresponding to interactions between aliphatic and aromatic protons this is unsurprising, given the significant contributions to these peaks from intra-molecular interactions.

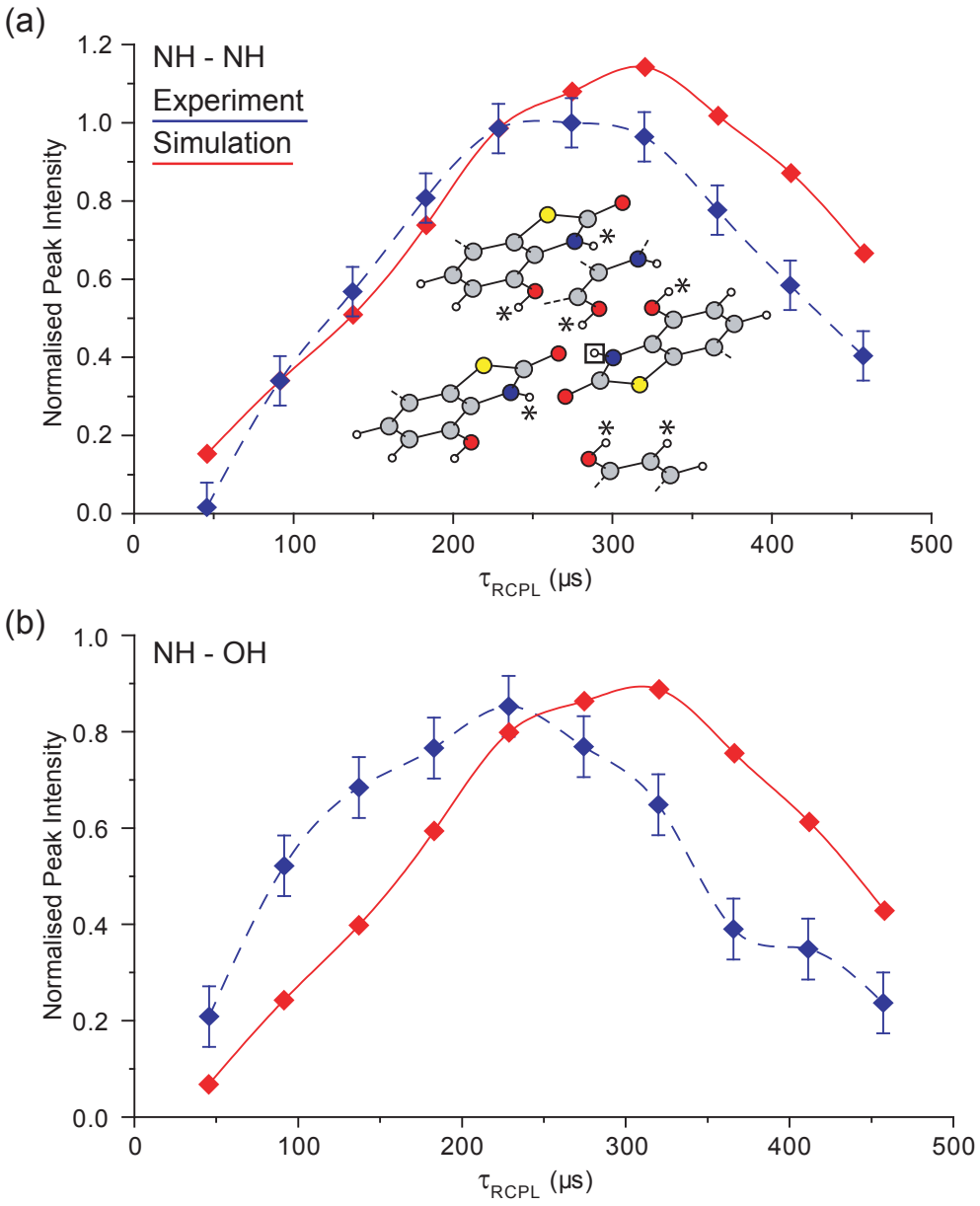

Figure 5.8: Comparison of simulated (solid red lines) and experimental (dashed blue lines) ^{1}H double-quantum build-up curves for the (a) NH–NH and (b) NH–OH interactions (magnetisation observed on the NH proton in both cases) in sibenadet HCl form I. The data points are normalised to the maximum point in the NH–NH curve in both simulation and experiment. Lines linking the points are included as a guide to the eye. The inset figure shows the eight spin system of nuclei used in this simulation. The observed NH proton is highlighted with a box, and the seven other protons included in the simulation are marked with asterisk symbols. The positions used were taken from the geometry optimised crystal structure.

Table 5.3: List of nuclei included in addition to the observed NH proton in the SPINEVOLUTION double-quantum build-up simulations. Table entries corresponding to inter-planar distances are italicised. Asterisks indicate inter-molecular distances.

^{1}H	δ_{SQ} / ppm	δ_{DQ} / ppm	Distance / Å
NH	10.9	21.8	2.62*
OH	7.6	18.5	2.87*
OH	*7.6*	*18.5*	*3.40**
NH	*10.9*	*21.8*	*3.53**
OH	7.6	18.5	3.62
OH	*7.6*	*18.5*	*3.68**
Aromatic	*6.6*	*17.3*	*3.82**

Conversely, the NH and OH region of the spectrum is predominantly due to intermolecular interactions. Changes in the length of the hydrogen bonds would be expected to result in a significant change in the value of the ^{1}H isotropic chemical shift [15]. However the observed values of 7.3 (OH) and 10.9 (NH) ppm in form II are in close agreement with the values of 7.6 (OH) and 10.9 (NH) ppm in form I. Consequently the similarity in the chemical shifts of the NH and OH protons, together with the presence of the same NH–NH and NH–OH peaks suggests the presence of a similar hydrogen bonded arrangement in form II to form I.

Figure 5.9 presents ^{1}H double-quantum build-up curves obtained from the DQ CRAMPS spectra of form I and form II sibenadet HCl. The curves due to the NH–NH and NH–OH peaks at the single-quantum frequency of the NH proton ($\delta_{SQ} = 10.6$ ppm) are shown. In both form I and form II, the NH–NH peak reaches a higher maximum intensity than the NH–OH peak. Consequently, as discussed in chapter 4, the recoupling time taken to reach the maximum may be taken as an indicator of the internuclear distance. Both curves reach a maximum after a total recoupling time of 274 μs, indicating a similar NH–NH distance in the two forms.

The NH–OH curves for both polymorphs reach their maximum intensity at the same total recoupling time of 229 μs. As expected for these lower intensity peaks, this is close to the peak in the NH–NH build-up curves. The relative intensities of these peaks may then be related to the relative NH–OH distance. The build-up curve for form II reaches a higher maximum intensity than the form I curve, indicating a larger root-sum-squared NH–OH dipolar coupling in form II than form I, relative to the NH–

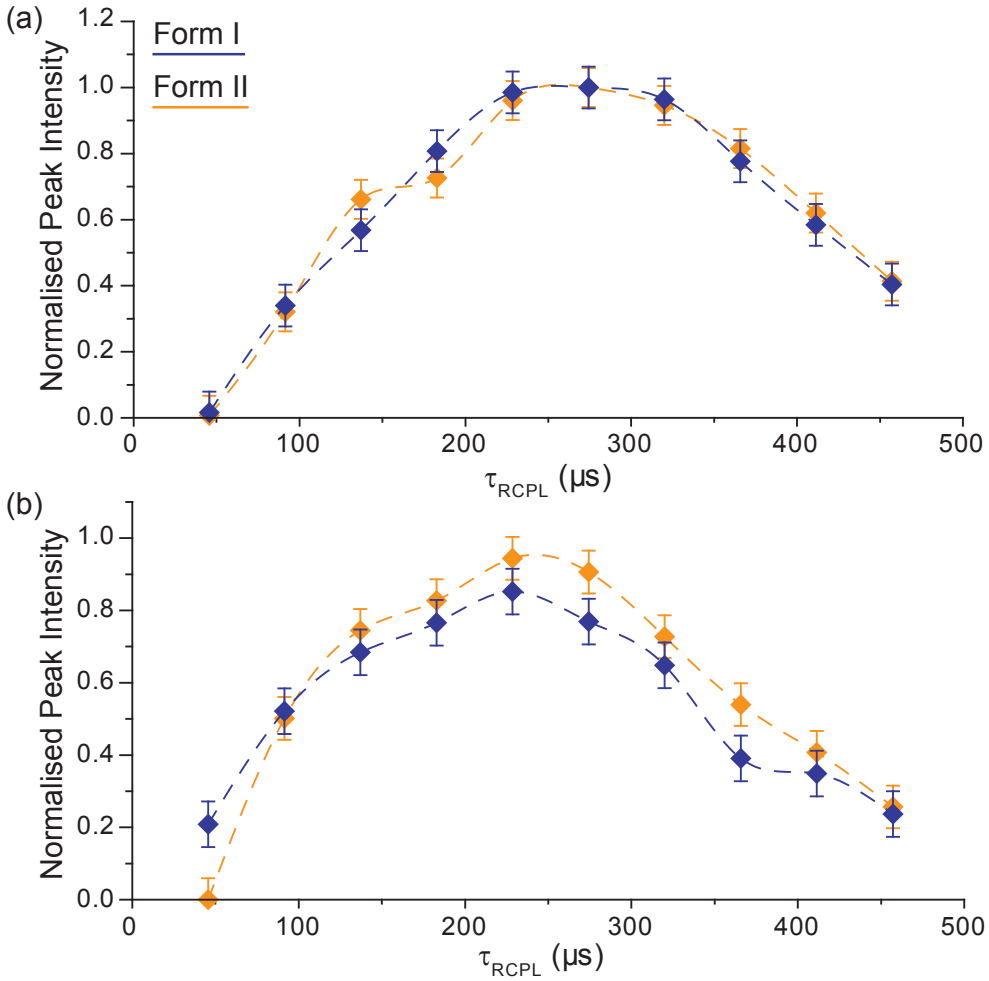

Figure 5.9: Experimental double-quantum build-up curves for the NH–NH peak in sibenadet HCl forms I and II (a) and the NH–OH peak at the OH single-quantum frequency (b). The curves show the variation in the peak intensity with total recoupling time. The data for each polymorph is normalised to the maximum point on the NH–NH curve for the respective polymorph. Dashed lines linking the peak intensities are included as guides for the eye.

NH coupling. This result implies that one or more of the NH–OH distances is shorter in form II than form I. Given the evidence for the presence of the same in-plane hydrogen bonding arrangement in both forms, it is likely that this difference is due to shorter inter-planar NH–OH distances.

5.4 Summary and Conclusions

This investigation has shown that the combination of density functional theory computations for a known crystal structure with ^{1}H solid-state NMR can be used to provide information on the intermolecular structure of a compound for which the crystal struc-

ture is not known. While single-crystal x-ray diffraction (combined with geometry optimisation calculations) provides accurate and comprehensive information on atomic positions, as is the case for sibenadet HCl form I, the reliance of solid-state NMR on localised, short-range interactions makes it a more applicable technique when studying systems such as form II, for which single crystals cannot be obtained. The use of the ^{1}H double-quantum experiment is particularly appropriate in this case. Whereas the original study of the sibenadet HCl polymorphs by Cosgrove *et. al* [125] included ^{13}C CP MAS solid-state NMR experiments, the results indicated possible differences between the polymorphs in terms of disorder, particularly in the phenyl ring section of the molecule, but provided no information on the hydrogen bonding arrangement in the benzothiazolone region. In contrast, the ^{1}H DQ CRAMPS experiment provided reliable information on the hydrogen bonding arrangement, through the analysis of double-quantum build-up curves. For form I, this was found to be in agreement with simulations on nuclear spin systems based on the geometry optimised structure. The small differences in the build-up behaviour of form II may therefore be taken as a reliable indication of subtle differences in the internuclear distances in forms I and II.

In summary, the results presented in this chapter show that ^{1}H DQ solid-state NMR experiments can play a significant role in investigations into the structure of crystalline organic materials, when used in combination with other techniques. Although in this case information on the intermolecular bonding was available for only a relatively small, yet key, region of the molecule, this data could potentially assist in the solving of the structure by techniques such as powder x-ray diffraction. As such this investigation shows the value of including ^{1}H DQ solid-state NMR experiments in the analysis of the solid-state structures exhibited by pharmaceutical compounds.

CHAPTER

SIX

PROBING INTERMOLECULAR CRYSTAL PACKING IN γ-INDOMETHACIN BY HIGH RESOLUTION ^{1}H SOLID-STATE NMR SPECTROSCOPY

6.1 Introduction

In chapter 5, it was shown that the analysis of ^{1}H double-quantum build-up curves, presented in chapter 4, could be extended to the study of organic crystalline materials for which the crystal structure is unknown. While the study of sibenadet HCl polymorphs was successful in characterising the hydrogen bonding arrangement in a limited region of the molecule, the study of intermolecular H–H interactions throughout the molecule was not possible, due to the large number of overlapping ^{1}H DQ resonances in the aliphatic and aromatic regions of the spectrum, meaning that build-up analysis was only possible for the DQ peaks corresponding to hydrogen bonded protons, which are at higher chemical shifts and therefore more isolated in the spectrum.

The work presented in this chapter applies similar ^{1}H DQ correlation solid-state NMR experiments, density functional theory calculations and density matrix simulations to the gamma polymorph of the active pharmaceutical ingredient indomethacin. γ-indomethacin is shown to have a similar ^{1}H DQ CRAMPS spectrum to sibenadet HCl, notably a crowded aromatic region, and more clearly defined peaks corresponding to a hydrogen bonded (OH) proton. Consequently while ^{1}H DQ build-up data may be obtained for interactions involving the OH, this is not possible for the aromatic–aromatic and aromatic–aliphatic H–H interactions. A new ^{1}H(DQ)–^{13}C correlation

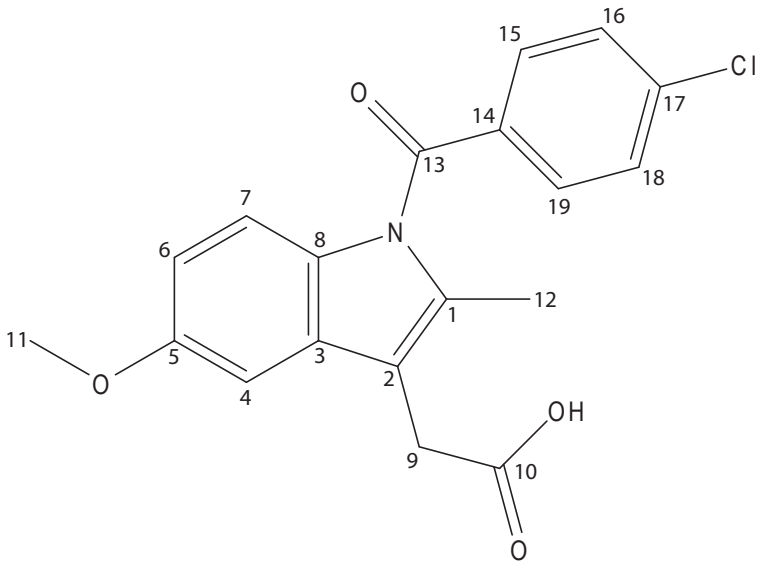

Figure 6.1: Molecular structure of indomethacin, showing the atomic labelling system used throughout this chapter.

experiment [59] is employed to improve the spectral resolution in this region, and consequently DQ build-up curves may be extracted for the interactions involving the aromatic protons in γ-indomethacin.

Indomethacin (also known as indometacin) is a widely used non-steroidal anti-inflammatory and anti-pyretic drug, developed in 1963 [129]. Indomethacin exists in a number of different polymorphs, including γ-indomethacin, which is studied in this work, as well as a metastable polymorph, α-indomethacin. The structures of both polymorphs have been determined by x-ray single crystal diffraction [130–132]. There is considerable interest in the study of new solid forms of indomethacin, including co-crystals and amorphous forms due to the poor solubility of indomethacin, which limits its bioavailability [133–137].

The molecular structure of indomethacin is shown in figure 6.1, which is annotated with the atomic labelling system used throughout this chapter for both carbon and hydrogen. Note that the atomic labelling system used in this chapter is the same as that used by Basavoju *et. al.* [134], however a number of other labelling systems have been employed throughout the published literature [66, 67, 138, 139]. Indomethacin has been widely studied using a variety of analyical techniques, including solid-state NMR studies of the alpha and gamma polymorphs, and amorphous forms by ^{13}C CPMAS [66, 138], and ^{1}H–^{13}C and ^{1}H–^{1}H DQ studies of an indomethacin-polymer dispersion [67].

6.2 Experimental and Computational Details

6.2.1 Solid-State NMR

^{1}H one-pulse, ^{1}H one-dimensional CRAMPS, ^{1}H DQ CRAMPS and ^{1}H–^{13}C refocussed INEPT correlation experiments were performed on a Bruker Avance II+ 600 spectrometer, operating at Larmor frequencies of 599.4 MHz for ^{1}H and 150.7 MHz for ^{13}C. A ^{1}H one-pulse experiment was performed using a Bruker 2.5 mm probe, at an MAS frequency of 30 kHz. For all other experiments, a Bruker 4 mm triple-resonance probe, operating in double-resonance mode, was used at an MAS frequency of 12.5 kHz. Throughout all experiments, ^{1}H $\pi/2$ pulse lengths of 2.5 μs and ^{13}C $\pi/2$ pulse lengths of 5 μs were used.

The ^{1}H one-dimensional CRAMPS experiment used windowed eDUMBO-1_{22} decoupling during acquisition. Each 24 μs eDUMBO-1_{22} cycle was divided into 320 steps of 75 ns. The duration and phase of the eDUMBO-1_{22} pre-pulses were optimised to 0.74 μs and 180° in order to minimise artefact intensity.

^{1}H DQ CRAMPS experiments were performed as described in chapter 5 (MAS at 12.5 kHz, dipolar recoupling using the POST-C7 sequence (ν_1 = 87.5 kHz), high-resolution achieved using the eDUMBO-1_{22} homonuclear decoupling scheme (ν_1 = 100 kHz)). The duration of the eDUMBO-1_{22} pre-pulses were optimised to 0.7 μs and 0.9 μs for t_1 and t_2 respectively, with the phases of the pulses also optimised. Scaling factors of 1.51 in F_1 and 1.63 in F_2 were determined by comparison with a spectrum recorded using an MAS frequency of 30 kHz and without the use of homonuclear decoupling.

^{1}H–^{13}C INEPT correlation experiments, described in section 3.3.2, were performed using eDUMBO-1_{22} decoupling in t_1 and during periods of free evolution. Each 32 μs eDUMBO-1_{22} cycle was divided into 320 steps of 100 ns. The durations of the pre-pulses for eDUMBO-1_{22} decoupling were 0.6 μs. TPPM heteronuclear decoupling with a phase shift of 15° was applied during t_2 acquisition at a ^{1}H nutation frequency of 100 kHz, using a pulse length of 4.8 μs. A 16 step phase cycle [102] was used to select the desired coherence transfer pathway. The duration of a $\pi/2$ pulse was 2.5 μs for ^{1}H and 5 μs for ^{13}C. Spin-echo durations of $\tau = \tau' = 1.12$ ms were used. A scaling factor of 1.89 was applied to the ^{1}H dimension (F_1). For each of the 80 t_1 FIDs, 320 transients

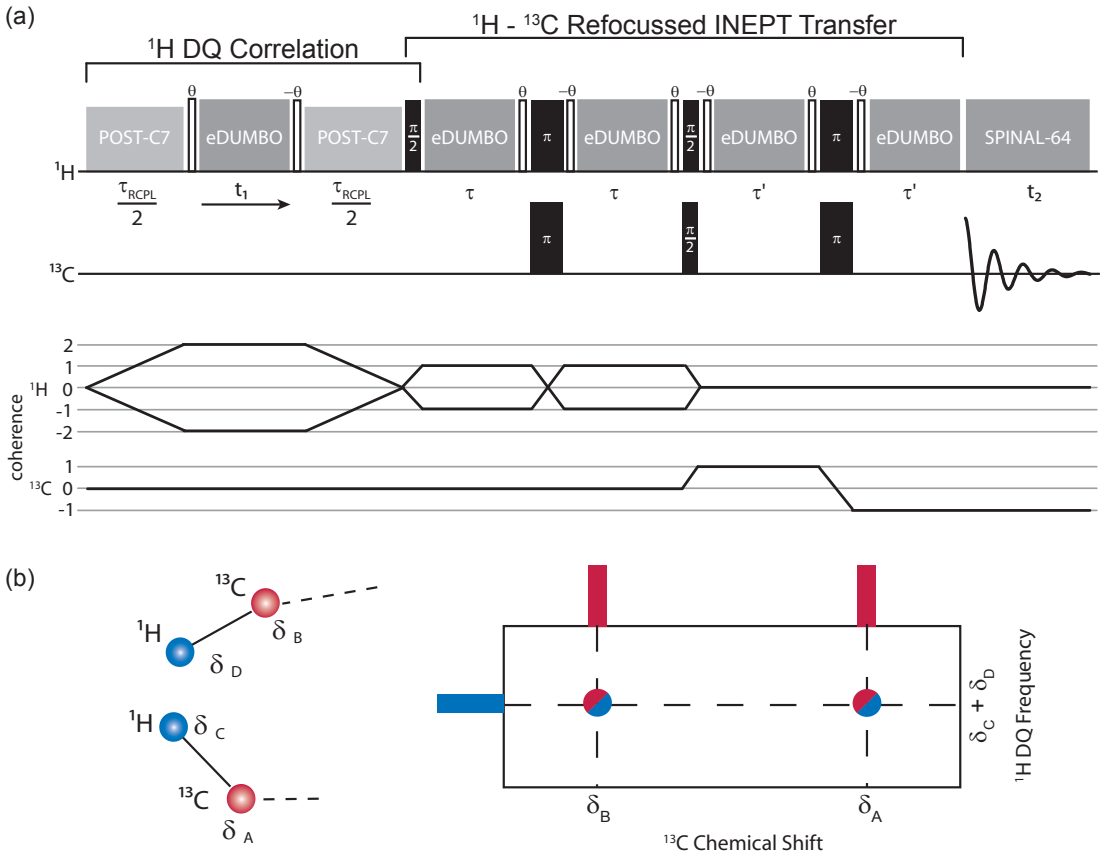

Figure 6.2: (a) Pulse sequence and coherence transfer pathway diagrams for the ^{1}H(DQ)–^{13}C(SQ) correlation experiment. The sequence comprises a standard ^{1}H DQ filtered correlation experiment, without a t_2 acquisition period, followed by a refocussed INEPT sequence to transfer the magnetisation to directly bonded ^{13}C nuclei. This sequence is a combination of the ^{1}H DQ CRAMPS and refocussed ^{1}H-^{13}C INEPT experiments discussed in chapter 3. (b) Schematic spectrum for a system of two ^{13}C nuclei, each directly bonded to ^{1}H nucleus, with the two ^{1}H nuclei in close proximity.

were added, using the States-TPPI method, with a recycle delay of 2.5 seconds. The total duration of a single experiment was 17.8 hours.

^{1}H(DQ)–^{13}C(SQ) correlation experiments [59] were performed on a Bruker Avance III 850 spectrometer, operating at a ^{1}H Larmor frequency of 850.2 MHz and a ^{13}C Larmor frequency of 213.7 MHz. A Bruker 3.2 mm triple-resonance probe, operating in double-resonance mode, was used at an MAS frequency of 12.5 kHz. POST-C7 pulses were applied at a ^{1}H nutation frequency of 87.5 kHz. A single POST-C7 element had a duration of 22.9 μs. As in the ^{1}H DQ CRAMPS experiments, the number of POST-C7 elements was varied in successive experiments from one to eight. eDUMBO-1_{22} decoupling was employed in t_1 and during periods of free evolution at a ^{1}H nutation frequency of 100 kHz, SPINAL-64 decoupling was applied during t_2 acquisition at a ^{1}H nutation frequency of 100 kHz and a pulse length of 4.86 μs. Each 32 μs eDUMBO-1_{22}

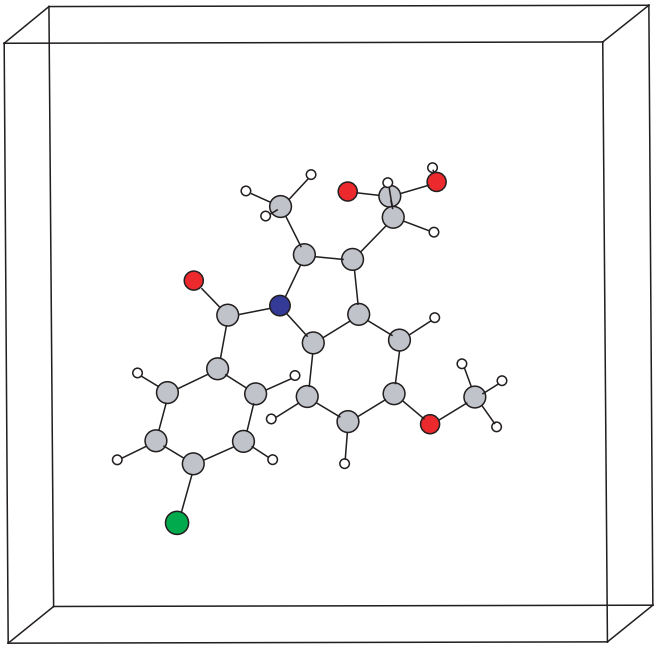

Figure 6.3: The supercell (15 × 15 × 15 Å) used to calculate the chemical shifts in an effectively isolated molecule. Although this unit is periodically repeated, the intermolecular distances are sufficiently large to negate intermolecular interactions.

cycle was divided into 320 steps of 100 ns. Spin-echo durations of $\tau = \tau' = 1.16$ ms were used. A 16 step phase cycle [59] was used to select the desired coherence transfer pathway. A scaling factor of 1.89 was applied to the ^{1}H DQ dimension (F_1). For each of the 130 t_1 slices, 320 transients were added, with a recycle delay of 2.5 seconds. The total duration of a single experiment was 28.9 hours. A pulse sequence and coherence transfer pathway diagram for this sequence are shown in figure 6.2(a). A schematic diagram of the spectrum resulting from such an experiment is shown in figure 6.2(b).

A ^{13}C CPMAS experiment was performed on a Bruker Avance III 500 spectrometer, operating at Larmor frequencies of 500.1 MHz for ^{1}H and 125.8 MHz for ^{13}C. ^{13}C magnetization was created by ramped cross polarization (100% - 50%) on the ^{1}H channel, while heteronuclear ^{1}H SPINAL-64 decoupling with pulses of duration 4.6 μs was applied during a t_2 acquisition time of 40 ms. 4096 transients were co-added for a recycle delay of 3 s.

6.2.2 Computational Details

Density functional theory calculations were performed as described previously in chapter 4, using the CASTEP software package (academic release version 4.3). All calculations used a cut-off energy of 1100 eV and a k-point spacing of 0.1 Å^{-1}. A geometry

optimisation calculation was performed on the x-ray diffraction crystal structure of γ-indomethacin (obtained from the CSD database, refcode INDMET03 [132]). The geometry optimisation was performed with the unit cell dimensions and the positions of all heavy (non-hydrogen) atoms constrained. Following geometry optimisation, the mean forces acting on each atomic species (in units of ev/Å) were: 0.009(H), 0.008(C), 0.008(N), 0.014(O) and 0.004(Cl).

Calculations of the shielding tensor for each nuclear site in the unit cell were performed using the GIPAW method, both for the geometry optimised crystal structure, and for an isolated molecule. This second calculation used a structure formed by extracting one indomethacin molecule from the optimised structure and placing it into a supercell of dimensions $15 \times 15 \times 15$ Å, with simple cubic periodicity re-introduced. A supercell of this size is sufficient to ensure that the calculated isolated molecule chemical shifts have converged for the case here of a moderately sized organic molecule [111]. The supercell containing the indomethacin molecule is shown in figure 6.3.

Density matrix simulations using the SPINEVOLUTION software package were performed using the method previously described in chapter 4, on eight-spin clusters of ^{1}H nuclei, using atomic positions taken from the geometry optimised crystal structure of γ-indomethacin.

6.3 Results

6.3.1 Assignment of ^{1}H and ^{13}C Chemical Shifts

One pulse ^{1}H spectra of γ-indomethacin recorded using fast MAS (30 kHz) and windowed eDUMBO-1_{22} homonuclear decoupling to achieve high resolution are shown in figure 6.4(a) and (b) respectively. A schematic representation of the spectrum using ^{1}H isotropic chemical shift values calculated for the geometry optimised structure using the GIPAW method is shown in figure 6.4(c). The calculated shifts are clustered into one group in the aliphatic region of the spectrum, two in the aromatic region, and a single peak at considerably higher ppm, corresponding to the OH proton. These results are consistent with the experimental spectra. While the use of homonuclear decoupling results in a slight improvement in resolution over fast MAS alone, it does not increase the number of resolved peaks in the one dimensional spectrum. The OH resonance is

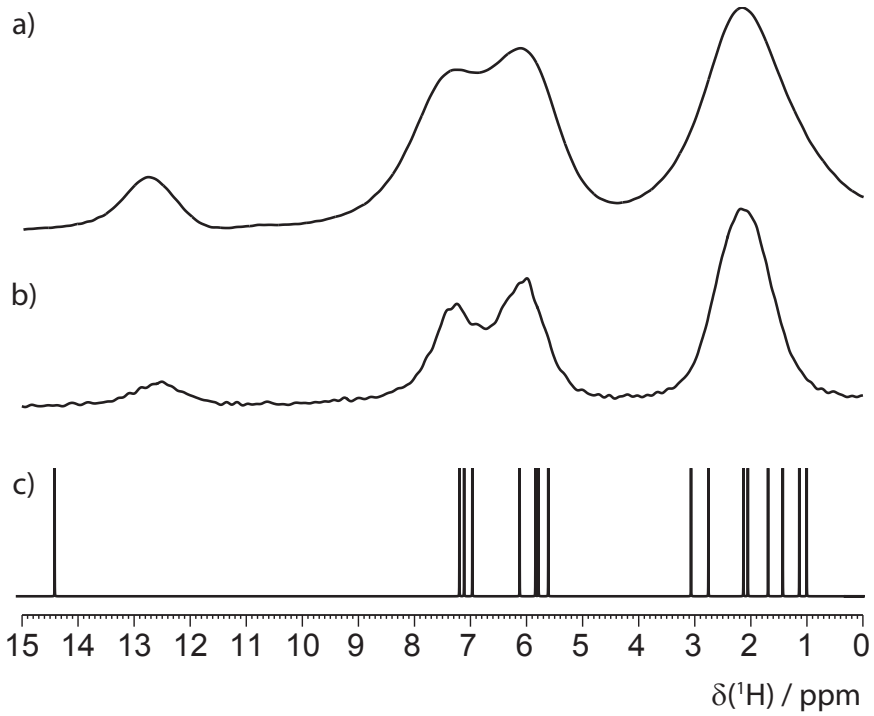

Figure 6.4: ^{1}H (600 MHz) spectra of γ-indomethacin. (a) 30 kHz MAS. (b) 12.5 kHz MAS with windowed eDUMBO-1_{22} homonuclear decoupling. In both cases, four transients were co-added with a recycle delay of 3 s. (c) A graphical representation of the GIPAW calculated chemical shifts.

observed at a lower chemical shift (by approx. 2 ppm) in experiment compared to the calculated value. This is consistent with previous observations [59, 140, 141] and may be attributed to the temperature dependence of the chemical shift of hydrogen bonded protons, specifically the chemical shift of hydrogen bonded protons is found to increase with decreasing temperature [59, 75, 140–142]. A higher chemical shift in calculation is therefore consistent as the calculations are performed on a system at an effective temperature of 0 K.

^{13}C chemical shifts of γ-indomethacin may be assigned using a ^{13}C CPMAS spectrum (figure 6.5), a ^{1}H(SQ-DUMBO)–^{13}C(SQ) refocussed INEPT spectrum (figure 6.6(a)), and the calculated (GIPAW) chemical shifts. A full list of calculated and experimental chemical shift values is presented in table 6.1. The CP spectrum contains peaks due to all carbon atoms in the molecule. There is no visible splitting of the peaks, consistent with the presence of one distinct molecule in the asymmetric unit cell. The spectrum is consistent with previously reported data [138].

Each peak in the refocussed INEPT spectrum corresponds to a one-bond C–H correlation (due to the use of short τ and τ' spin-echo periods of 1.12 ms), and the

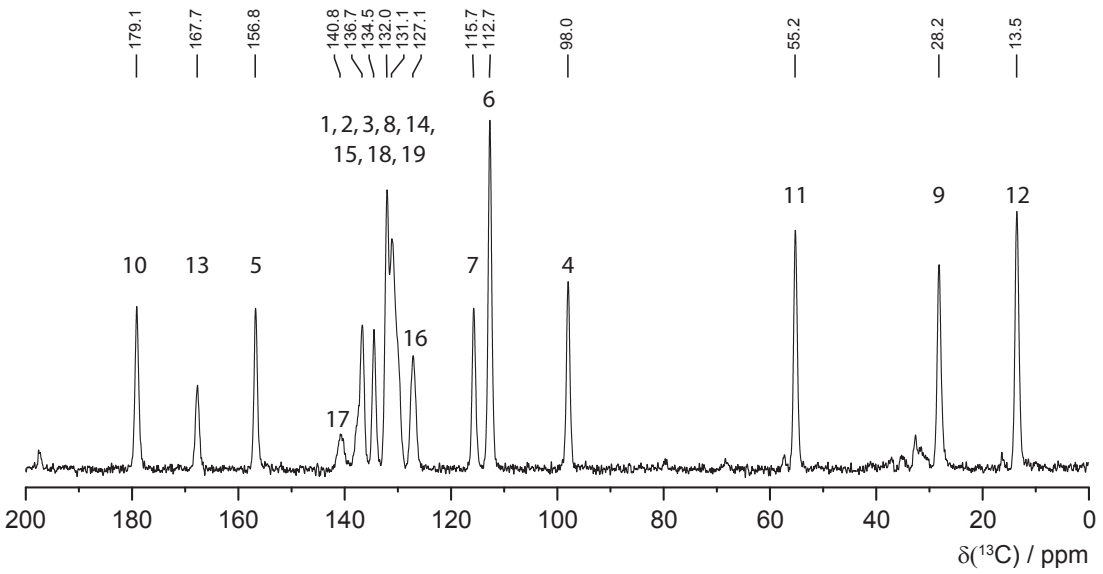

Figure 6.5: ^{13}C (125 MHz) CPMAS (12.5 kHz) spectrum of γ-indomethacin.

spectrum therefore only contains peaks corresponding to protonated ^{13}C nuclei. One peak is resolvable for each of the protonated aromatic carbon nuclei, with the exception of the C15 and C19 carbons, which overlap at 131.8 ppm in the ^{13}C dimension and 7.3 ppm in the ^{1}H dimension. The aliphatic region of the spectrum contains three peaks corresponding to the two methyl groups and the CH_2 group. The CH_2 is significantly reduced in intensity due to the strong dipolar interactions relative to the CH_3 and CH groups resulting in a faster dephasing of ^{1}H and ^{13}C transverse magnetisation.

The refocussed INEPT spectrum may also be used, again in conjunction with the GIPAW calculation results, to assign the aromatic proton resonances. Calculated and experimental values for the ^{1}H chemical are also listed in table 6.1. The two peaks resolvable in the aromatic region of the one dimensional ^{1}H spectra in figure 6.4 and the ^{1}H projection in figure 6.6(a) are found to correspond to protons in separate aromatic rings within the indomethacin molecule (with the exception of H16 which will be discussed later).

In order to investigate the effect of intermolecular interactions on the ^{1}H and ^{13}C chemical shifts, a GIPAW calculation was performed on an isolated molecule. The geometry optimised structure for the full crystal shows a hydrogen bonded dimer arrangement between two carboxyl groups. It is therefore unsurprising that the calculated chemical shifts of the carboxyl carbon and OH proton are significantly different in the full crystal and single molecule calculations, with differences of $|\delta_{cryst.} - \delta_{mol.}| = 8.4$ and

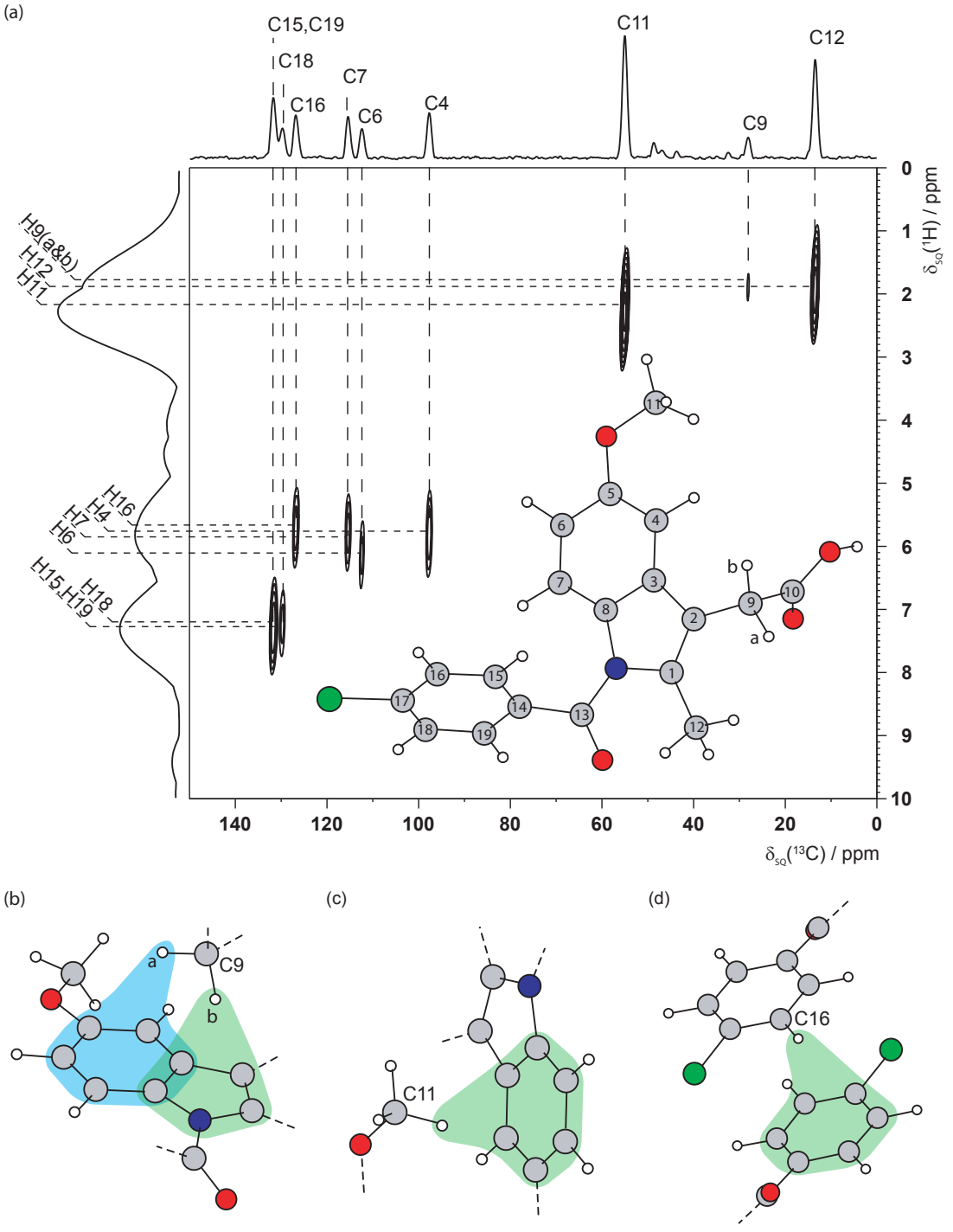

Figure 6.6: (a) A ^{1}H(SQ-DUMBO)–^{13}C(SQ) refocussed INEPT spectrum of γ-indomethacin, with skyline projections. Spin echo durations of $\tau = \tau' = 1.12$ ms were used. The base contour level is at 18% of the maximum peak intensity. A structural diagram of γ-indomethacin is shown as an inset. (b), (c) and (d) Selected portions of the geometry-optimised structure of γ-indomethacin, highlighting intermolecular interactions due to aromatic ring currents for the C9 (CH_2), C11 (CH_3) and the C16 (aromatic) protons respectively. These interactions lead to changes in the GIPAW calculated ^{1}H chemical shifts for the γ-indomethacin structure and for an isolated indomethacin molecule.

Table 6.1: Experimental[a] and calculated[b] (GIPAW) ^{13}C and ^{1}H isotropic chemical shifts for γ-indomethacin.

	$\delta(^{13}C)$			$\delta(^{1}H)$		
Site	Expt.	Calc.$_{CRYST.}$[c]	Calc.$_{ISOL.}$[d]	Expt.	Calc.$_{CRYST.}$[c]	Calc.$_{ISOL.}$[d]
1	134.5	140	140.2	-	-	-
2	112.7	115.2	114.9	-	-	-
3	132	132.4	131.5	-	-	-
4	97.7	95.6	92.6	5.8	5.8	6.3
5	156.7	158.4	158.9	-	-	-
6	112.4	111.1	111.3	6.1	6.1	5.8
7	115.5	115.4	113.6	5.8	5.9	5.8
8	131.1	131	130.4	-	-	-
9a	28.1	25.6	22.2	1.7[e]	1.4	3.3
9b					1.7	3.6
10	179	180.2	171.8	-	-	-
11	55.1	54.4	51.7	2.2	2.3[f]	3.5[f]
12	13.5	11.2	6.9	1.8	1.8[f]	2.1[f]
13	167.7	169.4	167.9	-	-	-
14	136.7	134	135	-	-	-
15	131.8	134.1	132.2	7.3	7.1	6.8
16	126.9	128	128.6	5.7	5.6	6.6
17	140.1	145.4	145.6	-	-	-
18	129.8	130.3	129.1	7.2	7	6.9
19	131.8	132.4	130.6	7.3	7.2	7.3
OH	-	-	-	12.7	14.4	7.2

[a] Determined from ^{13}C CPMAS (figure 6.5) and ^{13}C–^{1}H correlation (figure 6.6(a)) spectra.
[b] $\sigma_{\mathrm{REF}} = 169.5$ ppm for ^{13}C and 30.6 ppm for ^{1}H.
[c] Calculation for the full periodic crystal structure.
[d] Calculation for an isolated molecule.
[e] Only a single low intensity peak is observed for the CH_2 resonance.
[f] Average of the three calculated ^{1}H chemical shifts for the CH_3 group.

7.2 ppm for the carbon and proton, respectively. Differences between isolated molecule and full crystal chemical shifts of this magnitude are consistent with those found in studies of other hydrogen bonded systems [56, 143].

The chemical shifts of several other protons are also found to change significantly ($|\,\delta_{cryst.} - \delta_{mol.}\,| \geq 1.0$ ppm). Specifically both H9 (CH_2) protons experience a change of -1.9 ppm, the H11 (CH_3) protons change by -1.2 ppm, and the H16 aromatic proton changes by -1.0 ppm. These changes may be attributed to the absence of intermolecular interactions due to aromatic ring currents that are not present in the isolated molecule. Figures 6.6(b), (c) and (d) show sections of the geometry optimised crystal structure around the H9, H11 and H16 protons respectively, and highlight the

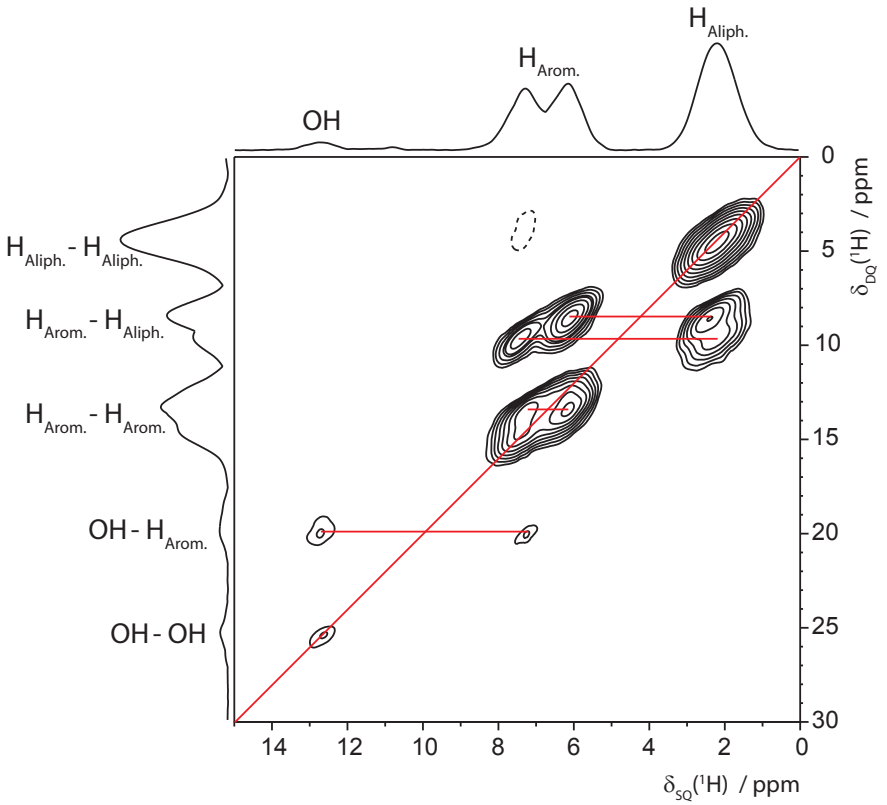

Figure 6.7: A Two-dimensional ^{1}H (600 MHz) DQ CRAMPS spectrum of γ-indomethacin, with skyline projections in both dimensions, recorded using the DQ CRAMPS pulse sequence described in chapter 3, at 12.5 kHz MAS. Three elements of the POST-C7 recoupling sequence were used in both the excitation and reconversion periods (corresponding to a total recoupling time of 138 μs). The *rf* nutation frequency was set to $\nu_1 = 87.5$ kHz during the recoupling periods, and to $\nu_1 = 100$ kHz for decoupling during the t_1 and t_2 periods. The base contour level is at 6% of the maximum peak intensity. The small negative peak at the $H_{arom.}$ SQ resonance is an artefact.

proximity of the protons in question to aromatic rings in adjacent molecules. It is evident that the change in chemical shift caused by the aromatic ring current interaction is responsible for the deviation of the H16 chemical shift from those of the other ^{1}H chemical shifts for the same aromatic ring. These changes in chemical shift of around 1–2 ppm between calculations on systems with and without intermolecular interactions are consistent with the differences found for aliphatic and aromatic protons in solid-state structures of small and moderately sized organic molecules [36, 73, 143–146].

6.3.2 ^{1}H DQ–SQ CRAMPS Results

A ^{1}H DQ CRAMPS spectrum, recorded at a ^{1}H Larmor frequency of 600 MHz, is shown in figure 6.7. As with the one dimensional ^{1}H spectra in figure 6.4, the projection in the single-quantum dimension only contains four resolved peaks. The double-quantum

peaks between $\delta_{DQ} = 2.2 + 2.2 = 4.4$ ppm and $\delta_{DQ} = 7.3 + 7.2 = 14.5$ ppm are due to $H_{aliph.}$–$H_{aliph.}$, $H_{aliph.}$–$H_{arom.}$ and $H_{arom.}$–$H_{arom.}$ proximities, including both intra- and inter-molecular ^{1}H proximities. As was the case for the sibenadet HCl polymorphs studied in chapter 5, these regions of the ^{1}H DQ CRAMPS spectrum are too crowded with overlapping peaks to resolve peaks due to individual interactions, and consequently the ^{1}H DQ build-up behaviour cannot be analysed using this experiment. A different approach is required, which will be discussed in section 6.3.3.

At higher DQ frequencies, peaks corresponding to interactions involving the OH proton are more clearly resolved. The on-diagonal peak at $\delta_{DQ} = 12.7+12.7 = 25.4$ ppm indicates an inter-molecular proximity between two OH protons. This is consistent with the optimised crystal structure which indicates a OH–OH distance of 2.38 Å. The pair of cross peaks at $\delta_{DQ} = 12.7 + 7.2 = 19.9$ ppm indicates a proximity between the OH proton and aromatic protons (predominantly H6 and H18). Both are also inter-molecular interactions, with OH–$H_{arom.}$ distances of 2.48 and 2.89 Å for H6 and H18, respectively, in the geometry optimised structure.

^{1}H double quantum build-up curves are plotted in figure 6.8 for the OH–OH and OH–$H_{arom.}$ peaks at the OH single-quantum frequency. These curves are shown in figures 6.8(a) and (b) (using blue dashed lines) as the normalised peak integral against the total recoupling time (the combined duration of the recoupling periods before and after t_1). The experimental DQ build-up curves are compared to the results of density matrix simulations (SPINEVOLUTION) of the ^{1}H DQ experiment. This simulation procedure was shown to produce results that agree closely with experiment for the dipeptide β-AspAla in chapter 4 and reference [1] and for the API sibenadet HCl in chapter 5. An system of eight ^{1}H nuclei was used, comprising the OH proton (on which the magnetisation was observed) and the seven closest protons from the geometry optimised crystal structure. This system is illustrated in figure 6.8(c) and listed in table 6.2. Note that since the simulated data is being compared to the experimental peaks observed at the OH single-quantum frequency, the same cluster of ^{1}H nuclei is used to obtain both the OH–OH and OH–$H_{arom.}$ build-up curves.

This cluster contains only one other OH proton (H–H proximity of 2.38 Å), hence this is the sole contribution to the OH–OH simulated DQ build-up curve. In contrast, the system contains five aromatic protons (H18, H6, H6, H15, H19) although the DQ

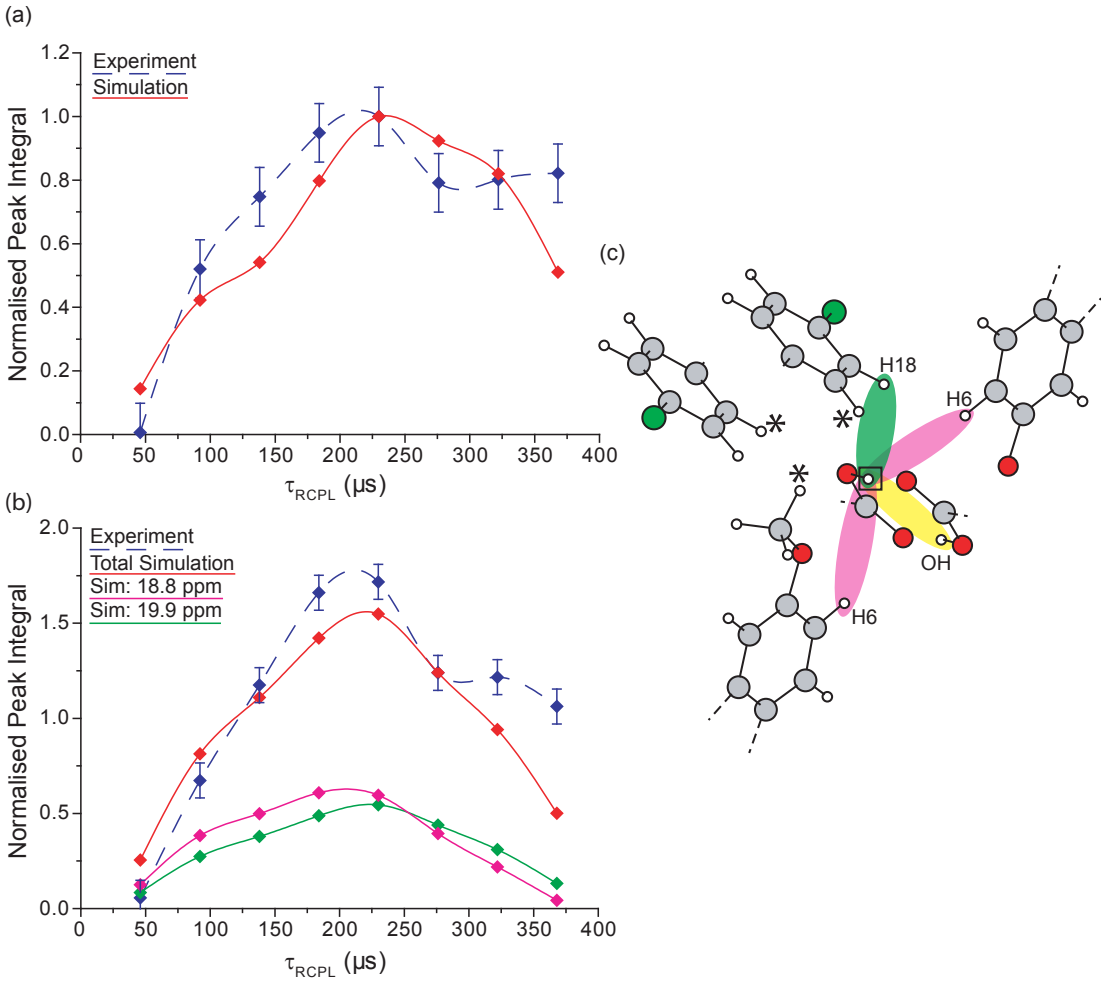

Figure 6.8: (a) and (b) ^{1}H DQ build-up curves (normalised peak integral against total recoupling time, τ_{RCPL}) for the (a) OH–OH peak at $\delta_{DQ} = 12.7 + 12.7 = 25.4$ ppm and (b) OH–$\mathrm{H_{arom.}}$ peak at $\delta_{DQ} = 12.7 + 7.2 = 19.9$ ppm. Integrated experimental intensities are marked in blue and are normalised to the maximum intensity at $\tau_{\mathrm{RCPL}} = 229$ μs for the OH–OH DQ peak. The experimental build-up is compared to simulations (SPINEVOLUTION) of the same experiment, which are shown as red points. (c) The cluster of eight atoms used for the simulations, centred on the OH proton (boxed). The OH–OH interaction is highlighted in yellow. The largest contributions to the OH-$\mathrm{H_{arom.}}$ peak are the OH–H6 and OH–H18 peaks which are highlighted in pink and green respectively. The individual build-up curves for these interactions are shown in (b) in the corresponding colour. The remaining protons included in the simulation are marked with asterisks. Lines linking the points in (a) and (b) are included as guides for the eye.

build-up behaviour is likely to be dominated by the relatively short ranged (<3.0 Å) H18 and H6 interactions due to the $1/r^3$ dependence of the dipolar interaction. Consequently the separate build-up curves due to each of the aromatic peaks were summed to produce the DQ build-up curve shown in red in figure 6.8(b). As anticipated, the simulation results indicate that the OH–H6 and OH–H18 peaks dominate the DQ build-up, the individual curves for these interactions are shown in figure 6.8(b) in pink and green respectively.

As with the previous cases of β-AspAla and sibenadet HCl, there is close agreement between experiment and simulation in the ^{1}H DQ build-up curves for γ-indomethacin. In both the OH–OH and OH–$H_{arom.}$ curves, the maximum intensity is observed at τ_{RCPL} = 229 μs (corresponding to five elements of POST-C7 recoupling at 12.5 kHz MAS). In chapter 4, it was shown that at a particular SQ frequency, the maximum intensity is observed for the DQ coherence corresponding to the shortest H–H distance. This behaviour is also exhibited in the results for γ-indomethacin. While the experimental data initially appear to contradict this result, with the OH–$H_{arom.}$ peak reaching a higher maximum intensity that the OH–OH curve, for a shortest H–H distance of 2.48 Å compared to 2.38 Å, this may be explained by examining the simulated data. The OH–$H_{arom.}$ peak is comprised of a number of different overlapping peaks, the maximum intensity of these individual peaks is found (in simulation) to be significantly lower than that of the OH–OH curve.

Furthermore, it was also shown in chapter 4 that in networks of strongly dipolar coupled spin-$\frac{1}{2}$ nuclei, the relative maximum intensity of different DQ peaks at the same SQ frequency is still given, to a good approximation, by the ratio of the squares of the dipolar coupling constants (and hence to the inverse ratio of the H–H distances to the sixth power). The DQ build-up data for γ-indomethacin is consistent with this relationship, specifically the ratio of r^6 for the two peaks (taking into account the multiple contributions to the OH–$H_{arom.}$peak) is:

$$\frac{2.38^6}{2.48^6} + \frac{2.38^6}{2.89^6} + \frac{2.38^6}{3.18^6} + \frac{2.38^6}{3.36^6} + \frac{2.38^6}{3.38^6} = 1.52$$

which is in excellent agreement with the simulated and experimental DQ build-up curves in figure 6.8.

Table 6.2: ^{1}H DQ frequencies and H–H distances[a] for the nearest seven ^{1}H nuclei to the OH and aromatic CH ^{1}H nuclei in the geometry optimised (CASTEP) crystal structure of γ-indomethacin. These clusters of atomic positions were used as input to SPINEVOLUTION density matrix simulations.

^{1}H	δ_{SQ}/ppm	δ_{DQ} /ppm	r/Å	^{1}H	δ_{SQ}/ppm	δ_{DQ}/ppm	r/Å
Centre: OH (δ_{SQ} = 12.7 ppm)				Centre: 15 (δ_{SQ} = 7.3 ppm)			
OH	12.7	25.4	2.38*	9b	1.7	9.0	2.29*
18	7.2	19.9	2.48*	16	5.7	13.0	2.46
6	6.1	18.8	2.89*	7	5.8	13.1	3.03
6	6.1	18.8	3.18*	9a	1.7	9.0	3.13*
11c	2.2	14.9	3.26*	OH	12.7	20	3.33*
15	7.3	20.0	3.33*	18	7.2	14.5	3.93*
19	7.3	20.0	3.38*	4	5.8	14.1	4.02*
Centre: 4 (δ_{SQ} = 5.8 ppm)				Centre: 16 (δ_{SQ} = 5.7 ppm)			
11a,b,c	2.2	8.0	2.30 2.35 3.63	11b,c	2.2	7.9	2.44* 2.65*
				15	7.3	13.0	2.46
9b	1.7	7.5	2.55				3.07*
12b,a	1.8	7.6	3.06* 3.27*	12a,b,c	1.8	7.5	3.69* 3.31*
11a	2.2	8.0	3.48*	OH	12.7	18.4	3.40*
Centre: 6 (δ_{SQ} = 6.1 ppm)				Centre: 18 (δ_{SQ} = 7.2 ppm)			
18	7.2	13.3	2.22*	6	6.1	13.3	2.22*
7	5.8	11.9	2.47	19	7.3	14.5	2.48
OH	12.7	18.8	2.89*	OH	12.7	19.9	2.48*
OH	12.7	18.8	3.18*	7	5.8	13.0	2.91*
9a	1.7	7.8	3.34*	12b	1.8	9.0	3.85*
11a	2.2	8.3	3.46*	15	7.3	14.5	3.93*
19	7.3	13.4	3.81*	11a	2.2	9.4	3.95*
Centre: 7 (δ_{SQ} = 5.8 ppm)				Centre: 19 (δ_{SQ} = 7.3 ppm)			
6	6.1	11.9	2.47	18	7.2	14.5	2.48
18	7.2	13.0	2.91*	11c	2.2	9.5	2.48*
15	7.3	13.1	3.03	12b,a	1.8	9.1	2.44*
12	1.8	7.6	3.62*				3.53*
11a	2.2	8.0	3.67*	OH	12.7	20.0	3.38*
19	7.3	13.1	3.69	7	5.8	13.1	3.69
12b	1.8	7.6	3.81*	6	6.1	13.4	3.81*

[a] Intermolecular proximities indicated by *.

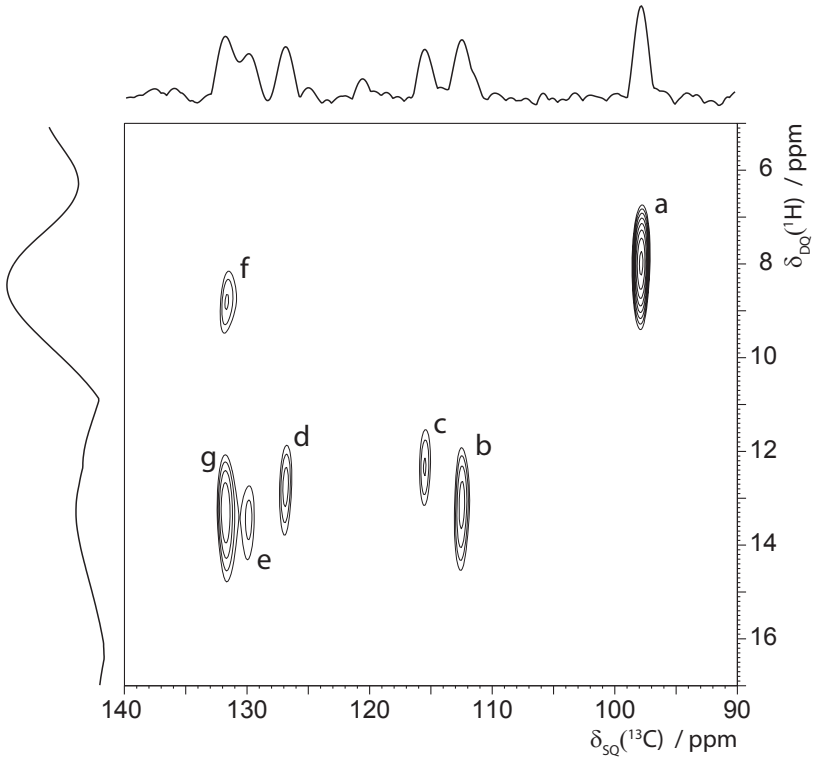

Figure 6.9: The aromatic region of a ^{1}H(850 MHz)(DQ)–^{13}C(213 MHz)(SQ) refocussed INEPT correlation spectrum of γ-indomethacin, with skyline projections. The spectrum was recorded at an MAS frequency of 12.5 kHz. eDUMBO-1_{22} homonuclear decoupling was applied on the ^{1}H channel during t_1 and spin-echo delays (τ and τ' in figure 6.2. SPINAL-64 decoupling was applied on the ^{1}H channel during t_2 acquisition. Three elements of the POST-C7 recoupling sequence were used in both the excitation and reconversion periods (corresponding to a total recoupling time of 138 μs. The *rf* nutation frequency was set to $\nu_1 = 87.5$ kHz during the recoupling periods, and to $\nu_1 = 100$ kHz for all decoupling periods. The base contour level is at 45% of the maximum peak intensity.

6.3.3 ^{1}H(DQ)–^{13}C(SQ) CRAMPS Results

The previous section showed that the use of eDUMBO-1_{22} homonuclear decoupling was not sufficient to resolve individual ^{1}H DQ peaks in the aromatic region ^{1}H DQ CRAMPS spectrum of γ-indomethacin, as many overlapping peaks due to different interactions are present in a relatively small area of the spectrum. Consequently it was impossible to extract DQ build-up curves from the spectrum. Sufficient resolution can be obtained through the use of a two-dimensional ^{1}H(DQ)–^{13}C(SQ) refocussed INEPT correlation experiment (pulse sequence shown in figure 6.2), which exploits the higher resolution attained by acquiring a ^{13}C spectrum.

A ^{1}H(DQ)–^{13}C(SQ) spectrum of γ-indomethacin is shown in figure 6.9. As in the case of the ^{1}H(SQ)–^{13}C(SQ) spectrum shown in figure 6.6, separate ^{13}C resonances are

Table 6.3: Assignment of resolved DQ peaks in the ^{1}H(DQ)–^{13}C(SQ) refocussed INEPT spectrum of γ-indomethacin in figure 6.9 to specific H–H proximities[a].

	$\delta_{Exp.}$/ppm					
Peak	^{13}C	^{1}H(DQ)	C Site	H–H proximity	$\delta_{DQ}(^{1}\mathrm{H})$/ppm	Distance(s)/Å
a	97.7	8.1	C4	H4–H12(a,c)	5.8 + 1.8 = 7.6	3.06*, 3.27*
			C4	H4–H9b	5.8 + 1.7 = 7.5	2.55*
			C4	H4–H11(a,b,c)	5.8 + 2.2 = 8.0	2.30, 2.35, 3.63
			C4	H4–H11(a)	5.8 + 2.2 = 8.0	3.48*
b	112.4	13.4	C6	H6–H7	6.1 + 5.8 = 11.9	2.47
			C6	H6–H18	6.1 + 7.2 = 13.3	2.22*
c	115.5	12.6	C7	H7–H6	5.8 + 6.1 = 11.9	2.47
			C7	H7–H18	5.8 + 7.2 = 13.0	2.91*
			C7	H7–H15	5.8 + 7.3 = 13.1	3.03
d	126.9	13.1	C16	H16–H15	5.7 + 7.3 = 13.0	2.46
e	129.8	13.7	C18	H18–H7	7.2 + 5.8 = 13.0	2.91
			C18	H18–H6	7.2 + 6.1 = 13.3	2.22*
			C18	H18–H19	7.2 + 7.3 = 14.5	2.48
f	131.8	8.9	C15	H15–H9b	7.3 + 1.7 = 9.0	2.29*
			C15	H15–H9a	7.3 + 1.7 = 9.0	3.13*
			C19	H19–H12(a,b)	7.3 + 1.8 = 9.1	2.44*, 3.53*
			C19	H19–H11c	7.3 + 2.2 = 9.5	2.48
g	131.8	13.5	C15	H15–H16	7.3 + 5.7 = 13.0	2.46
			C15	H15–H7	7.3 + 5.8 = 13.1	3.03
			C15	H15–H4	7.3 + 5.8 = 13.1	4.02*
			C19	H19–H18	7.3 + 7.2 = 14.5	2.48

[a] Intermolecular proximities are indicated by *.

resolved for six of the seven aromatic CH moieties (C15 and C19 again overlap). A short spin-echo duration ($\tau = \tau' = 1.16$ ms) ensures that ^{13}C resonances are correlated with ^{1}H DQ resonances involving a ^{1}H linked by one bond to the ^{13}C nucleus. Table 6.3 assigns each of the peaks labelled a–g in figure 6.9 to specific H–H interactions.

Although the higher resolution of the ^{1}H(DQ)–^{13}C(SQ) refocussed INEPT spectrum allows multiple ^{1}H DQ peaks to be resolved in the aromatic region, the peaks remain sufficiently broad in the ^{1}H DQ dimension that in general, the resolvable peaks are due to multiple H–H proximities. For example, the shortest $\mathrm{H_{arom.}}$–$\mathrm{H_{arom.}}$ distance of 2.22 Å between H6 and H18 (an intermolecular proximity) results in peaks at $\delta_{DQ} = 6.1 + 7.2 = 13.3$ ppm in the ^{1}H DQ dimension, at the ^{13}C chemical shifts of the C6 and C18 carbons in the ^{13}C dimension (112.4 and 129.8 ppm respectively). These peaks overlap with the H6–H7 (2.47 Å, $\delta_{DQ} = 6.1 + 5.8 = 11.9$ ppm) peak at the C6 chemical

shift, and with both the H18–H7 (2.47 Å, $\delta_{DQ} = 7.2 + 5.8 = 13.0$ ppm) and H18–H19 (2.47 Å, $\delta_{DQ} = 7.2 + 7.3 = 14.5$ ppm) peaks at the C18 chemical shift.

H4 is the only aromatic proton not to have a close proximity to another aromatic proton, although it is in close proximity to several aliphatic protons (both intra- and intermolecular interactions). Consequently the peak at the C4 chemical shift (97.7 ppm) is at 8.1 ppm in the ^{1}H DQ dimension, and there is no ^{1}H DQ peak at approximately 13 ppm.

The peak labelled "d" in the ^{1}H(DQ)–^{13}C(SQ) refocussed INEPT spectrum is unique in that it corresponds to a single H–H interaction, specifically the peak at the C16 chemical shift (126.9 ppm) is due to the intramolecular H16–H15 proximity (2.46 Å) between adjacent aromatic protons. The experimental double-quantum build-up curve for this peak is shown in figure 6.10(a) in blue. This is compared to a simulated ^{1}H DQ build-up curve in red. The simulation was performed using SPINEVOLUTION, on a cluster of eight nuclei comprised of H16 and the seven closest ^{1}H nuclei in the optimised crystal structure, with magnetisation observed on H16, this system is illustrated in figure 6.10(c) and listed in table 6.2. The experimental curve reaches a maximum at a total recoupling time of 183 μs, corresponding to the use of four elements of POST-C7 recoupling (at an MAS frequency of 12.5 kHz) for both excitation and reconversion of the DQ coherence. The maximum point in the simulated DQ build-up curve occurs at a slightly longer recoupling time ($\tau_{\mathrm{RCPL}} = 229$ μs), corresponding to the use of five elements of POST-C7 for both excitation and reconversion. This difference between experiment and simulation in terms of the time taken for the DQ build-up curves to reach maximum intensity is consistent with observations of ^{1}H DQ build-up in the dipeptide β-AspAla discussed in chapter 4; this is was attributed to the limited size of the simulated cluster.

A further interesting case to discuss is the build-up of the peak labelled "b" in figure 6.9. This peak corresponds to the H6–H18 (2.22 Å, $\delta_{DQ} = 6.1 + 7.2$ =13.3 ppm) and H6–H7 (2.47 Å, $\delta_{DQ} = 6.1 + 5.8$ =11.9 ppm) interactions. The experimentally observed build-up of this peak is shown in figure 6.10(c) in blue. This is compared to the sum of the simulated ^{1}H DQ build-up curves for the H6–H18 and H6–H7 curves, shown in red. These build-up curves were both obtained from simulations of ^{1}H DQ build-up observed on the H6 nucleus in a cluster comprising H6 and the seven closest protons

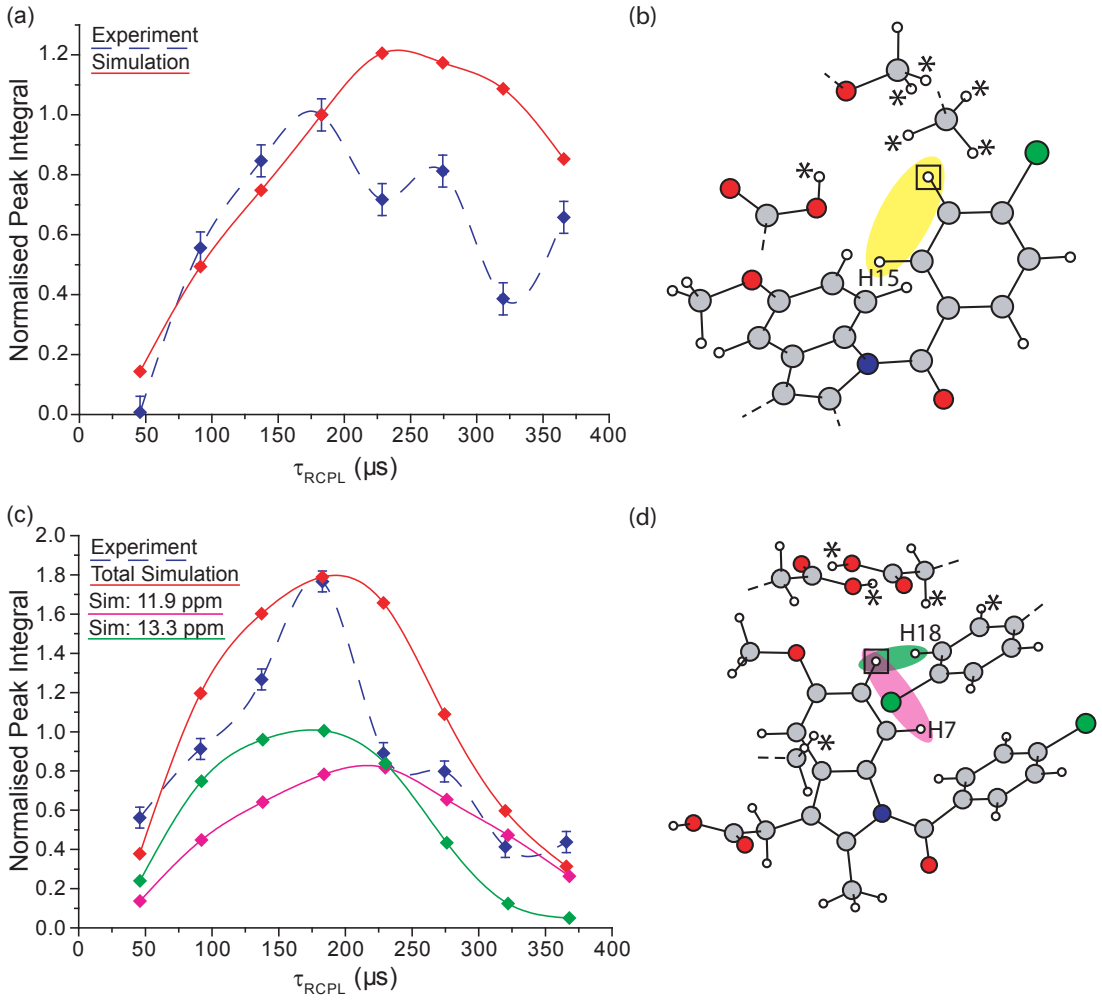

Figure 6.10: (a) and (c) ^{1}H DQ build-up curves (normalised peak integral against total recoupling time, τ_{RCPL}) for (a) peak d and (c) peak b in the ^{1}H(DQ)–^{13}C(SQ) refocussed INEPT spectrum shown in figure 6.9, corresponding to the ^{1}H DQ coherences for the (a) H16 and (c) H6 aromatic protons directly bound to the C16 and C6 carbons (^{13}C resonances of 127.2 and 112.8 ppm, respectively). Experimental data is shown in blue (normalised to the maximum intensity at τ_{RCPL}= 183 μs for peak d). Simulated (SPINEVOLUTION) peak intensities are shown in red (normalised to the maximum intensity at τ_{RCPL} = 183 μs for peak d). (b) and (d) The clusters of eight ^{1}H nuclei for simulations observing on H16 and H6, respectively, in each case the observed nucleus is boxed. Peak d is due to a single H16–H15 interaction, highlighted in yellow in (b). Peak b is due to two interactions, H6–H18 and H6–H7, highlighted in green and pink, respectively. The individual build-up curves for these interactions are shown in (c) in the corresponding colour. The remaining protons included in the simulations are marked in (b) and (d) with asterisks. Lines linking the points in (a) and (c) are included as guides for the eye.

in the optimised crystal structure, listed in table 6.2. The simulated system is also shown in figure 6.10(d), in which the H6–H18 and H6–H7 interactions are highlighted in green and pink, respectively. The individual ^{1}H DQ build-up curves for these two interactions are shown (in the corresponding colour) in figure 6.10(c). In terms of both the maximum peak intensity, and the recoupling time at which it is reached, there is excellent agreement between the experimental and (summed) simulated build-up data for peak b.

A comparison of the simulated ^{1}H DQ build-up of the H16–H15 peak (solid red line in figure 6.10(a)) and the H6–H18 (solid green line in 6.10(c)) shows that the H6–H18 peak reaches maximum intensity at a shorter recoupling time (183 μs compared to 229 μs), consistent with the shorter internuclear distance of 2.22 Å compared to 2.46 Å for H16–H15, following the guidelines for interpretation of ^{1}H DQ build-up curves summarised in chapter 4. Similarly the two build-up curves for H6–H18 and H6–H7 (green and pink curves, respectively, in figure 6.10(c)) may be analysed in terms of the ratio of the maximum intensity reached by the ^{1}H DQ build-up curves, as with the DQ build-up curves for peaks at the OH single-quantum frequency in the standard ^{1}H DQ CRAMPS spectrum in section 6.3.2. A greater maximum intensity is observed for the shorter H–H distance, again consistent with the guidelines established in chapter 4.

While the analysis of the two peaks discussed above shows good agreement between simulation and experiment, it is important to note that while the ^{1}H(DQ)–^{13}C(SQ) refocussed INEPT experiment results in enhanced resolution in comparison to the ^{1}H DQ CRAMPS experiment, this is achieved at the cost of an important disadvantage in terms of quantitative comparisons between the build-up of different peaks. Specifically, the refocussed INEPT transfer from ^{13}C to ^{1}H will depend on the ^{1}H and ^{13}C T_2' spin-echo dephasing times, which would typically be expected to differ for different CH moieties.

6.4 Summary and Conclusions

The results presented in this chapter demonstrate that in organic crystalline systems in which sufficient resolution cannot be obtained using a ^{1}H–^{1}H DQ CRAMPS experiment to resolve peaks corresponding to individual H–H proximities, the ^{1}H(DQ)–^{13}C(SQ)

refocussed INEPT experiment allows peaks corresponding to interactions involving individual ^{1}H nuclei to be resolved, via detection on the directly bonded ^{13}C. In the case of γ-indomethacin, this experiment was used to extract ^{1}H DQ build-up curves from the aromatic region of the spectrum. These experimental results were compared to eight-spin density matrix simulations, based on the geometry optimised crystal structure of γ-indomethacin.

In addition, the comparison of calculated (GIPAW) chemical shifts for the full optimised crystal structure of γ-indomethacin, and an indomethacin molecule effectively isolated by being placed in a very large unit cell, allowed the effect of intermolecular interactions to be investigated. Specifically it was found that, in addition to the expected differences due to the hydrogen bonding interactions at the carboxylic acid moiety, the chemical shift of several protons are influenced by aromatic ring currents in neighbouring molecules within the full unit cell. This investigation explained the relatively large deviation of the H16 chemical shift from that of the other protons in the same aromatic ring.

While the transfer of magnetisation from ^{1}H to ^{13}C allowed the extraction of the DQ build-up curves for individual peaks, this is at the cost of both limiting the quantitative analysis, due to the dependence of the INEPT transfer on the spin-echo dephasing times, and, at natural abundance, a significant increase in the time taken to record a spectrum (approximately 28 hours, in contrast to approximately two hours for a standard ^{1}H DQ CRAMPS spectrum).

Despite the limitations discussed above, the ^{1}H(DQ)–^{13}C(SQ) refocussed INEPT experiment overcomes the problem seen in the standard ^{1}H DQ CRAMPS spectra of γ-indomethacin and (in the previous chapter sibenadet HCl), of a lack of resolution in the aromatic region. This is likely to be a problem in the study by ^{1}H solid-state NMR of many similar organic molecules, and consequently the ^{1}H(DQ)–^{13}C(SQ) refocussed INEPT experiment has the potential to significantly expand the range of systems to which ^{1}H DQ build-up analysis may be applied.

CHAPTER

SEVEN

A STUDY OF POLYMORPHISM IN IBUPROFEN THROUGH ^{13}C SOLID-STATE NMR AND FIRST-PRINCIPLES CALCULATIONS

7.1 Introduction

Ibuprofen is a non-steroidal anti-inflammatory drug. Originally developed as a treatment for rheumatoid arthritis, it is now among the most commonly used analgesics [147] and is considered by the World Health Organisation to be one of the core medicines required for the operation of a basic health care system [148]. Ibuprofen exhibits stereochemistry, existing in two forms designated R(−)-ibuprofen and S(+)-ibuprofen (the pharmaceutically active isomer [149]), and is commonly marketed as a racemic mixture [150].

Racemic ibuprofen, the molecular structure of which is shown in figure 7.1 is known to exist in at least two polymorphic crystalline forms. Form I, until relatively recently the only known crystalline form, is the polymorph used in the pharmaceutical product. Form II is a polymorph produced by melting form I, before quenching to form an amorphous solid, which is then annealed at 258 K until form II emerges. This polymorph has been shown to exhibit physical differences to form I, notably a significantly lower melting point (290 K compared to 349 K), indicating a lower stability [151]. The crystal structure of form II has recently been solved by powder x-ray diffraction [152].

In this chapter, ibuprofen forms I and II are investigated using ^{13}C CP MAS solid-state NMR and density functional theory calculations. Form I was converted to an

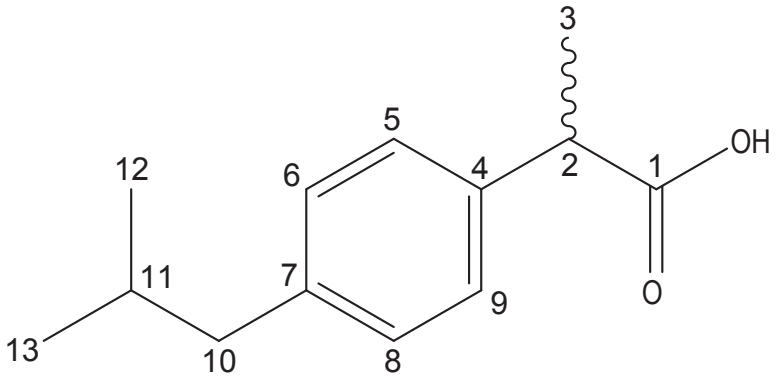

Figure 7.1: Molecular structure of ibuprofen, showing the numbering system used for carbon atoms used throughout this chapter.

amorphous solid by melting and rapidly quenching, and the emergence of form II from the amorphous form during annealing at 258 K was monitored using repeated ^{13}C CP-MAS experiments. The experimentally obtained carbon chemical shifts are compared to the values obtained from GIPAW calculations for the published crystal structures of form I and form II and an alternative structure for form II.

7.2 Experimental and Computational Details

This work has been performed in collaboration with Prof. Alastair Florence, at the University of Strathclyde, who provided the sample of form I ibuprofen, advice on the process for production of form II, and two structural models for form II.

7.2.1 Variable Temperature ^{13}C CP MAS Solid-State NMR Experiments

Experiments on ibuprofen were performed using a Bruker Avance III 500 spectrometer, operating at Larmor frequencies of 500.1 MHz for ^{1}H and 125.8 MHz for ^{13}C. All experiments were ^{13}C CP MAS (8 kHz), with transverse magnetisation transferred from ^{1}H using a 1 ms contact pulse, ramped from 50% to 100% power on the ^{1}H channel. During the 39.9 ms acquisition time, SPINAL-64 decoupling was applied on the ^{1}H channel at an *rf* frequency of 100 kHz and with a pulse duration of 4.6 μs. Unless otherwise stated, 256 transients were recorded and co-added. A 3 s recycle delay was used, resulting in a total acquisition time of approximately thirteen minutes.

Preparation of the sample in such a way that it would be possible to follow the

emergence of the crystalline form II from the amorphous form by solid-state NMR required the following pre-experiment set-up procedure. Powdered form I ibuprofen was packed into a standard Bruker 4mm MAS zirconia rotor, which was fitted with a boron nitride cap to ensure that the variations in temperature required to produce form II did not result in the rotor and cap becoming separated. The rotor was then placed in an oven and heated to (355 $\pm$ 1) K (above the melting point of 349 K) and held at that temperature for several minutes, to ensure a complete melt of the sample within the rotor. The rotor was then removed from the oven and quenched in liquid nitrogen (77 K) to rapidly solidify the sample. Meanwhile, a Bruker 4mm triple resonance probe, operating in double-resonance mode and tuned to ^{1}H and ^{13}C, was cooled using a Bruker BVT3000 variable temperature unit and a Bruker BCU-Xtreme refrigeration unit, using a cooling gas temperature of 258 K. The rotor was removed from the liquid nitrogen and inserted directly into the probe using the insert-eject mechanism.

In order to start magic angle spinning, it was necessary to interrupt the flow of cooling gas to the probe. The rotor was spun up to 4 kHz before resuming cooling, during which time the temperature measured inside the probe rose due to the application of room temperature bearing and drive gas flows and absence of cooling gas. During this interval the probe temperature did not rise above 272 K. Once the MAS frequency had reached 4 kHz, the cooling gas flow was resumed and the temperature measured inside the probe returned to 258 K. The MAS rate was then increased gradually, in steps of 500 Hz, up to the final frequency of 8 kHz. During this second phase of spin rate increase, the probe temperature remained in the range 258 ± 1 K.

Fifty ^{13}C CP MAS experiments were performed, using the parameters described previously in this chapter, while the cooling gas temperature was maintained at 258 K (above the reported glass transition temperature of 228 ± 1 K [151]). In order to follow the conversion of form I to form II as the temperature increased, a further two ^{13}C CP MAS experiments were then performed. Firstly after the cooling gas temperature had increased first to 273 K, then the cooling gas flow was switched off and the final ^{13}C experiment was performed after the sample had reached room temperature.

The discussion of the temperature throughout refers to the temperature of the cooling gas measured inside the probe. The temperature of the sample will differ from this value due to frictional heating caused by magic angle spinning. However, in this

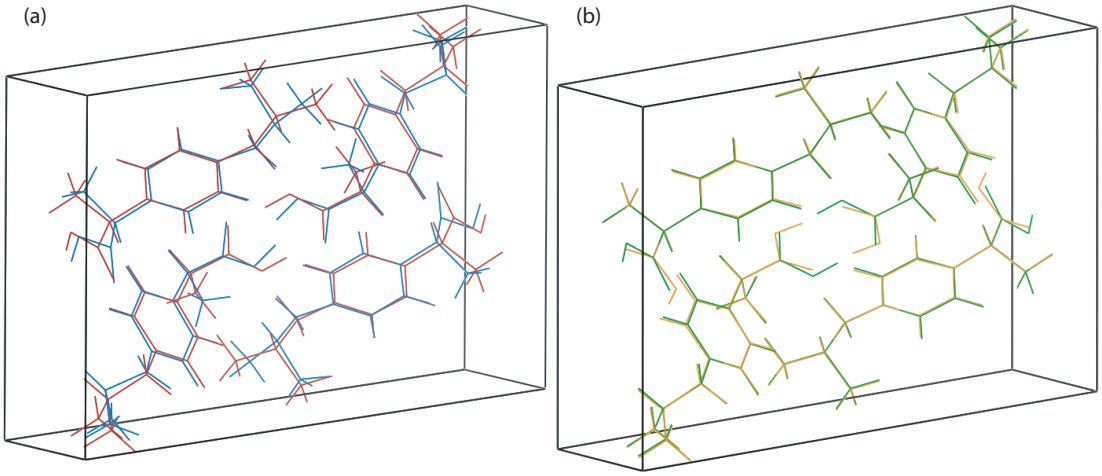

Figure 7.2: Ibuprofen form II structures. (a) Before (blue) and after (red) geometry optimisation. (b) The geometry optimised structures of form II(a) (green) and form II(b) (orange).

case due to the relatively low spinning frequency of 8 kHz, this heating effect is likely to be relatively small (< 10 K).

7.2.2 Computational Details

First-principles density functional theory (DFT) calculations were performed using CASTEP [48] version 4.3. Structural files for ibuprofen forms I and II were obtained from the Chemical Database Service CrystalWeb database (refcodes COTYOA for form I and IBPRAC04 for form II).

For each structure, a geometry optimisation calculation was performed, and the resulting structure was then used as input for a calculation using the GIPAW [50, 51] (Gauge-Including Projector Augmented-Wave) method to obtain the NMR chemical shielding parameters. Both stages of the calculation used a cut-off energy of 1100 eV. A Monkhurst-Pack grid with a k-point spacing of 0.1 Å^{-1} was used for the geometry optimisation stage, and with a spacing of 0.05 Å^{-1} for the NMR calculation. The PBE exchange-function correlational and ultrasoft pseudopotentials were used in all calculations. During the geometry optimisation stage of the calculation, the positions of all atoms were optimised. The importance of fully optimising the structure, rather than just the proton positions is shown in figure 7.2(a), which shows significant differences in the positions of carbon and oxygen atoms in the overlayed unit cells of form II before and after geometry optimisation. The geometry optimisation and NMR calculations for form II were performed on two different structures. The first, referred to as form II

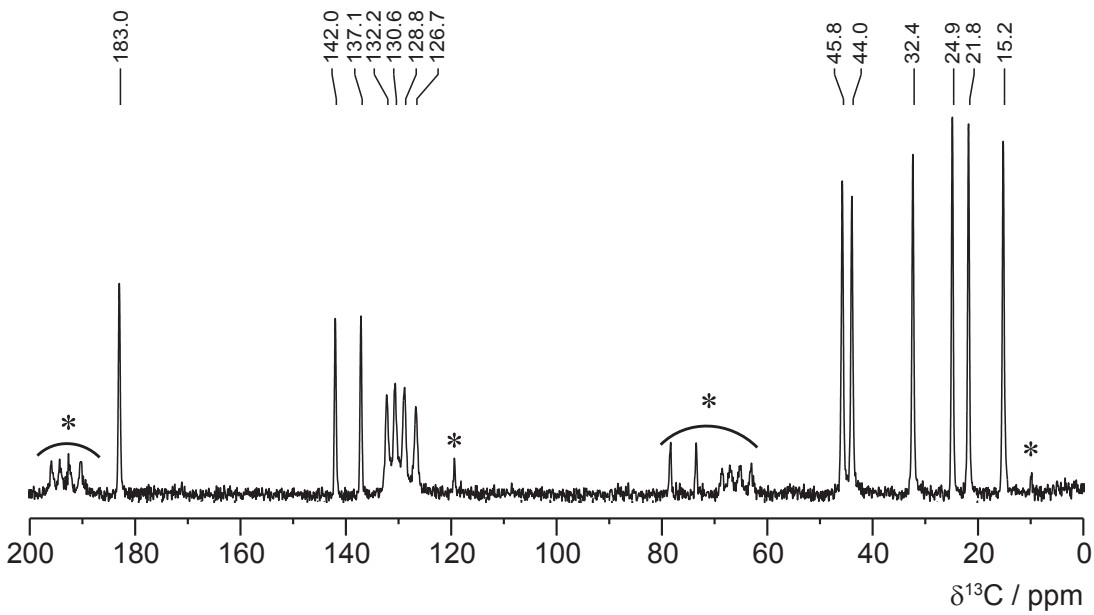

Figure 7.3: ^{13}C (125 MHz) CP MAS (8 kHz) spectrum of ibuprofen form I as received, as recorded at room temperature. Spinning sidebands are marked with an asterisk.

(a), is the (geometry optimised) published [152] structure. The second, referred to as form II (b), is the published structure with the carboxyl group rotated through 180° about the axis defined by the C7–C9 bond, as illustrated in the overlayed (geometry optimised) unit cells of form II(a) and form II(b) in figure 7.2(b). For form II(b), the carboxyl group was rotated before the geometry optimisation.

Following geometry optimisation, the average forces acting on each atomic species (in units of eV/Å) for each structure were: 0.015(H), 0.019(C) and 0.020(O) for form I; 0.013(H), 0.021(C) and 0.026(O) for form II(a); and 0.014(H), 0.023(C) and 0.024(O) for form II(b).

7.3 Results and Discussion

7.3.1 Form I Ibuprofen

A ^{13}C CP MAS spectrum of ibuprofen form I, recorded using the sample as received and at room temperature, is presented in figure 7.3. With the exception of spinning sidebands, one peak appears in the spectrum for each of the thirteen carbon atoms in a single ibuprofen molecule, indicating the presence of one distinct molecule in the asymmetric unit cell. The spectrum recorded for the ibuprofen sample is consistent with a ^{13}C CP MAS spectrum previously reported by Geppi *et. al.* [153].

Table 7.1: Experimental and calculated (GIPAW) ^{13}C chemical shifts for ibuprofen form I.

^{13}C Label (Fig. 7.1)	δ_{EXP}/ppm	δ_{CALC}/ppm
1	183.0	187.2[a]
2	45.8	46.4[b]
3	15.2	14.0[b]
4	137.1	137.0[a]
5	130.6	130.4[a]
6	128.8	128.6[a]
7	142.0	143.2[a]
8	132.2	132.1[a]
9	126.7	126.4[a]
10	44.0	46.0[b]
11	32.4	34.5[b]
12	24.9	22.9[b]
13	21.8	20.2[b]

[a] $\sigma_{REF} = 167.0$ ppm
[b] $\sigma_{REF} = 171.8$ ppm

Table 7.1 lists the experimentally obtained chemical shifts, compared to the GIPAW calculated values, and assigns all thirteen ^{13}C peaks to the molecular diagram in figure 7.1. Due to the significant separation of the aliphatic and aromatic regions of the spectrum, it was appropriate to choose separate reference values for each region. Reference values were chosen such that for each region, the mean values of the calculated and experimental chemical shifts coincided. This method reduced the effect of the over- and under-estimation of the high and low ppm ends of the spectrum respectively and has been previously used in the analysis of calculated solid-state NMR chemical shifts [111]. The calculated chemical shift value for the carboxyl carbon was referenced using the value for the aromatic region, although this peak was not included in the calculation of that reference value.

7.3.2 Form II Ibuprofen

Figure 7.6(a) shows ^{13}C CP MAS spectra recorded at time intervals of approximately 2.1 hours, showing the conversion between amorphous and form II ibuprofen. The initial ($t = 0$) spectrum has a very low signal to noise ratio, consistent with the presence of an amorphous solid. A sharp peak at 22.7 ppm is the dominant feature in the spectrum. This peak persists at longer times, although it is eventually obscured as the larger peak at 23.4 ppm emerges. After 2.1 hours, all peaks in the form II spectrum have

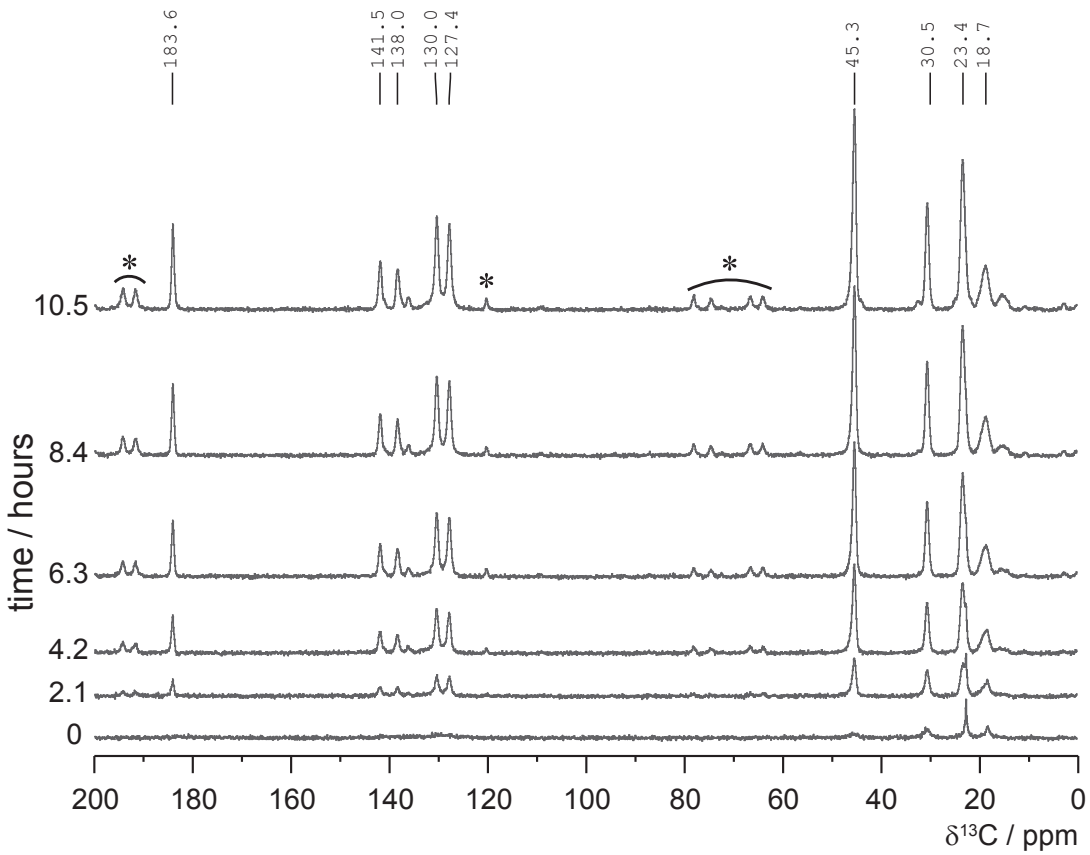

Figure 7.4: ^{13}C (125 MHz) CP MAS (8 kHz) spectra of ibuprofen recorded at a temperature of 258 K. The initial ($t = 0$) spectrum shows the amorphous solid. Spectra recorded at later times show the emergence of ibuprofen form II as the sample is annealed.

appeared. These peaks continue to increase in intensity throughout the remainder of the experimental period. This behaviour is consistent with the powder x-ray diffraction data reported in reference [152], which showed diffraction peaks consistent with the presence of form II emerging over a similar time scale (approximately five hours).

Comparison of the spectrum of form I with that of form II shows that several very weak peaks due to form I are present in the form II spectrum. These are most clearly visible in the aliphatic region of the form II spectrum, at 15.2 ppm, as a clearly resolvable, distinct peak, and at 21.8, 24.9, 32.4 and 44.0 ppm although these are partially obscured due to their close proximity to much more intense form II peaks. The presence of these form I peaks in the form II spectrum is shown in figure 7.5. These peaks grow in intensity as time progresses, suggesting that rather than indicating a remnant of form I that remained unmelted, a small amount of form I is produced during the annealing process, either directly from the amorphous solid, or via a conversion from form II. The form II spectrum also contains a relatively low intensity peak in the

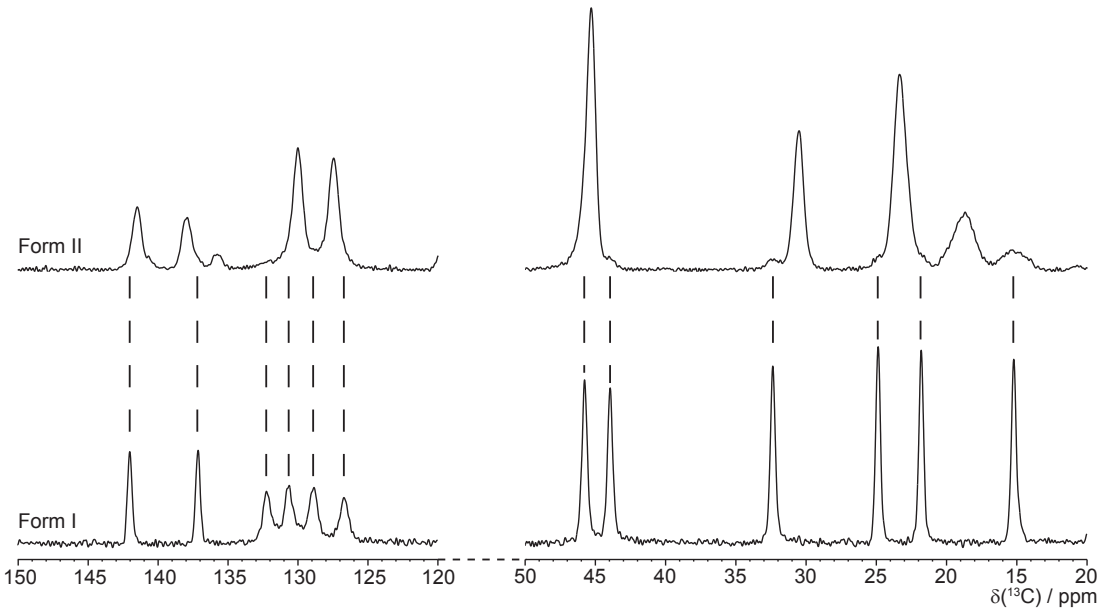

Figure 7.5: Comparison of the aliphatic and aromatic regions of the ^{13}C (125 MHz) CP MAS (8 kHz) spectra of ibuprofen form I (as received) and form II (annealed at 258 K for 10.5 hours). Dashed lines at the form I chemical shifts highlight the presence of form I peaks in the form II spectrum.

aromatic region, at 135.8 ppm. The cause of this peak is unclear, as it is considerably weaker than the surrounding form II aromatic peaks, does not correspond to a form I chemical shift (as shown in figure 7.5) and is not a spinning sideband.

Excluding the form I peaks, the anomalous peak at 135.8 ppm, and spinning sidebands; the form II spectrum contains nine peaks. As with form I, there is no evidence of any splitting of the peaks, indicating the presence of one distinct molecule in the ibuprofen form II asymmetric unit cell. However several of the peaks must now correspond to more than one carbon site in the ibuprofen molecule. Peaks were fitted to Gaussian functions and the integrals under each of the fitted peaks were measured. Regarding the aromatic region of the spectrum, the integral under the two peaks at 138.0 and 141.5 ppm in form II spectrum is 44% of the integral under the two peaks at 127.4 and 130.0 ppm. In comparison, in the form I spectrum, the integral under the two peaks at 137.1 and 142.0 ppm is 41% of the intergral under the four peaks between 126.7 and 132.2 ppm. The close agreement in these ratios indicates that the 127.4 and 130.0 ppm peaks in the form II spectrum are due to the four protonated aromatic carbons. A similar analysis shows that the peaks at 23.4 and 45.3 ppm in the form II spectrum are also each due to two distinct carbon atoms. The quantitative analysis of a CP spectrum is not normally possible in this way, due to the dependence of the peak

intensity on the heteronuclear dipolar coupling. However, in this case, the comparison between the peak integrals in the form I and form II spectra would be expected to largely negate this effect.

Following acquisition of the ^{13}C CP MAS spectra of ibuprofen form II at 258 K, two further spectra were recorded at 273 K and, with the cooling gas flow switched off, when the sample had returned to room temperature. The 273 K spectrum contains a mixture of form I and form II peaks, as shown in figure 7.6(b). The room temperature spectrum is shown in figure 7.6(c) and contains peaks consistent with the presence of ibuprofen form I. No discernible peaks due to form II are present in the spectrum, indicating a complete reconversion from form II to form I ibuprofen. This result differs slightly from the previously published investigation into form II ibuprofen using differential scanning calorimetry and x-ray diffraction experiments [151], which reported a melting of form II at 290 K, followed by recrystallisation of form I at 310 K. There is no evidence in the ^{13}C solid-state NMR results of the conversion from form II to form I involving an intermediate transition to a molten state, as reported by Dudognon *et. al.* [151]. Instead the form I appears to emerge directly from the form II upon heating. However, it is notable that if melting of the sample did occur, no peaks due to the liquid ibuprofen would be expected in the spectrum, as the dipolar interaction through which magnetisation is transferred in a CP experiment would be averaged to zero by the molecular motion. The only way in which the molten state may be apparent is through a reduction in the observed signal, however no such reduction was observed.

It is notable that throughout the reconverted form I spectrum, the peaks are significantly broader than in the initial form I spectrum. Line widths were measured using fitting to Gaussian functions as described previously. Full width at half maximum height (FWHMH) values were obtained for the fitted peaks. The values are listed in table 7.2. The increase in line width following the melt-quench process is consistent with observations by Barich *et. al.* [154], who attributed the change to an increase in anisotropic bulk magnetic susceptibility (ABMS) due to a decrease in particle size, or increase in the density of defects within ibuprofen crystals. ABMS, which may be calculated using DFT [55], can have a significant effect on the line widths in solid-state NMR spectra [155] and would be likely to be a factor in the line width in ibuprofen solid-state NMR spectra due to the presence of an aromatic ring in the molecule, which

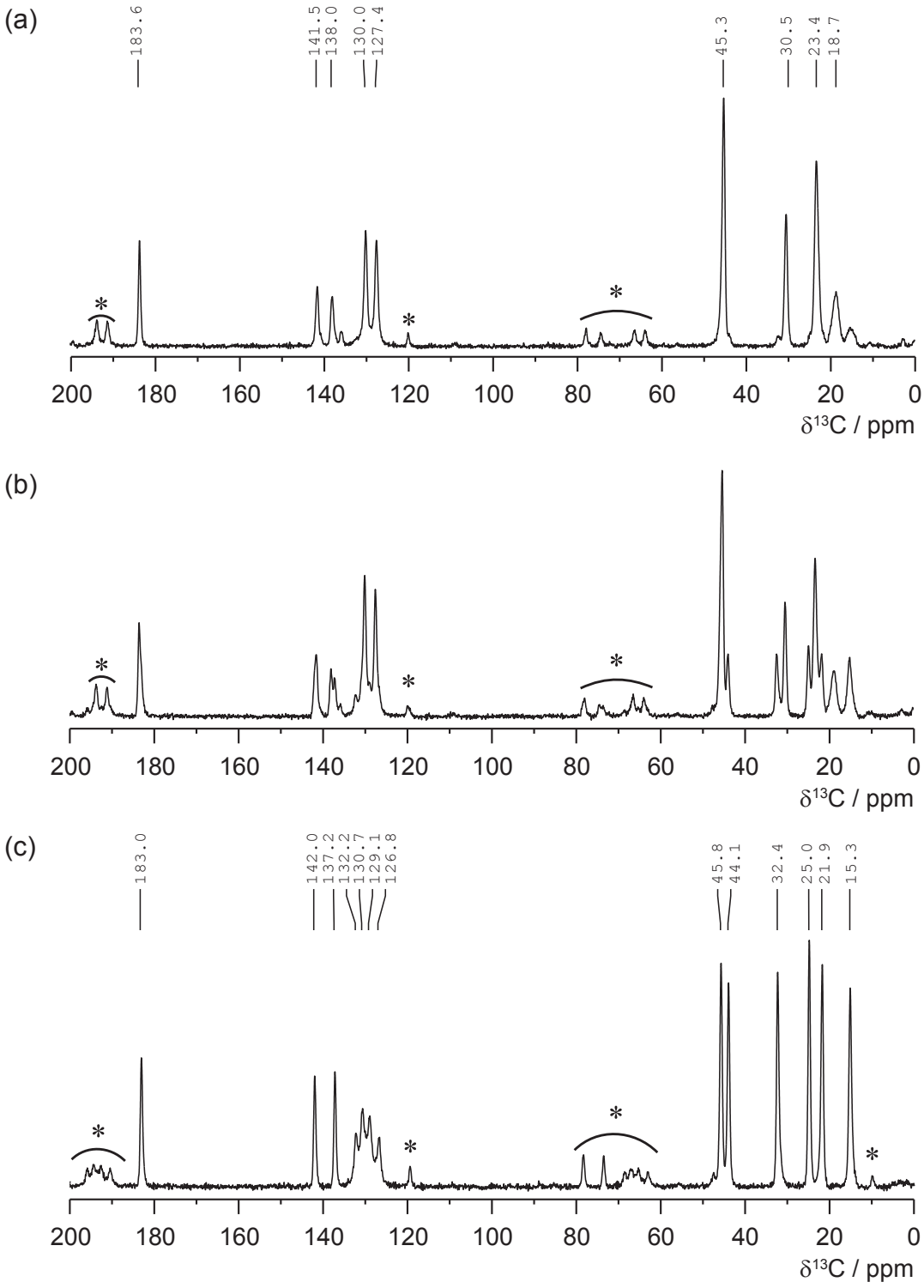

Figure 7.6: ^{13}C (125 MHz) CP MAS (8 kHz) spectra. (a) Ibuprofen form II - produced by quenching a melted sample and annealing for 10.5 hours. (b) Spectrum recorded after allowing the temperature of the form II sample to increase to 273 K. The spectrum contains peaks at chemical shifts characteristic of both forms I and II (c) Spectrum recorded after allowing the temperature of the form II sample to increase to room temperature. The spectrum contains only form I peaks, indicating a complete conversion from form II to form I. Spinning sidebands are marked with an asterisk in all spectra.

Table 7.2: Line widths for ibuprofen form I, recorded before and after conversion to form II

		Line Width (FWHMH)/Hz (±1 Hz)	
^{13}C Label	δ/ppm	As received	Reconverted (from form II)
1	183.0	51	81
2	45.8	60	89
3	15.2	55	100
4	137.1	47	75
5	130.6	117	222
6	128.9	103	212
7	142.0	48	79
8	132.2	102	142
9	126.7	100	156
10	44.0	59	85
11	32.4	54	88
12	24.9	50	80
13	21.8	50	87

acts as a source of ABMS [156].

Calculations of the isotropic chemical shift values were performed for both of the possible structure models for form II ibuprofen. As with the calculations for form I, separate reference values were used for the aromatic and aliphatic regions of the spectrum. The results of the GIPAW calculations, together with the experimental values, are presented in table 7.3. However there are only slight differences in the calculated chemical shifts for the two structures, and it is therefore difficult to determine which structure provides closer agreement with the experimental data. The mean values of the magnitude of the difference between the experimental and calculated chemical shifts for form I and each of the form II structures is presented in table 7.4. For each structure these data show a better agreement in the aromatic region of the molecule than the aliphatic, although all of the mean deviations from experiment are relatively small, and are within the typical errors seen in GIPAW chemical shift calculations [107].

In order to compare the calculated data for the two form II structures more robustly, the results for each are analysed in terms of the differences between the form I and form II results in both experiment and calculation. A quantity, Δ, defined as

$$\Delta = \left| \left(\delta_{Exp.}^{(\text{Form I})} - \delta_{Exp.}^{(\text{Form II})} \right) - \left(\delta_{Calc.}^{(\text{Form I})} - \delta_{Calc.}^{(\text{Form II})} \right) \right|$$

was calculated for each of the form II structures. This value is independent of the

Table 7.3: Experimental and computational values for ibuprofen form II ^{13}C chemical shifts.

		Form II (a)		Form II (b)	
^{13}C Label	$\delta_{\text{Exp.}}$/ppm	$\delta_{\text{Calc.}}$/ppm	Δ(a)/ppm[a]	$\delta_{\text{Calc.}}$/ppm	Δ(b)/ppm[a]
1	183.6	186.9[b]	0.6	187.3[d]	0.0
2	45.3	48.3[c]	2.9	47.2[e]	1.4
3	18.7	15.3[c]	1.8	15.3[e]	2.0
4	138.0	136.8[b]	0.7	137.2[d]	0.3
5	130.0	129.9[b]	0.6	129.8[d]	0.6
6	127.4	128.8[b]	2.0	129.4[d]	2.7
7	141.5	143.3[b]	1.0	142.9[d]	0.7
8	130.0	130.5[b]	1.0	130.4[d]	1.1
9	127.5	125.3[b]	1.6	124.9[d]	1.8
10	45.3	45.0[c]	1.9	45.4[e]	1.8
11	30.5	33.3[c]	1.1	33.5[e]	1.0
12	23.4	23.1[c]	2.1	23.5[e]	2.2
13	23.4	21.5[c]	0.2	21.6[e]	0.1

[a] $\Delta = \left| \left(\delta_{Exp.}^{(\text{Form I})} - \delta_{Exp.}^{(\text{Form II})} \right) - \left(\delta_{Calc.}^{(\text{Form I})} - \delta_{Calc.}^{(\text{Form II})} \right) \right|$
[b] $\sigma_{\text{REF}} = 166.6$ ppm
[c] $\sigma_{\text{REF}} = 171.4$ ppm
[d] $\sigma_{\text{REF}} = 166.5$ ppm
[e] $\sigma_{\text{REF}} = 171.7$ ppm

reference value used and as such it allows a direct comparison between the calculated and experimental chemical shift values. A smaller value of Δ is indicative of a smaller difference in the changes between form I and form II in experiment and calculation. The results of the GIPAW calculations for form II(a) and (b) structures, together with experimental chemical shift values, are presented in table 7.3.

The mean values of Δ for the form II (a) and (b), of 1.3 and 1.2 ppm, respectively, are extremely close, suggesting little difference between the two structures. As with the differences between experiment and calculation for the individual structures discussed previously, these values are relatively small and within the typical errors in GIPAW calculations. However, considering the values of Δ for the carboxyl carbon (C1) and the carbon atom to which it is directly bonded (C2) (the two atoms defining the axis about which the carboxyl group is rotated), significantly lower values of Δ are seen for these two nuclei in the calculation for the form II(b) structure. As the nuclei likely to be most strongly affected by the rotation of the carboxyl group, this may be taken as an indication of a better agreement with the form II(b) structure.

Table 7.4: Mean differences between experimental and calculated chemical shifts in form I and form II ibuprofen.

	Mean $\lvert\delta_{Exp.} - \delta_{Calc.}\rvert$	
	Aliphatic	Aromatic
Form I	1.6	0.4
Form II(a)	2.0	1.2
Form II(b)	1.7	1.2

7.4 Summary and Conclusions

The results presented in this chapter show that ^{13}C CP MAS solid-state NMR experiments can be used to differentiate between the well known, pharmaceutically used, form of ibuprofen, and the recently identified polymorph produced by annealing of the amorphous solid. Variable temperature solid-state NMR experiments can also be used to track the emergence of the crystalline form II from the amorphous solid, while the sample is annealed inside an NMR probe maintained at a stable temperature; and the reconversion from form II to form I as the sample is subsequently heated. Through ^{13}C solid state NMR it is also possible to observe the formation of small amounts of form I ibuprofen, in addition to the significantly larger amount of form II produced during the annealing process.

Assignment of all thirteen peaks in the form I spectrum, and all nine peaks in the form II spectrum was possible by comparison of the experimental data with calculated (GIPAW) isotropic chemical shifts. The comparison between two structural models for form II, as originally published and with a rotated carboxyl group, did not unambiguously determine a better agreement between the experimental ^{13}C CP MAS results and the GIPAW calculated chemical shift for one of the potential form II structures compared to the other. Geometry optimisation of the two structures indicated that the change in the orientation of the carboxyl group had little effect on the positions of the majority of the atomic positions within the crystal structure, and it is therefore unsurprising that the calculated chemical shifts for the two structures were very similar. However the GIPAW calculations did indicate a better agreement with experiment for regions of the molecule close to the carboxyl group, when it was rotated. Despite small differences, the calculated chemical shifts for both structures are in relatively close agreement with the experimental values, indicating that the same polymorph was

produced in this work as in the previously published studies [151, 152].

Consequently, this work demonstrates the applicability of variable-temperature solid-state NMR experiments in the study of solid-state transitions between polymorphs in organic crystalline materials. Additionally, the significant differences in atomic positions between the unoptimised and optimised structures of ibuprofen form II(a), and the close agreement between experimental and calculated ^{13}C chemical shifts for the geometry optimised structure shows the value of combining density functional theory calculations with routine ^{13}C CP MAS experiments in the investigation of pharmaceutical samples.

CHAPTER

EIGHT

SUMMARY AND OUTLOOK

The work presented in this thesis has focussed on the development of solid-state NMR techniques for studying the structure of crystalline organic molecules, specifically in application to the study of active pharmaceutical ingredients. The ^{1}H DQ correlation NMR experiment is an established method of probing internuclear distances in organic solids. The density-matrix simulation results presented in chapter 4 facilitate a greater understanding of the relationship between the build-up in intensity of ^{1}H DQ correlation peaks as the duration of the recoupling periods in the pulse sequence is changed, and the three-dimensional arrangement of ^{1}H nuclei in the solid-state. Specifically, it was demonstrated that while the recoupling time at which a maximum in the build-up curve is reached is related to H–H distance only for the most intense peak at a particular single-quantum frequency, the relative maximum intensities of ^{1}H DQ build-up curves for peaks observed at that SQ frequency yields information on relative H–H distances. The use of density-matrix simulations, which were shown to agree well with experimental data, allowed parameters to be changed in a way that would not be possible in a real experiment. This additional flexibility permitted the investigation of the effect of dipolar truncation due to the presence of a strongly dipolar coupled pair of ^{1}H nuclei (in this case a CH_2 group). Using simulations to selectively exclude a single nucleus from the system, it was shown that the presence of such a strong interaction reduces the reliability of relative H–H distance information gained from DQ build-up analysis.

The initial investigation into the build-up of ^{1}H DQ peaks in a simple dipeptide was then expanded to pharmaceutically relevant systems, specifically the APIs sibenadet

HCl and γ-indomethacin. In the former case, two polymorphs were studied, with a known crystal structure for one. The ^{1}H DQ spectra of the two polymorphs were shown to exhibit an extremely similar pattern of peaks, indicative of a similar intermolecular hydrogen-bonding arrangement. However, analysis of the ^{1}H DQ build-up behaviour of peaks corresponding to hydrogen bonded protons revealed subtle differences between the two polymorphic forms. As with sibenadet HCl, the analysis of ^{1}H DQ build-up curves in γ-indomethacin was effectively limited to the hydrogen bonded region of the molecule, due to the poor resolution in the remainder of the spectrum. Consequently, the recently developed ^{1}H(DQ)–^{13}C refocussed INEPT experiment was used to exploit the higher resolution of a ^{13}C spectrum, allowing ^{1}H DQ peaks for individual aromatic resonances to be resolved. While interpretation of the build-up behaviour of these peaks is not as straightforward as in the simple ^{1}H DQ CRAMPS experiment, due to the additional dependence of the intensity on the INEPT magnetisation transfer, it remains possible to investigate the intermolecular packing by comparing the data to simulation results.

The final experimental results chapter used the more established ^{13}C CPMAS experiment to investigate polymorphism in ibuprofen. ^{13}C spectra were obtained for both the well known polymorph, corresponding to the pharmaceutical product, and a recently discovered second polymorph. With the aid of GIPAW chemical shift calculations, it was possible to fully assign the spectra of both polymorphs. A potential modification to the crystal structure of the new polymorph was investigated using GIPAW calculations, although it was not possible to unambiguously determine a better agreement with the experimental data.

Density-functional theory calculations (both geometry optimisation and shielding tensor calculations using the GIPAW method) were used extensively throughout the investigations reported in this thesis. DFT calculations were used both to provide reliable proton-proton distances as input for simulations of the ^{1}H DQ build-up, and to calculate isotropic chemical shift values which aided in the assignment of ^{1}H and ^{13}C NMR spectra. In the study of γ-indomethacin, GIPAW calculations were also used to investigate the effect of intermolecular interactions on the experimentally observed ^{1}H chemical shifts, by comparison of calculations for the full unit cell and an effectively isolated molecule. While the chemical shift is clearly strongly influenced by the

supramolecular structure, there is no simple method for going directly from spectrum to structure in solid-state NMR. The ability to combine experiment and calculation in this way therefore plays an essential role in structural investigations using solid-state NMR.

In conclusion, these results represent an advancement in the use of solid-state NMR in structural studies of crystalline organic systems. In particular, the build-up analysis of the ^{1}H DQ CRAMPS and ^{1}H(DQ)–^{13}C refocussed INEPT experiments allows structural information in the form of relative internuclear distances to be obtained for a wide range of pharmaceutically relevant compounds. It has also been shown that solid-state NMR data provides complementary information to other techniques, such as DFT calculations and diffraction experiments, and therefore is a valuable technique to be used in conjunction with such methods.

APPENDIX

A

REPRESENTATIVE SPINEVOLUTION INPUT FILES

The example SPINEVOLUTION input files presented below were used for one of the simulations performed for the work presented in chapter 4 (specifically the $n_{RCPL} = 7$ CH(Asp) simulation).

For an up to date explanation of the structure of these files, see the consolidated reference document available on the SPINEVOLUTION website [157]. The commands specified in this document replace some of those stated in the original paper [42].

A.1 Main Input File

```
****** The System **********************
spectrometer(MHz) 500
spinning_freq(kHz) 12.5
channels          H1
nuclei            H1 H1 H1 H1 H1 H1 H1 H1
atomic_coords     dipeptide_8spin_h6.cor
cs_isotropic      12.9 7.5 7.5 7.5 7.5 4.1 2.7 2.2 ppm
csa_parameters    chasp.csa
j_coupling        *
quadrupole        *
dip_switchboard   on_8.dsw on_8.dsw off_8.dsw on_8.dsw on_8.dsw
csa_switchboard   *
exchange_nuclei   (2 3 5)
bond_len_nuclei   *
bond_ang_nuclei   *
tors_ang_nuclei   *
groups_nuclei     *
******* Pulse Sequence ****************************
CHN 1
```

```
timing(usec)      (PC7_12.5_7.seq) 0 (80)1024 (PC7_12.5_e.seq) 0.25
power(kHz)        *                0 0        *                1000
phase(deg)        *                0 0        *                270
freq_offs(kHz)    *                0 0        *                0
**************************VARIABLES**********************
select_2 = rowmatrix("-2")
******* Options etc ************************************
rho0              F1z
observables       I6p
EulerAngles       zcw34
n_gamma           16
line_broaden(Hz)  10
zerofill          *
FFT_dimensions    *
```

A.2 Supplementary Input Files

```
dipeptide_8spin_h6.cor
6.26943  2.54043  16.62039  H1  (molecule B)
3.74518  1.59953  16.10280  H2  (molecule A)
4.31689  0.72449  15.08679  H3  (molecule A)
5.37310  5.42899  13.66821  H3  (molecule C)
2.91184  1.00676  15.02928  H4  (molecule A)
4.92252  2.84152  14.55003  H6  (Observe)
2.86824  2.06057  12.78639  H7  (molecule A)
4.26844  1.39253  12.76722  H8  (molecule A)
```

```
chasp.csa
1  16.3  0.16  28  171  252
2  24.3  0.22  351 59   48
3  22.9  0.28  99  140  178
4  22.9  0.28  303 10   282
5  20.9  0.09  241 23   325
6  25.5  0.53  243 83   277
7  27.8  0.71  201 119  177
8  28.4  0.82  13  20   23
```

```
on_8.dsw                  off_8.dsw
*                         *
1 *                       0 *
1 1 *                     0 0 *
1 1 1 *                   0 0 0 *
1 1 1 1 *                 0 0 0 0 *
1 1 1 1 1 *               0 0 0 0 0 *
1 1 1 1 1 1 *             0 0 0 0 0 0 *
1 1 1 1 1 1 1 *           0 0 0 0 0 0 0 *
```

```
PC7_12.5_7.seq
2.857   87.5   51.43   0
11.429  87.5   231.43  0
8.571   87.5   51.43   0
2.857   87.5   102.86  0
11.429  87.5   282.86  0
8.571   87.5   102.86  0
2.857   87.5   154.29  0
11.429  87.5   334.29  0
8.571   87.5   154.29  0
2.857   87.5   205.72  0
11.429  87.5   25.72   0
8.571   87.5   205.72  0
2.857   87.5   257.15  0
11.429  87.5   77.15   0
8.571   87.5   257.15  0
2.857   87.5   308.58  0
11.429  87.5   128.58  0
8.571   87.5   308.58  0
2.857   87.5   360.00  0
11.429  87.5   180.00  0
8.571   87.5   360.00  0
```

REFERENCES

[1] J. P. Bradley, C. Tripon, C. Filip, and S. P. Brown. Determining relative proton-proton proximities from the build-up of two-dimensional correlation peaks in ^{1}H double-quantum MAS NMR: insight from multi-spin density-matrix simulations. *Phys. Chem. Chem. Phys.*, 11(32):6941–6952, 2009.

[2] E. M. Purcell, H. C. Torrey, and R.V. Pound. Resonance absorption by nuclear magnetic moments in a solid. *Phys. Rev.*, 69:37–38, 1946.

[3] F. Bloch, W. W. Hansen, and M. Packard. The nuclear induction experiment. *Phys. Rev.*, 70:474–485, 1946.

[4] E. R. Andrew, A. Bradbury, and R. G. Eades. Nuclear magnetic resonance spectra from a crystal rotated at high speed. *Nature*, 182(4650):1659–1659, 1958.

[5] E. R. Andrew, A. Bradbury, and R. G. Eades. Removal of dipolar broadening of nuclear magnetic resonance spectra of solids by specimen rotation. *Nature*, 183(4678):1802–1803, 1959.

[6] I.J. Lowe. Free induction decays of rotating solids. *Phys. Rev. Lett.*, 2(7):285–287, 1959.

[7] A. Samoson. Magic-angle spinning extensions. Encyclopedia of Magnetic Resonance, Wiley, 2007.

[8] P. K. Madhu. High-resolution solid-state NMR spectroscopy of protons with homonuclear dipolar decoupling schemes under magic-angle spinning. *Solid State Nucl. Magn. Reson.*, 35(1):2–11, 2009.

[9] P. Hodgkinson. Chapter 5 - high-resolution ^{1}H NMR spectroscopy of solids. *Ann. Rep. NMR Spectrosc.*, 72:185–223, 2011.

[10] M Lee and W. I. Goldburg. Nuclear-magnetic-resonance line narrowing by a rotating rf field. *Phys. Rev. A*, 140:1261–1271, 1965.

[11] J. S. Waugh, L.M. Huber, and U. Haeberlen. Approach to high-resolution NMR in solids. *Phys. Rev. Lett.*, 20:180–182, 1968.

[12] U. Haeberlen and J.S. Waugh. Coherent averaging effects in magnetic resonance. *Phys. Rev.*, 175:453–467, 1968.

[13] B. C. Gerstein, R. G. Pembleton, R. C. Wilson, and L. M. Ryan. High-resolution NMR in randomly oriented solids with homonuclear dipolar broadening - combined multiple pulse NMR and magic angle spinning. *J. Chem. Phys.*, 66(1):361–362, 1977.

[14] G. Scheler, U. Haubenreisser, and H. Rosenberger. High-resolution ^{1}H-NMR in solids with multiple-pulse sequences and magic-angle sample spinning at 270-MHz. *J. Magn. Reson.*, 44:134–144, 1981.

[15] R. K. Harris, P. Jackson, L. H. Merwin, and B.J. Say. Perspectives in high-resolution solid-state nuclear magnetic resonance, with emphasis on combined rotation and multiple-pulse spectroscopy. *J. Chem. Soc., Faraday Trans. 1*, 84:3649–3672, 1988.

[16] A. Bielecki, A. C. Kolbert, and M. H. Levitt. Frequency-switched pulse sequences - homonuclear decoupling and dilute spin NMR in solids. *Chem. Phys. Lett.*, 155(4-5):341–346, 1989.

[17] E. Vinogradov, P. K. Madhu, and S. Vega. High-resolution proton solid-state NMR spectroscopy by phase-modulated lee-goldburg experiment. *Chem. Phys. Lett.*, 314(5-6):443–450, 1999.

[18] D. Sakellariou, A. Lesage, P. Hodgkinson, and L. Emsley. Homonuclear dipolar decoupling in solid-state NMR using continuous phase modulation. *Chem. Phys. Lett.*, 319(3-4):253–260, 2000.

[19] B. Elena, G. de Paepe, and L. Emsley. Direct spectral optimisation of proton-proton homonuclear dipolar decoupling in solid-state NMR. *Chem. Phys. Lett.*, 398(4-6):532–538, 2004.

[20] S. R. Hartmann and E. L. Hahn. Nuclear double resonance in the rotating frame. *Phys. Rev.*, 128:2042–2053, 1962.

[21] A. Pines, M. G. Gibby, and J.S. Waugh. Proton-enhanced nuclear induction spectroscopy. a method for high resolution NMR of dilute spins in solids. *J. Chem. Phys.*, 56:1776–1777, 1972.

[22] A. Pines, M. G. Gibby, and J. S. Waugh. Proton-enhanced NMR of dilute spins in solids. *J. Chem. Phys.*, 59(2):569–590, 1973.

[23] J. Schaefer and E. O. Stejskal. ^{13}C nuclear magnetic-resonance of polymers spinning at magic angle. *J. Am. Chem. Soc.*, 98(4):1031–1032, 1976.

[24] T. Gullion and J. Schaefer. Rotational-echo double-resonance NMR. *J. Magn. Reson.*, 81:196–200, 1989.

[25] S. P. Brown. Probing proton-proton proximities in the solid state. *Prog. Nucl. Magn. Reson. Spectrosc.*, 50(4):199–251, 2007.

[26] B. H. Meier and W. L. Earl. Excitation of multiple quantum transitions under magic angle spinning conditions: Adamantane. *J. Chem. Phys.*, 85:4905–4911, 1986.

[27] B. H. Meier and W. L. Earl. A double-quantum filter for rotating solids. *J. Am. Chem. Soc.*, 109:7937–7942, 1987.

[28] R. Tycko and G. Dabbagh. Measurement of nuclear magnetic dipole-dipole couplings in magic angle spinning NMR. *Chem. Phys. Lett.*, 173:461–465, 1990.

[29] W. Sommer, J. Gottwald, D. E. Demco, and H. W. Spiess. Dipolar heteronuclear multiple-quantum NMR spectroscopy in rotating solids. *J. Magn. Reson., Ser. A*, 113:131–134, 1995.

[30] Y. K. Lee, N. D. Kurur, M. Helmle, O. G. Johannessen, N. C. Nielsen, and M. H. Levitt. Efficient dipolar recoupling in the NMR of rotating solids - a sevenfold symmetrical radiofrequency pulse sequence. *Chem. Phys. Lett.*, 242(3):304–309, 1995.

[31] M. Hohwy, H. J. Jakobsen, M. Eden, M. H. Levitt, and N. C. Nielsen. Broadband dipolar recoupling in the nuclear magnetic resonance of rotating solids: A compensated C7 pulse sequence. *J. Chem. Phys.*, 108(7):2686–2694, 1998.

[32] M. Carravetta, M. Eden, O. G. Johannessen, H. Luthman, P. J. E. Verdegem, J. Lugtenburg, A. Sebald, and M. H. Levitt. Estimation of carbon-carbon bond lengths and medium-range internuclear: Distances by solid-state nuclear magnetic resonance. *J. Am. Chem. Soc.*, 123(43):10628–10638, 2001.

[33] J. Baum, M. Munowitz, A. N. Garroway, and A. Pines. Multiple-quantum dynamics in solid-state NMR. *J. Chem. Phys.*, 83:2015–2025, 1985.

[34] I. Schnell, S. P. Brown, H. Y. Low, H. Ishida, and H. W. Spiess. An investigation of hydrogen bonding in benzoxazine dimers by fast magic-angle spinning and double-quantum ^{1}H NMR spectroscopy. *J. Am. Chem. Soc.*, 120(45):11784–11795, 1998.

[35] S. P. Brown, I. Schnell, J. D. Brand, K. Mullen, and H. W. Spiess. An investigation of pi-pi packing in a columnar hexabenzocoronene by fast magic-angle spinning and double-quantum ^{1}H solid-state NMR spectroscopy. *J. Am. Chem. Soc.*, 121(28):6712–6718, 1999.

[36] S. P. Brown, I. Schnell, J. D. Brand, K. Mullen, and H. W. Spiess. A ^{1}H double-quantum magic-angle spinning solid-state NMR investigation of packing and dynamics in triphenylene and hexabenzocoronene derivatives. *J. Mol. Struct.*, 521:179–195, 2000.

[37] I. Schnell, A. Lupulescu, S. Hafner, D. E. Demco, and H. W. Spiess. Resolution enhancement in multiple-quantum MAS NMR spectroscopy. *J. Magn. Reson.*, 133(1):61–69, 1998.

[38] S. P. Brown, A. Lesage, B. Elena, and L. Emsley. Probing proton-proton proximities in the solid state: High-resolution two-dimensional ^{1}H-^{1}H double-quantum CRAMPS NMR spectroscopy. *J. Am. Chem. Soc.*, 126(41):13230–13231, 2004.

[39] E. Vinogradov, P. K. Madhu, and S. Vega. Proton spectroscopy in solid state nuclear magnetic resonance with windowed phase modulated lee-goldburg decoupling sequences. *Chem. Phys. Lett.*, 354(3-4):193–202, 2002.

[40] P. Hodgkinson and L. Emsley. Numerical simulation of solid-state NMR experiments. *Prog. Nucl. Magn. Reson. Spectrosc.*, 36(3):201–239, 2000.

[41] M. Bak, J. T. Rasmussen, and N. C. Nielsen. Simpson: A general simulation program for solid-state NMR spectroscopy. *J. Magn. Reson.*, 147(2):296–330, 2000.

[42] M. Veshtort and R. G. Griffin. SPINEVOLUTION: a powerful tool for the simulation of solid and liquid state NMR experiments. *J. Magn. Reson.*, 178(2):248–282, 2006.

[43] P. Hodgkinson. pNMRsim: a general simulation program for large problems in solid-state NMR. URL: `http://www.dur.ac.uk/solids.nmr/software/pnmrsim/`.

[44] N. S. Barrow, J. R. Yates, S. A. Feller, D. Holland, S. E. Ashbrook, P. Hodgkinson, and S. P. Brown. Towards homonuclear J solid-state NMR correlation experiments for half-integer quadrupolar nuclei: experimental and simulated ^{11}B MAS spin-echo dephasing and calculated $^{2}J_{BB}$ coupling constants for lithium diborate. *Phys. Chem. Chem. Phys.*, 13:5778–5789, 2011.

[45] V. E. Zorin, M. Ernst, S. P. Brown, and P. Hodgkinson. Insights into homonuclear decoupling from efficient numerical simulation: Techniques and examples. *J. Magn. Reson.*, 192(2):183–196, 2008.

[46] J. M. Griffin, C. Tripon, A. Samoson, C. Filip, and S. P. Brown. Low-load rotor-synchronised hahn-echo pulse train (RS-HEPT) ^{1}H decoupling in solid-state NMR: factors affecting MAS spin-echo dephasing times. *Magn. Reson. Chem.*, 45:S198–S208, 2007.

[47] I. Scholz, P. Hodgkinson, B. H. Meier, and M. Ernst. Understanding two-pulse phase-modulated decoupling in solid-state NMR. *J. Chem. Phys.*, 130:114510, 2009.

[48] S. J. Clark, M. D. Segall, C. J. Pickard, P. J. Hasnip, M. J. Probert, K. Refson, and M. C. Payne. First principles methods using CASTEP. *Z. Kristallogr.*, 220(5-6):567–570, 2005.

[49] D. Vanderbilt. Soft self-consistent pseudopotentials in a generalized eigenvalue formalism. *Phys. Rev. B*, 41(11):7892–7895, 1990.

[50] C. J. Pickard and F. Mauri. All-electron magnetic response with pseudopotentials: NMR chemical shifts. *Phys. Rev. B*, 63(24), 2001.

[51] J. R. Yates, C. J. Pickard, and F. Mauri. Calculation of NMR chemical shifts for extended systems using ultrasoft pseudopotentials. *Phys. Rev. B*, 76(2), 2007.

[52] N. Mifsud, B. Elena, C. J. Pickard, A. Lesage, and L. Emsley. Assigning powders to crystal structures by high-resolution ^{1}H-^{1}H double quantum and ^{1}H-^{13}C J-INEPT solid-state NMR spectroscopy and first principles computation. a case study of penicillin G. *Phys. Chem. Chem. Phys.*, 8(29):3418–3422, 2006.

[53] E. Zurek, C. J. Pickard, and J. Autschbach. A density functional study of the ^{13}C NMR chemical shifts in functionalized single-walled carbon nanotubes. *J. Am. Chem. Soc.*, 110:11995–12004, 2007.

[54] A. Soleilhavoup, M. R. Hampson, S. J. Clark, J. S. O. Evans, and P. Hodgkinson. Using ^{17}O solid-state NMR and first principles calculation to characterise structure and dynamics in inorganic framework materials. *Magn. Reson. Chem.*, 45:S144–S155, 2007.

[55] A. J. Robbins, W. T. K. Ng, E. Jochym, T. W. Keal, S. J. Clark, D. J. Tozer, and P. Hodgkinson. Combining insights from solid-state NMR and first principles calculation: applications to the ^{19}F NMR of octafluoronaphthalene. *Phys. Chem. Chem. Phys.*, 9:2389–2396, 2007.

[56] A. C. Uldry, J. M. Griffin, J. R. Yates, M. Perez-Torralba, M. D. S. Maria, A. L. Webber, M. L. L. Beaumont, A. Samoson, R. M. Claramunt, C. J. Pickard, and S. P. Brown. Quantifying weak hydrogen bonding in uracil and 4-cyano-4 '-ethynylbiphenyl: A combined computational and experimental investigation of NMR chemical shifts in the solid state. *J. Am. Chem. Soc.*, 130(3):945–954, 2008.

[57] R. K. Harris, P. Hodgkinson, T. Larsson, A. Muruganantham, I. Ymen, D. S. Yufit, and V. Zorin. Characterization of polymorphs and solvates of terbutaline sulfate. *Cryst. Growth Des.*, 8(1):80–90, 2008.

[58] E. Salager, G. M. Day, R. S. Stein, C. J. Pickard, B. Elena, and L. Emsley. Powder crystallography by combined crystal structure prediction and high-resolution ^{1}H solid-state NMR spectroscopy. *J. Am. Chem. Soc.*, 132(8):2564–2566, 2010.

[59] A. L. Webber, B. Elena, J. M. Griffin, J. R. Yates, T. N. Pham, F. Mauri, C. J. Pickard, A. M. Gil, R. Stein, A. Lesage, L. Emsley, and S. P. Brown. Complete ^{1}H resonance assignment of beta-maltose from ^{1}H-^{1}H DQ-SQ CRAMPS and ^{1}H (DQ-DUMBO)-^{13}C SQ refocused INEPT 2D solid-state NMR spectra and first principles GIPAW calculations. *Phys. Chem. Chem. Phys.*, 12(26):6970–83, 2010.

[60] R. K. Harris, P. Hodgkinson, V. Zorin, J. N. Dumez, B. Elena-Herrmann, L. Emsley, E. Salager, and R. S. Stein. Computation and NMR crystallography of terbutaline sulfate. *Magn. Reson. Chem.*, 48:S103–S112, 2010.

[61] M. R. Mitchell, S. W. Reader, K. E. Johnston, C. J. Pickard, K. R. Whittle, and S. E. Ashbrook. ^{119}Sn MAS NMR and first-principles calculations for the investigation of disorder in stannate pyrochlores. *Phys. Chem. Chem. Phys.*, 13:488–497, 2011.

[62] Joel Bernstein. *Polymorphism in molecular crystals*. Oxford University Press, Oxford, Oxford, 2002.

[63] T. L. Threlfall. Analysis of organic polymorphs - a review. *Analyst*, 120(10):2435–2460, 1995.

[64] H. Eckert. Amorphous materials. Encyclopedia of Magnetic Resonance, 2007.

[65] C. Gustafsson, H. Lennholm, T. Iversen, and C. Nyström. Comparison of solid-state NMR and isothermal microcalorimetry in the assessment of the amorphous component of lactose. *Int. J. Pharm.*, 174:234–252, 1998.

[66] D. C. Apperley, A. H. Forster, R. Fournier, R. K. Harris, P. Hodgkinson, R. W. Lancaster, and T. Rades. Characterisation of indomethacin and nifedipine using variable-temperature solid-state NMR. *Magn. Reson. Chem.*, 43(11):881–892, 2005.

[67] T. N. Pham, S. A. Watson, A. J. Edwards, M. Chavda, J. S. Clawson, M. Strohmeier, and F. G. Vogt. Analysis of amorphous solid dispersions using 2D solid-state NMR and ^{1}H T_1 relaxation measurements. *Mol. Pharmaceutics*, 7:1667–1691, 2010.

[68] R. K. Harris. NMR crystallography: the use of chemical shifts. *Solid State Sci.*, 6(10):1025–1037, 2004.

[69] J. A. Ripmeester. Application of solid-state ^{13}C NMR to the study of polymorphs, clathrates and complexes. *Chem. Phys. Lett.*, 74:536–538, 1980.

[70] R. K. Harris. NMR studies of organic polymorphs & solvates. *Analyst*, 131(3):351–373, 2006.

[71] M. Geppi, G. Mollica, S. Borsacchi, and C. A. Veracini. Solid-state NMR studies of pharmaceutical systems. *Appl. Spectrosc. Rev.*, 43(3):202–302, 2008.

[72] J. M. Griffin, D. R. Martin, and S. P. Brown. Distinguishing anhydrous and hydrous forms of an active pharmaceutical ingredient in a tablet formulation using solid-state NMR spectroscopy. *Angew. Chem. Int. Ed.*, 46(42):8036–8038, 2007.

[73] S. P. Brown, T. Schaller, U. P. Seelbach, F. Koziol, C. Ochsenfeld, F. G. Klarner, and H. W. Spiess. Structure and dynamics of the host-guest complex of a molecular tweezer: Coupling synthesis, solid-state NMR, and quantum-chemical calculations. *Angew. Chem. Int. Ed.*, 40(4):717–720, 2001.

[74] S. P. Brown and H. W. Spiess. Advanced solid-state NMR methods for the elucidation of structure and dynamics of molecular, macromolecular, and supramolecular systems. *Chem. Rev.*, 101(12):4125–4155, 2001.

[75] S. P. Brown, X. X. Zhu, K. Saalwachter, and H. W. Spiess. An investigation of the hydrogen-bonding structure in bilirubin by ^{1}H double-quantum magic-angle spinning solid-state NMR spectroscopy. *J. Am. Chem. Soc.*, 123(18):4275–4285, 2001.

[76] G. R. Goward, I. Schnell, S. P. Brown, H. W. Spiess, H. D. Kim, and H. Ishida. Investigation of an N $\cdots$ H hydrogen bond in a solid benzoxazine dimer by ^{1}H–^{15}N NMR correlation techniques under fast magic-angle spinning. *Magn. Reson. Chem.*, 39:S5–S17, 2001.

[77] A. J. Aguiar, Jr. Krc, J., A. W. Kinkel, and J. C. Samyn. Effect of polymorphism on the absorption of chloramphenicol from chloramphenicol palmitate. *J. Pharm. Sci.*, 56(7):847–53, 1967.

[78] M. Draguet-Brughmans, R. Bouche, J. P. Flandre, and A. Vandenbulke. Polymorphism and bioavailability of pentobarbital. *Pharm. Acta Helv.*, 54:140–145, 1979.

[79] S. Kachi, M. Terada, and H. Hashimoto. Effects of amorphous and polymorphs of PF1022A, a new antinematode drug, on angiostrongylus costaricensis in mice. *Jpn. J. Pharmacol.*, 77:235–245, 1998.

[80] S. R. Chemburkar, J. Bauer, K. Deming, H. Spiwek, K. Patel, J. Morris, R. Henry, S. Spanton, W. Dziki, W. Porter, J. Quick, P. Bauer, J. Donaubauer, B. A. Narayanan, M. Soldani, D. Riley, and K. McFarland. Dealing with the impact of ritonavir polymorphs on the late stages of bulk drug process development. *Org. Process Res. Dev.*, 4(5):413–417, 2000.

[81] B. J. Price, J. W. Clitherow, and J. Bradshaw. Aminoalkyl furan derivatives. United States Patent No. 4128658, 1978.

[82] Malcolm H. Levitt. *Spin Dynamics.* Wiley, Chichester, 2001.

[83] Melinda J. Duer. *Introduction to Solid-State NMR Spectroscopy.* Blackwell, Oxford, Oxford, 2004.

[84] P. J. Hore, J. A. Jones, and S. Wimperis. *NMR: The Toolkit.* Oxford University Press, Oxford, 2000.

[85] O. W. Sorenson, G. W. Eich, M. H. Levitt, G. Bodenhausen, and R. R. Ernst. Product operator-formalism for the description of NMR pulse experiments. *Prog. Nucl. Magn. Reson. Spectrosc.*, 16:163–192, 1983.

[86] R. K. Harris, E. D. Becker, S. M. C. De Menezes, P. Granger, R. E. Hoffman, and K. W. Zilm. Further conventions for NMR shielding and chemical shifts (IUPAC recommendations 2008). *Pure Appl. Chem.*, 80(1):59–84, 2008.

[87] D. D. Traficante. Relaxation: An introduction. Encyclopedia of Magnetic Resonance, Wiley, 2007.

[88] W. P. Aue, E. Bartholdi, and R. R. Ernst. Two-dimensional spectroscopy. Application to nuclear magnetic resonance. *J. Chem. Phys.*, 64:2229–2246, 1976.

[89] C. Griesinger, O.W. Sorenson, and R. R. Ernst. 3-dimensional fourier spectroscopy - application to high-resolution NMR. *J. Magn. Reson.*, 84:14–63, 1989.

[90] G. M. Clore and A. M. Gronenborn. Two-, three-, and four-dimensional NMR methods for obtaining larger and more precise three-dimensional structures of proteins in solution. *Annu. Rev. Biophys. Bio.*, 20:29–63, 1991.

[91] D. J. States, R. A. Haberkorn, and D. J. Ruben. A two-dimensional nuclear overhauser experiment with pure absorption phase in four quadrants. *J. Magn. Reson.*, 48:286–292, 1982.

[92] P. Hodgkinson. Heteronuclear decoupling in the nmr of solids. *Prog. Nucl. Magn. Reson. Spectrosc.*, 46:197–222, 2005.

[93] A. E. Bennett, C. M. Rienstra, M. Auger, K. V. Lakshmi, and R. G. Griffin. Heteronuclear decoupling in rotating solids. *J. Chem. Phys.*, 103(16):6951–6958, 1995.

[94] B. M. Fung, A. K. Khitrin, and K. Ermolaev. An improved broadband decoupling sequence for liquid crystals and solids. *J. Magn. Reson.*, 142(1):97–101, 2000.

[95] A. Lesage, D. Sakellariou, S. Hediger, B. Elena, P. Charmont, S. Steuernagel, and L. Emsley. Experimental aspects of proton NMR spectroscopy in solids using phase-modulated homonuclear dipolar decoupling. *J. Magn. Reson.*, 163(1):105–113, 2003.

[96] D. P. Burum, M. Linder, and R. R. Ernst. Low-power multipulse line narrowing in solid-state NMR. *J. Magn. Reson.*, 44(1):173–188, 1981.

[97] M. H. Levitt. Symmetry-based pulse sequences in magic-angle spinning solid-state NMR. Encyclopedia of Magnetic Resonance, 2007.

[98] G. Metz, L. Wu, and S. O. Smith. Ramped-amplitude cross-polarization in magic-angle-spinning NMR. *J. Magn. Reson.*, 110:219–227, 1994.

[99] P. Caravatti, P. Neuenschwander, and R.R. Ernst. Characterisation of heterogeneous polymer blends by two-dimensional proton spin diffusion spectroscopy. *Macromolecules*, 18:119–122, 1985.

[100] G. A. Morris and R. Freeman. Enhancement of nuclear magnetic resonance signals by polarization transfer. *J. Am. Chem. Soc.*, 101:760–762, 1979.

[101] D. P. Burum and R. R. Ernst. Net polarization transfer via a J-ordered state for signal enhancement of low-sensitivity nuclei. *J. Magn. Reson.*, 39:163–168, 1980.

[102] B. Elena, A. Lesage, S. Steuernagel, A. Bockmann, and L. Emsley. Proton to carbon-13 INEPT in solid-state NMR spectroscopy. *J. Am. Chem. Soc.*, 127(49):17296–17302, 2005.

[103] M. Aluas, C. Tripon, J. M. Griffin, X. Filip, V. Ladizhansky, R. G. Griffin, S. P. Brown, and C. Filip. CHHC and ^{1}H–^{1}H magnetization exchange: Analysis by experimental solid-state NMR and 11-spin density-matrix simulations. *J. Magn. Reson.*, 199(2):173–187, 2009.

[104] M. C. Butler, J. N. Dumez, and L. Emsley. Dynamics of large nuclear-spin systems from low-order correlations in liouville space. *Chem. Phys. Lett.*, 477:377–381, 2009.

[105] M. D. Segall, P. J. D. Lindan, M. J. Probert, C. J. Pickard, P. J. Hasnip, S. J. Clark, and M. C. Payne. First-principles simulation: ideas, illustrations and the CASTEP code. *J. Phys.-Condens. Matter*, 14:2717–2744, 2002.

[106] J. R. Yates and C. J. Pickard. Computation of magnetic resonance parameters for crystalline systems: Principles. Encyclopedia of Magnetic Resonance, Wiley, 2007.

[107] R. K. Harris, P. Hodgkinson, C. J. Pickard, J. R. Yates, and V. Zorin. Chemical shift computations on a crystallographic basis: some relflections and comments. *Magn. Reson. Chem.*, 45:S174–S186, 2007.

[108] J. R. Yates, T. N. Pham, C. J. Pickard, F. Mauri, A. M. Amado, A. M. Gil, and S. P. Brown. An investigation of weak CH $\cdots$ O hydrogen bonds in maltose anomers by a combination of calculation and experimental solid-state NMR spectroscopy. *J. Am. Chem. Soc.*, 127(29):10216–10220, 2005.

[109] J. R. Yates, S. E. Dobbins, C. J. Pickard, F. Mauri, P. Y. Ghi, and R. K. Harris. A combined first principles computational and solid-state NMR study of a molecular crystal: flurbiprofen. *Phys. Chem. Chem. Phys.*, 7:1402–1407, 2005.

[110] R. K. Harris, S. A. Joyce, C. J. Pickard, S. Cadars, and L. Emsley. Assigning carbon-13 NMR spectra to crystal structures by the inadequate pulse sequence and first principles computation: a case study of two forms of testosterone. *Phys. Chem. Chem. Phys.*, 8(1):137–143, 2006.

[111] A. L. Webber, L. Emsley, R. M. Claramunt, and S. P. Brown. NMR crystallography of campho[2,3-c]pyrazole (Z'=6): Combining high-resolution ^{1}H-^{13}C solid-state MAS NMR spectroscopy and GIPAW chemical-shift calculations. *J. Phys. Chem. A*, 115:10435–10442, 2010.

[112] J. P. Perdew, K. Burke, and M. Ernzerhof. Generalized gradient approximation made simple. *Phys. Rev. Lett.*, 77(18):3865–3868, 1996.

[113] H. J. Monkhorst and J. D. Pack. Special points for brillouin-zone integrations. *Phys. Rev. B*, 13:5188–5192, 1976.

[114] C. H. Gorbitz. Crystal and molecular-structures of the isomeric dipeptides alpha-l-aspartyl-l-alanine and beta-l-aspartyl-l-alanine. *Acta Chem. Scand. Ser. B*, 41(9):679–685, 1987.

[115] A. Schleicher, K. Muller, and G. Kothe. 2-dimensional nuclear magnetic-resonance-relaxation spectroscopy of molecular-solids. *J. Chem. Phys.*, 92(11):6432–6440, 1990.

[116] J. Brus, H. Petrickova, and J. Dybal. Influence of local molecular motions on the determination of ^{1}H-^{1}H internuclear distances measured by 2D ^{1}H spin-exchange experiments. *Solid State Nucl. Magn. Reson.*, 23(4):183–197, 2003.

[117] V. E. Zorin. Gsim - visualisation and processing tool for NMR experiments and simulations. URL: `http://sourceforge.net/projects/gsim`.

[118] I. Schnell and H. W. Spiess. High-resolution ^{1}H NMR spectroscopy in the solid state: Very fast sample rotation and multiple-quantum coherences. *J. Magn. Reson.*, 151(2):153–227, 2001.

[119] R. Graf, D. E. Demco, J. Gottwald, S. Hafner, and H. W. Spiess. Dipolar couplings and internuclear distances by double-quantum nuclear magnetic resonance spectroscopy of solids. *J. Chem. Phys.*, 106(3):885–895, 1997.

[120] P. Hodgkinson and L. Emsley. The accuracy of distance measurements in solid-state NMR. *J. Magn. Reson.*, 139(1):46–59, 1999.

[121] D. E. Bugay. Solid-state nuclear magnetic resonance spectroscopy: Theory and pharmaceutical applications. *Pharm. Res.*, 10:317–327, 1993.

[122] S. Byrn, R. Pfeiffer, M. Ganey, C. Hoiberg, and G. Poochikian. Pharmaceutical solids - a strategic approach to regulatory considerations. *Pharm. Res.*, 12(7):945–954, 1995.

[123] R. V. Bonnert, R. C. Brown, D. Chapman, D. R. Cheshire, J. Dixon, F. Ince, E. C. Kinchin, A. J. Lyons, A. M. Davis, C. Hallam, S. T. Harper, J. F. Unitt, I. G. Dougall, D. M. Jackson, K. McKechnie, A. Young, and W. T. Simpson. Dual D-2-receptor and beta(2)-adrenoceptor agonists for the treatment of airway diseases. 1. discovery and biological evaluation of some 7-(2-aminoethyl)-4-hydroxybenzothiazol-2(3H)-one analogues. *J. Med. Chem.*, 41(25):4915–4917, 1998.

[124] M. E. Giles, C. Thomson, S. C. Eyley, A. J. Cole, C. J. Goodwin, P. A. Hurved, A. J. G. Morlin, J. Tornos, S. Atkinson, C. Just, J. C. Dean, J. T. Singleton, A. J. Longton, I. Woodland, A. Teasdale, B. Gregertsen, H. Else, M. S. Athwal, S. Tatterton, J. M. Knott, N. Thompson, and S. J. Smith. Development of a manufacturing process for sibenadet hydrochloride, the active ingredient of Viozan. *Org. Process Res. Dev.*, 8(4):628–642, 2004.

[125] S. D. Cosgrove, G. Steele, T. K. Austin, A. P. Plumb, B. Stensland, E. Ferrari, and K. J. Roberts. Understanding the polymorphic behavior of sibenadet hydrochloride through detailed studies integrating structural and dynamical assessment. *J. Pharm. Sci.*, 94(11):2403–2415, 2005.

[126] Daily Telegraph. AstraZeneca drops trial of Viozan lung drug. 28/6/2001, Retrieved online 21/2/2011. URL: `http://www.telegraph.co.uk/finance/2723739/AstraZeneca-drops-trial-of-Viozan-lung-drug.html`.

[127] S.P. Brown. Hydrogen bonding in crystalline organic solids. Encyclopedia of Magnetic Resonance, 2007.

[128] V. E. Zorin, S. P. Brown, and P. Hodgkinson. Quantification of homonuclear dipolar coupling networks from magic-angle spinning ^{1}H NMR. *Mol. Phys.*, 104(2):293–304, 2006.

[129] F. D. Hart and P. L. Boardman. Indomethacin: A new non-steroid anti-inflammatory agent. *Br. Med. J.*, 2:965, 1963.

[130] Kistenma.Tj and R. E. Marsh. Crystal and molecular structure of an antiinflammatory agent, indomethacin, 1-(para chlorobenzoyl)-5-methoxy-2-methylindole-3-acetic acid. *J. Am. Chem. Soc.*, 94(4):1340–1345, 1972.

[131] X. M. Chen, K. R. Morris, U. J. Griesser, S. R. Byrn, and J. G. Stowell. Reactivity differences of indomethacin solid forms with ammonia gas. *J. Am. Chem. Soc.*, 124:15012–15019, 2002.

[132] P. J. Cox and P. L. Manson. γ-indomethacin at 120 K. *Acta Crystallogr., Sect. E: Struct. Rep. Online*, 59:O986–O988, 2003.

[133] K. J. Crowley and G. Zografi. Cryogenic grinding of indomethacin polymorphs and solvates: Assessment of amorphous phase formation and amorphous phase physical stability. *J. Pharm. Sci.*, 91:492–507, 2002.

[134] S. Basavoju, D. Bostrom, and S. P. Velaga. Indomethacin-saccharin cocrystal: Design, synthesis and preliminary pharmaceutical characterization. *Pharm. Res.*, 25(3):530–541, 2008.

[135] M. Alleso, S. P. Velaga, A. Alhalaweh, C. Cornett, M. A. Rasmussen, F. van den Berg, H. L. de Diego, and J. Rantanen. Near-infrared spectroscopy for cocrystal screening. a comparative study with raman spectroscopy. *Anal. Chem.*, 80:7755–7764, 2008.

[136] M. S. Jung, J. S. Kim, A. Alhalaweh, W. Cho, S. J. Hwang, and S. P. Velaga. Bioavailability of indomethacin-saccharin cocrystals. *J. Pharm. Pharmacol.*, 62:1560–1568, 2010.

[137] A. Alhalaweh and S. P. Velaga. Formation of cocrystals from stoichiometric solutions of incongruently saturating systems by spray drying. *Cryst. Growth Des.*, 10:3302–3305, 2010.

[138] K. Masuda, S. Tabata, H. Kono, Y. Sakata, T. Hayase, E. Yonemochi, and K. Terada. Solid-state ¸NMR study of indomethacin polymorphism. *Int. J. Pharm.*, 318(1-2):146–153, 2006.

[139] J. B. Guilbaud, L. Cummings, and Y. Z. Khimyak. Encapsulation of indomethacin in PVP: Solid-state NMR studies. *Macromol. Symp.*, 251:41–46, 2007.

[140] C. J. Pickard, E. Salager, G. Pintacuda, B. Elena, and L. Emsley. Resolving structures from powders by NMR crystallography using combined proton spin diffusion and plane wave dft calculations. *J. Am. Chem. Soc.*, 129(29):8932–+, 2007.

[141] J. N. Dumez and C. J. Pickard. Calculation of NMR chemical shifts in organic solids: Accounting for motional effects. *J. Chem. Phys.*, 130(10), 2009.

[142] S. P. Brown, I. Schnell, J. D. Brand, K. Mullen, and H. W. Spiess. The competing effects of pi-pi packing and hydrogen bonding in a hexabenzocoronene carboxylic acid derivative: A ^{1}H solid-state MAS NMR investigation. *Phys. Chem. Chem. Phys.*, 2(8):1735–1745, 2000.

[143] J. Schmidt, A. Hoffman, H. W. Spiess, and D. Sebastiani. Bulk chemical shifts in hydrogen-bonded systems from first-principles calculations and solid-state NMR. *J. Phys. Chem. B*, 110:23204–23210, 2006.

[144] C. Ochsenfeld. An ab initio study of the relation between NMR chemical shifts and solid-state structures: hexabenzocoronene derivatives. *Phys. Chem. Chem. Phys.*, 2:2153–2159, 2000.

[145] C. Ochsenfeld, S.P. Brown, I. Schnell, J. Gauss, and H. W. Spiess. Structure assignment in the solid-state by the coupling of quantum chemical calculations with NMR experiments: A columnar hexabenzocoronene derivative. *J. Am. Chem. Soc.*, 123:2597–2606, 2001.

[146] C. Ochsenfeld, F. Koziol, S. P. Brown, T. Schaller, U. P. Seelbach, and F. G. Klarner. A study of a molecular tweezer host-guest system by a combination of quantum-chemical calculations and solid-state NMR experiments. *Solid State Nucl. Magn. Reson.*, 22:128–153, 2002.

[147] S. S. Adams. The propanoic acids: A personal perspective. *J. Clin. Pharmacol*, 32:317–323, 1992.

[148] World Health Organisation. WHO model list. URL: `http://whqlibdoc.who.int/hq/2005/a87017_eng.pdf`; retrieved 11/3/2011.

[149] S. S. Adams, P. Bresloff, and C. G. Manson. Pharmacological differences between the optical isomers of ibuprofen: evidence for metabolic inversion of ibuprofen. *J. Pharm. Pharmacol.*, 28:256–257, 1976.

[150] H. Cheng, J. D. Rogers, J. L. Demetriades, S. D. Holland, J. R. Seibold, and E. Depuy. Pharmacokinetics and bioinversion of ibuprofen enantiomers in humans. *Pharm. Res.*, 11:824–830, 1994.

[151] E. Dudognon, F. Danede, M. Descamps, and N. T. Correia. Evidence for a new crystalline phase of racemic ibuprofen. *Pharm. Res.*, 25(12):2853–2858, 2008.

[152] P. Derollez, E. Dudognon, F. Affouard, F. Danede, N. T. Correia, and M. Descamps. Ab initio structure determination of phase II of racemic ibuprofen by X-ray powder diffraction. *Acta Crystallogr., Sect. B: Struct. Sci*, 66:76–80, 2010.

[153] M. Geppi, S. Guccione, G. Mollica, R. Pignatello, and C. A. Veracini. Molecular properties of ibuprofen and its solid dispersions with eudragit RL100 studied by solid-state nuclear magnetic resonance. *Pharm. Res.*, 22:1544–1555, 2005.

[154] D. H. Barich, J. M. Davis, L. J. Schieber, M. T. Zell, and E. J. Munson. Investigation of solid-state NMR line widths of ibuprofen in drug formulations. *J. Pharm. Sci.*, 95(7):1586–1594, 2006.

[155] D. L. Vander Hart. Magnetic susceptibility and high resolution NMR of liquids and solids. Encyclopedia of Magnetic Resonance, Wiley, 2007.

[156] L. Pauling. The diamagnetic anisotropy of aromatic molecules. *J. Chem. Phys.*, 4:673–677, 1936.

[157] M. Veshtort. Spinevolution reference version 3.4.2. URL: `http://web.mit.edu/fbml/cmr/griffin-group/SPINEVOLUTION/SPINEVOLUTION%20v3.4.pdf`, 2010.